Acta Pharmacologica Sinica (2011) 32: 981–982
 1671-4083/11 $32.00
www.nature.com/aps

Research Highlight

Antcin A contributs to anti-inflammatory effect of *Niuchangchih* (*Antrodia camphorata*)

Zhen-ming LU, Zheng-hong XU*

Acta Pharmacologica Sinica (2011) 32: 981–982; doi: 10.1038/aps.2011.104

Inflammation is the responses of body to harmful stimuli in many pathological conditions. Prevention and treatment of inflammation are the main indication of a variety of natural products. Recently, *Niuchangchih* (*Antrodia camphorata*), a medicinal mushroom in Taiwan, has received considerable attention from the public due to its potent bioactivities, such as anti-inflammation, anti-cancer, immuno-modulatory and anti-hepatitis activities[1]. Till now, researchers have identified a total of 26 compounds from *Niuchangchih*, including 11 succinic/maleic acid derivatives, 8 triterpenoids, 1 benzenoids, 1 benzoquinone derivative, 5 miscellaneous compounds and polysaccharides, that possess anti-inflammatory effect[2, 3]. However, the mechanisms underlying their anti-inflammatory actions remain elusive.

A recent study by Chen *et al* elucidated the molecular mechanisms of anti-inflammation of *Niuchangchih*. The authors isolated and purified 5 major antcins (A, B, C, H, and K) from fruiting bodies of *Niuchangchih*. They found that antcin A was most similar to glucocorticoids among the 5 compounds in the chemical structure. Furthermore, they demonstrated in human lung cancer cell A549 that antcin A was the active ingredient responsible for the anti-inflammatory effect of *Niuchangchih*, which might act via the same molecular mechanism triggered by glucocorticoids[4]. Finally, they showed the docking of antcin A to glucocorticoid receptor (GR) in a molecular modeling study. Thus, via mimicking glucocorticoids, antcin A may diffuse across the cell membrane and bind to the cytosolic GR that forms a dimmer after dissociated from the heat-shock protein (HSP) and then translocates into the nucleus to initiate the suppression of inflammation at the gene regulation level. Molecular docking showed that C-7 of antcin A was attached to the hydrophobic side of the steroidal backbone of GR, while C-7 of the other antcins was attached to the hydrophilic group, thus being expelled when docking to the binding cavity of GR.

Chen's work is an important landmark in research of anti-inflammatory compounds in *Niuchangchih*. Hsien *et al* recently showed that the anti-inflammatory activity of antrocamphin A, another anti-inflammatory compound from *Niuchangchih*, resulted from suppressing pro-inflammatory molecule release via down-regulation of iNOS and COX-2 expression through NF-κB pathway[5]. Both the studies provide solid evidence for the potential of *Niuchangchih* to treat inflammation. To elucidate the mechanisms of action of antcin A and antrocamphin A *in vivo*, more animal experiments and randomized controlled clinical trials should be carried out. Since more than 20 compounds in *Niuchangchih* have been shown to possess anti-inflammatory activity[6–8], further studies are needed to elucidate their mechanisms. It is also of interest to figure out whether these compounds act synergistically or independently. Notably, most anti-inflammatory compounds in *Niuchangchih* have been derived from the fruiting bodies so far. Further research is needed to uncover whether they can also be produced in fermented mycelia. Besides antcin A and antrocamphin A, many unknown ingredients responsible for the anti-infammatory effects of *Niuchangchih* remain to be discovered.

Laboratory of Pharmaceutical Engineering, School of Medicine and Pharmaceutics, Jiangnan University, Wuxi 214122, China
Correspondence: Prof Zheng-hong XU (zhenghxu@jiangnan.edu.cn)

References

1 Ao ZH, Xu ZH, Lu ZM, Xu HY, Zhang XM, Dou WF. *Niuchangchih* (*Antrodia camphorata*) and its potential in treating liver diseases. J Ethnopharmacol 2009; 121: 194–212.

2 Geethangili M, Tzeng YM. Review of pharmacological effects of *Antrodia camphorata* and its bioactive compounds. Evid Based Complement Alternat Med 2011; 2011: 212641.

3 Chen CC, Liu YW, Ker YB, Wu YY, Lai EY, Chyau CC, *et al*. Chemical characterization and anti-inflammatory effect of polysaccharides fractionated from submerge-cultured *Antrodia camphorata*

mycelia. J Agric Food Chem 2007; 55: 5007–12.

4 Chen YC, Liu YL, Li FY, Chang CI, Wang SY, Lee KY, *et al*. Antcin A, a steroid-like compound from *Antrodia camphorata*, exerts anti-inflammatory effect via mimicking glucocorticoids. Acta Pharmacol Sin 2011; 32: 904–11.

5 Hsien YH, Chu FH, Wang YS, Chien SC, Chang ST, Shaw JF, *et al*. Antrocamphin A, an anti-inflammatory principal from the fruiting body of *Taiwanofungus camphoratus*, and its mechanisms. J Agric Food Chem 2010; 58: 3153–8.

6 Chen JJ, Lin WJ, Liao CH, Shieh PC. Anti-inflammatory benzenoids from *Antrodia camphorata*. J Nat Prod 2007; 70: 989–92.

7 Chien SC, Chen ML, Kuo HT, Tsai YC, Lin BF, Kuo YH. Anti-inflammatory activities of new succinic and maleic derivatives from the fruiting body of *Antrodia camphorata*. J Agric Food Chem 2008; 56: 7017–22.

8 Wu SJ, Leu YL, Chen CH, Chao CH, Shen DY, Chan HH, *et al*. Camphoratins A-J, potent cytotoxic and anti-inflammatory triterpenoids from the fruiting body of *Taiwanofungus camphoratus*. J Nat Prod 2010; 73: 1756–62.

Acta Pharmacologica Sinica (2011) 32: 983–990
 1671-4083/11 $32.00
www.nature.com/aps

Review

Gold nanoparticles in cancer therapy

Zhao-Zhin Joanna LIM[1], Jia-En Jasmine LI[1, 2], Cheng-Teng NG[1, 2], Lin-Yue Lanry YUNG[2, *], Boon-Huat BAY[1, *]

[1]*Department of Anatomy, National University of Singapore, Singapore;* [2]*Department of Chemical and Biomolecular Engineering, National University of Singapore, Singapore*

The rapid advancement of nanotechnology in recent years has fuelled a burgeoning interest in the field of nanoparticle research, in particular, its application in the medical arena. A constantly expanding knowledge based on a better understanding of the properties of gold nanoparticles (AuNPs) coupled with relentless experimentation means that the frontiers of nanotechnology are constantly being challenged. At present, there seems to be heightened interest in the application of AuNPs to the management of cancer, encompassing diagnosis, monitoring and treatment of the disease. These efforts are undertaken in the hope of revolutionizing current methods of treatment and treatment strategies for a multifactorial disease such as cancer. This review will focus on the current applications of AuNPs in cancer management.

Keywords: gold nanoparticles; cancer therapeutics; cancer diagnosis; photothermal therapy; radiation therapy

Acta Pharmacologica Sinica (2011) 32: 983–990; doi: 10.1038/aps.2011.82; published online 11 Jul 2011

Introduction

According to the World Health Organization (WHO), cancer accounted for 7.9 million deaths in 2007 making it the leading cause of death in the world. Deaths from cancer around the globe are expected to climb upwards with an estimated 12 million deaths by cancer in 2030[1]. The frontiers of cancer research are therefore consistently challenged in order to advance the most effective means of cancer diagnosis, monitoring and treatment. Findings gleaned from cancer research would inevitably benefit mankind and save countless lives.

Current therapies employed for the treatment of cancer include surgery, chemotherapy and radiation therapy among others. While these methods have been accepted and practiced for decades, they have their drawbacks and side effects. Surgical removal of tumors is restricted mainly to large, resectable and accessible tumors. Chemotherapeutic drugs target rapidly dividing cells, and thus not only kill cancer cells, but also destroy normal cells like bone marrow cells and immune cells[2]. This gives rise to widespread "collateral damage" in the patient's body. Radiation therapy involves the use of high-energy radiation like X-rays and gamma rays to destroy tumor cells, and inevitably causes deleterious effects to healthy tissues along the radiation path[3].

* To whom correspondence should be addressed.
E-mail antbaybh@nus.edu.sg (Boon-Huat BAY);
cheyly@nus.edu.sg (Lin-Yue Lanry YUNG)
Received 2011-01-18 Accepted 2011-05-23

In light of the shortcomings of current treatment modalities for cancer, a critical thrust towards improving cancer therapy is to specifically target therapeutic agents to tumor cells while sparing healthy tissues from harm. This is one of the emerging interests in nanotechnology research. Nanotechnology refers to the manufacture of materials having nanoscale dimensions between 1 nm and 100 nm[4]. The small size of these nanomaterials confers their uniqueness with chemical and physical properties that are distinct from their bulk materials[5]. The rapid expansion in nanomaterial research increases the future prospect of novel diagnostic methods and treatment of diseases that plague mankind. This branch of nanotechnology in disease diagnosis, monitoring and treatment has been termed "nanomedicine" by the National Institutes of Health in the USA[4].

Among the many nanomaterials being developed for nanomedicine applications, this review will focus on gold nanoparticles (AuNPs) and their potential as tumor sensors, drug delivery agents and enhancers in plasmonic photothermal therapy for the eradication of cancers. The use of AuNPs is gaining popularity in these areas of research for several reasons. Firstly, AuNPs are considered to be relatively biologically non-reactive and therefore suitable for *in vivo* applications compared to the very toxic cadmium and silver NPs[6] although various groups (as explained in the later sections) are challenging this view. Other advantageous qualities include the strong optical properties of AuNPs due to localized surface plasmon resonance (LSPR)[7], easily controllable surface

chemistry which enables versatility in adding surface functional groups[8], and lastly, the ease in control over particle size and shape during synthesis[9]. AuNPs may be considered to be fully multifunctional, with the possibility of combining different desired functionalities in one molecular-sized package. All these factors contribute to the strong interest and preference for the use of AuNPs over other NPs[10]. Examples of other nanomaterials for biomedical applications can be found in other published papers which expound on the utilization of quantum dots[11, 12], functionalized fullerene-based nanomaterials[13] and magnetic NPs[14, 15] for the diagnosis and treatment of human diseases.

AuNPs and cytotoxicity

As the utility of AuNPs largely depends on the degree of inherent toxicity, studies on the toxicological profile of these NPs are discussed proceeding to their usage in cancer management. Since NPs exhibit properties which are markedly different from that of their much larger counterparts, their behaviour and effects cannot be extrapolated from information derived from their bulk materials. Bulk gold has generally been considered an inert metal valued for medicinal purposes[16] and AuNPs have been thought to be likewise. In the literature, AuNPs have been reported to lack the ability to induce adverse and acute toxicity[17] and are thus deemed to be biocompatible entities for use in biomedical applications[17, 18]. However, recent studies have shown that there could be more to AuNP toxicity than already surmised and that the extent of toxicity response is closely associated with the size of the AuNPs[19, 20]. Investigations have revealed that decreasing the size of NPs correlated with more widespread tissue distribution, heightened potential to deeper penetration within certain tissues, more effective internalization by cells, and increased toxic effects[21]. In terms of surface functionality, studies have shown that modification of the AuNP surface affect its uptake, interactions with cellular constituents and cytotoxicity[22, 23].

In vitro studies on cytotoxicity of AuNPs

Multiple studies have shown that AuNPs exert their cytotoxicity through the induction of oxidative stress. For example, when exposed to 1.4 nm AuNPs, HeLa cervical carcinoma cells exhibited increased reactive oxygen species (ROS) production and oxidative stress, leading to protein and lipid oxidation, severely impaired mitochondrial function, and eventually cell death[23]. The same investigators showed that Z-VAD-fmk, a caspase inhibitor was unable to rescue the cells from dying, leading to the conclusion that cells were killed by necrosis. Furthermore, genome-wide mRNA expression analysis verified that treatment with AuNPs caused up-regulation of stress-related and inflammation-related genes and a concomitant decrease in the expression of cell cycle genes. It appears that continual production of endogenous ROS within the cell exhausted the intracellular antioxidant pool and therefore induced irreversible damage that eventually lead to necrosis.

Oxidative stress was observed in MRC-5 fetal human lung fibroblast cells following exposure to 20 nm AuNPs[24] with concomitant down-regulation of cell cycle genes such as Cyclin B2 and B1 and DNA damage response genes. In a follow-up study, the same investigators observed the presence of autophagy (validated by biochemical and morphological parameters) concurrent with oxidative stress in the lung fibroblasts following uptake of AuNPs[25]. It was also demonstrated in the same study that AuNP treatment led to the up-regulation of antioxidants and expression of stress-response genes and proteins, lending support to the hypothesis that oxidative stress could be a manifestation of AuNP cytotoxicity.

In vivo studies on cytotoxicity of AuNPs

In a recent study, blue mussel *Mytilus edulis* was observed to experience oxidative stress within 24 h of exposure to AuNPs[26], indicating the possible impact of AuNPs to the ecosystem and aquatic animals. The same investigators also proposed the use of *M edulis* as an ideal animal model for environmental toxicology studies of NPs. Another *in vivo* study utilized zebrafish embryos to assess the feasibility of AuNPs as probes for embryonic imaging[27]. In this study, the real-time effects of AuNPs on zebrafish embryos were investigated, and results showed that owing to the random diffusion of AuNPs to various parts of the embryo, toxic effects influencing the developmental outcome of the embryo were largely stochastic in nature. Among the 76% of zebrafish embryos that survived, only a minority (2%) of zebrafish embryos exhibited deformities while the remaining 74% developed normally. The authors therefore proposed that given its relatively non-toxic nature, AuNPs could be exploited for *in vivo* imaging applications for embryonic studies.

For mammals, however, there is at present limited information regarding the *in vivo* toxicity of AuNPs. Studies have largely focused on the biodistribution of AuNPs in the body. A rat model study revealed the size-dependent organ distribution of AuNPs following intravenous (iv) administration. For 10 nm AuNPs, the distribution was found to be widespread, permeating the blood and organs of the cardio-respiratory system, immune system (such as spleen and thymus) and reproductive system, liver, kidney, and brain, whereas larger AuNPs (50, 100, and 250 nm) were localized only to the blood, liver and spleen[28]. A similar study conducted using 15, 50, 100, and 200 nm AuNPs showed that while the AuNPs with the largest dimension could only accumulate minimally in organs following iv administration into mice, AuNPs with the smallest dimension were detected in all tissues including blood and other organs such as the liver, lung, spleen, kidney, brain, stomach, and heart[29]. The results imply that smaller size AuNPs are more accessible to various tissues in the body and therefore the propensity to cause widespread harm, if any.

Another group of researchers assessed the *in vivo* toxicity of 13 nm AuNPs coated with poly (ethylene) glycol (PEG) in mice and showed that following iv injection of AuNPs, the NPs accumulated in mouse liver and spleen for up to a week, and induced acute inflammation and apoptosis in the liver[30]. The same group of investigators also demonstrated that iv administration of 4 nm or 100 nm PEG-coated AuNPs in mice

induced up-regulation of common genes associated with apoptosis, cell cycle, inflammation, and metabolic process in liver tissues[31].

A major challenge in the field of investigating *in vivo* cytotoxicity of NPs is the plausibility of translating observed cellular and immunological toxicity in animal models to humans, since there are distinct intra- and interspecies variations which need to be considered.

Applications of AuNPs in cancer management

AuNPs as sensors for probing and imaging tumor cells

AuNPs are good candidates for labelling applications because of their ability to interact strongly with visible light. Upon exposure to light, free electrons in gold atoms are excited to a state of collective oscillation known as surface plasmon resonance (SPR), conferring gold the ability to absorb and scatter visible light[32]. In labelling applications, AuNPs are targeted and accumulated at the site of interest and based on their optical scattering properties, they enable visualization of the region under study. AuNPs may then be detected by any of the following ways: phase contrast optical microscopy, dark field microscopy, photothermal imaging, and photoacoustic imaging[33]. In addition, owing to its high atomic weight, AuNPs remain the preferred label for visualization and immuno-staining at the ultrastructural level using transmission electron microscopy[34].

A crucial step in successful cancer therapy involves early diagnosis. The strong optical scattering properties of AuNPs, coupled with their relative biocompatibility, make them suitable as probes for cancer imaging. Through the conjugation of antibodies specific for antigens overexpressed on tumor cells, AuNPs can be directed to tumor cells, thus pin pointing their precise location in the body (Figure 1). It has been demonstrated that antibody-conjugated hollow gold nanospheres can be used for the surface-enhanced Raman spectroscopy (SERS) imaging of tumor biomarkers which are overexpressed in MCF7 breast cancer cells[35]. Raman scattering is a phenomenon that results from the inelastic collision of photons with molecules where energy, which is either lost or gained, translates to a change in the frequency of the scattered photons. This unique shift of frequency depends on the characteristic energy of molecular vibrations constituting the signal, hence a Raman spectrum consisting of different signals from molecular vibrations forms a "vibrational fingerprint" of a molecule[36]. In SERS, these Raman signals are amplified several folds by nanostructures present in the vicinity of the molecules. Gold and silver have been shown to cause significant enhancement[37] and are thus the favoured nanostructures used as sensors[24]. By attaching a reporter to SERS sensors, targeted sensitive probing of molecules or structures within cells may be achieved[36].

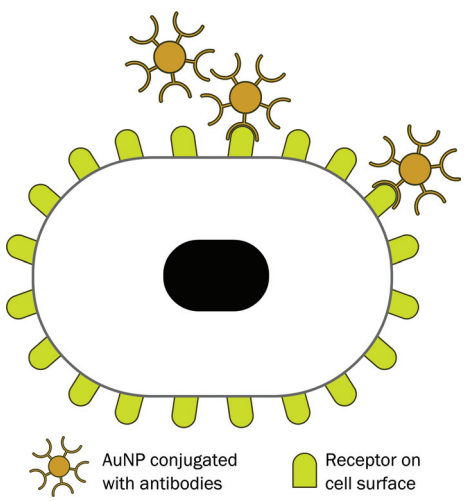

Figure 1. Schematic diagram showing the localization of antibody conjugated gold to receptors present on the plasma membrane of cells.

Recent studies have demonstrated the potential use of AuNPs for *in vivo* targeted imaging of cancer using Raman spectroscopy. Large optical enhancements can possibly be achieved in the detection of tumors in live animals owing to the 14–15 orders of magnitude signal amplification by AuNPs[38]. Following the conjugation of AuNPs with appropriate ligands, cancer markers such as epidermal growth factor receptors present on the surface of human cancer cells and in xenograft tumor models could be targeted for detection. This shows the potential of using AuNPs for biomedical imaging in live subjects. However, it is important to note that the successful optical imaging performed in mice cannot be directly scaled up for *in vivo* imaging of human subjects because the optical signals possess limited tissue penetration ability[39]. At present, optical imaging only appears useful for tissues close to the skin surface or accessible by endoscopy. Hence, additional technological improvements are needed before Raman scattering by AuNPs can be used in a clinical setting.

The utility of AuNPs as novel biosensors for the detection of tumor cells can be demonstrated through the use of a screen-printed carbon electrode (SPCE) coupled with a NP-based electrocatalytic method[40]. Using this technique, *in situ* tumor cell proliferation was detected and quantified via the reaction of cell surface proteins with specific antibodies conjugated to AuNPs. Human tumor HMy2 cells (human leukocyte antigen (HLA-DR) class II positive B cells) and human tumor PC-3 cells (HLA-DR class II negative prostrate carcinoma) were first grown on the surface of SPCEs, following which they were incubated with a commercial monoclonal antibody (mAb) specific to DR molecules conjugated to AuNPs (direct method) or unconjugated mAb followed by secondary antibodies conjugated to AuNPs (indirect method). When hydrogen ions were catalytically reduced to hydrogen in the presence of AuNPs, the amount of AuNPs (and thus a corresponding indication of the quantity of attached tumor cells) could be quantified. In both methods, the AuNP immunosensor was able to distinguish DR-positive tumor cells from DR-negative tumor cells, showing the efficiency of this novel biosensor in detecting specific tumor cells.

AuNPs as drug delivery agents targeted to cancer cells

A prominent application of AuNPs is their use as vehicles for delivery of molecules into cells. AuNPs have been described as "promising nanocarriers for therapeutics" owing to their ease of synthesis and functionalization, relative biocompatibility[41] as well as low toxicity in preliminary assays[9]. However, various factors need to be considered in designing an effective drug delivery system. The properties of AuNPs such as their size, charge and surface chemistry have been shown to affect the uptake of AuNPs into cells as well as their subsequent intracellular fate. In addition, effective drug delivery strategies must take into account the nature of drug-AuNP interaction (covalent/non-covalent binding) as well as the means of drug release following introduction of the drug-AuNP complexes to cells[42]. If AuNPs are used solely as carriers into cells, it is also critical to monitor any toxic effects of residual materials in the cell after delivery; a biodegradable NP vector whose lifespan is limited to the therapeutic window of the drug would be ideal[43]. If the NP vector is cleared from the system once its purpose is reached, it will reduce exposure and limit its toxic effects in the body.

Another issue of concern is the penetration rate of AuNPs into tumors and the specificity of the target sites. Particularly, the epithelial and endothelial barriers are considered to be the main hindrance for the NPs to overcome. Penetration enhancers like metalloproteases against basement membranes and toxins against intracellular tight junctions, may be useful in aiding the uptake of drug-loaded AuNPs into the tumor[44]. Another factor to be considered is the AuNP retention in blood circulation. Some researchers have found that particle retention is also size-dependent and longer circulation time is correlated to higher rate of reaching tumor target[45]. In addition, most studies have only investigated on drug delivery to solid tumors, where it is site specific and easier for quantification of results. It remains to be seen if AuNPs will be effective against non-solid cancers like leukemia where strategies for targeting and treating such cancers can be different from that for solid tumors.

Drug attachment and release from NPs is another challenging area. While the ease of surface modification is what makes AuNP attractive for drug delivery, the strength of drug attachment and timing of the release needs to be suitably controlled to produce the highest therapeutic efficacy. Foremost, the method of release at the tumor site is dependent on how the drug is attached to the AuNP, whether covalently or through non-covalent binding. Generally, drugs in the active form are loaded non-covalently while the covalent-conjugation of the drug to AuNP is in the pro-drug form, thereby requiring a second reaction to release the drug from the attachment as well as to activate it. Although there have been quite a number of strategies proposed for the triggering of drug release at the tumor site, they can generally be narrowed down to three methods: light or photothermal release[46, 47], glutatione-mediated[48], and non-covalent encapsulation of the active drug with subsequent off-loading by diffusion through the membrane[9]. The others are principally a modification of one or a combination of these methods. Thus far, the *in vitro* works done by Kim *et al*[9] have yielded promising results. However, more work is required as there is still the need to assess if these methods are practical for application *in vivo*.

Similarly in the field of cancer therapy, AuNPs are currently being explored as potential drug delivery agents for the introduction of drugs into tumor cells[49]. Cells are known to take up colloidal AuNPs of various shapes and sizes[22] either by specific (via ligand-receptor interaction) or non-specific means. An example of AuNPs being taken up by breast cancer cells *in vitro* is shown in Figure 2. In order to ensure the specific killing of cancer cells while sparing healthy cells, AuNPs were conjugated with appropriate surface ligands which directed them only to tumor cells (Figure 3). Huang *et al* (2008) have described two methods for tumor targeting: the first involved conjugation of AuNPs to PEG, and the second involved conjugation of AuNPs with specific antibodies which

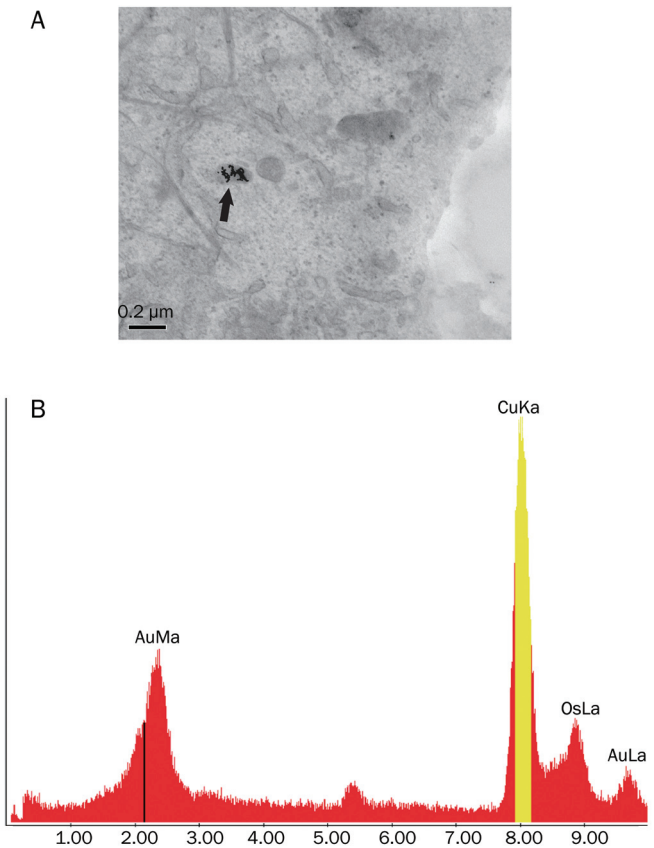

Figure 2. Transmission electron microscopy (TEM) of AuNP treated MCF-7 breast cancer cells. The cells were treated with 1 nmol/L AuNP for 72 h. (A) A cluster of AuNPs (indicated by an arrow) is found in the cytoplasm of a cell. Bar=0.2 μm. (B) TEM specimens were subjected for elemental analysis with a CM120 BioTWIN electron microscope coupled with a Philips EDAX Microanalysis system. The electron dense particles in AuNP treated cells showed the presence of two peaks corresponding to the gold M shell (2.2 KeV) and L shell (9.7 KeV). The treatment sample, registered a P/B ratio (ratio of the intensity of the detected element against the background) of 230.27 (Au L shell). For the element to be significantly present in the sample, the P/B ratio value needs to be 3.0 and above.

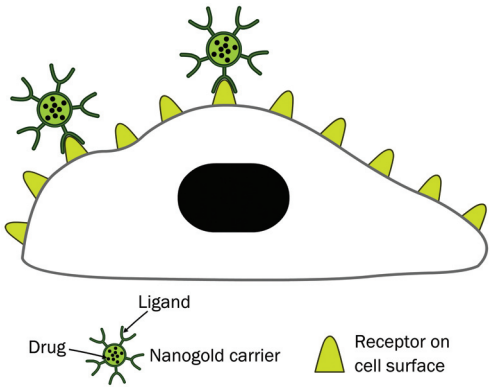

Figure 3. Schematic diagram showing AuNP carriers conjugated with anticancer drugs and ligands which are recognized by receptors on the surface of tumor cells.

bind unique biomarkers expressed on tumor cells[50]. PEG prevented AuNP aggregation and lengthened their retention time in blood. This facilitated the preferential accumulation of AuNPs in tumor cells over healthy cells because of the elevated permeability of poorly differentiated blood vessels around tumors following angiogenesis (Figure 4), as well as the decreased clearance rate caused by the deficit of functional lymphatic vessels in tumors[4]. Using PEG is considered a passive targeting approach, as opposed to the active targeting of tumor cells through the help of specific antibodies. Following cellular uptake, AuNPs are stored in endosomal/lysosomal vesicles. In order to liberate these AuNPs and introduce the drug which has been delivered into the cell cytoplasm, the NPs need to be modified by the conjugation of membrane-translocating sequence-based peptides which enable them to traverse monolayers[51].

Tumor necrosis factor-alpha (TNF-α) is a potent, multi-

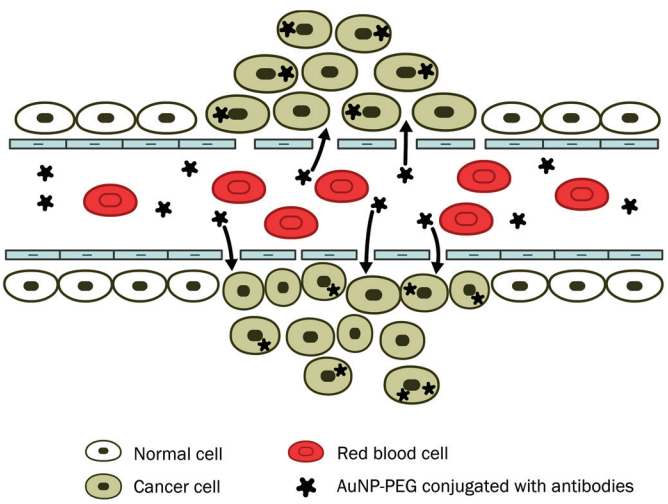

Figure 4. Schematic diagram showing accumulation of ligand-targeted gold nanoparticles conjugated with anticancer drugs in cancer cells mediated via extravasation of the gold nanocarriers through gaps in the endothelial cells ("leaky tumor vasculature").

functional cytokine which not only plays a critical role in inflammation and immunity, but also exhibits anticancer properties[52]. However, its systemic toxicity due to their indiscriminate actions on both normal and malignant tissues is well established[16]. Indeed, it was shown in one study using the mouse model that increasing doses of native TNF correlated with the severity of toxicities observed[49]. In the same study, it was revealed that in contrast to native TNF, TNF conjugated to a colloidal gold platform interspersed with thiol-derivatized PEG was more efficacious in reducing tumor burden in a colon cancer xenograft model, without causing death of the animals.

A Phase 1 clinical trial on the PEGylated colloidal gold–TNF construct (CYT-6091) conducted in patients with advanced stage solid cancers has shown potential[53]. The CYT-6091 complex appears to be well-tolerated in this first clinical trial on human subjects although fever developed in two patients, which was not unexpected (as evidenced by preclinical data) and were easily controlled. It is unclear if the fever was due to a reaction to the AuNPs or the recombinant TNF (rhTNF) construct. It appears that the AuNP and rhTNF construct produces less adverse reaction than the rhTNF alone even at the highest drug-AuNP concentrations in the pre-clinical findings. Dose-limiting toxic reaction of hypotension was also not seen in any patient under the trial although there were some retrafficking of leukocytes. AuNPs were found in the tumor as well as in the liver biopsies but no toxic adverse effects were observed. In sum, the authors concluded that the clinical results correlated well with the preclinical data, which bodes well for future translational studies for AuNPs. However, it must be borne in mind that data generated with one type of AuNP may not be extrapolated to other kinds of AuNPs with a different shape, size or surface modification.

In a separate study, the effect of incorporating PEG-coated AuNPs with TNF-α for the targeting killing of SCK mammary carcinomas grown in mice combined with heat treatment has also been investigated[54]. While AuNPs loaded with TNF-α alone and heat treatment alone showed tumor growth delay, the most drastic effect was observed when TNF-α loaded AuNPs were intravenously introduced, followed by local heating. This combination treatment proved effective in decreasing the *in vivo* and *in vitro* tumor cell survival rates, demonstrating the prospect of using AuNPs as drug delivery carriers coupled with subsequent thermal treatment for effective eradication of tumor cells.

The effects of AuNPs conjugated with methotrexate (MTX) in inducing cytoxicity *in vitro* and anti-tumorigenic effects *in vivo* have been reported[55]. It was observed that accumulation of Au-MTX in tumor cells occurred more rapidly and at higher concentrations than those treated with free MTX. As a result, enhanced cytotoxic effects were also present in several tumor cell lines compared with an identical dosage of free MTX. These results warrant further investigation as they suggest that the conjugation of AuNPs with a chemotherapeutic drug such as MTX was more efficacious than the administration of free MTX alone, displaying the potential of AuNPs as drug carriers targeting only tumor cells.

However, given the vast array of AuNPs of different shapes and sizes, it is still unclear which type(s) of AuNPs would be the most suitable for drug delivery applications[39]. It is likely that this variety of AuNPs will be custom made to suit the needs for patient treatment. The use of AuNPs in such a manner is not without its disadvantages. There are inherent problems and potential problems to the use of NPs in the delivery of drugs to the target site such as size of the NP and drug conjugate, intratumoral pressure and differential expression of receptors at the tumor site. Optimism towards the utilization of AuNPs as drug delivery vectors into cells should be kept in check as many of the complications regarding targeted drug delivery as well as the toxicity of NPs to cells is a concern yet to be fully addressed. Therefore, the use of AuNPs prior to appropriate assessment of their toxic effects may reap more harm than benefit.

AuNPs in plasmonic photothermal therapy

Traditionally, heat has been used in the treatment of cancer via the induction of hyperthermia, a condition in which cells are subjected to high temperatures which kill them. While the sources of heat varies from microwaves, radiowaves, ultrasound waves to laser light in the past, such approaches to cancer therapy have not been widely used because of the consequential damage to normal tissues surrounding the targeted tumor. With the advent of nanotechnology, diverse nanostructures have been manufactured for the purpose of photothermal therapeutics. Noble metal NPs such as AuNPs (and including Au nanospheres, nanorods, and nanocages) attract particular interest because they possess enhanced absorption cross-sections[50, 56]. Their strong absorbance enables effective laser therapy with minimal "collateral damage" to the surrounding healthy tissue. The mechanism by which AuNPs exert their photothermal effect is through SPR. This leads to the formation of a heated electron gas which then cools rapidly within about 1 ps through exchanging energy with the NP lattice. The NP lattice in turn heats up the surrounding environment through the rapid transfer of energy spanning only about 100 ps[57]. The speed at which energy is converted and dissipated to the surrounding environment presents an efficient means of rapidly inducing hyperthermia in the vicinity of AuNPs following irradiation with light. Irreversible cell damage resulting from denaturation of proteins and disruption of cell membrane will occur in the areas subjected to high temperatures.

The underlying concept of using antibody-conjugated AuNPs hinges on the necessity of tumor cells in expressing characteristic biomarkers, which are otherwise absent or expressed in significantly lower levels in normal cells. The successful detection and eradication of breast carcinoma cells overexpressing human epidermal growth factor receptor 2 (HER2) through the usage of anti-HER2 immunotargeted gold nanoshells with subsequent irradiation by near infra-red light to potentiate the gold nanoshells-induced photothermal effect has been reported[58]. The antibody-mediated targeting of AuNPs to tumor cells was considered to be the more specific and efficient of the two approaches to tumor targeting. It is apparent from here that plasmonic AuNPs exhibit vast potential in the field of photothermal cancer therapy by providing a means to specifically target tumor cells.

AuNPs in radiation therapy

Numerous studies have revealed that AuNPs may have important applications as radiosensitizers (which are drugs that potentiate the effect of radiation for cancer therapy). A study on mice bearing subcutaneous EMT-6 mammary carcinomas showed that not only were AuNPs (1.9 nm in diameter) non-toxic in nature and cleared from the body via the kidneys, they possessed the ability to enhance the effect of X-ray therapy leading to a remarkable survival rate of 86% as opposed to 20% with X-rays alone and 0% with AuNPs alone[59]. However, it is crucial to note that while 1.9 nm AuNPs seem to show potential as radiation enhancing agents, a recent study discovered evidence for acute cytotoxicity, DNA damage and apoptosis mediated by oxidative stress induced by cellular uptake of 1.9 nm AuNPs[60]. There is a need for further understanding of cellular responses to AuNPs when exploring their potential to be used in radiation therapy to cure cancer.

The effectiveness of AuNPs as radiosensitizers seems to be closely related to their surface functionality. While the above studies utilized uncoated AuNPs, another study showed that 5 nm AuNPs coated with the gadolinium chelating agent dithiolated diethylenetriaminepentaacetic gadolinium (Au@DTDTPA:Gd) did not exhibit radiosensitizing effect in both tumor cells *in vitro* and *in vivo* models (MC7-L1 tumor-bearing mice)[61]. Instead, a chemotherapeutic effect was observed, which warrants further investigation. The authors suggest that the radiosensitizing properties of AuNPs could possibly be strongly reliant on the nature of their coating. However, the discrepancy over the radiosensitizing effects of AuNPs may also be attributed to the different dimensions of AuNPs used as well as the type of tumor cells under study.

AuNPs as antiangiogenic agents

Interestingly, AuNPs have been reported to possess antiangiogenic property[62]. The exact mechanism of action is still not clearly understood but it was observed that AuNPs bind preferentially to vascular permeability factor/vascular endothelial growth factor (VPF/VEGF)-165 and basic fibroblast growth factor (bFGF) primarily through the heparin-binding domain. This has led researchers to suggest that AuNPs are able to inhibit angiogenesis by preventing the downstream signaling effects of these mitogens on angiogenesis in cancer cells[63].

Conclusion

The field of NP research presents exciting potential for biomedical applications. Together with an expanding knowledge base on the properties and effects of AuNPs, they are currently explored as potential tools for cancer therapy. Presently, exploiting AuNPs as sensitive probes in the detection and imaging of tumors for diagnostic purposes, delivery agents for the specific targeting of chemotherapeutic drugs to tumor

cells, and enhancers in plasmonic photothermal therapy and radiation therapy for the eradication of tumor cells appear to show promise. In nanomedicine, the ultimate aim is to utilize NPs efficiently for the *in vivo* targeted killing of tumor cells with no or minimal side effects. However, even the concept of attaching ligands to the NPs so as to allow them to hone to the tumor appears logical and simple but is in fact fraught with difficulties. In this light, NP research is still at its infancy since many factors remain to be optimized before the application of NPs in cancer therapy becomes a clinical reality.

Acknowledgements

The authors are grateful to Song-Lin BAY for her assistance in preparing the figures. This work was supported by research funding from the Singapore Ministry of Education Academic Research Fund Tier 1 via grant R279-000-205-112 and Tier 2 via grant MOE2008-T2-1-046, and the National University of Singapore Environmental Research Institute (NERI) via grant R706-000-002-646.

References

1 Cancer [homepage on the Internet]. Geneva: World Health Organization. Accessed Oct 21, 2010. Available from: http://www.who.int/cancer/en/.
2 Wagstaff KM, Jans DA. Nuclear drug delivery to target tumour cells. Eur J Pharmacol 2009; 625: 174–80.
3 Boisselier E, Astruc D. Gold nanoparticles in nanomedicine: preparations, imaging, diagnostics, therapies and toxicity. Chem Soc Rev 2009; 38: 1759–82.
4 Liu Y, Miyoshi H, Nakamura M. Nanomedicine for drug delivery and imaging: a promising avenue for cancer therapy and diagnosis using targeted functional nanoparticles. Int J Cancer 2007; 120: 2527–37.
5 Lanone S, Boczkowski J. Biomedical applications and potential health risks of nanomaterials: molecular mechanisms. Curr Mol Med 2006; 6: 651–63.
6 Lewinski N, Colvin V, Drezek R. Cytotoxicity of nanoparticles. Small 2008; 4: 26–49.
7 Jain KK. The role of nanobiotechnology in drug discovery. Adv Exp Med Biol 2009; 655: 37–43.
8 DeLong RK, Reynolds CM, Malcolm Y, Schaeffer A, Severs T, Wanekaya A. Functionalized gold nanoparticles for the binding, stabilization, and delivery of therapeutic DNA, RNA, and other biological macromolecules. Nanotechnol Sci Appl 2010; 2010: 53–63.
9 Kim C, Ghosh P, Rotello V. Multimodal drug delivery using gold nanoparticles. Nanoscale 2009; 1: 61–7.
10 Cobley CM, Chen J, Cho EC, Wang LV, Xia Y. Gold nanostructures: a class of multifunctional materials for biomedical applications. Chem Soc Rev 2011; 40: 44–56.
11 Zrazhevskiy P, Gao X. Multifunctional quantum dots for personalized medicine. Nano Today 2009; 4: 414–28.
12 Biju V, Itoh T, Anas A, Sujith A, Ishikawa M. Semiconductor quantum dots and metal nanoparticles: syntheses, optical properties, and biological applications. Anal Bioanal Chem 2008; 391: 2469–95.
13 Partha R, Conyers JL. Biomedical applications of functionalized fullerene-based nanomaterials. Int J Nanomedicine 2009; 4: 261–75.
14 Sun C, Lee JS, Zhang M. Magnetic nanoparticles in MR imaging and drug delivery. Adv Drug Deliv Rev 2008; 60: 1252–65.
15 Sun C, Veiseh O, Gunn J, Fang C, Hansen S, Lee D, *et al*. *In vivo* MRI detection of gliomas by chlorotoxin-conjugated superparamagnetic nanoprobes. Small 2008; 4: 372–9.
16 Powell AC, Paciotti GF, Libutti SK. Colloidal gold: a novel nanoparticle for targeted cancer therapeutics. Methods Mol Biol 2010; 624: 375–84.
17 Connor E, Mwamuka J, Gole A, Murphy C, Wyatt M. Gold nanoparticles are taken up by human cells but do not cause acute cytotoxicity. Small 2005; 1: 325–7.
18 Shukla R, Bansal V, Chaudhary M, Basu A, Bhonde RR, Sastry M. Biocompatibility of gold nanoparticles and their endocytotic fate inside the cellular compartment: a microscopic overview. Langmuir 2005; 21: 10644–54.
19 Pan Y, Neuss S, Leifert A, Fischler M, Wen F, Simon U, *et al*. Size-dependent cytotoxicity of gold nanoparticles. Small 2007; 3: 1941–9.
20 Chen YS, Hung YC, Liau I, Huang GS. Assessment of the *in vivo* toxicity of gold nanoparticles. Nanoscale Res Lett 2009; 4: 858–64.
21 Johnston H, Hutchison G, Christensen F, Peters S, Hankin S, Stone V. A review of the *in vivo* and *in vitro* toxicity of silver and gold particulates: particle attributes and biological mechanisms responsible for the observed toxicity. Crit Rev Toxicol 2010; 40: 328–46.
22 Chithrani B, Ghazani A, Chan W. Determining the size and shape dependence of gold nanoparticle uptake into mammalian cells. Nano Lett 2006; 6: 662–8.
23 Pan Y, Leifert A, Ruau D, Neuss S, Bornemann J, Schmid G, *et al*. Gold nanoparticles of diameter 1.4 nm trigger necrosis by oxidative stress and mitochondrial damage. Small 2009; 5: 2067–76.
24 Li J, Zou L, Hartono D, Ong C, Bay B, Yung L. Gold nanoparticles induce oxidative damage in lung fibroblasts *in vitro*. Adv Mater 2008; 20: 138–42.
25 Li J, Hartono D, Ong C, Bay B, Yung L. Autophagy and oxidative stress associated with gold nanoparticles. Biomaterials 2010; 31: 5996–6003.
26 Tedesco S, Doyle H, Blasco J, Redmond G, Sheehan D. Oxidative stress and toxicity of gold nanoparticles in *Mytilus edulis*. Aquat Toxicol 2010; 100: 178–86.
27 Browning L, Lee K, Huang T, Nallathamby P, Lowman J, Xu X. Random walk of single gold nanoparticles in zebrafish embryos leading to stochastic toxic effects on embryonic developments. Nanoscale 2009; 1: 138–52.
28 De Jong W, Hagens W, Krystek P, Burger M, Sips A, Geertsma R. Particle size-dependent organ distribution of gold nanoparticles after intravenous administration. Biomaterials 2008; 29: 1912–9.
29 Sonavane G, Tomoda K, Makino K. Biodistribution of colloidal gold nanoparticles after intravenous administration: effect of particle size. Colloids Surf B Biointerfaces 2008; 66: 274–80.
30 Cho W, Cho M, Jeong J, Choi M, Cho H, Han B, *et al*. Acute toxicity and pharmacokinetics of 13 nm-sized PEG-coated gold nanoparticles. Toxicol Appl Pharmacol 2009; 236: 16–24.
31 Cho W, Kim S, Han B, Son W, Jeong J. Comparison of gene expression profiles in mice liver following intravenous injection of 4 and 100 nm-sized PEG-coated gold nanoparticles. Toxicol Lett 2009; 191: 96–102.
32 Kumar S, Harrison N, Richards-Kortum R, Sokolov K. Plasmonic nanosensors for imaging intracellular biomarkers in live cells. Nano Lett 2007; 7: 1338–43.
33 Sperling R, Rivera Gil P, Zhang F, Zanella M, Parak W. Biological applications of gold nanoparticles. Chem Soc Rev 2008; 37: 1896–908.
34 Roth J. The silver anniversary of gold: 25 years of the colloidal gold marker system for immunocytochemistry and histochemistry. Histochem Cell Biol 1996; 106: 1–8.

35 Lee S, Chon H, Lee M, Choo J, Shin S, Lee Y, *et al*. Surface-enhanced Raman scattering imaging of HER2 cancer markers overexpressed in single MCF7 cells using antibody conjugated hollow gold nanospheres. Biosens Bioelectron 2009; 24: 2260–3.
36 Kneipp J, Kneipp H, Wittig B, Kneipp K. Novel optical nanosensors for probing and imaging live cells. Nanomedicine 2010; 6: 214–26.
37 Kneipp K, Kneipp H, Kneipp J. Surface-enhanced Raman scattering in local optical fields of silver and gold nanoaggregates-from single-molecule Raman spectroscopy to ultrasensitive probing in live cells. Acc Chem Res 2006; 39: 443–50.
38 Qian X, Peng X, Ansari D, Yin-Goen Q, Chen G, Shin D, *et al*. *In vivo* tumor targeting and spectroscopic detection with surface-enhanced Raman nanoparticle tags. Nat Biotechnol 2008; 26: 83–90.
39 Cai W, Gao T, Hong H, Sun J. Applications of gold nanoparticles in cancer nanotechnology. Nanotechnol Sci Appl 2008; 1: 17–32.
40 de la Escosura-Muñiz A, Sánchez-Espinel C, Díaz-Freitas B, González-Fernández A, Maltez-da Costa M, Merkoçi A. Rapid identification and quantification of tumor cells using an electrocatalytic method based on gold nanoparticles. Anal Chem 2009; 81: 10268–74.
41 Lee SH, Bae KH, Kim SH, Lee KR, Park TG. Amine-functionalized gold nanoparticles as non-cytotoxic and efficient intracellular siRNA delivery carriers. Int J Pharm 2008; 364: 94–101.
42 Duncan B, Kim C, Rotello VM. Gold nanoparticle platforms as drug and biomacromolecule delivery systems. J Control Release 2010; 148: 122–7.
43 De Jong W, Borm P. Drug delivery and nanoparticles: applications and hazards. Int J Nanomedicine 2008; 3: 133–49.
44 Sakamoto J, Annapragada A, Decuzzi P, Ferrari M. Antibiological barrier nanovector technology for cancer applications. Expert Opin Drug Deliv 2007; 4: 359–69.
45 Zhang G, Yang Z, Lu W, Zhang R, Huang Q, Tian M, *et al*. Influence of anchoring ligands and particle size on the colloidal stability and *in vivo* biodistribution of polyethylene glycol-coated gold nanoparticles in tumor-xenografted mice. Biomaterials 2009; 30: 1928–36.
46 Bikram M, Gobin AM, Whitmire RE, West JL. Temperature-sensitive hydrogels with SiO_2-Au nanoshells for controlled drug delivery. J Control Release 2007; 123: 219–27.
47 Agasti SS, Chompoosor A, You CC, Ghosh P, Kim CK, Rotello VM. Photoregulated release of caged anticancer drugs from gold nanoparticles. J Am Chem Soc 2009; 131: 5728–9.
48 Hong R, Han G, Fernandez JM, Kim BJ, Forbes NS, Rotello VM. Glutathione-mediated delivery and release using monolayer protected nanoparticle carriers. J Am Chem Soc 2006; 128: 1078–9.
49 Paciotti GF, Myer L, Weinreich D, Goia D, Pavel N, McLaughlin RE, *et al*. Colloidal gold: a novel nanoparticle vector for tumor directed drug delivery. Drug Deliv 2004; 11: 169–83.
50 Huang X, Jain P, El-Sayed I, El-Sayed M. Plasmonic photothermal therapy (PPTT) using gold nanoparticles. Lasers Med Sci 2008; 23: 217–28.
51 Koch A, Reynolds F, Merkle H, Weissleder R, Josephson L. Transport of surface-modified nanoparticles through cell monolayers. Chembiochem 2005; 6: 337–45.
52 van Horssen R, Ten Hagen T, Eggermont A. TNF-alpha in cancer treatment: molecular insights, antitumor effects, and clinical utility. Oncologist 2006; 11: 397–408.
53 Libutti SK, Paciotti GF, Byrnes AA, Alexander HR Jr, Gannon WE, Walker M, *et al*. Phase I and pharmacokinetic studies of CYT-6091, a novel PEGylated colloidal gold-rhTNF nanomedicine. Clin Cancer Res 2010; 16: 6139–49.
54 Visaria R, Griffin R, Williams B, Ebbini E, Paciotti G, Song C, *et al*. Enhancement of tumor thermal therapy using gold nanoparticle-assisted tumor necrosis factor-alpha delivery. Mol Cancer Ther 2006; 5: 1014–20.
55 Chen Y, Tsai C, Huang P, Chang M, Cheng P, Chou C, *et al*. Methotrexate conjugated to gold nanoparticles inhibits tumor growth in a syngeneic lung tumor model. Mol Pharm 2007; 4: 713–22.
56 Liu C, Li BQ, Mi CC. Fast transient thermal analysis of gold nanoparticles in tissue-like medium. IEEE Trans Nanobioscience 2009; 8: 271–80.
57 Link S, El-Sayed MA. Shape and size dependence of radiative, non-radiative and photothermal properties of gold nanocrystals. Int Rev Phys Chem 2000; 19: 409–53.
58 Loo C, Lowery A, Halas N, West J, Drezek R. Immunotargeted nanoshells for integrated cancer imaging and therapy. Nano Lett 2005; 5: 709–11.
59 Hainfeld J, Slatkin D, Smilowitz H. The use of gold nanoparticles to enhance radiotherapy in mice. Phys Med Biol 2004; 49: N309–15.
60 Butterworth KT, Coulter JA, Jain S, Forker J, McMahon SJ, Schettino G, *et al*. Evaluation of cytotoxicity and radiation enhancement using 1.9 nm gold particles: potential application for cancer therapy. Nanotechnology 2010; 21: 295101.
61 Hébert E, Debouttière P, Lepage M, Sanche L, Hunting D. Preferential tumour accumulation of gold nanoparticles, visualised by magnetic resonance imaging: Radiosensitisation studies *in vivo* and *in vitro*. Int J Radiat Biol 2010; 86: 692–700.
62 Mukherjee P, Bhattacharya R, Wang P, Wang L, Basu S, Nagy JA, *et al*. Antiangiogenic properties of gold nanoparticles. Clin Cancer Res 2005; 11: 3530–4.
63 Bhattacharya R, Mukherjee P. Biological properties of "naked" metal nanoparticles. Adv Drug Deliv Rev 2008; 60: 1289–306.

Acta Pharmacologica Sinica (2011) 32: 991–998
 1671-4083/11 $32.00
www.nature.com/aps

Original Article

Rosiglitazone protects neuroblastoma cells against advanced glycation end products-induced injury

Li WANG[1], Chun-jiang YU[2], Wei LIU[3], Lu-yang CHENG[1], Yi-na ZHANG[1, *]

Department of [1]Geriatrics and [2]Neurology, the Second Affiliated Hospital of Harbin Medical University, Harbin 150086, China; [3]Department of Neurology, Haidian Hospital, Beijing 100080, China

Aim: To investigate the protective effects of rosiglitazone (RGZ) against the neuronal toxicity induced by advanced glycation end products (AGEs) and the underlying mechanisms.
Methods: Neuroblastoma cell line SH-SY5Y was used. Cell viability and apoptosis were assessed using MTT assay and flow cytometry, respectively. Superoxide dismutase (SOD) and catalase activities were measured using biochemical methods. Intracellular reactive oxygen species (ROS) were monitored using 2',7'-dichlorodihydro-fluorescein diacetate (DCFH-DA). Secreted β-amyloid$_{1-42}$ (Aβ$_{1-42}$) level was assessed by ELISA. The expression of mRNA of Bcl2, Bax, Caspase3, Aβ precursor protein (APP), β-site APP-cleaving enzyme 1 (BACE1), and insulin degrading enzyme (IDE) were measured using quantitative real-time PCR (Q-PCR), and their protein levels were examined using Western blot.
Results: RGZ (0.1–10 μmol/L) significantly increased the cell viability that was reduced by AGEs (1000 μg/mL). RGZ (10 μmol/L) significantly ameliorated AGEs-triggered downregulation of SOD and catalase, and production of ROS. It also reversed Bcl2 downregulation, Bax upregulation and Caspase3 expression caused by AGEs. Moreover, it significantly attenuated AGEs-induced Aβ secretion and APP protein upregulation. RGZ did not affect BACE1 expression, but induced IDE expression, which promoted degradation of Aβ. All the effects were blocked by the specific PPARγ antagonist GW9662 (10 μmol/L).
Conclusion: RGZ protects the euroblastoma cells against AGEs-induced injury via its anti-oxidative, anti-apoptotic and anti-inflammatory properties that seems to be mediated by PPARγ activation. The results suggest a beneficial role for RGZ in the treatment of Alzheimer's disease.

Keywords: Alzheimer's disease; advanced glycation end products; rosiglitazone; apoptosis; β-amyloid; PPARγ; SH-SY5Y cells

Acta Pharmacologica Sinica (2011) 32: 991–998; doi: 10.1038/aps.2011.81; published online 18 Jul 2011

Introduction

Although the pathogenesis of sporadic Alzheimer's disease (AD) is not clearly understood, it is likely dependent on several age-related factors[1]. Diabetes is one of the most important risk factors for AD, and the multiple mechanisms connecting the two diseases have been proposed[1]. The pathological complications of diabetes affect several organ systems including the brain[2], which undergoes changes that could increase the risk of cognitive disorders including AD[3]. However, details of the association between diabetes and dementia have not yet been fully elucidated. Hyperglycemia is accompanied by accelerated formation of advanced glycation end-products (AGEs), which have been associated with increased amyloid deposition and neurofibrillary tau tangle formation[4]. Moreover, AGEs have been demonstrated to cause oxidative stress and inflammatory responses as well as cytotoxicity in neuronal cells[5–10]. An emerging body of evidence also suggests that AGEs decrease mitochondrial activity and lead to energy depletion[11, 12].

The central pathological event in AD is the progressive accumulation of amyloid-β (Aβ) in the brain. Aβ derives from sequential cleavage of the β-amyloid precursor protein (APP) by β- and γ-secretase. β-secretase (β-site APP-cleaving enzyme 1, BACE1) cleaves the ectodomain of APP, producing an APP C-terminal fragment. This fragment is further cleaved within the transmembrane domain by γ-secretase, resulting in the release of a family of Aβ peptides with different C-terminal variants, predominantly Aβ$_{40}$ and Aβ$_{42}$[13]. In addition, the level of Aβ is determined by the balance between its generation and turnover[14]. Aβ is degraded by endopeptidases, among which insulin-degrading enzyme (IDE) is predominant. IDE mediates much of the degradation of soluble

* To whom correspondence should be addressed.
E-mail yinazhlu@163.com
Received 2011-02-20 Accepted 2011-05-19

monomeric Aβ[13].

Peroxisome proliferator-activated receptors (PPARs) are a family of three related nuclear receptors (α, γ, and δ) that act as transcription factors in the regulation of genes responsible for lipid and energy metabolism. PPARγ is of particular importance for lipid and carbohydrate metabolism, and participates in the regulation of serum glucose levels and insulin sensitivity[14]. Two thiazolidinedione agonists of PPARγ, pioglitazone and rosiglitazone (RGZ), are widely prescribed for the treatment of type 2 diabetes mellitus[14]. There is now an extensive body of evidence that has demonstrated the efficacy of these agonists in reducing neuronal cell loss in *in vitro* models of neurotoxicity, *in vivo* models of cerebral ischemia-reperfusion injury, Parkinson's disease, and amyotrophic lateral sclerosis[15–23]. In particular, recent animal and clinical trials of RGZ have shown significant improvement in memory and cognition in animal models of AD, and AD patients, respectively[24]. Thus, PPARγ represents an important new therapeutic research target for the treatment of AD. However, the mechanisms mediating this potential beneficial effect remain to be fully elucidated.

AGEs may contribute to the etiology of many disease processes, including AD[15], by accumulating on β-amyloid plaques and exerting chronic oxidative stress via receptor-mediated mechanisms. Accordingly, in this study AGEs were used to induce neuronal toxicity in SH-SY5Y neuroblastoma cells *in vitro* to investigate the protective effects of RGZ. The antioxidative and anti-apoptotic properties of RGZ were also evaluated. The investigation therefore provides further insights into the mechanisms whereby RGZ exerts a beneficial effect in AD.

Materials and methods

Chemicals

Fetal bovine serum (FBS), Dulbecco's modified Eagle's medium (DMEM), trypsin-ethylenediaminetetracetic acid (EDTA), and antibiotics for cell culture were from Gibco/BRL Life Technologies (Grand Island, NY, USA). RGZ maleate tablets were purchased from SmithKline Beecham Pharmaceuticals (West Sussex, UK). GW9662, an inhibitor of PPARγ, was purchased from Cayman Chemical (Ann Arbor, MI, USA). All other chemicals and reagents, unless otherwise noted, were obtained from Sigma Chemical (St Louis, MO, USA).

Preparation of AGE-BSA

AGE-bovine serum albumin (BSA) was prepared by incubating 20 g/L BSA with 0.5 mol/L glucose at 37 °C for 3 months under sterile conditions, as described previously[16–18]. Control non-glycated BSA was incubated under the same conditions except for the absence of glucose. At the end of the incubation period, preparations were dialyzed against phosphate buffered saline (PBS) for 48 h while stirring to remove unincorporated glucose. The protein concentration was determined by Lowry assay. AGEs protein-specific fluorescence determinations were performed by measuring emission at 440 nm and excitation at 370 nm using a fluorescence spectrophotometer (F-3000, Hitachi, Japan).

Cell culture

The neuroblastoma cell line SH-SY5Y was grown in DMEM and Ham's F12 nutrient mixture (DMEM/F12; 1:1) routinely supplemented with 10% FBS, 100 units/mL penicillin, and 100 μg/mL streptomycin, and incubated at 37 °C in a humidified atmosphere of 5% CO_2. All experiments were carried out 24–36 h after cells were seeded. During AGEs studies, the growth medium was treated with 1000 μg/mL AGE-BSA or non-glycated BSA in the presence or absence of 10 μmol/L RGZ or 10 μmol/L of the PPARγ antagonist GW9662 for 24 h.

Cell viability assay

Methylthiazoletetrazolium (MTT) was dissolved in PBS at a concentration of 5 mg/mL. After 48 h incubation, 25 μL of the MTT solution was added to each well of 96-well plates and incubated for 4 h at 37 °C in a humidified atmosphere of 5% CO_2. At the end of the incubation period, the medium were discarded using a suction pump. The extraction buffer of 20% *w/v* sodium dodecyl sulfate (SDS) in 50% of N,N-dimethylformamide in demineralized water (50:50, *v/v*) was prepared at pH 4.7. The absorbance was determined at 570 nm. The A_{570} was taken as an index of cell viability and the activity of mitochondria. The net absorbance from the plates of cells cultured with the control medium (not treated) was considered as 100% cell viability and mitochondrial activity.

Measurement of the activity of superoxide dismutase (SOD) and catalase (CAT)

The SH-SY5Y cells were washed twice with PBS and lysed in 200 μL of lysis buffer. The supernatants were obtained by centrifugation at 14000×*g* at 4 °C for 10 min, and antioxidant enzyme activity assays were performed on the resulting supernatants. The protein content was determined by Lowry's method. The superoxide dismutase (SOD) activity was determined by mixing the reaction mixture with the samples. After adding one unit of SOD and 0.005 unit xanthine oxidase, the absorbance was read at 550 nm for 5 min. The SOD activity was calculated as:

$$\text{Inhibition (\%)} = \frac{\text{absorbance/min}_{\text{uninhibited}} - \text{absorbance/min}_{\text{inhibited}}}{\text{absorbance/min}_{\text{uninhibited}} - \text{absorbance/min}_{\text{blank}}} \times 100$$

Catalase activity was determined by adding 995 μL of 30 mmol/L H_2O_2 to 5 μL of cell lysate. The disappearance of H_2O_2 was monitored at 240 nm. The catalase activity was calculated as:

$$\text{Concentration} = \frac{\text{absorbance–control}}{43.6\ \text{M}^{-1}\text{cm}^{-1}} \times \text{path length (1 cm)}$$

Measurement of intracellular reactive oxygen species (ROS)

Intracellular reactive oxygen species (ROS) were monitored by using the fluorescent probe 2′,7′-dichlorodihydrofluorescein

diacetate (DCFH-DA). Intracellular H_2O_2, or low molecular weight peroxides, oxidize DCFH-DA to the highly fluorescent compound dichlorofluorescein (DCF). SH-SY5Y cells were seeded in 96-well plates and were incubated with increasing concentrations of AGEs and/or RGZ for 24 h. Cells were incubated with 10 μmol/L DCFH-DA at 37 °C for 30 min, then washed twice with PBS, and finally the fluorescence intensity of DCF was measured in a microplate-reader at excitation wavelength 485 nm and emission wavelength 538 nm.

Apoptosis assay

Apoptosis was measured according to the manufacturer's instructions (Bioscience Research Reagents, Temecula, CA, USA). Briefly, SH-SY5Y cells were collected by trypsin-EDTA, washed with PBS, resuspended in 100 μL of binding buffer and stained with 3 μL of fluorescein isothiocyanate-labeled Annexin-V and 2 μL of propidium iodide (PI). After 15 min of incubation, the cells were immediately analyzed by flow cytometry.

Quantitative real time polymerase chain reaction (Q-PCR)

The total RNA was extracted from the cells and converted to cDNA, according to the manufacturer's instructions. The total RNA (3 μg) was converted to cDNA by reverse transcriptase using a SuperScript™ II Reverse Transcriptase kit. Q-PCR of the cDNA samples was performed with an iCycler iQ™ Real-Time Detection System. Primer Sequences for quantitative PCR are indicated in Table 1. Five microliters of cDNA template was amplified in a mixture of 12.5 μL of iQ SYBR Green Supermix, primer, and sterile water in a final volume of 25 μL. For all experiments, the negative controls used water instead of cDNA for the PCR reaction. The data were normalized by subtracting the difference of the threshold cycle values between the target gene of interest and the β-actin housekeeping gene.

Western blot

After treatments, the cells were collected and homogenized in lysis buffer containing a mixture of protease inhibitors. Cell extracts, prepared by centrifugation at 16 000×*g*, were resolved by SDS-PAGE. Proteins were then transferred onto a nitrocellulose membrane, and blotted with the appropriate primary antibodies: polyclonal rabbit anti-Bcl2 (Santa Cruz), polyclonal rabbit anti-cleaved Caspase3 (Cell Signaling, Beverly, MA, USA), polyclonal rabbit anti-Bax (Santa Cruz), monoclonal mouse anti-BACE1 (Chemicon), polyclonal rabbit anti-APP (Zymed, San Francisco, CA, USA), polyclonal goat anti-IDE (Santa Cruz), polyclonal mouse anti-β-actin (Santa Cruz). Anti-mouse and anti-rabbit as well as anti-goat secondary antibodies were coupled to horseradish peroxidase (Santa Cruz). The detection was performed by using an ECL Plus kit (Amersham Biosciences, Milan, Italy). Relative expressions of proteins were quantified by densitometric scanning of the X-ray films with a GS 700 Imaging Densitometer (Bio-Rad) and a computer program. β-actin was used for standardization of the samples.

Aβ detection

$A\beta_{1\text{-}42}$ were detected using a human β-amyloid$_{1\text{-}42}$ ELISA kit (BioSource) and conditioned medium. The kit protocol was followed to prepare samples. Briefly, the plate was washed four times with wash buffer. The standard peptide was resuspended and serial dilutions were prepared. Dilutions of the samples to be tested were also prepared. Standards or samples (100 μL) were added to the appropriate wells of the precoated microtiter plate and incubated for 2 h at room temperature. They were washed four times with wash buffer. The diluted detection antibody (rabbit polyclonal $A\beta_{1\text{-}42}$, 100 μL) was placed into the wells and incubated for 2 h at room temperature. The samples were then washed four times with wash buffer. One hundred microliters of the HRP-conjugated

Table 1. Primer sequences and PCR reaction condition used in this study.

Gene name	Gene Bank ID	PCR primers (5′–3′)	Tm (°C)	Length of PCR product
APP	NM_001136016	Forward: GAGACACCTGGGGATGAGAATG Reverse: GCTTGACGTTCTGCCTCTTCC	60	122 bp
BACE1	NM_012104	Forward: TACCAACCAGTCCTTCCGC Reverse: CCGTGGATGACTGTGAGATG	60	116 bp
Bax	NM_004324	Forward: AGTGTCTCAAGCGCATCGG Reverse: CCCAGTTGAAGTTGCCGTC	60	141 bp
Bcl2	NM_000633	Forward: ATGTGTGTGGAGAGCGTCAAC Reverse: CAGTTCCACAAAGGCATCCC	60	135 bp
Caspase3	NM_032991	Forward: AGAACTGGACTGTGGCATTG Reverse: CACAAAGCGACTGGATGAAC	60	164 bp
IDE	NM_004969	Forward: GCCGAAGCCTTGTCTCAACT Reverse: CAAATAGGCCATGTTACAGTGCAA	60	79 bp
β-actin	NM_001101	Forward: CCCAGCACAATGAAGATCAAGATCAT Reverse: ATCTGCTGGAAGGTGGACAGCGA	60	101 bp

anti-rabbit antibody was added to the wells and incubated for 2 h at room temperature. The wells were washed four times with wash buffer and then 100 μL of chromogen solution was added to each well. The wells were incubated for 30 min at room temperature, protected from light, and then 100 μL of stop solution was added to each well. Optical density was measured at 450 nm. The results were calculated from a standard curve. The data represent the means from experiments done in triplicate.

Statistical analysis

The statistical significance of the differences was determined using one-way ANOVA followed by the Scheffe *F* test. Differences in which the probability (*P*)-value<0.05 were considered statistically significant. All graphs represent the mean±standard deviation (SD) for three separate experiments.

Results

RGZ ameliorates AGEs-induced neuronal insult

To determine the cytotoxic effects of AGEs at various concentrations for 24 h in SH-SY5Y cells, MTT assays were performed to assess cell viability. As shown in Figure 1A, AGEs treatment at a range of 100–2000 μg/mL resulted in a reduction of cell viability from up to 14% to 25% in a concentration-dependent manner. Therefore, AGEs at 1000 μg/mL was used to induce neuronal insults in the following experiments. In order to investigate the protective effect of RGZ, SH-SY5Y cells were treated with 1000 μg/mL AGEs and RGZ with or without the PPAR-γ inhibitor GW9662, for 24 h. As shown in Figure 1B, RGZ significantly attenuated the decrease in AGEs-induced neuronal viability in a concentration-dependent manner. In contrast, GW9662 treatment reversed the protective effect of RGZ on AGEs-induced neuronal insult (Figure 1D), whereas GW9662 alone did not affect the cell viability (Figure 1C). These results suggest that RGZ protecting from AGEs-induced neurotoxicity in SH-SY5Y cells is associated with PPARγ.

RGZ inhibits oxidative stress induced by AGEs in SH-SY5Y cells

To determine the effects of RGZ on oxidative stress induced by AGEs in SH-SY5Y cells, ROS production and the activities of antioxidant enzymes were measured. As expected, RGZ significantly attenuated AGEs-induced ROS production (Figure 2A), and the reduction of the activities of SOD as well as catalase (Figure 2B and 2C, respectively). Similarly, the PPARγ antagonist GW9662 eliminated the upregulatory effects of RGZ on the activities of SOD and catalase in this process. But reduction of ROS induced by RGZ was not blocked by PPARγ antagonist GW9662. These results indicate that the cytotoxic effect of AGEs on SH-SY5Y cells may be mediated by oxidative stress, while RGZ ameliorated AGEs-induced downregulation

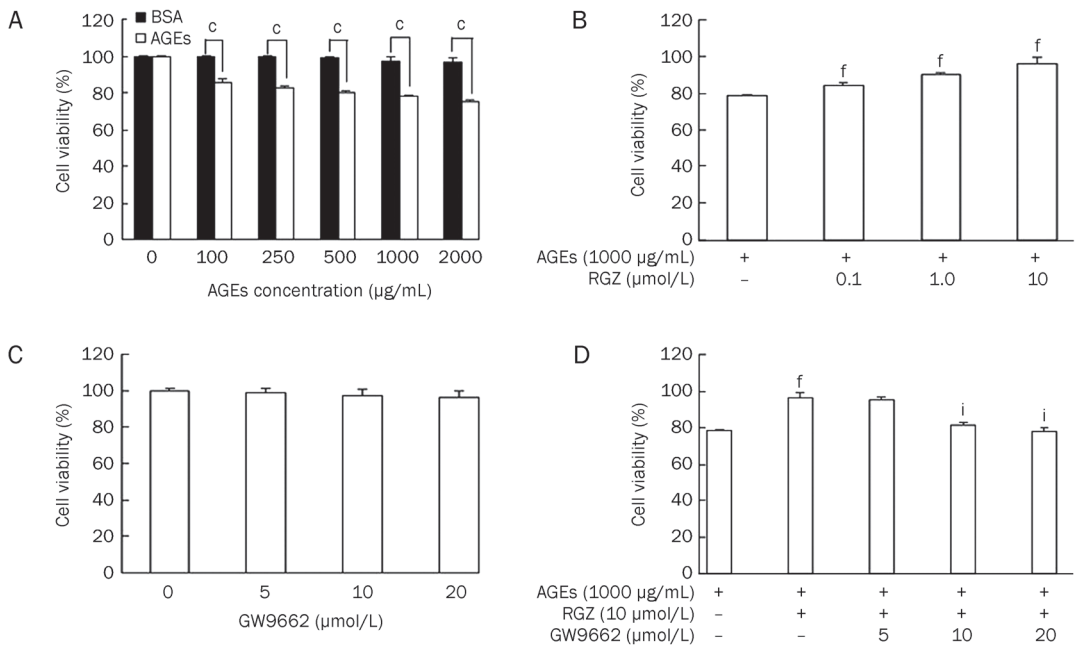

Figure 1. Effects of RGZ on the cell viability of SH-SY5Y cells treated with AGEs. (A) Cytotoxicity of AGEs in SH-SY5Y cells. SH-SY5Y cells grown to confluence were incubated with AGEs or a non-glycated control at concentration of 0, 100, 250, 500, 1000, and 2000 μg/mL. After incubation for 24 h, cell viability was quantified by MTT assay. Note that AGEs decreased cell viability in a concentration-dependent manner. (B) RGZ ameliorated AGEs-induced neuronal insult in SH-SY5Y cells. SH-SY5Y cells were treated with 1000 μg/mL AGEs in the absence or presence of 0.1, 1.0, 10 μmol/L RGZ for 24 h. (C) GW9662 did not affect cell viability of SH-SY5Y cells. SH-SY5Y cells were treated with 0, 5, 10, or 20 μmol/L GW9662 alone for 24 h. (D) RGZ ameliorated AGEs-induced neuronal insult in SH-SY5Y cells was eliminated by GW9662, an antagonist for PPARγ. SH-SY5Y cells were treated with 1000 μg/mL AGEs and 10 μmol/L RGZ with or without GW9662 for 24 h. Data are shown as mean±SD (*n*=3 independent experiments). ^{c}P<0.01 compared with the control group. ^{f}P<0.01 compared with AGEs-treated group. ^{i}P<0.01 compared with AGEs+RGZ-treated group.

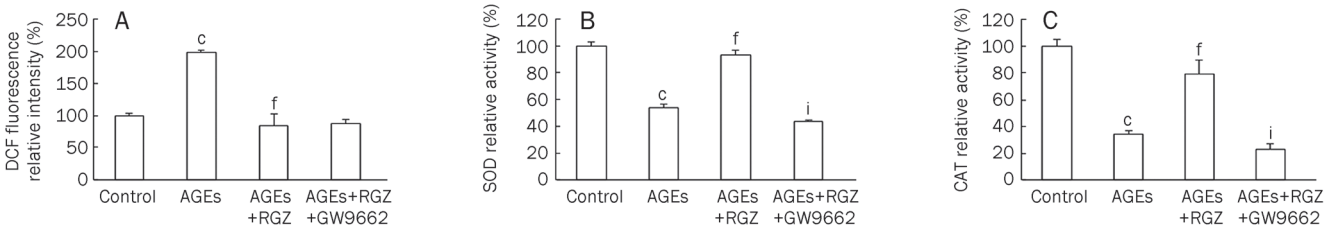

Figure 2. Effects of RGZ on the activities of SOD and catalase as well as the production of ROS in AGEs-treated SH-SY5Y cells. SOD and CAT activity as well as ROS levels were determined in SH-SY5Y cells after incubation with AGEs (1000 μg/mL) for 24 h with or without 10 μmol/L RGZ and 10 μmol/L GW9662. (A) ROS production. (B) SOD activity. (C) Catalase activity. Data are shown as mean±SD (n=3 independent experiments). ^{c}P<0.01 compared with the control group. ^{f}P<0.01 compared with AGEs-treated group. ^{i}P<0.01 compared with AGEs+RGZ-treated group.

of SOD and CAT activities in a PPARγ-dependent manner.

RGZ prevents cell apoptosis induced by AGEs in SH-SY5Y cells

Cell apoptosis was evaluated by Annexin V and propidium iodide (PI) double-staining. As shown in Figure 3, treatment with AGEs for 24 h (Figure 3B) resulted in a 10% increase in apoptosis of SH-SY5Y cells when compared to controls (Figure 3A), 11.48% *vs* 1.36% apoptotic cells. In contrast, RGZ treatment (Figure 3C) attenuated cell apoptosis up to 4% when compared to AGEs treatment alone (Figure 3B). The anti-apoptotic effect of RGZ was blocked by GW9662 (Figure 3D), indicating the involvement of PPARγ in this process.

Effects of RGZ on Bcl2 and Bax as well as Caspase3 expression in AGEs-treated SH-SY5Y cells

The apoptosis-relevant molecules Bcl2 and Bax, as well as Caspase3, were determined by Q-PCR and Western blot, respectively. As shown in Figure 4, exposure to AGEs resulted in an upregulation of pro-apoptotic Bax (Figure 4B and 4E) and a downregulation of anti-apoptotic Bcl2 (Figure 4A and 4D) both in mRNA and protein levels as well as activation of Caspase3 (Figure 4C and 4F). RGZ treatment markedly reversed the effect of AGEs on these molecules. Similarly, PPARγ antagonist GW9662 eliminated the anti-apoptotic effects of RGZ in AGEs-treated SH-SY5Y cells. These observations suggest that RGZ could suppress the AGEs-induced apoptosis via PPAR-γ activation.

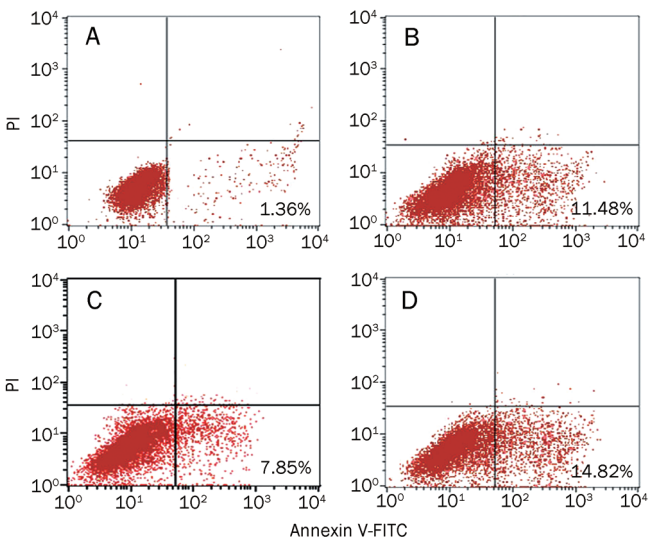

Figure 3. Effects of RGZ on AGEs-induced apoptosis in SH-SY5Y cells. SH-SY5Y cells were incubated with AGEs (1000 μg/mL) for 24 h with or without 10 μmol/L RGZ and 10 μmol/L GW9662. (A) The non-glycated control for 24 h. (B) The glyco-AGE (AGEs) 1000 μg/mL for 24 h. (C) AGEs (1000 μg/mL) with RGZ (10 μmol/L) for 24 h. (D) AGEs (1000 μg/mL) and RGZ (10 μmol/L) as well as GW9662 (10 μmol/L) for 24 h. Annexin fluorescence intensity was determined by flow cytometric analysis (FACS).

Effects of RGZ on $A\beta_{1-42}$ secretion and APP expression as well as BACE1 activity in AGEs-treated SH-SY5Y cells

To evaluate whether the effect of RGZ on AGEs-induced neuronal insults is related to APP processing, the mRNA and protein levels of APP and BACE1, as well as $A\beta_{1-42}$, were determined. It showed that exposure to AGEs significantly increased the mRNA and protein levels of APP (Figure 5A and 5C) and BACE1 (Figure 5B and 5D), as well as $A\beta_{1-42}$ (Figure 6A). However, RGZ treatment only attenuated AGEs-induced upregulation of APP proteins (Figure 5C), and not APP mRNA levels (Figure 5A). There were no changes in mRNA and protein levels of BACE1 after treatment with RGZ when compared to AGEs treatment alone (Figure 5B and 5D). In addition, RGZ treatment resulted in a notable reduction of APP protein and $A\beta_{1-42}$ in SH-SY5Y cells (Figure 5C and 6A). This effect was abrogated by the PPARγ antagonist GW9662 (Figure 5C and 6A), suggesting a role for PPARγ in the amelioration of AGEs-induced APP protein regulation and $A\beta_{1-42}$ secretion by RGZ.

Effects of RGZ on IDE expression in AGEs-treated SH-SY5Y cells

To confirm the assumption that the attenuation of Aβ secretion by the PPARγ agonist RGZ is mediated by IDE, the mRNA and protein levels of IDE were also determined in SH-SY5Y cells following exposure to RGZ. As shown in Figure 6B and 6C, there were no significant changes in either mRNA or protein levels of IDE in SH-SY5Y cells treated with AGEs alone. However, RGZ treatment resulted in an upregulation of IDE indicated by an increase in its mRNA and protein levels (Figure 6B and 6C). In contrast, PPARγ antagonist GW9662

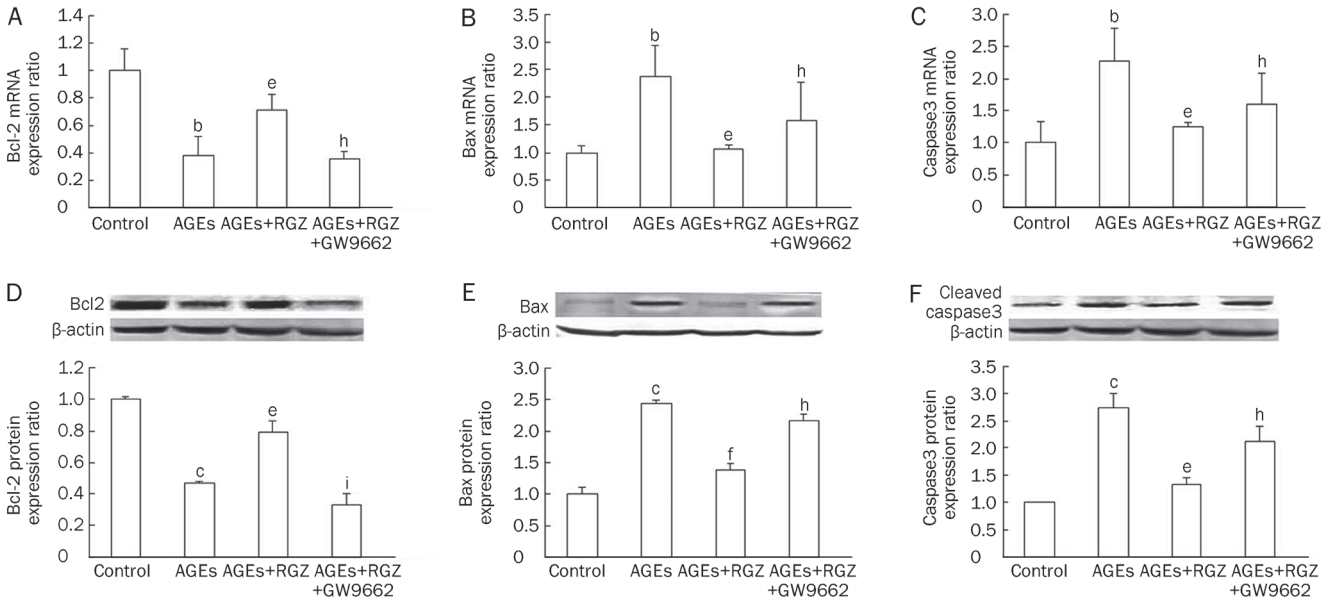

Figure 4. Effects of RGZ on Bcl2 and Bax as well as Caspase3 expression in AGEs-treated SH-SY5Y cells. SH-SY5Y cells were treated with 1000 μg/mL AGEs for 24 h, with or without incubation of 10 μmol/L RGZ and 10 μmol/L GW9662. (A) The mRNA of Bcl2. (B) The mRNA of Bax. (C) The mRNA of activated Caspase3. (D) The protein expression of Bcl2. (E) The protein expression of Bax. (F) The protein expression of activated Caspase3. Data are shown as mean±SD (n=3 independent experiments). $^{b}P<0.05$, $^{c}P<0.01$ compared with the control group. $^{e}P<0.05$, $^{f}P<0.01$ compared with AGEs-treated group. $^{h}P<0.05$, $^{i}P<0.01$ compared with AGEs+RGZ-treated group.

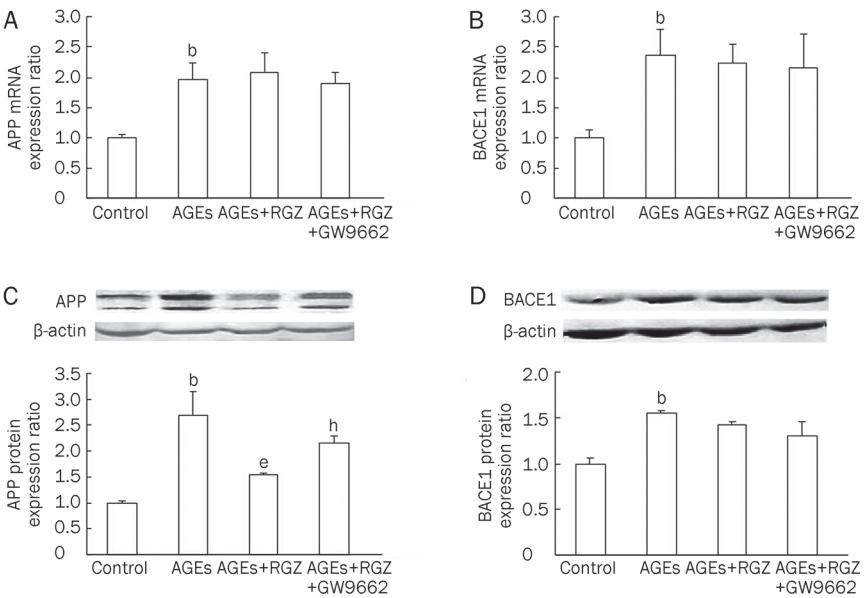

Figure 5. Effects of RGZ on the expression of APP and BACE1 in AGEs-treated SH-SY5Y cells. SH-SY5Y cells were treated with 1000 μg/mL AGEs for 24 h, with or without incubation of 10 μmol/L RGZ and 10 μmol/L GW9662. (A) The mRNA expression of APP. (B) The mRNA expression of BACE1. (C) The protein expression of APP. (D) The protein expression of BACE1. Data are shown as mean±SD (n=3 independent experiments). $^{b}P<0.05$ compared with the control group. $^{e}P<0.05$ compared with AGEs-treated group. $^{h}P<0.05$ compared with AGEs+RGZ-treated group.

significantly eliminated the effect of RGZ on the mRNA and protein levels of IDE (Figure 6B and 6C). These results indicate that PPARγ is involved in the regulation of IDE expression by RGZ in AGEs-induced SH-SY5Y cells.

Discussion

Accumulating evidence indicates that AGEs formation and oxidative stress are important pathways leading to neuronal cell death in AD[4, 19, 20]. The production of AGEs has not been established *in vitro*. However, a recent study showed that extensively-modified, non-physiological AGEs formed under *in vitro* conditions may exert the same biological effects as AGEs-rich serum obtained from diabetic patients[21]. Therefore, AGE-BSA was used in this study.

PPARγ agonists have been proposed as an alternative for the treatment of AD because of their anti-inflammatory and anti-oxidative effect[24]. In this study, we investigated the protective effect of the PPARγ agonist RGZ on AGEs-induced

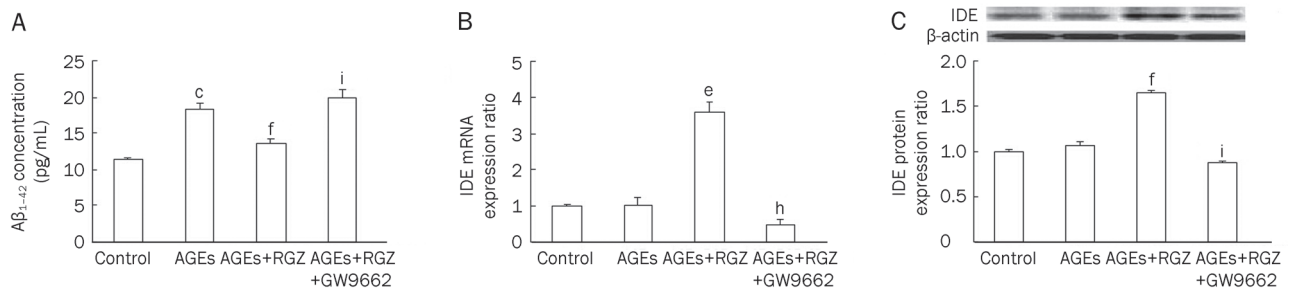

Figure 6. Effects of RGZ on the secretion of $A\beta_{1-42}$ and mRNA as well as protein levels of IDE in AGEs-treated SH-SY5Y cells. SH-SY5Y cells were treated with 1000 μg/mL AGEs for 24 h, with or without incubation of 10 μmol/L RGZ and 10 μmol/L GW9662. (A) The level of $A\beta_{1-42}$ was measured by ELISA. (B) The mRNA expression of IDE. (C) The protein expression of IDE. Bars show the mean±SD (n=3 independent experiments). $^{b}P<0.05$, $^{c}P<0.01$ compared with the control group. $^{e}P<0.05$, $^{f}P<0.01$ compared with AGEs-treated group. $^{h}P<0.05$, $^{i}P<0.01$ compared with AGEs- and RGZ-treated group.

injury in human neuroblastoma SH-SY5Y cells. SH-SY5Y cells were chosen for their expression of PPARγ, and thus are a valuable cell model to study PPARγ-mediated effects on neuronal cells[22]. A novel finding of this study is that RGZ at relatively low concentrations protects against AGEs-induced cytotoxicity in SH-SY5Y cells through anti-oxidation and anti-apoptosis effects, as well as reducing Aβ production.

The antioxidant activity of RGZ may contribute to its neuroprotective action[23]. In the present study, RGZ protected neuronal cells from AGEs-induced injury via its antioxidant activity. Treatment with RGZ at a concentration of 10 μmol/L was capable of reducing AGEs-induced oxidative stress by upregulating the antioxidant enzyme activities of SOD and catalase (Figure 2B and 2C). SOD and CAT promoters contain the PPAR response element[25]. Thus the PPARγ agonist RGZ may potentially regulate the expression of SOD and CAT. The increase in anti-oxidative capacity by RGZ may contribute to its protection of SH-SY5Y cells against ROS caused by AGEs.

There is now a body of evidence that has demonstrated the efficacy of PPARγ agonists in protecting neuronal cells from apoptosis[26, 27]. However, how RGZ protects against AGEs-induced apoptosis in neuronal cells is poorly understood. The present study demonstrated that AGEs caused a significant suppression of Bcl2 expression levels which were restored by treatment with RGZ (Figure 4A and 4D). Restoration of Bcl2 expression was abrogated by the PPARγ pharmacological specific inhibitor GW9662, indicating that the anti-apoptotic effect of RGZ is dependent on PPARγ. In addition, the present results indicate that RGZ prevents the increase of Bax and Caspase3 in AGEs-induced SH-SY5Y cells (Figure 4B, 4C, 4E, and 4F), which effects were also blocked by PPARγ antagonist GW9662. Therefore, these findings, taken together, support the notion that RGZ-mediated cytoprotection is due to its inhibition of the oxidative stress and mitochondrial apoptotic pathway in a PPARγ-dependent manner.

PPARγ involvement in ameliorating AD-related pathology has been the focus of studies that have been directed at dissecting the mechanisms through which PPARγ regulates Aβ metabolism[28–30]. Sastre and colleagues[30] reported that PPARγ agonists modulate the processing of APP through regulation of β-secretase, whereas Camacho and co-workers[28] demonstrated that PPARγ did not affect expression or activity of any of the secretases involved in the generation of Aβ, but instead induces a fast, cell-bound clearing mechanism responsible for the removal of the Aβ peptide from the medium. In the present study, RGZ treatment resulted in a dramatic reduction of Aβ secretion, which was accompanied by a reduction of APP at a post-transcriptional level (Figure 5A, 5C, and 6A). Moreover, RGZ did not affect either mRNA or protein levels of BACE1 in this process (Figure 5B and 5D), indicating that RGZ decreases Aβ secretion by promoting its degradation. IDE is a protease that has been demonstrated to play a key role in Aβ degradation[31]. However, little is known about the cellular regulation of IDE in this process. The present study demonstrates that the PPARγ agonist RGZ regulates the transcription and translation of IDE in neuronal cells (Figure 6B and 6C). Given that RGZ does not affect the expression of BACE1 involved in the generation of Aβ, this indicates that RGZ may regulate Aβ degradation rather than generation in neuronal cells.

In summary, RGZ protects SH-SY5Y cells against AGEs-induced cytotoxicity. Its anti-oxidative and anti-apoptotic as well as anti-inflammatory properties, such as reducing Aβ secretion and enhancing Aβ degradation, render this effective molecule potentially protective against AGEs-induced cytotoxicity. This report may offer a useful strategy for the treatment of progressive neurodegenerative diseases such as AD.

Acknowledgements

We thank Medjaden Bioscience Limited for assisting in the preparation of this manuscript. This research was supported by Educational Commission Foundation of Heilongjiang Province of China (No 11531080).

Author contribution

Prof Yi-na ZHANG designed the research; Dr Chun-jiang YU wrote and revised the manuscript; Dr Li WANG performed the experiments; Dr Wei LIU assisted with the experiments; and Dr Lu-yang CHENG assisted with the data statistical

analysis.

References

1 Guglielmotto M, Aragno M, Tamagno E, Vercellinatto I, Visentin S, Medana C, *et al*. AGEs/RAGE complex upregulates BACE1 via NF-kappaB pathway activation. Neurobiol Aging 2010. doi: 10.1016/j.neurobiolaging.2010.05.026
2 McCall AL. The impact of diabetes on the CNS. Diabetes 1992; 41: 557–70.
3 Wang SH, Sun ZL, Guo YJ, Yuan Y, Li L. PPARγ-mediated advanced glycation end products regulation of neural stem cells. Mol Cell Endocrinol 2009; 307: 176–84.
4 Munch G, Schinzel R, Loske C, Wong A, Durany N, Li JJ, *et al*. Alzheimer's disease — synergistic effects of glucose deficit, oxidative stress and advanced glycation endproducts. J Neural Transm 1998; 105: 439–61.
5 Mruthinti S, Sood A, Humphrey CL, Swamy-Mruthinti S, Buccafusco JJ. The induction of surface beta-amyloid binding proteins and enhanced cytotoxicity in cultured PC-12 and IMR-32 cells by advanced glycation end products. Neuroscience 2006; 142: 463–73.
6 Woltjer RL, Maezawa I, Ou JJ, Montine KS, Montine TJ. Advanced glycation endproduct precursor alters intracellular amyloid-beta/A beta PP carboxy-terminal fragment aggregation and cytotoxicity. J Alzheimers Dis 2003; 5: 467–76.
7 Loske C, Neumann A, Cunningham AM, Nichol K, Schinzel R, Riederer P, *et al*. Cytotoxicity of advanced glycation endproducts is mediated by oxidative stress. J Neural Transm 1998; 105: 1005–15.
8 Gasic-Milenkovic J, Loske C, Deuther-Conrad W, Munch G. Protein "AGEing" — cytotoxicity of a glycated protein increases with its degree of AGE-modification. Z Gerontol Geriatr 2001; 34: 457–60.
9 Deuther-Conrad W, Loske C, Schinzel R, Dringen R, Riederer P, Munch G. Advanced glycation endproducts change glutathione redox status in SH-SY5Y human neuroblastoma cells by a hydrogen peroxide dependent mechanism. Neurosci Lett 2001; 312: 29–32.
10 Wei Y, Chen L, Chen J, Ge L, He RQ. Rapid glycation with D-ribose induces globular amyloid-like aggregations of BSA with high cytotoxicity to SH-SY5Y cells. BMC Cell Biol 2009; 10: 10.
11 Kuhla B, Loske C, Garcia De Arriba S, Schinzel R, Huber J, Munch G. Differential effects of "Advanced glycation endproducts" and beta-amyloid peptide on glucose utilization and ATP levels in the neuronal cell line SH-SY5Y. J Neural Transm 2004; 111: 427–39.
12 de Arriba SG, Stuchbury G, Yarin J, Burnell J, Loske C, Munch G. Methylglyoxal impairs glucose metabolism and leads to energy depletion in neuronal cells — protection by carbonyl scavengers. Neurobiol Aging 2007; 28: 1044–50.
13 Selkoe DJ. Alzheimer's disease: genes, proteins, and therapy. Physiol Rev 2001; 81: 741–66.
14 Yki-Jarvinen H. Thiazolidinediones. N Engl J Med 2004; 351: 1106–18.
15 Sasaki N, Fukatsu R, Tsuzuki K, Hayashi Y, Yoshida T, Fujii N, *et al*. Advanced glycation end products in Alzheimer's disease and other neurodegenerative diseases. Am J Pathol 1998; 153: 1149–55.
16 Bucala R, Tracey KJ, Cerami A. Advanced glycosylation products quench nitric oxide and mediate defective endothelium-dependent vasodilatation in experimental diabetes. J Clin Invest 1991; 87: 432–8.
17 Doi T, Vlassara H, Kirstein M, Yamada Y, Striker GE, Striker LJ. Receptor-specific increase in extracellular matrix production in mouse mesangial cells by advanced glycosylation end products is mediated via platelet-derived growth factor. Proc Natl Acad Sci U S A 1992; 89: 2873–7.
18 Pugliese G, Pricci F, Romeo G, Pugliese F, Mene P, Giannini S, *et al*. Upregulation of mesangial growth factor and extracellular matrix synthesis by advanced glycation end products via a receptor-mediated mechanism. Diabetes 1997; 46: 1881–7.
19 Takeuchi M, Kikuchi S, Sasaki N, Suzuki T, Watai T, Iwaki M, *et al*. Involvement of advanced glycation end-products (AGEs) in Alzheimer's disease. Curr Alzheimer Res 2004; 1: 39–46.
20 Sato T, Shimogaito N, Wu X, Kikuchi S, Yamagishi S, Takeuchi M. Toxic advanced glycation end products (TAGE) theory in Alzheimer's disease. Am J Alzheimers Dis Other Demen 2006; 21: 197–208.
21 Yamagishi S, Inagaki Y, Okamoto T, Amano S, Koga K, Takeuchi M. Advanced glycation end products inhibit *de novo* protein synthesis and induce TGF-beta overxepression in proximal tubular cells. Kidney Int 2003; 63; 464–73.
22 Miglio G, Rosa AC, Rattazzi L, Collino M, Lombardi G, Fantozzi R. PPARgamma stimulation promotes mitochondrial biogenesis and prevents glucose deprivation-induced neuronal cell loss. Neurochem Int 2009; 55: 496–504.
23 Jung TW, Lee JY, Shim WS, Kang ES, Kim SK, Ahn CW, *et al*. Rosiglitazone protects human neuroblastoma SH-SY5Y cells against MPP^+ induced cytotoxicity via inhibition of mitochondrial dysfunction and ROS production. J Neurol Sci 2007; 253: 53–60.
24 Landreth G, Jiang Q, Mandrekar S, Heneka M. PPARgamma agonists as therapeutics for the treatment of Alzheimer's disease. Neurotherapeutics 2008; 5: 481–9.
25 Pistrosch F, Passauer J, Fischer S, Fuecker K, Hanefeld M, Gross P. In type 2 diabetes, rosiglitazone therapy for insulin resistance ameliorates endothelial dysfunction independent of glucose control. Diabetes Care 2004; 27: 484–90.
26 Fuenzalida K, Quintanilla R, Ramos P, Piderit D, Fuentealba RA, Martinez G, *et al*. Peroxisome proliferator-activated receptor gamma up-regulates the Bcl-2 anti-apoptotic protein in neurons and induces mitochondrial stabilization and protection against oxidative stress and apoptosis. J Biol Chem 2007; 282: 37006–15.
27 Wang YL, Frauwirth KA, Rangwala SM, Lazar MA, Thompson CB. Thiazolidinedione activation of peroxisome proliferator-activated receptor gamma can enhance mitochondrial potential and promote cell survival. J Biol Chem 2002; 277: 31781–8.
28 Camacho IE, Serneels L, Spittaels K, Merchiers P, Dominguez D, De Strooper B. Peroxisome-proliferator-activated receptor gamma induces a clearance mechanism for the amyloid-beta peptide. J Neurosci 2004; 24: 10908–17.
29 d'Abramo C, Massone S, Zingg JM, Pizzuti A, Marambaud P, Dalla Piccola B, *et al*. Role of peroxisome proliferator-activated receptor gamma in amyloid precursor protein processing and amyloid beta-mediated cell death. Biochem J 2005; 391: 693–8.
30 Sastre M, Dewachter I, Landreth GE, Willson TM, Klockgether T, van Leuven F, *et al*. Nonsteroidal anti-inflammatory drugs and peroxisome proliferator-activated receptor-gamma agonists modulate immunostimulated processing of amyloid precursor protein through regulation of beta-secretase. J Neurosci 2003; 23: 9796–804.
31 Cook DG, Leverenz JB, McMillan PJ, Kulstad JJ, Ericksen S, Roth RA, *et al*. Reduced hippocampal insulin-degrading enzyme in late-onset Alzheimer's disease is associated with the apolipoprotein E-epsilon4 allele. Am J Pathol 2003; 162: 313–9.

Acta Pharmacologica Sinica (2011) 32: 999–1008
 1671-4083/11 $32.00
www.nature.com/aps

Original Article

Involvement of RhoA/ROCK in myocardial fibrosis in a rat model of type 2 diabetes

Hong ZHOU[1], Yong-jun LI[2, *], Mian WANG[1], Li-hui ZHANG[1], Bing-yan GUO[2], Zhan-sheng ZHAO[1], Feng-ling MENG[1], Yong-gui DENG[1], Rui-ying WANG[1]

Department of [1]Endocrinology and [2]Cardiology, the Second Hospital of Hebei Medical University, Shijiazhuang 050000, China

Aim: To investigate whether activation of RhoA/Rho kinase (ROCK) is involved in myocardial fibrosis in diabetic hearts.
Methods: A rat model of type 2 diabetes was established using high fat diet combined with streptozotocin (30 mg/kg, ip). Animals were randomly divided into 3 groups: control rats, untreated diabetic rats that received vehicle and treated diabetic rats that received Rho-kinase inhibitor fasudil hydrochloride hydrate (10 $mg{\cdot}kg^{-1}{\cdot}d^{-1}$, ip, for 14 weeks). Cardiac contractile function was evaluated *in vivo*. The morphological features of cardiac fibrosis were observed using immunohistochemistry and TEM. The mRNA expression of JNK, TGFβ1, type-I, and type-III procollagen was assessed with RT-PCR. The phosphorylation of MYPT1, JNK and Smad2/3, as well as the protein levels of TGFβ1 and c-Jun, were evaluated using Western blotting.
Results: In untreated diabetic rats, myocardial fibrosis was developed and the heart contractility was significantly reduced as compared to the control rats. In the hearts of untreated diabetic rats, the mRNA expression level and activity of JNK were upregulated; the expression of TGFβ1 and phosphorylation of Smad2/3 were increased. In the hearts of treated diabetic rat, activation of JNK and TGFβ/Smad was significantly decreased, myocardial fibrosis was reduced, and cardiac contractile function improved.
Conclusion: The data suggest that fasudil hydrochloride hydrate ameliorates myocardial fibrosis in rats with type 2 diabetes at least in part through inhibiting the JNK and TGFβ/Smad pathways. Inhibition of RhoA/ROCK may be a novel therapeutic target for prevention of diabetic cardiomyopathy.

Keywords: diabetes; myocardial fibrosis; Rho kinase; c-Jun NH_2-terminal kinase; transforming growth factor-β

Acta Pharmacologica Sinica (2011) 32: 999–1008; doi: 10.1038/aps.2011.54; published online 11 Jul 2011

Introduction

Diabetes mellitus (DM) has emerged as a major threat to the health of humans throughout the world. Long-term DM results in the development of diabetic cardiomyopathy, which is characterized histologically by myocardial fibrosis. DM-induced cardiac remodeling may participate in diastolic and systolic dysfunction, leading to congestive heart failure. Moreover, it can occur during the early stages of DM[1, 2], and is closely related to a high prevalence of mortality from cardiovascular events in DM. However, specific drugs for the prevention or treatment of diabetic cardiomyopathy are not available. Treatment of heart failure is empirical because a class of agent that favorably affects outcomes has not been discovered. Thus, a more thorough understanding of the pathogenesis of diabetic cardiomyopathy and the development of new pharmacologic treatments are needed.

RhoA is a member of the Ras superfamily of GTP-binding proteins. Its downstream effector, Rho-kinases (ROCK), regulates various biological functions in cells, including the adherence, migration, proliferation, apoptosis and gene expression of cells[3, 4]. Also, the RhoA/ROCK pathway plays an important pathophysiological part in hypertension[5] and stroke[6]. There is growing evidence that RhoA/ROCK signaling mediates the glomerular matrix accumulation of proteins in diabetic nephropathy. The ROCK inhibitor fasudil can suppress renal fibrosis and can reduce proteinuria[7, 8]. The inhibition of ROCK attenuates cardiac fibrosis in angiotensin II-induced cardiac hypertrophy *in vivo*[9, 10]. Mitogen-activated protein kinases (MAPKs) are important mediators of signal transduction from the cell surface to the nucleus. c-Jun NH_2-terminal kinase (JNK) is one of the major members of MAPKs, and JNK activation is also implicated in cardiac fibrosis[11, 12]. Recent studies show that there is signal crosstalk between RhoA/ROCK and JNK pathways[13]. The pro-sclerotic growth factor,

* To whom correspondence should be addressed.
E-mail lyjbs2009@yeah.net
Received 2010-01-23 Accepted 2011-04-13

transforming growth factor β (TGFβ), plays a major part in the fibrosis and dysfunction of organs[14, 15]. Hence, the blockade of its expression and action represents an important therapeutic target.

A high-fat diet with injection of low-dose streptozotocin (STZ) for the induction of type 2 DM in rats has been found to be a good model for DM research[16, 17]. This type of model replicates the natural history and metabolic characteristics of type 2 DM in humans.

The purpose of the present study was to understand the roles of RhoA/ROCK, JNK, and TGFβ/Smad pathways in DM-induced cardiac remodeling. We also wished to ascertain the effects of fasudil on myocardial fibrosis in rats with type 2 DM, with the objective of providing a novel target for the treatment of diabetic cardiomyopathy.

Materials and methods

The experimental protocol was approved by the Ethics Review Committee for Animal Experimentation of Hebei Medical University (Shijiazhuang, China).

Experimental animals

Female Sprague–Dawley (SD) rats (initially weighing 180–200 g) were procured from the Laboratory Animal Centre of Hebei Medical University. Rats were housed in standard cages (4 rats/cage) and maintained under a controlled room temperature (22±2 °C) and humidity (55%±5%) with a 12-h:12-h light–dark cycle. After acclimatization, rats were randomly assigned to receive a standardized diet (18% fat, 25% protein, and 57% carbohydrate) as the normal control group or a high-fat diet (HFD, 40% fat, 13% protein, and 47% carbohydrate) for 6 weeks. At the end of 6 weeks, as previously described[16, 17], control rats were injected (ip) with vehicle [0.1 mol/L citric acid buffer (pH 4.5)] once and given a standard diet sequentially. HFD rats were injected (ip) with low-dose (30 mg/kg) of STZ (Sigma-Aldrich, St Louis, MO, USA) and given a high-fat diet sequentially. Blood glucose (BG) was measured in whole blood collected from the tail vein by a portable glucometer (Accu-Chek Active, Roche Diagnostics Limited, Mannheim, Germany). Body weight (BW) and BG levels were recorded every week. Rats with BG levels above 16.7 mmol/L and that were stable for 4 weeks were considered to be diabetic. At week 10, hyperinsulinemic-euglycemic clamp techniques were performed, and fasting insulin (FINS), fasting blood glucose (FBG), total cholesterol (TC) and triglyceride (TG) were measured.

Control rats remained on a standard diet and were treated with ip injection of sterile vehicle every day. Diabetic rats were randomly divided into two groups: (i) treated diabetic rats maintained on a high-fat diet and received fasudil hydrochloride hydrate (hereafter termed "fasudil"; 10 $mg \cdot kg^{-1} \cdot d^{-1}$; ip) (Tianjin Hongri Company, Tianjin, China) every day for 14 weeks; and (ii) untreated diabetic rats treated with injection (ip) of sterile vehicle every day for 14 weeks. Systolic arterial blood pressure (SABP) was measured monthly by tail-cuff micro-photoelectric plethysmography. At week 24, cardiac contractile function was evaluated. Fasting plasma was collected for further measurement of FINS, FBG, TG, TC, and glycosylated hemoglobin (HbA1c). The homeostasis model assessment for insulin resistance (HOMA-IR) was calculated as FBG×FINS/22.5 and was used assessing insulin resistance[18].

The rats were killed, the hearts were harvested and dried weights were recorded. A piece of tissue from the left ventricle was fixed in 4% paraformaldehyde and embedded in paraffin for histological examination. The remaining tissues were snap-frozen in liquid nitrogen and stored at -80 °C until processing for extraction of mRNA and protein.

Hyperinsulinemic-euglycemic clamp techniques

As previously described[19], rats were fasted for 12–14 h overnight before the clamp study began. Rats were anesthetized by an injection of pentobarbital sodium (48 mg/kg; ip). The right jugular vein was cannulated for the infusion of glucose (using separate catheters) and insulin; the left carotid artery was cannulated for blood sampling. The glucose solution and insulin solution were stored respectively in two digital syringe pumps, and jointed by a "Y" connector to the jugular catheter. Insulin (Novolin R, Novo Nordisk Pharmaceuticals, Bagsvaerd, Denmark) was infused at 11 $mU \cdot kg^{-1} \cdot min^{-1}$ (insulin concentration 100 mU/mL) through the jugular vein catheter and BG levels serially monitored using a glucometer. The insulin infusion rate was permanent. When BG levels were within euglycemic levels (5.0±0.5 mmol/L), infusion of 5% glucose was started. The glucose infusion rate (GIR) was adjusted every 5–10 min (as needed) to maintain the BG level at a euglycemic level. Steady state was achieved by 60 min and maintained for 30 min. The mean GIR was calculated based on GIR readings corresponding to the last six samplings.

Measurement of cardiac contractile function

The cardiac contractile function *in vivo* was measured at week 24. Rats were anesthetized with pentobarbital sodium (48 mg/kg; ip). A miniaturized combined catheter-micromanometer was inserted in the right common carotid artery to measure the aortic blood pressure. It was then advanced in the left ventricle to measure left ventricular (LV) pressure-volume loops. Heart rate (HR), left ventricular systolic pressure (LVSP), left ventricular end-diastolic pressure (LVEDP) and maximum change velocity of left ventricular pressure in the isovolumic contraction or relaxation period ($\pm dp/dt_{max}$) were measured by a BL-420E Data Acquisition & Analysis System (TME Technology Company Limited, Chengdu, China).

Studies using transmission electron microscopy (TEM) and immunohistochemistry

Specimens were fixed in 4% paraformaldehyde containing 0.25% glutaraldehyde and 4.5% sucrose. Ultra-thin sections obtained from the embedded blocks were examined using a TEM (H-7500; Hitachi, Tokyo, Japan). Masson staining for collagen and streptavidin-biotin-peroxidase complex (SABC) immunohistochemistry staining for type-I collagen and type-III collagen (rabbit antibodies from Santa Cruz Biotechnol-

ogy, Santa Cruz, CA, USA) were undertaken after 4-μm thick sections were obtained from the paraffin-embedded cardiac samples using previously described methods[20]. Results were expressed as the mean percentage area of 10 random fields for each section.

Isolation of RNA and reverse transcription-polymerase chain reaction (RT-PCR)

Total mRNA from heart tissues was extracted using TRIzol reagent according to the manufacturer's protocol. The purity of isolated RNA was identified by ultraviolet spectrometry. Single-strand cDNA was synthesized by reverse transcription using oligo (dT) primer and M-MLV reverse transcriptase (Promega, Fitchburg, WI, USA), which was used as a template in the subsequent PCR analysis. Forward and reverse primers were synthesized and purified by Shanghai Sangon Biotechnology, Incorporated (Shanghai, China). The primers were JNK: forward 5′-TCAGAATCCGAACGAGACAAAAT-3′ and reverse 5′-AAGCCAGAGTCCTTCACAGACAA-3′; 469 bp. TGFβ1: forward 5′-CCAAGGAGACGGAATACAGG-3′ and reverse 5′-GTGTTGGTTGTAGAGGGC AAG-3′; 411 bp. For type-I procollagen: forward 5′-TTCACCTACAGCACGCTTGT-3′ and reverse 5′-TTGGGATGGAGGGAGTTTAC-3′; 196 bp. For type-III procollagen: forward 5′-TTGAATATCAAACACGCAAGGC-3′ and reverse 5′-GGTCACTTTCACTGGTTGACGA-3′; 201 bp. For GAPDH: forward 5′-GATGGGTGTGAACCACGAGAAA-3′ and reverse 5′-ACGGATACATTGGGGGTAGGAA-3′; 330 bp. The JNK amplification condition was pre-denaturation at 94 °C for 5 min, denaturation at 94 °C for 30 s, annealing at 61 °C for 30 s, and extension at 72 °C for 30 s, a total of 30 cycles. The amplification condition for TGFβ1, type-I procollagen, type-III procollagen and GAPDH was pre-denaturation at 94 °C for 5 min, denaturation at 94 °C for 30 s, annealing at 55 °C for 30 s, and extension at 72 °C for 30 s, a total of 28 cycles. The PCR products underwent electrophoresis and were scanned with a gel image analysis system (UVP, Upland, CA, USA). The intensity of TGFβ1, JNK, type-I and type-III procollagen was standardized to that of GAPDH mRNA.

Western blot analyses

The heart tissues of rats were lysed. Protein was extracted and measured using a bicinchoninic acid (BCA) Protein Assay Kit (Pierce, Rockford, IL, USA). Approximately 50 μg of protein was separated by 10% sodium dodecyl sulfate-polyacrylamide gel electrophoresis (SDS-PAGE) and transferred to polyvinylidene fluoride (PVDF) membranes. The membranes were blocked with 5% fat-free milk in TBST buffer (20 mmol/L Tris-HCl, pH 7.5, 150 mmol/L NaCl and 0.05% Tween 20), and subsequently incubated with the following primary antibodies: anti-MYPT1, anti-JNK, and anti-TGFβ1 (Bioworld Technology, Minnesota, MN, USA); anti-phospho-MYPT1 (Thr^{853}) and anti-phospho-JNK (T183/Y185) (Cell Signaling Technology, Danvers, MA, USA); anti-phospho-Smad2/3 ($Ser^{423/425}$), anti-c-Jun and anti-β-actin (Santa Cruz Biotechnology) at 4 °C overnight. The mixture was washed and then incubated for 1 h with horseradish peroxidase (HRP)-conjugated secondary antibodies (KPL, Incorporated, Gaithersburg, MA, USA). The membranes were developed using ECL kit (Pierce). Quantification of bands was done by gel densitometry with a gel image analysis system (UVP). The phosphorylation level was normalized by total protein-band densitometry individually.

Statistical analysis

The SPSS 13.0 statistical software pack (SPSS, Chicago, IL, USA) was used for analysis. Data are mean±SD. All groups were tested for normal distribution and equal variance. Differences between two groups (at week 10) were assessed by the Student's *t*-test. Differences among three groups (at week 24) were assessed using one-way analysis of variance followed by the Student-Newman-Keuls' test if the *F* value was significant. $P<0.05$ was considered statistically significant.

Results

Insulin sensitivity and biochemical parameters

Insulin sensitivity and biochemical parameters at week 10 are presented in Table 1. Diabetic rats had higher values of FBG, FINS, TG and BW compared with those in control rats, but there was no significant difference with respect to TC level. The GIR of diabetic rats was lower than that of control rats. These results suggested decreased insulin sensitivity and the development of insulin resistance in diabetic rats. That is, establishment of a model of type 2 DM in rats was successful.

At week 24, compared with control rats, the levels of FBG, FINS, HbA1c, and HOMA-IR were significantly increased in untreated diabetic rats and fasudil-treated diabetic rats. There were no significant differences in these indices between untreated diabetic rats and treated diabetic rats, suggesting that 10 $mg \cdot kg^{-1} \cdot d^{-1}$ fasudil administered had no effects on glucose metabolism and insulin resistance (Table 2). Com-

Table 1. Effects of HFD+STZ on BW and biochemical parameters in rats at week 10. Mean±SD. $^cP<0.01$ compared with control group.

Group	*n*	BW (g)	FBG (mmol/L)	FINS (mU/L)	GIR ($mg \cdot kg^{-1} \cdot min^{-1}$)	TG (mmol/L)	TC (mmol/L)
Control	6	276.65±33.18	5.76±0.60	51.88±11.40	11.40±1.24	0.26±0.07	1.62±0.22
Diabetes	6	328.2±21.72^c	20.10±3.52^c	107.19±14.61^c	5.89±1.05^c	1.12±0.22^c	1.71±0.30

Differences between two groups were assessed by the Student's *t*-test. *n*, number of rats; BW, body weight; FBG, fasting blood glucose; FINS, fasting insulin; GIR, glucose infusion rate; TG, triglyceride; TC, total cholesterol.

pared with control rats, TC and TG levels were significantly increased whereas BW was reduced in untreated diabetic rats and fasudil-treated diabetic rats. There were no significant differences in these indices between untreated diabetic rats and treated diabetic rats, suggesting that 10 $mg \cdot kg^{-1} \cdot d^{-1}$ fasudil administered did not affect lipid metabolism and body weight. Heart weight (HW) and the ratio of HW to BW (HW/BW) was significantly increased in untreated diabetic rats compared with control rats, there were no significant differences in HW and HW/BW between control rats and treated diabetic rats. There were no significant differences in SABP among the three groups (Table 3). These results suggested that diabetic rats incurred cardiac hypertrophy, and that fasudil treatment significantly suppressed the development of cardiac hypertrophy independent of blood pressure, blood lipid and glycemic control.

Parameters of cardiac contractile function

At week 24, compared with control rats, untreated diabetic hearts showed significantly reduced LVSP and $\pm dp/dt_{max}$ whereas LVEDP was significantly increased. Treatment with fasudil significantly enhanced LVSP, $\pm dp/dt_{max}$, and decreased LVEDP. There were no significant differences in HR among the three groups. The results indicated that fasudil effectively improved the contractile function of hearts from diabetic rats (Table 4).

Immunohistochemistry and TEM study

Representative patterns of Masson staining demonstrating cardiac fibrosis are shown in Figure 1A. The deposition of collagen in the myocardial interstitium from untreated diabetic hearts was significantly increased compared with that seen in control rats. However, treatment with fasudil significantly

Table 2. Effects of fasudil on glucose metabolism parameters in rats at week 24. Mean±SD. $^{c}P<0.01$ compared with control group.

Group	*n*	FBG (mmol/L)	FINS (mU/L)	HbA1c (%)	HOMA-IR
Control	9	5.44±0.33	54.83±11.74	11.85±0.75	13.70±3.91
Diabetes	8	20.48±3.12^{c}	85.44±18.10^{c}	19.38±3.30^{c}	92.72±17.42^{c}
DM+fas	8	23.10±5.28	83.10±13.14	20.96±1.46	81.43±12.81

Differences among three groups were assessed using one-way analysis of variance followed by the Student-Newman-Keuls' test if the *F* value was significant. DM+fas: diabetic rats treated with fasudil; *n*, number of rats; FBG, fasting blood glucose; FINS, fasting insulin; HbA1c, hemoglobin A1c; HOMA-IR, homeostasis model assessment for insulin resistance, is calculated as FBG (mmol/L)×FINS (mU/L)/22.5.

Table 3. Effects of fasudil on TG, TC, BW, HW, HW/BW, and SABP in rats at week 24. Mean±SD. $^{b}P<0.05$, $^{c}P<0.01$ compared with control group. $^{f}P<0.01$ compared with diabetes group.

Group	*n*	TG (mmol/L)	TC (mmol/L)	BW (g)	HW (g)	HW/BW ($\times 10^{-3}$)	SABP (mmHg)
Control	9	0.31±0.11	1.69±0.35	349.10±40.01	0.91±0.06	2.60±0.10	119±4
Diabetes	8	2.07±0.28^{c}	3.06±0.27^{c}	297.06±35.1^{b}	1.03±0.09^{c}	3.48±0.17^{c}	123±7
DM+fas	8	2.02±0.56	2.95±0.33	301.77±37.39	0.86±0.07^{f}	2.67±0.14^{f}	121±4

Differences among three groups were assessed using one-way analysis of variance followed by the Student-Newman-Keuls' test if the *F* value was significant. DM+fas, diabetic rats treated with fasudil; *n*, number of rats; TG, triglyceride; TC, total cholesterol; BW, body weight; HW, heart weight; HW/BW, ratio of heart weight/body weight; SABP, systolic arterial blood pressure.

Table 4. Effects of fasudil on hemodynamics in rats at week 24. Mean±SD. $^{b}P<0.05$, $^{c}P<0.01$ compared with control group. $^{e}P<0.05$, $^{f}P<0.01$ compared with diabetes group.

Group	*n*	HR (beat/min)	LVSP (mmHg)	LVEDP (mmHg)	$+dp/dt_{max}$ (mmHg/s)	$-dp/dt_{max}$ (mmHg/s)
Control	7	327±37	139±21	3.51±0.72	6909±597	6811±625
Diabetes	7	341±44	101±17^{b}	10.99±2.21^{c}	3746±402^{c}	3417±409^{c}
DM+fas	6	337±42	131±24^{e}	4.88±1.17^{f}	6517±601^{f}	5937±513^{f}

Differences among three groups were assessed using one-way analysis of variance followed by the Student-Newman-Keuls' test if the *F* value was significant. DM+fas, diabetic rats treated with fasudil; *n*, number of rats; HR, heart rate; LVSP, left ventricular systolic pressure; LVEDP, left ventricular end-diastolic pressure; $\pm dp/dt_{max}$, maximum change velocity of left ventricular pressure in the isovolumic contraction or relaxation period.

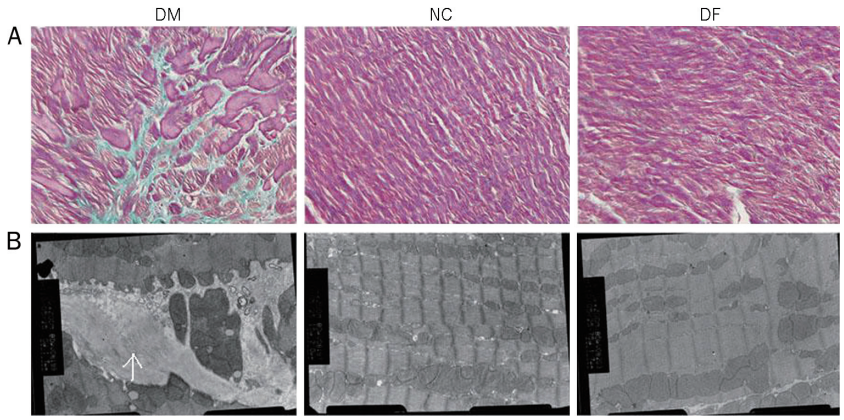

Figure 1. (A) Cardiac matrix deposition in Masson-stained sections of diabetic group (DM), control group (NC), and diabetic rats treated with fasudil group (DF). Heart tissues from the DM group show focal regions of fibrosis (blue) in the interstitium (collagen area 10.15%±0.79%, $P<0.01$ *vs* NC: 2.42%±0.33% and DF: 2.20%±0.31%). Magnification, ×400. The number of rats in each group was six. (B) Representative electron micrograph obtained from the DM, NC, and DF. In diabetic rat hearts, "packages" of collagen fibrils (arrow) can also be seen between myocardiocytes (magnification, ×6000). The control heart shows regular myofibrillar organization with evident Z lines (magnification, ×5000). The ultrastructural appearance of diabetic rats treated with fasudil is similar to that of control rats (magnification, ×6000).

reduced the deposition of collagen. To identify collagen features in the cardiac fibrotic areas, SABC immunohistochemistry staining for type-I and type-III collagen was undertaken. An increase in deposition of type-I and type-III collagen was shown in untreated diabetic rats compared with that seen in control rats (38.4%±8.2% and 15.9%±4.6% *vs* 11.2%±2.9% and 4.3%±1.5%, respectively, $P<0.01$). This increase was completely inhibited by treatment with fasudil (13.7%±4.1% and 5.1%±2.3%, respectively, $P<0.01$ *vs* DM) (Figure 2A and 2B).

The results of TEM observations showed the ultrastructure of the myocardium (Figure 1B). Untreated diabetic rats showed dense packages of collagen fibrils between cardiomyocytes, and large areas of cytoplasm had lost their regular myofibrillar organization. Control rats showed fibrils with Z lines regularly organized in the cardiomyocytes. The cardiac morphology of fasudil-treated diabetic rats was similar to that of control rats: regularly organized cytoplasm with numerous myofibrils arranged in parallel.

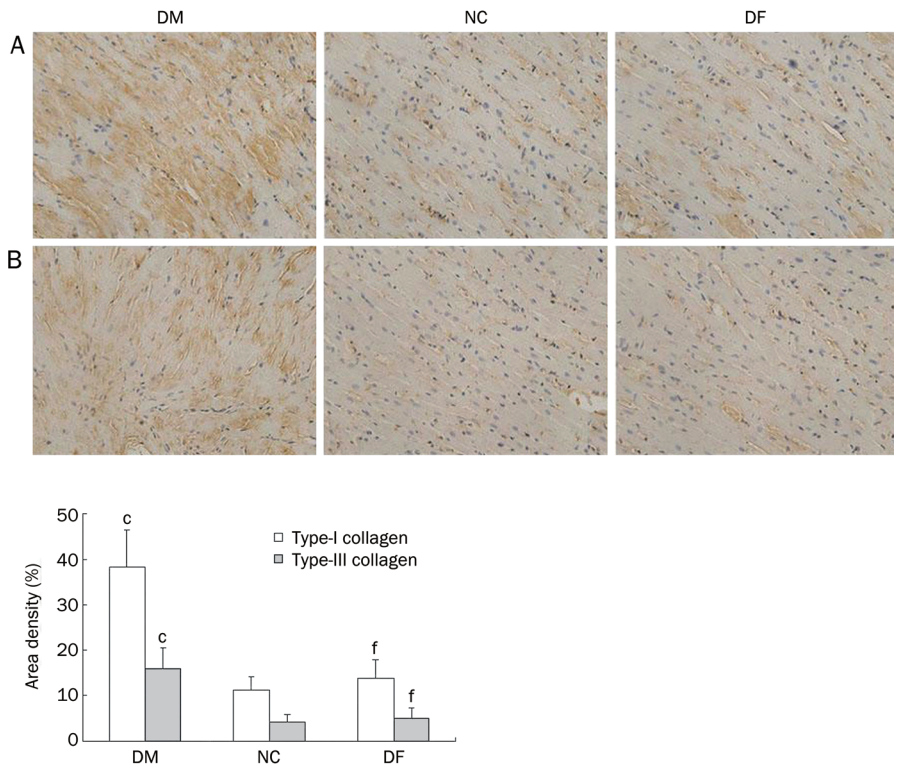

Figure 2. Immunostaining for type-I collagen (A) and type-III collagen (B) in the hearts of diabetic group (DM), control group (NC), and diabetic rats treated with fasudil group (DF). A brown color denotes positive staining. Diabetes is associated with increased immunostaining of type-I and type-III collagen in interstitial areas, whereas there is minimal immunostaining in control animals. Treatment of diabetic rats with fasudil was associated with a reduction in immunostaining of type-I and type-III collagen. Magnification, ×400. The number of rats in each group was six. $^{c}P<0.01$ *vs* NC; $^{f}P<0.01$ *vs* DM.

Gene expression in LV tissues

Compared with control rats, mRNA expression of type-I and type-III procollagen (Figure 3A and 3B) was significantly upregulated in hearts from untreated diabetic rats, but this expression was inhibited by treatment with fasudil. mRNA expression of JNK and TGFβ1 (Figure 3C and 3D) was significantly increased in the hearts of untreated diabetic rats; the upregulation of mRNA expression of JNK and TGFβ1 was blocked by treatment with fasudil. These results suggested that fasudil had inhibitory effects on DM-induced gene upregulation of type-I and type-III procollagen, JNK and TGFβ1.

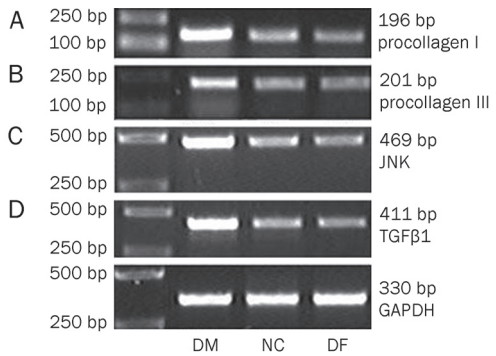

Figure 3. The mRNA expression of type-I procollagen (A), type-III procollagen (B), JNK (C), and TGFβ1 (D) in diabetic rats (DM), control rats (NC) and diabetic rats treated with fasudil (DF) was evaluated by RT-PCR. Intensity of type-I and type-III procollagen, JNK, and TGFβ1 were standardized to that of GAPDH. The number of rats in each group was six. The mRNA expression of type-I, type-III procollagen, JNK, and TGFβ1 were significantly increased in DM, $P<0.01$ *vs* NC. The gene expression was decreased in DF, $P<0.01$ *vs* DM.

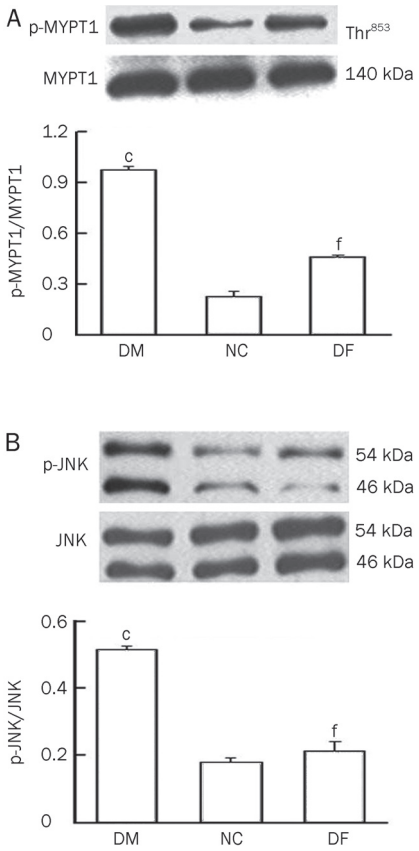

Figure 4. The phosphorylation of MYPT1 (A) and JNK (B) in diabetic rats (DM), control rats (NC), and diabetic rats treated with fasudil (DF) was measured by Western blot analyses. The activity of ROCK and JNK was expressed as p-MYPT1/MYPT1 and p-JNK/JNK, respectively. The number of rats in each group was six. $^{c}P<0.01$ *vs* NC; $^{f}P<0.01$ *vs* DM.

Protein expression in LV tissues

ROCK can inhibit myosin phosphatase by phosphorylating myosin phosphatase target subunit-1 (MYPT1)[21], so we measured MYPT1 phosphorylation as a maker of ROCK activity. The phosphorylation of MYPT1 was significantly increased in hearts from untreated diabetic rats, and this phosphorylation was inhibited by treatment with fasudil (Figure 4A). The phosphorylation of JNK (Figure 4B) and Smad2/3 (Figure 5A), as well as the protein levels of TGFβ1 (Figure 5B) and c-Jun (Figure 5C), were significantly enhanced in hearts from untreated diabetic rats, which were attenuated by treatment with fasudil. These results suggested that fasudil inhibited activation of the JNK and TGFβ1/Smad2/3 pathways.

Discussion

Several studies have reported that rats fed a HFD develop insulin resistance[22, 23]. Low-dose STZ is known to induce a mild impairment of insulin secretion that is similar to a feature of late-stage type 2 DM[16, 24]. In the present study, at week 10, the rats fed a HFD combined with low-dose STZ exhibited hyperglycemia, hyperlipidemia and hyperinsulinemia. The GIR of rats fed a HFD combined with low-dose STZ (as shown by the hyperinsulinemic-euglycemic clamp) was lower than that of control rats. Results suggested development of insulin resistance in rats fed a HFD combined with low-dose STZ. Hence, we had successfully established type 2 DM in rats, and this model would closely mimic the natural history and metabolic characteristics of type 2 DM in humans.

Long-term DM results in the development of diabetic cardiomyopathy independently of hypertension and coronary heart disease. Cardiac failure due to ventricular dysfunction is a characteristic of diabetic cardiomyopathy and occurs during the early stages of DM[25]. The present study revealed that hearts from diabetic rats showed significantly reduced contractility and prolonged diastole *in vivo*, which are hallmarks of diabetic cardiomyopathy. These findings are in agreement with other studies[26–28]. Consistent with their impaired cardiac function, diabetic rats developed myocardial fibrosis, the marked fibrotic regions (as observed by immunohistochemical staining), as well as deposition of collagen fibers in the interstitial spaces among cardiomyocytes (as observed by TEM), our observations are similar to those described in other reports[29, 30]. Increased myocardial fibrosis is a major factor responsible for myocardial stiffness and eventual systolic

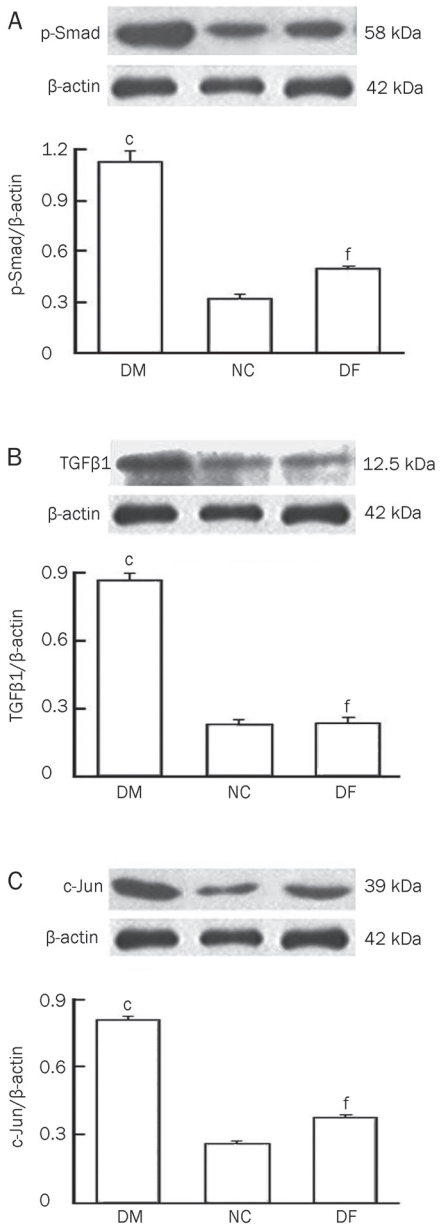

Figure 5. The phosphorylation of Smad2/3 (p-Smad2/3) (A), the protein levels of TGFβ1 (B) and c-jun (C) in diabetic rats (DM), control rats (NC) and diabetic rats treated with fasudil (DF) were evaluated by Western blot analyses. p-Smad2/3, c-jun, and TGFβ1 protein levels were standardized respectively to that of β-actin as the internal control. The number of rats in each group was six. $^{c}P<0.01$ *vs* NC; $^{f}P<0.01$ *vs* DM.

dysfunction[31, 32]. Our most significant finding is that treatment with fasudil attenuated interstitial myocardial fibrosis in diabetic rats and improved cardiac dysfunction. These effects were independent of blood pressure, blood lipid and glycemic control. The molecular mechanisms relating to the effects of fasudil on cardiac remodeling in diabetic hearts need to be elucidated.

RhoA/ROCK controls a wide variety of signal transduction pathways. ROCK exists as two isoforms: ROCK1 and ROCK2. They share an overall homology of 92% in their kinase domains. Two major families of ROCK inhibitors, fasudil and Y-27632, are extensively used. They are non-isoform-selective ROCK inhibitors that target their ATP-dependent kinase domains and are therefore equipotent in terms of inhibiting both ROCK1 and ROCK2. Furthermore, at higher concentrations, these ROCK inhibitors could also inhibit other serine-threonine kinases, such as PKA and PKC[33]. Nevertheless, compared with the other kinases, fasudil and its active metabolite, hydroxyfasudil, are relatively more selective for ROCKs, with hydroxyfasudil being slightly more selective than fasudil and Y-27632[33]. Fasudil is the only ROCK inhibitor practically available for long-term use *in vivo*. ROCK regulates not only the actin cytoskeleton but also the expression of genes associated with tissue fibrosis[10, 34]. Data from some studies[35, 36] suggest diabetes impairs cardiac function through upregulation of RhoA. The increase in RhoA expression and activity in diabetic hearts resulted in increased phosphorylation of ROCK targets, LIM kinase and ezrin/radixin/moesin, leading to an increase in actin polymerization which might be associated with cardiac dysfunction. The inhibition of the RhoA/ROCK pathway improved the contractile function of the diabetic heart. However, the precise mechanism is not fully clear behind upregulated RhoA/ROCK in diabetes. It has been suggested that RhoA activation regulates cardiac contractility and gene expression through the MAPK superfamily[28, 37]. Recent studies[12, 38, 39] demonstrated that JNK is an important mediator of the fibrotic process. As a downstream target of JNK, c-Jun acts as transcription factor for numerous genes, and overexression of these genes is often associated with organ fibrosis. The present study explored the roles of Rho/ROCK and JNK pathways in myocardial fibrosis of diabetic cardiomyopathy, and results showed that hyperglycemia not only activated ROCK, but also upregulated the expression/activity of JNK and subsequent c-Jun protein levels. Fasudil not only inhibited ROCK activity but also repressed JNK over-activation in diabetic hearts, leading to a reduction in collagen production in hearts and an improvement in cardiac function. Moreover, the inhibitory effect of fasudil on collagen fibers was regulated at least as far upstream as the transcriptional level because treatment with fasudil suppressed the mRNA expression of type-I and type-III procollagen. The study demonstrated that activation of RhoA/ROCK was essential for myocardial fibrosis in diabetic rats. Fasudil could suppress myocardial fibrosis in diabetic rats, which might be associated with inhibition of JNK activation and subsequent expression of c-Jun. It has been reported that ROCK can directly activate JNK to stimulate c-Jun expression, the activity of which is independent of the ability of ROCK to promote actin polymerization[40]. Fasudil (10–30 $mg \cdot kg^{-1} \cdot d^{-1}$) can suppress renal interstitial fibrosis in insulin-resistant diabetic rats[7, 8]. ROCK inhibition also improves pressure overload-induced cardiac hypertrophy and dysfunction[41]. Our findings are in agreement with the results of those studies[7, 8, 40, 41].

Collagen gene expression is also regulated by the Smad signaling pathway, which is activated by TGFβ[14, 15]. ROCK plays

a part in mediating renal fibrosis through a TGFβ-dependent mechanism *in vivo*[9]. TGFβ activation in diabetic hearts led to increased production of collagen, indicating that the action of TGFβ also has an important role in cardiac fibrosis[15]. In the present study, in addition to examining TGFβ1 mRNA and protein expression, we also assessed its biological effects by evaluating one of its specific intracellular actions: phosphorylation of the TGFβ1 receptor-activated protein Smad2/3. The phosphorylation of Smad2/3 was increased in diabetic rat hearts, in tandem with increased TGFβ1 mRNA and protein expression. The results showed the increased production of TGFβ1 and activation of its signaling pathway in diabetic rats hearts. Treatment with fasudil led to a decrease in the level of TGFβ1 expression and phosphorylated Smad2/3. Our findings are consistent with the results of renal injury studies[9, 42]. The study indicated that fasudil attenuated the augmentation actions of TGFβ1 in diabetic rats.

Insulin signaling is essential for normal glucose homeostasis. ROCK1 have been demonstrated as a novel regulator of glucose homeostasis and insulin sensitivity *in vivo*[43]. However, studies of the effects of ROCK inhibitors on glucose metabolism *in vivo* have yielded conflicting results. Kikuchi *et al*[7] found that a low-dose of fasudil (30 $mg \cdot kg^{-1} \cdot d^{-1}$) did not affect glucose and lipid metabolism, but high-dose fasudil (100 $mg \cdot kg^{-1} \cdot d^{-1}$) could ameliorate the metabolic disorder. Chronic treatment of obese *db*/*db* mice with fasudil (10 $mg \cdot kg^{-1} \cdot d^{-1}$) was reported to have no effect on blood glucose levels and blood pressure[8]. Differences that emerged among these studies may be correlated with the use of different inhibitors, doses, treatment times and animal models. In present study, a low-dose of fasudil (10 $mg \cdot kg^{-1} \cdot d^{-1}$) have no effects on BG, insulin resistance and BW, as well as lipid metabolism and blood pressure in diabetic rats. The cardiac protective effects of fasudil were independent of blood pressure and glycemic control.

The present study provides evidence that RhoA/ROCK, JNK, and TGFβ/Smad pathways are involved in myocardial fibrosis in rats with type 2 diabetes. JNK and Smad2/3 may be the downstream signaling molecule of the RhoA/ROCK pathway. It is plausible that the RhoA/ROCK signaling pathway is associated with nuclear signal transduction at least in part through the JNK and TGFβ/Smad pathways, which regulates the expression of genes and proteins that are pertinent to myocardial fibrosis. Our current findings should shed some light on a better understanding of the role of RhoA/ROCK pathway in the pathogenesis of diabetic cardiomyopathy. However, there were some experimental limitations in our study. First, to better understand the mechanism of action involved, cell culture study is needed to verify the cause-effect relationship with regards to the role of these signaling molecules in diabetic cardiac fibrosis. Second, it is known that diabetic cardiomyopathy is associated with significant increased oxidative stress which could lead to JNK activation and increased TGFβ[29, 44], so the contents of oxidative stress in the heart should be described. Third, there are only small number of rats in the study, this maybe limits statistical power and their results.

Treatments used to prevent the development/progression of diabetic cardiomyopathy are not fully effective. Fasudil is the only ROCK inhibitor approved for human use. Importantly, several studies have documented the beneficial effects of ROCK inhibitors in patients with cardiovascular diseases and cerebral vasospasm[6, 45–47]. The present study suggests that Rho/ROCK is substantially involved in remodeling of the myocardial matrix in diabetic rats, which may be associated with activation of the JNK pathway and TGFβ/Smad pathway. Fasudil suppresses myocardial fibrosis in diabetic rats at least in part by inhibiting activation of JNK and TGFβ/Smad, and these beneficial structural effects of fasudil are independent of blood pressure and glycemic control. Inhibition of the Rho/ROCK pathway may be a novel therapeutic target for prevention of diabetic cardiomyopathy.

Acknowledgements

This research was supported by a grant from Hebei Province Department of Health, Hebei, China (a principal item, grant number 20090007). The authors thank Kai-xia ZHANG, Chunfang ZHAO and Rong ZHANG MD for their technical assistance.

Author contribution

Yong-jun LI and Hong ZHOU designed research; Zhan-sheng ZHAO, Hong ZHOU, Mian WANG, and Feng-ling MENG performed research; Rui-ying WANG, Yong-gui DENG, Bing-yan GUO, and Li-hui ZHANG analyzed data; and Hong ZHOU and Yong-jun LI wrote the paper.

References

1 Gustafsson I, Hildebrandt P. Early failure of the diabetic heart. Diabetes Care 2001; 24: 3–4.
2 Poirier P, Bogaty P, Garneau C, Marois L, Dumesnil JG. Diastolic dysfunction in normotensive men with well-controlled type 2 diabetes: importance of maneuvers in echocardiographic screening for preclinical diabetic cardiomyopathy. Diabetes Care 2001; 24: 5–10.
3 Riento K, Ridley AJ. Rocks: multifunctional kinases in cell behaviour. Nat Rev Mol Cell Biol 2003; 4: 446–56.
4 Rikitake Y, Liao JK. Rho GTPases, statins, and nitric oxide. Circ Res 2005; 97: 1232–5.
5 Masumoto A, Hirooka Y, Shimokawa H, Hironaga K, Setoguchi S, Takeshita A. Possible involvement of Rho-kinase in the pathogenesis of hypertension in humans. Hypertension 2001; 38: 1307–10.
6 Shibuya M, Hirai S, Seto M, Satoh S, Ohtomo E, Fasudil Ischemic Stroke Study Group. Effects of fasudil in acute ischemic stroke: results of a prospective placebo-controlled double-blind trial. J Neurol Sci 2005; 238: 31–9.
7 Kikuchi Y, Yamada M, Imakiire T, Kushiyama T, Higashi K, Hyodo N, *et al*. A Rho-kinase inhibitor, fasudil, prevents development of diabetes and nephropathy in insulin-resistant diabetic rats. J Endocrinol 2007; 192: 595–603.
8 Kolavennu V, Zeng L, Peng H, Wang Y, Danesh FR. Targeting of RhoA/ROCK signaling ameliorates progression of diabetic nephropathy independent of glucose control. Diabetes 2008; 57: 714–23.
9 Nishikimi T, Akimoto K, Wang X, Mori Y, Tadokoro K, Ishikawa Y, *et al*. Fasudil, a Rho-kinase inhibitor, attenuates glomerulosclerosis in Dahl salt-sensitive rats. J Hypertens 2004; 22: 1787–96.

10 Wang YX, da Cunha V, Martin-McNulty B, Vincelette J, Li W, Choy DF, *et al*. Inhibition of Rho-kinase by fasudil attenuated angiotensin II-induced cardiac hypertrophy in apolipoprotein E deficient mice. Eur J Pharmacol 2005; 512: 215–22.
11 Omura T, Yoshiyama M, Matsumoto R, Kusuyama T, Enomoto S, Nishiya D, *et al*. Role of c-Jun NH_2-terminal kinase in G-protein-coupled receptor agonist-induced cardiac plasminogen activator inhibitor-1 expression. J Mol Cell Cardiol 2005; 38: 583–92.
12 Hao GH, Niu XL, Gao DF, Wei J, Wang NP. Agonists at PPAR-gamma suppress angiotensin II-induced production of plasminogen activator inhibitor-1 and extracellular matrix in rat cardiac fibroblasts. Br J Pharmacol 2008; 153: 1409–19.
13 Ohtsu H, Mifune M, Frank GD, Saito S, Inagami T, Kim-Mitsuyama S, *et al*. Signal-crosstalk between Rho/ROCK and c-Jun NH_2-terminal kinase mediates migration of vascular smooth muscle cells stimulated by angiotensin II. Arterioscler Thromb Vasc Biol 2005; 25: 1831–6.
14 Zyadeh FN, Sharma K, Erickson M, Wolf G. Stimulation of collagen gene expression and protein synthesis in murine mesangial cells by high glucose in mediated by autocrine activation of transforming growth factor-β. J Clin Invest 1994; 93: 536–42.
15 Martin J, Kelly DJ, Mifsud SA, Zhang Y, Cox AJ, See F, *et al*. Tranilast attenuates cardiac matrix deposition in experimental diabetes: role of transforming growth factor β. Cardiovasc Res 2005; 65: 694–701.
16 Srinivasan K, Viswanad B, Asrat L, Kaul CL, Ramarao P. Combination of high-fat diet-fed and low-dose streptozotocin-treated rat: a model for type 2 diabetes and pharmacological screening. Pharmacol Res 2005; 52: 313–20.
17 Islam MS, Choi H. Nongenetic model of type 2 diabetes: a comparative study. Pharmacology 2007; 79: 243–9.
18 Matthews DR, Hosker JP, Rudenski AS, Naylor BA, Treacher DF, Turner RC. Homeostasis model assessment: insulin resistance and beta-cell function from fasting plasma glucose and insulin concentrations in man. Diabetologia 1985; 28: 412–9.
19 Tran TT, Gupta N, Goh T, Naigamwalla D, Chia MC, Koohestani N, *et al*. Direct measure of insulin sensitivity with the hyperinsulinemic-euglycemic clamp and surrogate measures of insulin sensitivity with the oral glucose tolerance test: correlations with aberrant crypt foci promotion in rats. Cancer Epidemiol Biomarkers Prev 2003; 12: 47–56.
20 Tzanidis A, Hannan RD, Thomas WG, Onan D, Autelitano DJ, See F, *et al*. Direct actions of urotensin II on the heart: implications for cardiac fibrosis and hypertrophy. Circ Res 2003; 93: 246–53.
21 Wakino S, Hayashi K, Kanda T, Tatematsu S, Homma K, Yoshioka K, *et al*. Peroxisome proliferator-activated receptor gamma ligands inhibit Rho/Rho kinase pathway by inducing protein tyrosine phosphatase SHP-2. Circ Res 2004; 95: e45–55.
22 Tanaka S, Hayashi T, Toyoda T, Hamada T, Shimizu Y, Hirata M, *et al*. High-fat diet impairs the effects of a single bout of endurance exercise on glucose transport and insulin sensitivity in rat skeletal muscle. Metabolism 2007; 56: 1719–28
23 Flanagan AM, Brown JL, Santiago CA, Aad PY, Spicer LJ, Spicer MT. High-fat diets promote insulin resistance through cytokine gene expression in growing female rats. J Nutr Biochem 2008; 19: 505–13.
24 Reed MJ, Meszaros K, Entes LJ, Claypool MD, Pinkett JG, Gadbois TM, *et al*. A new rat model of type 2 diabetes: the fat-fed, streptozotocin-treated rat. Metabolism 2000; 49: 1390–4.
25 Redfield MM, Jacobsen SJ, Burnett JC Jr, Mahoney DW, Bailey KR, Rodeheffer RJ. Burden of systolic and diastolic ventricular dysfunction in the community: appreciating the scope of the heart failure epidemic. JAMA 2003; 289: 194–202.
26 Vadlamudi RV, Rodgers RL, McNeill JH. The effect of chronic alloxan- and streptozotocin-induced diabetes on isolated rat heart performance. Can J Physiol Pharm 1982; 60: 902–11.
27 Norby FL, Aberle NS, Kajstura J, Anversa P, Ren J. Transgenic over-expression of insulin-like growth factor I prevents streptozotocin-induced cardiac contractile dysfunction and beta-adrenergic response in ventricular myocytes. J Endocrinol 2004; 180: 175–82.
28 Ren J, Duan J, Thomas DP, Yang X, Sreejayan N, Sowers JR, *et al*. IGF-I alleviates diabetes-induced RhoA activation, eNOS uncoupling, and myocardial dysfunction. Am J Physiol Regul Integr Comp Physiol 2008; 294: R793–802.
29 Aragno M, Mastrocola R, Alloatti G, Vercellinatto I, Bardini P, Geuna S, *et al*. Oxidative stress triggers cardiac fibrosis in the heart of diabetic rats. Endocrinology 2008; 149: 380–8.
30 Jin D, Takai S, Sugiyama T, Hayashi T, Fukumoto M, Oku H, *et al*. Long-term angiotensin II blockade may improve not only hyperglycemia but also age-associated cardiac fibrosis. J Pharmacol Sci 2009; 109: 275–84.
31 Yamamoto K, Masuyama T, Sakata Y, Nishikawa N, Mano T, Yoshida J, *et al*. Myocardial stiffness is determined by ventricular fibrosis, but not by compensatory or excessive hypertrophy in hypertensive heart. Cardiovasc Res 2002; 55: 76–82.
32 Kai H, Kuwahara F, Tokuda K, Imaizumi T. Diastolic dysfunction in hypertensive hearts: roles of perivascular inflammation and reactive myocardial fibrosis. Hypertens Res 2005; 28: 483–90.
33 Rikitake Y, Kim HH, Huang Z, Seto M, Yano K, Asano T, *et al*. Inhibition of Rho kinase (ROCK) leads to increased cerebral blood flow and stroke protection. Stroke 2005; 36: 2251–7.
34 Fukushima M, Nakamuta M, Kohjima M, Kotoh K, Enjoji M, Kobayashi N, *et al*. Fasudil hydrochloride hydrate, a Rho-kinase (ROCK) inhibitor, suppresses collagen production and enhances collagenase activity in hepatic stellate cells. Liver Int 2005; 25: 829–38.
35 Lin G, Craig GP, Zhang L, Yuen VG, Allard M, McNeill JH, *et al*. Acute inhibition of Rho-kinase improves cardiac contractile function in streptozotocin-diabetic rats. Cardiovasc Res 2007; 75: 51–8.
36 Soliman H, Craig GP, Nagareddy P, Yuen VG, Lin G, Kumar U, *et al*. Role of inducible nitric oxide synthase in induction of RhoA expression in hearts from diabetic rats. Cardiovasc Res 2008; 79: 322–30.
37 Kobayashi N, Horinaka S, Mita S, Nakano S, Honda T, Yoshida K, *et al*. Critical role of Rho-kinase pathway for cardiac performance and remodeling in failing rat hearts. Cardiovasc Res 2002; 55: 757–67.
38 Chen X, Tian Y, Yao L, Zhang J, Liu Y. Hypoxia stimulates proliferation of rat neural stem cells with influence on the expression of cyclin D1 and c-Jun N-terminal protein kinase signaling pathway *in vitro*. Neuroscience 2010; 165: 705–14.
39 Zhou CH, Wu XH, Wu YQ. Nobiletin, a dietary phytochemical, inhibits vascular smooth muscle cells proliferation via calcium-mediated c-Jun N-terminal kinases pathway. Eur J Pharmacol 2009; 615: 55–60.
40 Marinissen MJ, Chiariello M, Tanos T, Bernard O, Narumiya S, Gutkind JS. The small GTP-binding protein RhoA regulates c-jun by a ROCK-JNK signaling axis. Mol Cell 2004; 14: 29–41.
41 Phrommintikul A, Tran L, Kompa A, Wang B, Adrahtas A, Cantwell D, *et al*. Effects of a Rho kinase inhibitor on pressure overload induced cardiac hypertrophy and associated diastolic dysfunction. Am J Physiol Heart Circ Physiol 2008; 294: H1804–14.
42 Sun GP, Kohno M, Guo P, Nagai Y, Miyata K, Fan YY, *et al*. Involvements of Rho-kinase and TGF-beta pathways in aldosterone-induced renal injury. J Am Soc Nephrol 2006; 17: 2193–201.
43 Lee DH, Shi J, Jeoung NH, Kim MS, Zabolotny JM, Lee SW, *et al*. Targeted disruption of ROCK1 causes insulin resistance *in vivo*. J Biol Chem 2009; 284: 11776–80.

44 Han MJ, Kim BY, Yoon SO, Chung AS. Cell proliferation induced by reactive oxygen species is mediated via mitogen-activated protein kinase in Chinese hamster lung fibroblast (V79) cells. Mol Cells 2003; 15: 94–101.

45 Kishi T, Hirooka Y, Masumoto A, Ito K, Kimura Y, Inokuchi K, *et al*. Rho-kinase inhibitor improves increased vascular resistance and impaired vasodilation of the forearm in patients with heart failure. Circulation 2005; 111: 2741–7.

46 Masumoto A, Mohri M, Shimokawa H, Urakami L, Usui M, Takeshita A. Suppression of coronary artery spasm by the Rho-kinase inhibitor fasudil in patients with vasospastic angina. Circulation 2002; 105: 1545–7.

47 Shimokawa H, Hiramori K, Iinuma H, Hosoda S, Kishida H, Osada H, *et al*. Anti-anginal effect of fasudil, a Rho-kinase inhibitor, in patients with stable effort angina: a multicenter study. J Cardiovasc Pharmacol 2002; 40: 751–61.

Acta Pharmacologica Sinica (2011) 32: 1009–1018
 1671-4083/11 $32.00
www.nature.com/aps

Original Article

Vasorelaxant and antihypertensive effects of formononetin through endothelium-dependent and -independent mechanisms

Tao SUN, Rui LIU, Yong-xiao CAO*

Department of Pharmacolgy, Xi-an Jiaotong University College of Medicine, Xi-an 710061, China

Aim: To investigate the mechanisms underlying the vasorelaxant effect of formononetin, an *O*-methylated isoflavone, in isolated arteries, and its antihypertensive activity *in vivo*.
Methods: Arterial rings of superior mesenteric arteries, renal arteries, cerebral basilar arteries, coronary arteries and abdominal aortas were prepared from SD rats. Isometric tension of the arterial rings was recorded using a myograph system. Arterial pressure was measured using tail-cuff method in spontaneously hypertensive rats.
Results: Formononetin (1–300 μmol/L) elicited relaxation in arteries of the five regions that were pre-contracted by KCl (60 mmol/L), U46619 (1 μmol/L) or phenylephrine (10 μmol/L). The formononetin-induced relaxation was reduced by removal of endothelium or by pretreatment with *L*-NAME (100 μmol/L). Under conditions of endothelium denudation, formononetin (10, 30, and 100 μmol/L) inhibited the contraction induced by KCl and that induced by $CaCl_2$ in Ca^{2+}-free depolarized medium. In the absence of extracellular Ca^{2+}, formononetin (10, 30, and 100 μmol/L) depressed the constriction caused by phenylephrine (10 μmol/L), but did not inhibit the tonic contraction in response to the addition of $CaCl_2$ (2 mmol/L). The contraction caused by caffeine (30 mmol/L) was not inhibited by formononetin (100 μmol/L). Formononetin (10 and 100 μmol/L) reduced the change rate of Ca^{2+}-fluorescence intensity in response to KCl (50 mmol/L). In spontaneously hypertensive rats, formononetin (5, 10, and 20 mg/kg) slowly lowered the systolic, diastolic and mean arterial pressure.
Conclusion: Formononetin causes vasodilatation via two pathways: (1) endothelium-independent pathway, probably due to inhibition of voltage-dependent Ca^{2+} channels and intracellular Ca^{2+} release; and (2) endothelium-dependent pathway by releasing NO. Both the pathways may contribute to its antihypertensive effect.

Keywords: formononetin; arterial rings; vasodilatation; voltage-dependent Ca^{2+} channel; intracellular Ca^{2+} release; nitric oxide; spontaneously hypertensive rats; blood pressure

Acta Pharmacologica Sinica (2011) 32: 1009–1018; doi: 10.1038/aps.2011.51

Introduction

Hypertension is one of the most common cardiovascular diseases, which is a major risk factor for endothelial dysfunction, metabolic syndrome, diabetes, renal dysfunction, congestive heart failure, coronary artery diseases and stroke[1]. Clinically, various antihypertensive drugs such as diuretics, centrally acting adrenergic drugs, vasodilators, calcium channel blockers and angiotensin converting enzyme/receptor blockers have been used to treat hypertension. However, the efficacy of these drugs is only 40%–60%, and usually two or more antihypertensive drugs from different categories need to be combined to achieve optimal results. In addition, the side effects from these medications are an important concern[2].

To develop a safe and effective way for managing hypertension has long been a challenge for medical researchers and doctors. Many traditional Chinese medicinal herbs with vasorelaxant properties are conventionally used to treat hypertension[3]. Recently, interest in the use of medicinal herbs has risen exponentially, due to their low toxicity and wonderful therapeutical performance[4]. Therefore, we started a project to find a novel antihypertensive compound with vasorelaxant activity from traditional Chinese medicinal plants that are used as antihypertensive agents.

Phytoestrogens are plant substances found in many foods, which are structurally or functionally similar to estradiol. They have attracted much attention because of their potential beneficial role in prevention and treatment of cardiovascular diseases, bone metabolism disorders, breast cancers,

* To whom correspondence should be addressed.
E-mail yxy@xjtu.edu.cn
Received 2010-11-30 Accepted 2011-03-29

and menopausal symptoms[5–9]. Isoflavones are a class of phytoestrogens naturally sourced from legumes such as soy beans and red clover[10]. Some isoflavones have been reported for treatment of hypertension, coronary heart diseases and cardiac infarct[11–14] through dilating arteries and increasing blood flow[15, 16]. Formononetin, an *O*-methylated isoflavone, is contained in the roots of *Astragalus membranaceus*[17, 18], liquorice[19], black cohosh[20, 21] and *Trifolium pratense* L[22]. Medicinal herbs containing formononetin have been used to treat cardiovascular diseases including hypertension in Asia for centuries[23]. Recently, Wu *et al* reported that formononetin has a vasorelaxant activity in isolated rat aorta rings[9]. However, the antihypertensive activity of formononetin and its vasorelaxant effect on arteries in different regions have not yet been studied. The aim of the present study was to determine whether formononetin is contributory to treating hypertension, and further to explore the potential mechanisms of its antihypertensive activity.

Materials and methods

Drugs and reagents

Formononetin was supplied by Department of Chemistry, Shaanxi Normal University, China. Phenylephrine, 9,11-dideoxy-11 alpha, 9 alpha-epoxymethano-prostaglandin F_2 alpha (U46619), 5-hydroxytryptamine (5-HT), noradrenaline, Triton X-100, propranolol, glibenclamide, tetraethylammonium, acetylcholine chloride (ACh), indomethacin, N^{ω}-nitro-*L*-arginine methyl ester (*L*-NAME), verapamil, lacidipine, sodium nitroprusside (SNP), caffeine, and dimethyl sulphoxide (DMSO) were purchased from Sigma Aldrich (St Louis, MO, USA). Fluo-3/AM was obtained from Biotium (Hayward, CA, USA). All other reagents were of analytical grade. Formononetin was dissolved in DMSO for *in vitro* use and dissolved in 10% Tween 80 solution for *in vivo* use. Fluo-3/AM and glibenclamide were dissolved in DMSO. Indomethacin was dissolved in ethanol. Other substances were dissolved in double distilled water. The concentrations are expressed as the final molar concentrations in the tissue baths.

Animals

Sprague-Dawley (SD) rats were obtained from Experimental Animal Center of Xi-an Jiaotong University College of Medicine, China. Male spontaneously hypertensive rats (SHRs) aged 20 weeks were obtained from Shanghai Slack Laboratory Animal Co Ltd, China. The study was approved by Ethics Committee of Xi-an Jiaotong University College of Medicine according to the principles outlined in the Declaration of Helsinki.

Arterial rings preparation

SD rats weighing 250–300 g were sacrificed by CO_2. The rat superior mesenteric arteries, renal arteries, cerebral basilar arteries, coronary arteries, and abdominal aortas were gently removed. The arteries were immersed in cold oxygenated Krebs solution containing the following composition (mmol/L): NaCl 119, $NaHCO_3$ 15, KCl 4.6, $MgCl_2$ 1.2, NaH_2PO_4 1.2, $CaCl_2$ 1.5 and glucose 5.5. The arteries were dissected free of adhering tissue under a microscope. In the endothelium-denuded experiments, the endothelium was denuded by perfusion of the vessels for 10 s with 0.1% Triton X-100 followed by another 10 s with Krebs solution[24]. The vessels were then cut into 1 mm cylindrical segments.

Myograph experiments

The artery segments were threaded on two 40-μm-diameter stainless steel wires and mounted in Mulvany-Halpern myographs (Danish Myo Technology A/S, Aarhus, Denmark). One wire was connected to a force displacement transducer and attached to an analog-to-digital converter unit (AD Instruments, Hastings, UK). The other wire was attached to a movable displacement device, allowing fine adjustments of vascular tension by varying the distance between the wires. The data were recorded using Chart™ (AD Instruments, Hastings, UK). The mounted artery segments were immersed in temperature-controlled (37 °C) tissue baths containing 5 mL Krebs solution. The solution was continuously gassed with 5% CO_2 in O_2 resulting in a physiological pH at 7.4. The artery segments were equilibrated for 1.5 h before the experiments, and the cerebral artery and coronary artery segments were given a resting tension of 1.5 mN, while other segments a 3-mN tension. The contractile capacity of each vessel segment was tested by exposing the segment to a K^+-rich Krebs solution (with 60 mmol/L KCl) in which NaCl was exchanged for an equimolar concentration of KCl. Two reproducible high-K^+ contractions were obtained for standardization of the preparations.

The completeness of endothelium denudation was tested with ACh (10 μmol/L) after cerebral basilar arteries and coronary arteries were pre-contracted with 0.3 μmol/L 5-HT, and mesenteric arteries, renal arteries and abdominal aortas were pre-contracted with 10 μmol/L noradrenaline. No relaxation in response to ACh in the denuded preparation was regarded as functional removal of the endothelium. The endothelium was considered intact when such an ACh response caused more than 30% relaxation[25].

To determine the relaxant effect, the segments were pre-contracted, and once the sustained tension was obtained, formononetin (1–300 μmol/L) was added cumulatively to induce a concentration-dependent response. Some experiments were performed in both endothelium-intact and endothelium-free mesenteric arteries to determine whether the relaxant effect of formononetin was endothelium-dependent. Phenylephrine and formononetin were added after some mesenteric artery rings were pre-treated with *L*-NAME and/or indomethacin for 20 min so as to determine the involvement of nitric oxide (NO), prostaglandins (PGs) and endothelium-derived hyperpolarizing factor (EDHR) in the relaxant effect of formononetin. In order to evaluate the role of potassium (K^+) channels and β-adrenoceptors in the vasorelaxant effect of formononetin, some mesenteric artery rings were pre-treated with tetraethylammonium, $BaCl_2$, glibenclamide, or propranolol for 20 min before the addition of vasoconstrictor and formononetin.

To determine the involvement of voltage-dependent Ca^{2+} channels (VDCC), α_1-adrenoceptors and 5-HT receptors in the relaxant effect of formononetin, concentration-response curves of KCl, $CaCl_2$ in Ca^{2+}-free depolarized medium, phenylephrine and 5-HT in the presence of formononetin were constructed. Some mesenteric artery rings were incubated in a Ca^{2+}-free Krebs solution to determine whether the relaxant effect of formononetin was due to its inhibition of intracellular Ca^{2+} release or extracellular Ca^{2+} influx[26, 27].

The smooth muscle function was assessed at the end of each experiment. The mesenteric arteries, renal arteries and abdominal aortas were pre-constricted with phenylephrine (10 μmol/L), while the cerebral basilar arteries and coronary arteries were pre-contracted with 0.3 μmol/L 5-HT. Concentration-dependent vasorelaxation to the endothelium-independent vasodilator (SNP: 0.1 nmol/L–10 μmol/L) was tested. Only experiments on vessels with SNP-induced relaxation being more than 95% were accounted as valid[28].

Determination of tissue $[Ca^{2+}]_i$ in the mesenteric artery

SD rats weighing 120–130 g were sacrificed by CO_2, and the superior mesenteric arteries were gently removed. The arteries were immersed in cold HEPES-Krebs solution (pH 7.4) of the following composition (mmol/L): NaCl 135, KCl 5, $MgSO_4$ 1.2, $CaCl_2$ 2.5, glucose 10 and HEPES 8.4. Tissues adhering to the arteries were cleaned under a microscope. Each mesenteric artery was cut into ring segments with a length of about 3 mm and mounted on a U-shaped stainless steel wire. The artery rings with the wire were placed in the bottom of the chamber close to cover glass, followed by immediate immersion in HEPES-Krebs solution containing 10 μmol/L Fluo-3/AM, which was then added with DMSO, formononetin (10 μmol/L), formononetin (100 μmol/L) and verapamil (1 μmol/L), respectively. After 30 min, the artery rings were washed three times with HEPES-Krebs solution (pH 7.4) containing DMSO, formononetin (10 and 100 μmol/L) and verapamil (1 μmol/L), respectively. A real-time confocal microscope (FV1000, Olympus, Tokyo, Japan) was employed to obtain the fluorescent images. The image frame was continuously acquired every 1.107 s, and the images were stored in a high-speed hard disk. The artery rings were observed immediately after dye loading to acquire the fluorescent images of the resting state. Following the acquisition of resting response, the specimens were exposed to 50 mmol/L KCl and the images were acquired continuously[29]. The fluorescence intensity was calculated from individual image utilizing FV10-ASW (version 1.7, Olympus, Tokyo, Japan), and the changes of fluorescence intensity versus time were plotted. The change rate (%) of fluorescence intensity induced by KCl was calculated based on the formula below:

[(fluorescence intensity after exposure to KCl – fluorescence intensity before exposure to KCl)/fluorescence intensity before exposure to KCl]×100.

The change rate of fluorescence intensity reflected the change of $[Ca^{2+}]_i$.

Measurement of arterial pressure

SHRs weighing 250–300 g were divided into 5 groups (n=6–8 per group). Arterial pressure measurement was carried out via a non-invasive tail-cuff plethysmography method (CODA 6, Kent Scientific, Torrington, CT, USA)[30] once every day for a succession of five days to get the rats adapted to the operation. Right before the drug administration, the arterial pressure was measured. Then formononetin (5, 10, and 20 mg/kg), lacidipine (0.06 mg/kg) and saline containing 10% Tween 80 were injected via tail vein, respectively. The arterial pressure was assessed 0.5, 1, 2, 3, and 4 h after the administration.

Statistical analysis

Data are expressed as mean±SEM, and the differences between means were evaluated using SPSS for Windows 13.0 (SPSS, Chicago, IL, USA)[31]. Relaxant responses in each segment are expressed as a percentage of relaxation from the precontraction. E_{max} and R_{max} represent the maximal contraction and the maximal relaxation induced by vasoconstrictors and formononetin, respectively. Comparisons were made using 2-way ANOVA followed by Fischer's least significant difference *post-hoc* tests. Statistical significance was set at P<0.05. The EC_{50} was calculated by nonlinear regression analysis using the computer program GraphPad Prism 5 (San Diego, CA, USA).

Results

Relaxing responses of arteries to formononetin

KCl (60 mmol/L) or U46619 (1 μmol/L) was added to the baths to induce precontraction of the segments of rat mesenteric arteries, renal arteries, cerebral arteries, coronary arteries and abdominal aortas, respectively. The segments of rat mesenteric arteries, renal arteries and abdominal aortas were precontracted by phenylephrine (10 μmol/L). After sustained contraction was obtained, formononetin (1–300 μmol/L) was added cumulatively to the baths. Formononetin elicited a concentration-dependent relaxation in the rat artery segments pre-contracted by KCl (Figure 1A, Table 1), U46619 (Figure 1B, Table 2) or phenylephrine (Figure 1C, Table 3).

Table 1. Relaxation responses induced by formononetin in rat arterial segments pre-contracted by 60 mmol/L K^+; supplemental data for Figure 1A. Data are expressed as mean±SEM. n=6–8. ^bP<0.05, ^cP<0.01 *vs* cerebral artery. ^fP<0.01 *vs* coronary artery.

Artery	60 mmol/L K^+ (mN)	Formononetin		Control (DMSO)
		R_{max} (%)	EC_{50} (μmol/L)	R_{max} (%)
Mesenteric artery	7.19±0.42	96.2±1.0^b	14.9±1.8^{cf}	7.3±2.2
Abdominal aorta	9.01±0.71	96.7±1.7^b	19.1±4.1^{cf}	7.2±4.1
Renal artery	7.70±0.65	93.4±2.0	24.0±5.8	5.6±2.8
Coronary artery	5.31±0.56	91.8±5.8	36.3±3.5	4.8±2.1
Cerebral artery	5.30±0.52	86.1±3.9	37.9±4.9	7.2±6.1

R_{max}, maximum relaxation to formononetin or DMSO (control).

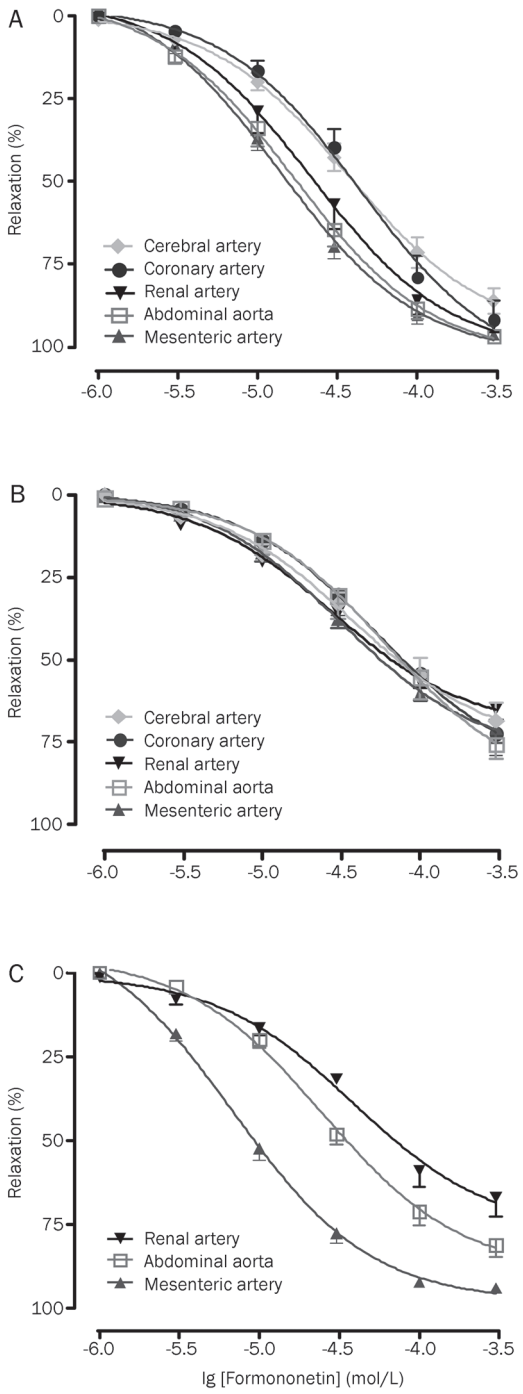

Figure 1. Cumulative concentration-response curves of formononetin. Rat isolated cerebral arteries, coronary arteries, renal arteries, abdominal aorta, and mesenteric arteries pre-contracted by 60 mmol/L K^+ (A) and 1 μmol/L U46619 (B), respectively; renal arteries, abdominal aorta, and mesenteric arteries pre-contracted by 10 μmol/L phenylephrine (C). Data are shown as mean±SEM. *n*=7–8 arteries.

Table 2. Relaxation responses induced by formononetin in rat arterial segments pre-contracted by 1 μmol/L U46619; supplemental data for Figure 1B. Data are expressed as mean±SEM. *n*=6–8.

Artery	1 μmol/L U46619 (mN)	Formononetin		Control (DMSO)
		R_{max} (%)	EC_{50} (μmol/L)	R_{max} (%)
Mesenteric artery	12.47±0.74	73.8±3.1	41.8±6.9	2.9±3.5
Abdominal aorta	13.88±0.70	75.8±4.3	59.8±17.0	6.0±2.2
Renal artery	10.65±0.63	65.0±3.3	33.8±6.5	2.9±2.0
Coronary artery	5.55±0.66	72.4±6.7	68.6±21.3	4.5±1.1
Cerebral artery	5.83±0.49	68.6±5.7	40.9±5.9	5.7±1.2

R_{max}, maximum relaxation to formononetin or DMSO (control).

Table 3. Relaxation responses induced by formononetin in rat arterial segments pre-contracted by 10 μmol/L phenylephrine (PE); supplemental data for Figure 1C. Data are expressed as mean±SEM. *n*=6–8. $^bP<0.05$, $^cP<0.01$ *vs* renal artery. $^eP<0.05$, $^fP<0.01$ *vs* abdominal aorta.

Artery	10 μmol/L PE (mN)	Formononetin		Control (DMSO)
		R_{max} (%)	EC_{50} (μmol/L)	R_{max} (%)
Mesenteric artery	7.96±0.70	94.0±1.5^{ce}	7.7±0.9^{cf}	8.1±2.1
Abdominal aorta	7.18±0.67	81.3±3.5^{b}	24.3±1.9^{c}	6.7±1.5
Renal artery	8.72±1.50	67.0±5.8^{e}	33.0±4.4^{e}	7.8±2.9

R_{max}, maximum relaxation to formononetin or DMSO (control).

Involvement of endothelium

Formononetin (1–300 μmol/L) concentration-dependently relaxed rat mesenteric artery segments pre-contracted by phenylephrine (10 μmol/L) with or without endothelium (Figure 2). Removal of endothelium suppressed the relaxing response to formononetin (R_{max}=96.25%±1.72% in endothelium-intact arteries, R_{max}=56.84%±1.89% in endothelium-denuded arteries, $P<0.05$), suggesting that the vasodilatation was partially endothelium-dependent.

Effects of NOS and cyclo-oxygenase (COX) inhibitors on the relaxing response to formononetin

Before treatment with formononetin in phenylephrine (10 μmol/L)-induced precontraction, rat mesenteric artery segments with endothelium were co-incubated with *L*-NAME (NOS inhibitor, 100 μmol/L), indomethacin (COX inhibitor, 10 μmol/L) or *L*-NAME (100 μmol/L)+indomethacin (10 μmol/L) for 20 min. Figure 2 showed that *L*-NAME and *L*-NAME+indomethacin attenuated the concentration-response curves of formononetin, while indomethacin lightly attenuated the concentration-relaxation curves of formononetin.

Effects of β-adrenoceptor and K^+ channels blockers on the relaxing response to formononetin

Before the addition of formononetin and 60 mmol/L KCl to the baths, the endothelium-denuded mesenteric artery segments were treated with propranolol (1 μmol/L), glibenclamide (10 μmol/L), tetraethylammonium (300 μmol/L) or bar-

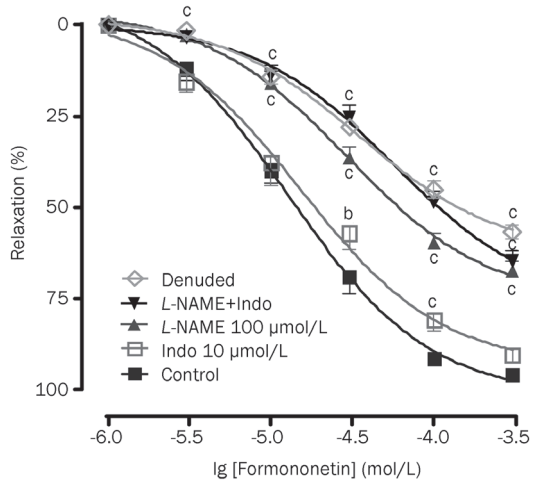

Figure 2. Effects of *L*-NAME (100 μmol/L), indomethacin (Indo, 10 μmol/L) and *L*-NAME+Indo (100 μmol/L+10 μmol/L) on the relaxing responses induced by formononetin in mesenteric arteries with intact endothelium, and effects of formononetin on mesenteric arteries with endothelium denuded and with endothelium intact (control). Rat isolated mesenteric arteries were pre-contracted by phenylephrine. Data are shown as mean±SEM. n=7–8 arteries. ^bP<0.05, ^cP<0.01 *vs* control.

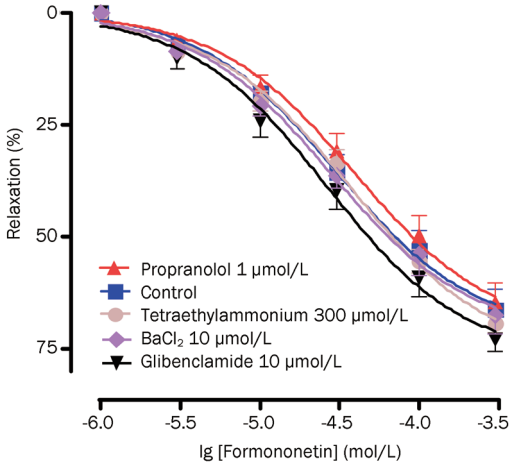

Figure 3. The vasorelaxant effect of formononetin in endothelium-free artery in the presence of propranolol (1 μmol/L), tetraethylammonium (300 μmol/L), $BaCl_2$ (10 μmol/L), or glibenclamide (10 μmol/L). Relaxation is expressed as a percentage of decrease in the maximal tension induced by 60 mmol/L K^+. Data are shown as mean±SEM. n=7–8 arteries. (control: in the absence of blockers)

ium chloride (10 μmol/L) for 20 min in order to test whether or not β-adrenoceptors, ATP sensitive K^+ channels, calcium-activated K^+ channels and inwardly rectifying K^+ channels were involved in the formononetin-induced relaxation. As shown in Figure 3, these blockers, compared with control (in the absence of blockers), did not shift the concentration-relaxation curves of formononetin significantly. No matter the blockers were present or not, the R_{max} and EC_{50} of formononetin in the endothelium-denuded artery segments showed no significant difference (P>0.05).

Effects of formononetin on K^+-induced contraction

Krebs solution was replaced with high KCl (10, 20, 40, and 80 mmol/L)-Krebs solutions 20 min after the treatment with DMSO (control) or formononetin (10, 30, and 100 μmol/L). The concentration-contraction curves of the endothelium-denuded rat mesenteric artery segments for KCl were constructed. Compared with control, formononetin shifted the concentration-contraction curves of KCl towards the right in a non-parallel manner (P<0.05, Figure 4A). The E_{max} of vasoconstrictive response to KCl was decreased and the EC_{50} value of KCl was increased by formononetin (P<0.05, Table 4).

Effects of formononetin on Ca^{2+}-induced contractions in Ca^{2+}-free depolarized Krebs solution

The endothelium-denuded rat mesenteric artery segments were exposed to Ca^{2+}-free and K^+-rich solution containing EDTA (100 μmol/L) and KCl (60 mmol/L) for 20 min. Then, $CaCl_2$ (0.01–10 mmol/L) was added cumulatively to the baths after treatment with DMSO (control) or formononetin (10, 30, and 100 μmol/L) for 15 min, and the concentration-response curves of $CaCl_2$ were constructed. Formononetin, compared with control, shifted the concentration-response curves of $CaCl_2$ towards the right in a non-parallel manner (P<0.05, Figure 4B). The E_{max} of vasoconstrictive response to $CaCl_2$ was decreased and the EC_{50} value of $CaCl_2$ was increased by formononetin (P<0.05, Table 4).

Effects of formononetin on phenylephrine- and 5-HT-induced contraction

The endothelium-denuded rat mesenteric artery segments

Table 4. EC_{50} values of different agonists contracting rat mesenteric arteries without endothelium after incubation with formononetin (For). Data are expressed as mean±SEM. n=6–8. ^bP<0.05, ^cP<0.01 *vs* control (DMSO).

Agonist		EC_{50} value			
		Control	For 10 μmol/L	For 30 μmol/L	For 100 μmol/L
KCl	mmol/L	30.1±0.95	31.7±0.6	32.7±0.8^b	38.0±0.8^c
$CaCl_2$	mmol/L	0.44±0.04	0.52±0.07	0.59±0.05^b	0.80±0.04^c
Phenylephrine	μmol/L	0.77±0.21	0.95±0.25	1.30±0.25	1.42±0.19^b
5-HT	μmol/L	0.77±0.14	1.14±0.23	1.23±0.18	2.13±0.09^c

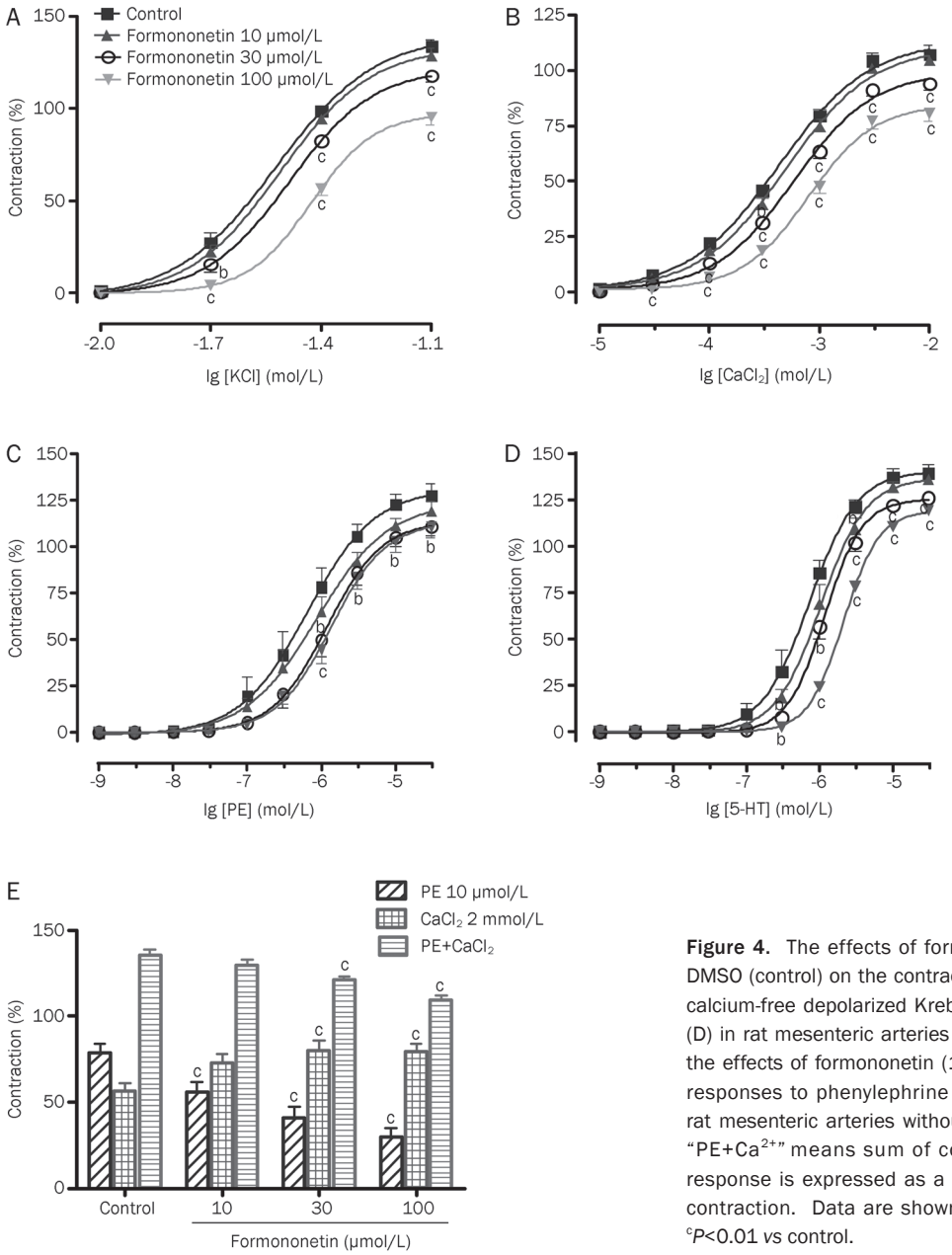

Figure 4. The effects of formononetin (10, 30, and 100 μmol/L) and DMSO (control) on the contractile responses to potassium (A), calcium in calcium-free depolarized Krebs solution (B), phenylephrine (C), and 5-HT (D) in rat mesenteric arteries without endothelium. Bar graph (E) shows the effects of formononetin (10, 30, and 100 μmol/L) on the contractile responses to phenylephrine (PE, 10 μmol/L) and $CaCl_2$ (2 mmol/L) in rat mesenteric arteries without endothelium in Ca^{2+}-free Krebs solution. "PE+Ca^{2+}" means sum of contractions to PE and Ca^{2+}. Contractile response is expressed as a percentage of the 60 mmol/L K^+ induced contraction. Data are shown as mean±SEM. n=8 arteries. $^bP<0.05$, $^cP<0.01$ *vs* control.

were pre-treated with DMSO (control) or formononetin (10, 30, and 100 μmol/L) for 20 min. Phenylephrine or 5-HT (0.001–30 μmol/L) was cumulatively added to the baths. Formononetin inhibited the phenylephrine- or 5-HT-induced vasoconstriction and concentration-dependently shifted the concentration-contraction curves towards the right in a non-parallel manner with a decreased E_{max} (Figure 4C, 4D). The EC_{50} of phenylephrine and 5-HT were increased by formononetin ($P<0.05$, Table 4).

Effects of formononetin on the contraction induced by phenylephrine dependent upon intracellular and extracellular calcium

The endothelium-denuded rat mesenteric artery segments were exposed to Ca^{2+}-free Krebs solution containing DMSO (control) or formononetin (10, 30, and 100 μmol/L) for 10 min in order to remove the extracellular Ca^{2+}, followed by addition of 10 μmol/L phenylephrine inducing phasic contractions caused by the release of intracellular Ca^{2+}. When the maximal contraction was obtained, $CaCl_2$ of 2 mmol/L was added to induce a tonic contraction evoked by the extracellular Ca^{2+} influx[32]. The results showed formononetin concentration-dependently inhibited the contraction induced by phenylephrine, but increased the $CaCl_2$-induced contraction (Figure 4E).

Effects of formononetin on the contraction induced by caffeine in Ca^{2+}-free solution

After the endothelium-denuded rat mesenteric artery segments were incubated with DMSO or formononetin (100

μmol/L) for 20 min in Ca^{2+}-free medium, artery contractions to caffeine (30 mmol/L) were obtained. The contractions induced by caffeine in the presence or absence of formononetin were 18.3%±1.8% and 18.0%±1.7% (contractile response is expressed as a percentage of the contraction induced by 60 mmol/L K^+), respectively. These data showed that formononetin did not affect the vasoconstriction induced by caffeine in Ca^{2+}-free solution (n=8 arteries, P>0.05).

Effects of formononetin on Ca^{2+} fluorescence intensity in rat mesenteric artery

Figure 5 presented the time course of the change rate of fluorescence intensity induced by 50 mmol/L KCl in rat mesenteric arteries. It could be seen that formononetin (10 and 100 μmol/L) concentration-dependently inhibited the change rate of fluorescence intensity.

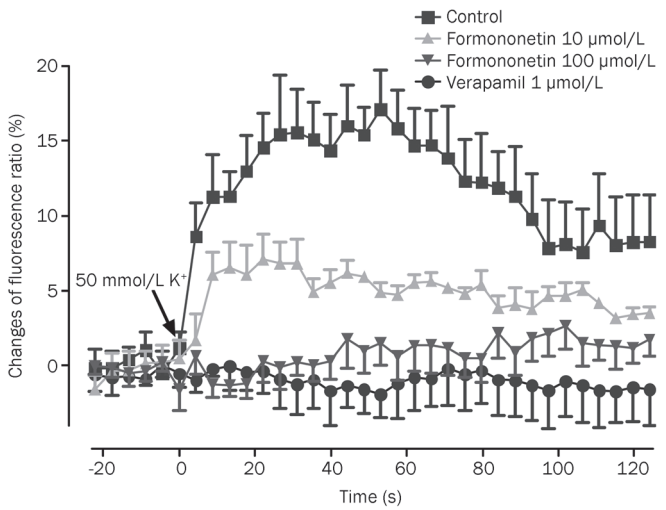

Figure 5. Effects of formononetin (10 and 100 μmol/L), verapamil (1 μmol/L), and DMSO (control) on Ca^{2+} fluorescence intensity in rat mesenteric arteries. The change rate of fluorescence intensity reflexes the change of intracellular Ca^{2+} concentration ($[Ca^{2+}]_i$). Each point represents the mean±SEM of five experiments.

Effects of formononetin on the SHR arterial pressure

The SHR arterial pressure was determined before drug administration. Then formononetin (5, 10, and 20 mg/kg), lacidipine (0.06 mg/kg) and saline containing 10% Tween 80 (control) were injected via tail vein. The arterial pressure was measured 0.5, 1, 2, 3, and 4 h after injection. It was found that formononetin lowered the systolic, diastolic and mean arterial pressures of the SHRs (Figure 6). The decline of arterial pressure reached the peak at 2 to 3 h after the treatment with formononetin, while the peak of the pressure decline induced by lacidipine was at 30 min after treatment.

Discussion

There have already been many reports about the antihyper-

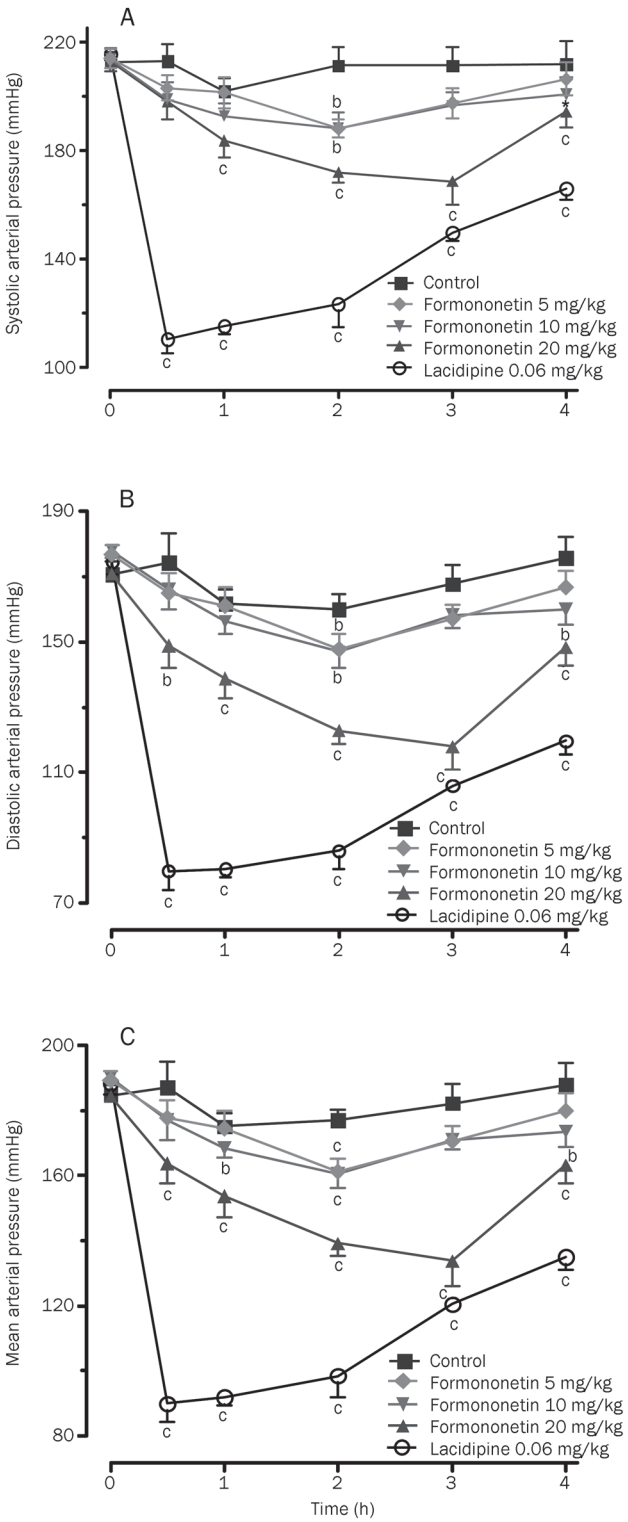

Figure 6. The effects of formononetin (5, 10, and 20 mg/kg), lacidipine (0.06 mg/kg), and saline containing 10% Tween 80 (control) on systolic arterial pressure (A), diastolic arterial pressure (B) and mean arterial pressure (C) of the SHRs. Formononetin and lacidipine were intravenously administered. Data are shown as mean±SEM. n=8. ^bP<0.05, ^cP<0.01 *vs* control.

tensive effects of some isoflavones[11]. However, no pharmacological or clinical study has been carried out to test the antihypertensive properties of formononetin. Our study first investigated the antihypertensive potential of formononetin, and the results show that formononetin can lower the arterial pressure in SHRs.

One of the key mechanisms of antihypertensive drugs is to lower the vascular resistance by directly dilating the blood vessels. Our experimental results show that formononetin can relax the arteries pre-contracted by vasoconstrictors, indicating that the antihypertensive activities of formononetin maybe stem from the vasorelaxant activity. This is in concert with the previous findings that formononetin relaxes rat isolated aorta[9] and some isoflavones have vasorelaxant activities[15]. We have found that mesenteric artery is more sensitive to formononetin than abdominal aorta and renal artery in precontraction by phenylephrine, and meanwhile mesenteric artery is one of peripheral arteries which contribute more resistance than aorta in hypertension, and therefore we chose to study the vasorelaxant mechanism of formononetin on mesenteric artery.

The vasorelaxant activity of antihypertensive drugs is achieved by influencing both vascular endothelial and vascular smooth muscle cells. Endothelium plays an important role in regulating the function of cardiovascular system. It synthesizes and releases several vasodilator substances, mainly including vasodilator PGs, NO, and EDHF[33]. The removal of endothelium markedly attenuates the relaxant response of arteries to formononetin, suggesting that the relaxation is endothelium-dependent. NO causes vascular relaxation by stimulating the production of cGMP and/or causing membrane hyperpolarization[34]. *L*-NAME, a NOS inhibitor, inhibits the relaxation of formononetin, indicating that the vasorelaxant activity of formononetin is related to NO release. Similar findings are reported elsewhere[9]. The vasorelaxant effect of PGs is realized through increasing intracellular cAMP levels[35]. We have found that indomethacin has little effect on the concentration-relaxation curves of formononetin, and therefore PG biosynthesis is little involved in the formononetin-induced relaxation. EDHF dilates arteries by increasing the membrane permeability of vascular smooth muscle cells to K^+[35]. The formononetin-induced relaxation in the mesenteric arteries without endothelium is not significantly different from that in the mesenteric arteries incubated with indomethacin+*L*-NAME, suggesting that other factors like EDHF are not involved in the endothelium-dependent relaxation. The relaxing response to formononetin has remained after the denudation of endothelial cells, indicating the involvement of endothelium-independent mechanism. Thus, it is conceivable that formononetin directly act on vascular smooth muscles as well as endothelial cells.

Vascular smooth muscle cells are also contributory to the vasorelaxant activity of antihypertensive drugs. β-adrenoceptors and K^+ channels are important regulators of arterial tone. β-adrenoceptor-induced relaxation is mediated by the increase of the intracellular cAMP concentration and/or activation of K^+ channels[36]. Opening of K^+ channels leads to membrane potential hyperpolarization and closure of voltage-dependent channels, which decreases Ca^{2+} entry and causes vasodilation[37]. In our experiments, propranolol, glibenclamide, tetraethylammonium and $BaCl_2$ did not affect the endothelium-independent relaxant response to formononetin in rat mesenteric arteries, suggesting that the K^+ channels and β-adrenoceptors are not involved in the vascular relaxation processes, which is in accordance with the previous findings that K^+ channel inhibitors did not affect the relaxation of genistein and zearalanone, two phytoestrogens, in rabbit coronary arteries[38]. By contrast, Wu *et al* proposed that formononetin caused opening of iberiotoxin-sensitive Ca^{2+}-activated K^+ channels and glibenclamide-sensitive adenosine triphosphate (ATP)-dependent K^+ channels in rat aorta[9]. This discordance may lie in the different responses of mesenteric artery and aorta to drugs[39].

There are two kinds of Ca^{2+} channels in smooth muscle cells: VDCC and receptor-operated Ca^{2+} channels (ROCC). KCl-induced contraction is due to membrane depolarization, leading to increased Ca^{2+} influx through VDCC. Formononetin inhibits the contraction induced by KCl in Krebs solution and $CaCl_2$ in high-K^+ depolarization medium, suggesting that formononetin may inhibit VDCC. This is in accordance with some previous findings[38].

Phenylephrine- or 5-HT-induced contraction in solution containing Ca^{2+} is due to activation of α_1-adrenoceptors or 5-HT receptors, which leads to an increase in intracellular calcium concentration via activation of the inositol phosphate cascade, releasing intracellular calcium and promoting the entry of extracellular calcium through ROCC[40, 41]. In the present study, formononetin treatment results in a rightward shift of concentration-contraction curves of phenylephrine or 5-HT in a non-parallel manner in medium with Ca^{2+}, suggesting that formononetin can inhibit ROCC or Ca^{2+} release from intracellular stores. Our further experiments show that formononetin inhibits the contraction induced by phenylephrine in Ca^{2+}-free solution while the tonic contraction evoked by the extracellular Ca^{2+} influx is increased, but the total contraction induced by $CaCl_2$ and phenylephrine is decreased by formononetin. These results suggest that formononetin inhibits intracellular Ca^{2+} release from Ca^{2+} stores in vascular smooth muscle cells, but does not inhibit the extracellular Ca^{2+} influxing through ROCC. This is partly consistent with some previous findings[42]. The increased contraction induced by $CaCl_2$ may be a compensatory mechanism of suppressed Ca^{2+} release. Thus, it is likely that Ca^{2+} mobilization in smooth muscle cells is inhibited by formononetin.

The release of intracellular Ca^{2+} is mainly regulated by ryanodine receptor system and inositol 1,4,5-trisphosphate (IP3) receptor system. The former may function through a Ca^{2+}-induced Ca^{2+} release mechanism when the receptors are activated by caffeine[43]. The latter induces Ca^{2+} release directly when the receptors are bound to IP3. Furthermore, formononetin does not affect the caffeine-induced contraction in endothelium-denuded arteries, which rules out the possible involvement of ryanodine receptors. Therefore, it is likely that

the IP3 receptor contributes to Ca^{2+} release.

Laser scanning confocal microscope and fluorescent probe are widely employed to monitor dynamic changes of $[Ca^{2+}]_i$ in various cells and tissues[29]. Our finding that formononetin inhibits the KCl-induced increase of $[Ca^{2+}]_i$ in rat mesenteric artery further proves that formononetin decreases intracellular calcium.

In summary, formononetin, with antihypertensive potential, has multiple targets and a moderate effect in lowering arterial pressure, which is different from typical antihypertensive drugs. Besides, being a natural compound, formononetin may have little toxic effect. What's more, formononetin possesses antioxidant property[44], and it increases the expression of eNOS[9] and lowers blood lipid[45], which will be beneficial in preventing and treating the complications of hypertension, such as cardiac and vascular remodeling, lipid abnormalities and atherosclerosis. Therefore, formononetin may be of value in treating and preventing hypertension.

Acknowledgements

This study was supported by grant from the National Natural Science Foundation of China (No 30772566).

Author contribution

Tao SUN and Yong-xiao CAO designed the research; Tao SUN and Rui LIU performed the experiments; and Tao SUN and Yong-xiao CAO analyzed the data and wrote the paper.

References

1 Ogihara T, Matsuzaki M, Matsuoka H, Shimamoto K, Shimada K, Rakugi H, *et al*. The combination therapy of hypertension to prevent cardiovascular events (COPE) trial: rationale and design. Hypertension Res 2005; 28: 331–8.

2 Yeh CT, Huang WH, Yen GC. Antihypertensive effects of Hsian-tsao and its active compound in spontaneously hypertensive rats. J Nutr Biochem 2009; 20: 866–75.

3 Kwan CY. Vascular effects of selected antihypertensive drugs derived from traditional medicinal herbs. Clin Exp Pharmacol Physiol Suppl 1995; 22: S297–9.

4 Ryu SY, Oh KS, Kim YS, Lee BH. Antihypertensive, vasorelaxant and inotropic effects of an ethanolic extract of the roots of *Saururus chinensis*. J Ethnopharmacol 2008; 118: 284–9.

5 Atkinson C, Compston JE, Day NE, Dowsett M, Bingham SA. The effects of phytoestrogen isoflavones on bone density in women: a double-blind, randomized, placebo-controlled trial. Am J Clin Nutr 2004; 79: 326–33.

6 Jarred RA, Keikha M, Dowling C, McPherson SJ, Clare AM, Husband AJ, *et al*. Induction of apoptosis in low to moderate-grade human prostate carcinoma by red clover-derived dietary isoflavones. Cancer Epidemiol Biomarkers Prev 2002; 11: 1689–96.

7 Nestel P, Fujii A, Zhang L. An isoflavone metabolite reduces arterial stiffness and blood pressure in overweight men and postmenopausal women. Atherosclerosis 2007; 192: 184–9.

8 Ososki AL, Kennelly EJ. Phytoestrogens: a review of the present state of research. Phytother Res 2003; 17: 845–69.

9 Wu JH, Li Q, Wu MY, Guo DJ, Chen HL, Chen SL, *et al*. Formononetin, an isoflavone, relaxes rat isolated aorta through endothelium-dependent and endothelium-independent pathways. J Nutr Biochem 2009; 21: 613–20.

10 Chin-Dusting JP, Boak L, Husband A, Nestel PJ. The isoflavone metabolite dehydroequol produces vasodilatation in human resistance arteries via a nitric oxide-dependent mechanism. Atherosclerosis 2004; 176: 45–8.

11 Adlercreutz H, Hamalainen E, Gorbach S, Goldin B. Dietary phytooestrogens and the menopause in Japan. Lancet 1992; 339: 1233.

12 Breinholt V, Hossaini A, Svendsen GW, Brouwer C, Nielsen E. Estrogenic activity of flavonoids in mice. The importance of estrogen receptor distribution, metabolism and bioavailability. Food Chem Toxicol 2000; 38: 555–64.

13 Reinli K, Block G. Phytoestrogen content of foods — a compendium of literature values. Nutr Cancer 1996; 26: 123–48.

14 Tham DM, Gardner CD, Haskell WL. Clinical review 97: potential health benefits of dietary phytoestrogens: a review of the clinical, epidemiological, and mechanistic evidence. J Clin Endocrinol Metab 1998; 83: 2223–35.

15 Chin-Dusting JP, Fisher LJ, Lewis TV, Piekarska A, Nestel PJ, Husband A. The vascular activity of some isoflavone metabolites: implications for a cardioprotective role. Br J Pharmacol 2001; 133: 595–605.

16 Walker HA, Dean TS, Sanders TA, Jackson G, Ritter JM, Chowienczyk PJ. The phytoestrogen genistein produces acute nitric oxide-dependent dilation of human forearm vasculature with similar potency to 17beta-estradiol. Circulation 2001; 103: 258–62.

17 Ma W, Nomura M, Takahashi-Nishioka T, Kobayashi S. Combined effects of fangchinoline from *Stephania tetrandra* Radix and formononetin and calycosin from *Astragalus membranaceus* Radix on hyperglycemia and hypoinsulinemia in streptozotocin-diabetic mice. Biol Pharm Bull 2007; 30: 2079–83.

18 Ma X, Tu P, Chen Y, Zhang T, Wei Y. Preparative isolation and purification of calycosin and formononetin from *Astragalus membranaceus* Bge var mongholicus (Bge) Hsiao by high-speed counter-current chromatography. Se Pu 2005; 23: 299–301.

19 Reiners W. 7-hydroxy-4′-methoxy-isoflavone (formononetin) from liquorice root. On substances contained in liquorice root. II. Experientia 1966; 22: 359.

20 Avula B, Wang YH, Smillie TJ, Khan IA. Quantitative determination of triterpenoids and formononetin in rhizomes of black cohosh (*Actaea racemosa*) and dietary supplements by using UPLC-UV/ELS detection and identification by UPLC-MS. Planta Med 2009; 75: 381–6.

21 Jiang B, Kronenberg F, Balick MJ, Kennelly EJ. Analysis of formononetin from black cohosh (*Actaea racemosa*). Phytomedicine 2006; 13: 477–86.

22 Schultz G. Isoflavone glucoside formononetin-7-glucoside and biochanin A-7-glucoside in *Trifolium pratense* L. Naturwissenschaften 1965; 52: 517.

23 Zhang BQ, Hu SJ, Qiu LH, Zhu JH, Xie XJ, Sun J, *et al*. Effects of *Astragalus membranaceus* and its main components on the acute phase endothelial dysfunction induced by homocysteine. Vasc Pharmacol 2007; 46: 278–85.

24 Adner M, Cantera L, Ehlert F, Nilsson L, Edvinsson L. Plasticity of contractile endothelin-B receptors in human arteries after organ culture. Br J Pharmacol 1996; 119: 1159–66.

25 Sandhu H, Xu CB, Edvinsson L. Upregulation of contractile endothelin type B receptors by lipid-soluble cigarette smoking particles in rat cerebral arteries via activation of MAPK. Toxicol Appl Pharmacol 2010; 249: 25–32.

26 Cao YX, Zheng JP, He JY, Li J, Xu CB, Edvinsson L. Induces vasodilatation of rat mesenteric artery *in vitro* mainly by inhibiting receptor-mediated Ca^{2+}-influx and Ca^{2+}-release. Arch Pharm Res 2005; 28: 709-15.

27 Cao YX, Zhang W, He JY, He LC, Xu CB. Ligustilide induces vasodilatation via inhibiting voltage dependent calcium channel and receptor-mediated Ca^{2+} influx and release. Vascul Pharmacol 2006; 45: 171–6.
28 Wiest R, Jurzik L, Moleda L, Froh M, Schnabl B, von Horsten S, *et al*. Enhanced Y1-receptor-mediated vasoconstrictive action of neuropeptide Y (NPY) in superior mesenteric arteries in portal hypertension. J Hepatol 2006; 44: 512–9.
29 Hashimoto T, Ohata H, Nobe K, Sakai Y, Honda K. A novel approach for the determination of contractile and calcium responses of the basilar artery employing real-time confocal laser microscopy. J Pharmacol Toxicol Methods 2007; 56: 79–86.
30 Nguyen P, Peltsch H, de Wit J, Crispo J, Ubriaco G, Eibl J, *et al*. Regulation of the phenylethanolamine *N*-methyltransferase gene in the adrenal gland of the spontaneous hypertensive rat. Neurosci Lett 2009; 461: 280–4.
31 Inc S. SPSS Base 13.0 for Windows: Users Guide 2004.
32 Broekaert A, Godfraind T. A comparison of the inhibitory effect of cinnarizine and papaverine on the noradrenaline- and calcium-evoked contraction of isolated rabbit aorta and mesenteric arteries. Eur J Pharmacol 1979; 53: 281–8.
33 Kawabata A, Nakaya Y, Ishiki T, Kubo S, Kuroda R, Sekiguchi F, *et al*. Receptor-activating peptides for PAR-1 and PAR-2 relax rat gastric artery via multiple mechanisms. Life Sci 2004; 75: 2689–702.
34 Bonaventura D, Oliveira FS, Lunardi CN, Vercesi JA, da Silva RS, Bendhack LM. Characterization of the mechanisms of action and nitric oxide species involved in the relaxation induced by the ruthenium complex. Nitric Oxide 2006; 15: 387–94.
35 Higueras J, Sarria B, Ortiz JL, Cortijo J, Maruenda A, Barbera M, *et al*. Halothane inhibits endothelium-dependent relaxation elicited by acetylcholine in human isolated pulmonary arteries. Eur J Pharmacol 1997; 326: 175–81.
36 Huang Y, Kwok KH. Beta-adrenoceptor-mediated relaxation inhibited by tetrapentylammonium ions in rat mesenteric artery. Life Sci 1998; 62: PL19–25.
37 Mustafa S, Thulesius O. Hyperthermia-induced vasoconstriction of the carotid artery and the role of potassium channels. J Stroke Cerebrovasc Dis 2005; 14: 122–6.
38 Figtree GA, Griffiths H, Lu YQ, Webb CM, MacLeod K, Collins P. Plant-derived estrogens relax coronary arteries *in vitro* by a calcium antagonistic mechanism. J Am Coll Cardiol 2000; 35: 1977–85.
39 Chan HY, Yao X, Tsang SY, Chan FL, Lau CW, Huang Y. Different role of endothelium/nitric oxide in 17beta-estradiol- and progesterone-induced relaxation in rat arteries. Life Sci 2001; 69: 1609–17.
40 Ford WR, Broadley KJ. Effects of adenosine receptor agonists on induction of contractions to phenylephrine of guinea-pig aorta mediated via intra- or extracellular calcium. Gen Pharmacol 1999; 33: 143–50.
41 Hirafuji M, Ebihara T, Kawahara F, Hamaue N, Endo T, Minami M. Inhibition by docosahexaenoic acid of receptor-mediated Ca^{2+} influx in rat vascular smooth muscle cells stimulated with 5-hydroxytryptamine. Eur J Pharmacol 2001; 427: 195–201.
42 Ajay M, Gilani AU, Mustafa MR. Effects of flavonoids on vascular smooth muscle of the isolated rat thoracic aorta. Life Sci 2003; 74: 603–12.
43 Leijten PA, van Breemen C. The effects of caffeine on the noradrenaline-sensitive calcium store in rabbit aorta. J Physiol 1984; 357: 327–39.
44 Mu H, Bai YH, Wang ST, Zhu ZM, Zhang YW. Research on antioxidant effects and estrogenic effect of formononetin from *Trifolium pratense* (red clover). Phytomedicine 2009; 16: 314–9.
45 Wang QY, Meng QH, Zhang ZT, Tian ZJ, Liu H. Synthesis, solubility, lipids-lowering and liver-protection activities of sulfonated formononetin. Yao Xue Xue Bao 2009; 44: 386–9.

Acta Pharmacologica Sinica (2011) 32: 1019–1024
 1671-4083/11 $32.00
www.nature.com/aps

Original Article

Involvement of REST corepressor 3 in prognosis of human hepatitis B

Ji-hua XUE, Min ZHENG, Xiao-wei XU, Shan-shan WU, Zhi CHEN, Feng CHEN*

State Key Laboratory for Diagnosis and Treatment of Infectious Diseases, the First Affiliated Hospital, School of Medicine, Zhejiang University, Hangzhou 310003, China

Aim: To examine the potential correlation between serum REST corepressor 3 (RCOR3) level and the outcome of patients with hepatitis B.

Methods: Concanavalin A (ConA)-induced mouse hepatitis model was used. The mRNA level of RCOR3 in mouse liver was measured using GeneChip array and real-time PCR. One hundred seventy-seven patients with hepatitis B and 34 healthy individuals were categorized into six groups including mild chronic hepatitis, moderate chronic hepatitis B, severe hepatitis B (SHB), cirrhosis, hepatocellular carcinoma (HCC) and healthy control. Serum levels of human RCOR3 were measured using ELISA.

Results: In the mouse hepatitis model, the mRNA level of RCOR3 in liver was reduced early after exposure to ConA, then increased after 6 h of exposure. There was no significant difference in the serum RCOR3 level between the mild chronic hepatitis B and the control groups. The serum RCOR3 level was significantly increased in the moderate chronic hepatitis B group, but significantly reduced in SHB, cirrhosis and HCC groups, as compared with the control group. Moreover, the serum RCOR3 levels in SHB, cirrhosis and liver cancer patients were significantly lower than those in the patients with moderate chronic hepatitis B and with mild chronic hepatitis B. Rank correlation analysis revealed a significant correlation between serum RCOR3 level and total bilirubin (r=-0.305, P<0.01). There was no significant correlation between RCOR3 on one hand, and alanine transaminase (r=0.014, P>0.05) or aspartate transaminase (r=-0.079, P>0.05) on the other hand.

Conclusion: Serum RCOR3 level may reflect the degree of liver damage, which might be a potential biomarker for the outcome of patients with hepatitis B.

Keywords: hepatitis B; REST corepressor 3; biomarker; total bilirubin; concanavalin A

Acta Pharmacologica Sinica (2011) 32: 1019–1024; doi: 10.1038/aps.2011.49; published online 18 Jul 2011

Introduction

Chronic infection with hepatitis B virus (HBV) is a common and serious liver disease that affects individuals worldwide. Current treatment of chronic hepatitis B is disappointingly limited. It is reported that there are more than 2 billion HBV carriers at present globally, and among them, about 360 million patients suffer from chronic hepatitis, cirrhosis or hepatocellular carcinoma (HCC)[1, 2].

RCOR3 is a member of the REST (repressor element-1-silencing transcription factor) corepressor (CoREST) family that functions as a corepressor for REST, which regulates neuronal gene expression and determines the fate of neural stem cells. The CoREST family consists of RCOR1, also known as CoREST, RCOR2, and RCOR3. REST (also known as neuron-restrictive silencer factor, NRSF) is an essential vertebrate zinc finger transcription factor[3], which can bind to the conservative sequence of neuron-restrictive silencer element DNA (NRSE DNA)[4]. The REST gene is highly expressed in non-neuronal cells and neuronal precursor cells, but it is expressed much less in differentiated neurons[5].

To date, it has been shown that REST does not work independently. The dynamic and multiplex function of REST is achieved through the REST-dependent recruitment of distinct modular macromolecular complexes. Thus, REST serves as a hub for recruiting multiple chromatin-modifying proteins, including multiple histone deacetylases (HDACs) and lysine specific demethylases (LSD; for example, LSD1)[6–8]. The N-terminal domain of NRSF can combine with mSin3A/B, and the C-terminal domain can bind to CoREST[9, 10]. The histone modifiers are able to interact directly with either REST or its corepressors, such as CoREST[11] or mSin3[9, 12–14], and thus block the transcription of certain genes[15].

* To whom correspondence should be addressed.
E-mail zjuchenfeng@gmail.com
Received 2010-12-16 Accepted 2011-03-29

In a previous study, we obtained the gene expression profile of livers from mice in a concanavalin A (ConA)-induced hepatitis model by GeneChip array[16, 17]. ConA-induced hepatic injury in mice has long been established as a model of immunologically induced hepatocyte injury because its histological features highly resemble those of viral or drug-induced acute hepatitis in humans[18]. The hepatocyte injury is associated with massive hepatocellular degeneration and lymphoid infiltration of the liver[19]. The hepatic injury induced by ConA depends mainly upon T-cell activation[20], which raises the plasma levels of various cytokines such as tumor necrosis factor-alpha (TNF-α), interferon (IFN)-γ, interleukin (IL)-6, *etc*[21]. Hence, we used the ConA-induced hepatitis model and selected microarray to explore the pathogenic mechanism of human fulminant hepatitis. In this study, 26 differentially expressed genes associated with hepatitis B were selected. However, only the expression of RCOR3 attracted our interest, for RCOR3 was suitable to be used as a biomarker. Considering the clinical significance of RCOR3 remains largely unknown, we herein studied the serum RCOR3 levels of patients with hepatitis B to explore the potential correlation between serum RCOR3 and the outcome of hepatitis B patients.

Materials and methods

ConA-induced hepatitis model in mice

Male BALB/c mice, weighing about 25 g, were housed under standard animal laboratory conditions in the Animal Center of Zhejiang Academy of Medical Sciences. This study was approved by the local Ethical Committee of the Academy. The mice were subjected to a tail vein injection of ConA (type V, Sigma Chemical Co, USA) at 20 mg/kg body weight, and phosphate-buffered saline (PBS) was used as a control. The mice were sacrificed at 1, 3, or 6 h separately. All animals received humane care in accordance with the guidelines established by the National Science Council of China. Mouse liver samples were collected and fixed in 4% phosphate-buffered paraformaldehyde. Paraffin tissue sections were prepared and subjected to hematoxylin-eosin (H&E) staining for standard histological examination. The extent of liver injury was also evaluated by determining serum ALT, AST, STB, and LDH using the standard Reitman-Frankel method. The results can be seen in our previous articles[16, 17].

Microarray analysis

Total RNA extracted from mouse liver samples was reverse transcribed and labeled with biotin. The biotinylated cDNAs were then hybridized to 12 individual Affymetrix GeneChips Mouse 430 2.0 Arrays (Affymetrix, Inc, Santa Clara, CA, USA), which contain 45101 probes in total according to the manufacturer's instructions. Significant differentially expressed genes at each time point were filtered by analysis of variance (ANOVA) and corrected by the random variance model (RVM)[22]. To assess whether the significance of one particular sample occurred by random chance, the false discovery rate (FDR) was estimated to determine whether the differences of certain genes were truly significant by repeating the comparison test and the permutation test 1000 times. A P-value<0.05 and FDR<0.05 were considered the threshold for true significance.

Real-time PCR

The original amount of RCOR3 mRNA was measured by real-time PCR with a SYBR Green PCR Kit (Applied Biosystems, Foster City, CA, USA) using the ABI PRISM 7900 sequence detector (Applied Biosystems, Foster City, CA, USA). A volume of 20 μL of amplification reactions contained 2×SYBR Green Realtime PCR Master Mix, 0.4 μmol/L primers, and 1 μL of template cDNA. The mRNA of the housekeeping gene β-actin was used as an endogenous control. The sequences for the primers used are as follows: RCOR3 forward primer, 5′-AGTATCCCAGATGCCAAAT-3′; RCOR3 reverse primer, 5′-GGAAAGGGCGTGAAGTTA-3′; β-actin forward primer, 5′-CGTTGACATCCGTAAAGACC-3′; and β-actin reverse primer, 5′-AACAGTCCGCCTAGAAGCAC-3′. Thermal cycling was carried out for 5 min at 95 °C, followed by 40 cycles of 30 s at 95 °C, 30 s at 57 °C, and 30 s at 72 °C. We performed the PCR amplifications in duplicate for each sample and the expression of RCOR3 was normalized against β-actin. Analysis of variance (ANOVA) was used to compare the differences of gene expression levels between groups. A P-value<0.05 was considered statistically significant.

Patients and samples

One hundred and seventy-seven patients with hepatitis B were selected from the Infectious Department of the First Affiliated Hospital of College of Medicine, Zhejiang University, referring to the guideline of prevention and treatment for chronic hepatitis B (2010 version)[23]. Thirty-four healthy people who had undertaken a medical examination in 2009 at the First Affiliated Hospital of College of Medicine, Zhejiang University, were included as the control group. The demographic characteristics of all subjects are summarized in Table 1. All patients provided informed consent prior to participating in the study; the experimental protocols used in this study were approved by the Ethics Committee of the First Affiliated Hospital of College of Medicine, Zhejiang University.

ELISA

Commercially available ELISA kits (Groundwork Biotechnol-

Table 1. Demographic of subjects.

Group	*n*	Gender		Age
		Male	Female	(Mean±SD)
Health control	34	11	23	26.74±5.71
Mild chronic hepatitis B	25	18	7	32.80±9.74
Moderate chronic hepatitis B	38	23	15	36.34±9.55
Severe hepatitis B	24	21	3	40.88±10.76
Cirrhosis	60	43	17	50.10±10.74
Liver cancer	30	29	1	56.13±11.84

ogy Diagnosticate Ltd) were utilized to determine serum levels of human RCOR3 following the manufacturer's instruction. ELISA samples were read at the wavelength of 450 nm and a standard curve was constructed using the *OD* values. Assays were performed in duplicate.

Statistical analysis

All of the data were processed by SPSS 13.0 software and presented as means±SD. An ANOVA and LSD test were used for comparisons among the groups and between paired data, respectively. When the data were not normally distributed, the Mann-Whitney U test and the one-way non parametric ANOVA (Kruskal Wallis test) were used to compare quantitative variables between two groups of observation and in more than two groups of data, respectively. Spearman rank correlation test was used for correlation analysis.

Results

Expression of RCOR3 in ConA-induced mouse hepatitis

A GeneChip array was performed to screen differentially expressed genes in a model of ConA-induced mouse hepatitis. The data were analyzed by ANOVA and corrected with the randomized variance model. As a result, 1473 genes with significant *P*-values and a false discovery rate (FDR) of less than 0.05 were identified; among these genes, we selected 26 differentially expressed genes that were associated with hepatitis B. However, other genes, with the exception of RCOR3, were either validated to be meaningless or not secretory proteins and cannot be used as biomarkers. The expression of RCOR3 attracted our interest, and its differential expression was very notable. Intriguingly, the expression of RCOR3 was decreased at 1 h and 3 h post ConA exposure, but increased at the 6 h time point (Figure 1).

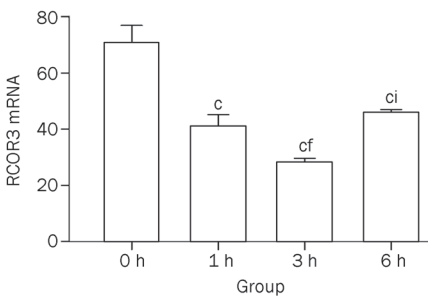

Figure 1. GeneChip array data on the expression of RCOR3 in a model of ConA-induced mouse hepatitis at the indicated time points. The horizontal axis represents time, and the vertical axis shows the mRNA levels of RCOR3. $^{c}P<0.01$ compared with the 0 h group; $^{f}P<0.01$ compared with the 1 h group; $^{i}P<0.01$ compared with the 3 h group.

Validation of RCOR3 expression by real-time PCR

Real-time PCR was performed to verify the expression of RCOR3 in a model of ConA-induced mouse hepatitis. As shown in Figure 2, RCOR3 mRNA was significantly induced at the 6 h time point in comparison with the 0 h group ($P<0.05$). Meanwhile, there was a significant increase in the mRNA level of RCOR3 at the 3 h and 6 h time points compared with the 1 h group ($P<0.05$ and $P<0.01$, respectively), and these results (Figure 2) showed some differences in comparison with the results of the GeneChips Arrays, which showed that the expression of RCOR3 was decreased at 1 h and 3 h post ConA exposure, but increased at the 6 h time point. However, the mRNA level of RCOR3 in real-time PCR array was significantly reduced at the 1 h time point, but was induced in the liver after ConA exposure at the 3 h and 6 h time points in comparison with the 0 h group. Despite the minor difference with the results of the GeneChips Arrays, the overall trend was that the mRNA level of RCOR3 was reduced early after ConA exposure and then induced after 6 h of exposure.

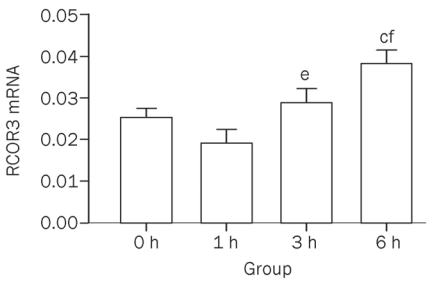

Figure 2. Real-time PCR validation of RCOR3 expression in a model of ConA-induced mouse hepatitis at the indicated time points. The horizontal axis represents time, and the vertical axis shows the mRNA levels of RCOR3. $^{c}P<0.01$ compared with the 0 h group; $^{e}P<0.05$, $^{f}P<0.01$ compared with the 1 h group.

Comparison of hepatitis-associated markers among patients with hepatitis B

As shown in Table 2, the serum ALT levels of mild chronic hepatitis B patients, moderate chronic hepatitis B patients, severe hepatitis B (SHB) patients, cirrhosis patients and HCC patients were significantly increased compared with the healthy control group. Meanwhile, there was a significant increase in serum ALT levels in patients with moderate chronic hepatitis B and SHB in comparison with patients with mild chronic hepatitis B. Moreover, serum ALT levels in cirrhosis and liver cancer patients remarkably declined compared with moderate chronic hepatitis B patients and severe hepatitis patients. Compared with the healthy control group, the serum AST levels of mild chronic hepatitis B patients, moderate chronic hepatitis B patients, SHB patients, cirrhosis patients and HCC patients were evidently increased. Meanwhile, there was a significant increase in serum AST levels in patients with moderate chronic hepatitis B, SHB, cirrhosis and liver cancer in comparison with patients with mild chronic hepatitis B. In addition, the serum TB levels in moderate chronic hepatitis B patients, SHB patients, cirrhosis patients and HCC patients were significantly higher than that of the healthy control group. An increase of serum TB levels in patients with moderate chronic hepatitis B, SHB, cirrhosis and liver cancer

Table 2. Levels of hepatitis-associated serum markers in ConA-induced mice hepatitis (mean±SD).

Group	*n*	ALT	AST	TB
Health control	34	15.26±7.71	20.04±4.82	13.11±4.95
Mild chronic hepatitis B	25	88.33±94.98[c]	58.5±39.68[c]	13.19±4.97
Moderate chronic hepatitis B	38	280.84±428.22[cf]	153.47±301.69[cf]	25.41±23.06[cf]
Severe hepatitis B	24	211.12±245.81[ce]	198.83±234.68[cf]	305.04±123.80[cfi]
Cirrhosis	60	73.92±76.19[cil]	103.8±102.28[cf]	101.37±126.82[cfil]
Liver cancer	30	94.22±119.36[cil]	102.78±69.40[cf]	78.78±126.42[cfhl]

[c]*P*<0.01 compared with health control; [e]*P*<0.05, [f]*P*<0.01 compared with mild chronic hepatitis B; [h]*P*<0.05, [i]*P*<0.01 compared with moderate chronic hepatitis B; [l]*P*<0.01 compared with severe hepatitis B. ALT, alanine transaminase; AST, aspartate transaminase; TB, total bilirubin.

was observed in comparison with the mild chronic hepatitis B patients. In comparison with the moderate chronic hepatitis B patients, the serum TB levels of SHB, cirrhosis and liver cancer patients were remarkably increased. Moreover, the serum TB levels in cirrhosis and liver cancer patients remarkably declined compared with severe hepatitis patients.

Serum RCOR3 levels in patients with hepatitis B

As shown in Table 3, there was no significant difference in serum RCOR3 levels between the mild chronic hepatitis B patients and the healthy control group. However, compared with the healthy control group, the serum RCOR3 levels were significantly increased in patients with moderate chronic hepatitis B and significantly decreased in patients with SHB, cirrhosis and HCC. Moreover, the serum RCOR3 levels in SHB, cirrhosis and liver cancer patients remarkably declined compared with the moderate chronic hepatitis B patients and mild chronic hepatitis B patients. Taken together, serum RCOR3 levels were increased in patients with mild chronic hepatitis B and moderate chronic hepatitis B and were decreased in patients with SHB, cirrhosis and liver cancer.

Table 3. Serum RCOR3 levels in HBV patients (mean±SD).

Group	*n*	RCOR3 (ng/mL)
Health control	34	1.21±0.34
Mild chronic hepatitis B	25	1.68±1.13
Moderate chronic hepatitis B	38	1.68±0.57[c]
Severe hepatitis B	24	0.92±0.43[cfi]
Cirrhosis	60	0.95±0.42[cfi]
Hepatocellular carcinoma	30	1.03±0.35[cfi]

[c]*P*<0.01 compared with health control; [f]*P*<0.01 compared with mild chronic; [i]*P*<0.01 compared with moderate chronic. RCOR3, REST corepressor 3.

Correlation of serum RCOR3 and hepatitis B-associated serum markers

As shown in Table 4, rank correlation analysis demonstrated that there was a significant correlation between serum RCOR3 and TB (*r*=-0.305, *P*<0.01), while there was no significant correlation between ROCR3 and ALT (*r*=0.014, *P*>0.05) or AST (*r*=-0.079, *P*>0.05).

Table 4. Correlation between serum RCOR3 and hepatitis B-associated markers in HBV patients.

Characteristics	*r* value	*P* value
ALT	0.014	>0.05
AST	-0.079	>0.05
TB	-0.305	<0.01

ALT, alanine transaminase; AST, aspartate transaminase; TB, total bilirubin.

Discussion

REST, also known as NRSF or X box repressor (XBR), is the first identified system-wide transcription repressor implicated in vertebrate neuronal development[4, 24–27]. However, more and more studies have provided evidence that REST plays an essential role in non-neuronal tissues[28] by functioning as a transcription silencer or activator[29–34]. For example, REST was reported to be a critical regulator in medulloblastoma cells and may serve as a therapeutic target for medulloblastoma[35]. The profound context-specificity of the functional repertoire of REST is further highlighted by its dual role as a tumor suppressor and oncoprotein[36–38].

The results of the GeneChip Arrays and real-time PCR indicated that the mRNA level of RCOR3 was initially reduced and then subsequently induced following ConA treatment. However, an RCOR3 ELISA on human serum showed that RCOR3 levels were initially induced and then reduced. It is possible that different samples and distinct RCOR3 detection methods (mouse liver tissue for GeneChip Arrays and real-time PCR; human plasma for ELISA) are responsible for the observed differences in RCOR3 levels.

RCOR3 is a member of the CoREST family and functions as a corepressor for REST, which mediates repression by REST. The significant increase of serum RCOR3 levels in mild chronic hepatitis B or moderate chronic hepatitis B patients in comparison with normal cases indicates the enhanced function of RCOR3 at the very early stage of hepatitis B, which

may lead to the repression of certain genes and thus be helpful to inhibit the progression of the disease. However, the significant decline of serum RCOR3 levels in patients with SHB, cirrhosis and HCC with the development of disease indicates the impaired function of RCOR3, which may aggravate certain diseases.

To summarize, our data showed that serum RCOR3 levels may reflect the degree of liver damage, and the assessment of serum RCOR3 in patients with hepatitis B could be helpful to the classification and intervention of the disease. Compared with the most common serum markers of hepatitis, such as ALT, AST, or TB, RCOR3 might be a more ideal biomarker that reflects the process or outcome of HB because the variation in ALT, AST or TB levels is rather intensive among the HB patients. This study also provides new insights into the potential role of the NRSE-NRSF system in non-neuronal tissues at both the physiological and pathological conditions. Nevertheless, the role of RCOR3 (REST) in the development of hepatitis B remains obscure. More systematic and comprehensive investigations are still needed to deepen our understanding on the biological significance of RCOR3. In future research, we would like to explore the mechanisms of how RCOR3 (REST) participates in the development of hepatitis B. Because REST regulates different groups of target genes in different cell types[39], we intend to identify the potential REST targets and test whether liver injury could be reversed by interfering with the expression of RCOR3.

Acknowledgements

This work was supported by the National Basic Research Program 2007CB512905, National Natural Science Foundation 30571664, and the State S&T Projects (11th Five Year) 2008ZX10002-007, Zhejiang Province Science & Technology Program 2008C23045.

Author contribution

Feng CHEN and Zhi CHEN designed the experiments; Ji-hua XUE, Min ZHENG, Xiao-wei XU, and Shan-shan WU performed the experiments; Ji-hua XUE and Shan-shan WU analyzed the data; and Ji-hua XUE and Feng CHEN wrote the paper.

References

1 Shepard CW, Simard EP, Finelli L, Fiore AE, Bell BP. Hepatitis B virus infection: epidemiology and vaccination. Epidemiol Rev 2006; 28: 112–25.
2 Da Villa G, Nuri B, Ghisetti V, Picciotto L, Ponzetto A, Angoni R, *et al*. Epidemiology of hepatitis B and delta virus infection in Albania: an approach to universal vaccination. Res Virol 1995; 146: 245–8.
3 Chen ZF, Paquette AJ, Anderson DJ. NRSF/REST is required *in vivo* for repression of multiple neuronal target genes during embryogenesis. Nat Genet 1998; 20: 136–42.
4 Schoenherr CJ, Anderson DJ. The neuron-restrictive silencer factor (NRSF): a coordinate repressor of multiple neuron-specific genes. Science 1995; 267: 1360–3.
5 Palm K, Belluardo N, Metsis M, Timmusk T. Neuronal expression of zinc finger transcription factor REST/NRSF/XBR gene. J Neurosci 1998; 18: 1280–96.
6 Ooi L, Wood IC. Chromatin crosstalk in development and disease: lessons from REST. Nat Rev Genet 2007; 8: 544–54.
7 Ballas N, Mandel G. The many faces of REST oversee epigenetic programming of neuronal genes. Curr Opin Neurobiol 2005; 15: 500–6.
8 Hsieh J, Gage FH. Epigenetic control of neural stem cell fate. Curr Opin Genet Dev 2004; 14: 461–9.
9 Roopra A, Sharling L, Wood IC, Briggs T, Bachfischer U, Paquette AJ, *et al*. Transcriptional repression by neuron-restrictive silencer factor is mediated via the Sin3-histone deacetylase complex. Mol Cell Biol 2000; 20: 2147–57.
10 You A, Tong JK, Grozinger CM, Schreiber SL. CoREST is an integral component of the CoREST- human histone deacetylase complex. Proc Natl Acad Sci U S A 2001; 98: 1454–8.
11 Andres ME, Burger C, Peral-Rubio MJ, Battaglioli E, Anderson ME, Grimes J, *et al*. CoREST: a functional corepressor required for regulation of neural-specific gene expression. Proc Natl Acad Sci U S A 1999; 96: 9873–8.
12 Grimes JA, Nielsen SJ, Battaglioli E, Miska EA, Speh JC, Berry DL, *et al*. The co-repressor mSin3A is a functional component of the REST-CoREST repressor complex. J Biol Chem 2000; 275: 9461–7.
13 Huang Y, Myers SJ, Dingledine R. Transcriptional repression by REST: recruitment of Sin3A and histone deacetylase to neuronal genes. Nat Neurosci 1999; 2: 867–72.
14 Naruse Y, Aoki T, Kojima T, Mori N. Neural restrictive silencer factor recruits mSin3 and histone deacetylase complex to repress neuron-specific target genes. Proc Natl Acad Sci U S A 1999; 96: 13691–6.
15 Roopra A, Qazi R, Schoenike B, Daley TJ, Morrison JF. Localized domains of G9a-mediated histone methylation are required for silencing of neuronal genes. Mol Cell 2004; 14: 727–38.
16 Chen F, Zhu HH, Zhou LF, Li J, Zhao LY, Wu SS, *et al*. Genes related to the very early stage of ConA-induced fulminant hepatitis: a gene-chip-based study in a mouse model. BMC Genomics 2010; 11: 240.
17 Cao QY, Chen F, Li J, Wu SS, Wang J, Chen Z. A microarray analysis of early activated pathways in concanavalin A-induced hepatitis. J Zhejiang Univ Sci B 2010; 11: 366–77.
18 Kaneko Y, Harada M, Kawano T, Yamashita M, Shibata Y, Gejyo F, *et al*. Augmentation of Valpha14 NKT cell-mediated cytotoxicity by interleukin 4 in an autocrine mechanism resulting in the development of concanavalin A-induced hepatitis. J Exp Med 2000; 191: 105–14.
19 Miyazawa Y, Tsutsui H, Mizuhara H, Fujiwara H, Kaneda K. Involvement of intrasinusoidal hemostasis in the development of concanavalin A-induced hepatic injury in mice. Hepatology 1998; 27: 497–506.
20 Tiegs G, Hentschel J, Wendel A. A T cell-dependent experimental liver injury in mice inducible by concanavalin A. J Clin Invest 1992; 90: 196–203.
21 Gantner F, Leist M, Lohse AW, Germann PG, Tiegs G. Concanavalin A-induced T-cell-mediated hepatic injury in mice: the role of tumor necrosis factor. Hepatology 1995; 21: 190–8.
22 Wright GW, Simon RM. A random variance model for detection of differential gene expression in small microarray experiments. Bioinformatics 2003; 19: 2448–55.
23 Chinese Society of Hepatology and Chinese Society of Infectious Diseases, Chinese Medical Association. The guideline of prevention and treatment for chronic hepatitis B. Zhonghua Liu Xing Bing Xue Za Zhi 2011; 32: 405–15.
24 Chong JA, Tapia-Ramirez J, Kim S, Toledo-Aral JJ, Zheng Y, Boutros MC, *et al*. REST: a mammalian silencer protein that restricts sodium channel gene expression to neurons. Cell 1995; 80: 949–57.

25 Mori N, Schoenherr C, Vandenbergh DJ, Anderson DJ. A common silencer element in the SCG10 and type II Na^+ channel genes binds a factor present in nonneuronal cells but not in neuronal cells. Neuron 1992; 9: 45–54.
26 Scholl T, Stevens MB, Mahanta S, Strominger JL. A zinc finger protein that represses transcription of the human MHC class II gene, DPA. J Immunol 1996; 156: 1448–57.
27 Kraner SD, Chong JA, Tsay HJ, Mandel G. Silencing the type II sodium channel gene: a model for neural-specific gene regulation. Neuron 1992; 9: 37–44.
28 Kuwahara K, Saito Y, Ogawa E, Takahashi N, Nakagawa Y, Naruse Y, *et al*. The neuron-restrictive silencer element-neuron-restrictive silencer factor system regulates basal and endothelin 1-inducible atrial natriuretic peptide gene expression in ventricular myocytes. Mol Cell Biol 2001; 21: 2085–97.
29 Kuwabara T, Hsieh J, Nakashima K, Taira K, Gage FH. A small modulatory dsRNA specifies the fate of adult neural stem cells. Cell 2004; 116: 779–93.
30 Sun YM, Greenway DJ, Johnson R, Street M, Belyaev ND, Deuchars J, *et al*. Distinct profiles of REST interactions with its target genes at different stages of neuronal development. Mol Biol Cell 2005; 16: 5630–8.
31 Ballas N, Grunseich C, Lu DD, Speh JC, Mandel G. REST and its corepressors mediate plasticity of neuronal gene chromatin throughout neurogenesis. Cell 2005; 121: 645–57.
32 Bessis A, Champtiaux N, Chatelin L, Changeux JP. The neuron-restrictive silencer element: a dual enhancer/silencer crucial for patterned expression of a nicotinic receptor gene in the brain. Proc Natl Acad Sci U S A 1997; 94: 5906–11.
33 Yoo J, Jeong MJ, Lee SS, Lee KI, Kwon BM, Kim DS, *et al*. The neuron restrictive silencer factor can act as an activator for dynamin I gene promoter activity in neuronal cells. Biochem Biophys Res Commun 2001; 283: 928–32.
34 Su X, Kameoka S, Lentz S, Majumder S. Activation of REST/NRSF target genes in neural stem cells is sufficient to cause neuronal differentiation. Mol Cell Biol 2004; 24: 8018–25.
35 Lawinger P, Venugopal R, Guo ZS, Immaneni A, Sengupta D, Lu W, *et al*. The neuronal repressor REST/NRSF is an essential regulator in medulloblastoma cells. Nat Med 2000; 6: 826–31.
36 Guardavaccaro D, Frescas D, Dorrello NV, Peschiaroli A, Multani AS, Cardozo T, *et al*. Control of chromosome stability by the beta-TrCP-REST-Mad2 axis. Nature 2008; 452: 365–9.
37 Majumder S. REST in good times and bad: roles in tumor suppressor and oncogenic activities. Cell Cycle 2006; 5: 1929–35.
38 Singh SK, Kagalwala MN, Parker-Thornburg J, Adams H, Majumder S. REST maintains self-renewal and pluripotency of embryonic stem cells. Nature 2008; 453: 223–7.
39 Liu Z, Liu M, Niu G, Cheng Y, Fei J. Genome-wide identification of target genes repressed by the zinc finger transcription factor REST/NRSF in the HEK 293 cell line. Acta Biochim Biophys Sin (Shanghai) 2009; 41: 1008–17.

Acta Pharmacologica Sinica (2011) 32: 1025–1030
 1671-4083/11 $32.00
www.nature.com/aps

Original Article

Aristolochic acid induces apoptosis of human umbilical vein endothelial cells *in vitro* by suppressing PI3K/Akt signaling pathway

Hong SHI[1, 2], Jiang-min FENG[1, *]

[1]*Department of Nephrology, First Affiliated Hospital of China Medical University, Shenyang 110001, China;* [2]*Department of Nephrology, Second Hospital of Fushun, Fushun 113001, China*

Aim: To investigate whether aristolochic acid (AA) induced the apoptosis of human umbilical vein endothelial cells (HUVECs) *in vitro* and the underlying mechanism.
Methods: HUVECs were treated with AA (5, 10 or 20 μg/mL) for 12, 24 and 48 h. Cell viabilities were determined with MTT assay. Hoechst 33258 staining and flow cytometry were used to examine the apoptosis of HUVECs. Western blotting was used to evaluate Akt phosphorylation. Bcl-2 and Bax levels were measured using Western blotting and RT-PCR assays.
Results: Treatment of HUVECs with AA significantly decreased the cell viabilities in dose- and time-dependent manners. Morphological changes of apoptosis were observed in AA-treated cells. AA inhibited Akt activation, which was attenuated by pretreatment of the cells with LY294002 (20 μmol/L) or wortmannin (50 nmol/L). Furthermore, AA reduced Bcl-2 levels and increased Bax levels.
Conclusion: AA induces apoptosis of HUVECs *in vitro* via the PI3K/Akt signaling pathway and by modulating the ratio Bcl-2 and Bax.

Keywords: aristolochic acid; HUVECs; apoptosis; PI3K/Akt signaling pathway

Acta Pharmacologica Sinica (2011) 32: 1025–1030; doi: 10.1038/aps.2011.74; published online 18 Jul 2011

Introduction

Aristolochic acid (AA), an active component of the Chinese herbal medicines derived from the *Aristolochia* species, has been implicated in AA nephropathy (AAN), which is a progressive tubulointerstitial nephropathy. Studies indicated that blood vessel impairment was present in AAN[1, 2], and could be one of the causes for the progressive tubulointerstitial damage. In renal biopsy samples of AAN patients, the abnormal ultrastructure of endothelial cells within the microvasculature and marked injury of peritubular capillaries were accompanied by low vascular endothelial growth factor (VEGF) levels[3] in tubular cells. It was further indicated that endothelial injury was related to the deterioration of renal function in AAN[4].

It is well known that VEGF is an important endogenous proangiogenic molecule, which can induce angiogenesis by acting directly on the endothelium *in vivo*[5]. VEGF potently blocks the execution of apoptosis of endothelial cells[6–8]. Withdrawal of *VEGF* by targeted inactivation of the VEGF gene results in massive endothelial cell apoptosis[9, 10]. Apoptotic endothelial cell death may critically disturb the integrity of the endothelial monolayer and thereby contribute to vascular injury.

VEGF could activate the survival-promoting PI3K/Akt pathway[6, 11, 12]. Activation of the serine/threonine kinase Akt in turn stimulates the phosphorylation of pro-apoptotic proteins such as Bad and consequently inhibits apoptosis execution[13]. Moreover, Akt activates the endothelial nitric oxide (NO) synthase, leading to enhanced synthesis of NO[14, 15], which promotes endothelial cell survival by inhibiting the cysteine protease activity of caspases via *S*-nitrosylation of the reactive cysteine residue[16]. In addition, recent studies have demonstrated that a PI3K/Akt-dependent enhancement in the expression of the anti-apoptotic protein survivin is important for the apoptosis protective effects of angiogenic factors[17–19]. Finally, VEGF mediates the upregulation of the anti-apoptotic protein Bcl-2[20]. Thus, the impairment of the intracellular survival signals activated by VEGF has deleterious effects on vessel development.

These data suggests possible inhibitory effect of AA on vessel development indirectly. The objective of the current study was to investigate the direct effects of AA on vascular endothelial cells *in vitro* and to explore the underlying

* To whom correspondence should be addressed.
E-mail fengjiangmin2007@hotmail.com
Received 2010-11-01 Accepted 2011-04-26

mechanisms.

Materials and methods

Cell culture and drug treatment

Human umbilical vein endothelial cells (HUVECs) (American Type Culture Collection, Rockville, MD, USA) were cultured in Dulbecco's modified Eagle's medium (DMEM) (Gibco, USA) supplemented with 10% fetal bovine serum (Haoyang Biotech Co, China), 100 U/mL penicillin and 100 μg/mL streptomycin at 37 °C in a humidified incubator containing 5% CO_2 and 95% air. For drug treatment, HUVECs were incubated with 5, 10 or 20 μg/mL AA (Sigma, USA) for 12, 24, or 48 h. HUVECs were also pretreated with specific PI3K inhibitor, LY294002 at 20 μmol/L or wortmannin at 50 nmol/L (Beyotime Institute of Biotechnology, China) for 30 min prior to treatment with 10 μg/mL AA.

Cell viability assays

Cell viability was assessed by the tetrazolium-based semi-automated colorimetric 3-(4,5-dimethylthiazol-2-yl)-2,5-diphenyltetrazolium bromide (MTT) reduction assay (Sigma, USA). Cells were seeded at a density of 1×10^4 cells/well in 96-well plates. After 24 h incubation, cells were treated with AA at 5, 10, or 20 μg/mL for 12, 24, or 48 h. MTT assays were performed as instructed by the manufacturer and absorbance was read at 490 nm using a microplate reader (Sunrise RC, Tecan, Switzerland). Relative cell viability was expressed as the percentage of the control.

Hoechst 33258 staining assays

Morphological evaluation of apoptosis was performed using Hoechst 33258 (Beyotime Institute of Biotechnology) according to the manufacturer's instructions. Cells were fixed with 4% paraformaldehyde for 10 min at 4 °C and stained with Hoechst 33258 for 10 min at room temperature in the dark. Nuclear morphology was then examined under a fluorescent microscope (Leica, Wetzlar, Germany).

Flow cytometric studies

Flow cytometry using annexin V-FITC and propidium iodide (PI) double staining was performed using the annexin V-FITC apoptosis detection kit (Jinmei Biotech Co, China). Cells were harvested, washed twice with cold PBS and resuspended at 1×10^6 cells/mL in 100 μL binding buffer (10 mmol/L Hepes/NaOH, pH 7.4, 140 mmol/L NaCl and 2.5 mmol/L $CaCl_2$). Annexin V-FITC (5 μL) and 10 μL PI (20 μg/mL) were added to the cell suspension (100 μL) in the dark followed by incubation at room temperature for 15 min in the dark and then mixed with 400 μL binding buffer, and flow cytometry (FACScalibur, Becton-Dickison, USA) was carried out within 1 h. Data analysis was performed using the Modifit Flow Cytometry Software.

Western blotting studies

HUVECs were lysed using RIPA lysis buffer containing 50 mmol/L Tris-HCl (pH 7.4), 150 mmol/L NaCl, 1% sodium deoxycholate, 1% NP-40, 1 mmol/L phenylmethylsulfonyl fluoride and 1 mmol/L EDTA. Protein concentration was determined by Bradford assay (Bio-Rad, USA). Samples containing 10 μg total protein were resolved by 12% sodium dodecyl sulfate polyacrylamide gel electrophoresis (SDS-PAGE) and then electrophoretically transferred to a polyvinylidene difluoride membrane. The membranes were incubated with 5% non-fat dried milk in TBS-Tween 20 (10 mmol/L Tris-buffered saline with 0.1% Tween 20) at room temperature for 1 h, and then incubated with anti-phospho-S473 Akt polyclonal antibody, anti-Bcl-2 polyclonal antibody, or anti-Bax polyclonal antibody (ABZOOM, USA) overnight at 4 °C. After incubation with goat anti-rabbit horseradish peroxidase-conjugated secondary antibody (Santa Cruz Biotechnology, USA) for 2 h at room temperature, the immune complexes were visualized by enhanced chemiluminescence methods. Band intensity was analyzed by the Scion Image software and compared with the internal standard β-actin.

Caspase-3 activity assay

Caspase-3 activity was assessed via a colorimetric assay according to the manufacturer's protocols (BD Biosciences, USA). After treatment, the cells were collected by trypsinization and washed twice with ice-cold PBS followed by centrifugation. The cellular pellet was resuspended in cell lysis buffer and incubated on ice for 10 min. Lysates were centrifuged for 1 min at 10000 revolutions per minute, and the supernatants were assayed for caspase-3 activity in reaction buffer/DTT Mix. After addition of caspase-3 substrate (Ac-DEVD-pNA), samples were incubated for 4 h at 37 °C and caspase-3 activity (pNA) was measured by a spectrofluorometer (Bio-Rad, USA) at 405 nm. Caspase-3 activity was expressed as the fold of the control.

RT-PCR analysis

The cells were harvested after AA treatment and washed twice in cold PBS. Total RNA was extracted using the TRIzol reagent (Invitrogen, USA) according to the manufacturer's instructions and RNA was dissolved in RNase-free water. The concentration and purity of RNA were determined using a UV300 spectrophotometer at 260 nm and 280 nm. Complementary DNA (cDNA) was synthesized in a volume of 20 μL with a cDNA synthesis kit (Takara Biotechnology, China) according to the manufacturer's protocol. The obtained cDNA was amplified by PCR. The sequences of primers used were: 5′-TAATTGCCAAGCACCGCTTC-3′ (sense) and 5′-CCAGGTATGCATCATGTGAG-3′ (antisense) for Bcl-2; 5′-AGTAACATGGAGCTGCAGAG-3′ (sense) and 5′-ACAAAGATGGTCACGGTCTG-3′ (antisense) for Bax; 5′-TCTACAATGAGCTGCGTGTG-3′ (sense) and 5′-GGATGTCCACGTCACACTTC-3′ (antisense) for β-actin. The PCR conditions were: 95 °C for 2 min; 30 cycles of 95 °C for 45 s, 55 °C for 45 s, and 72 °C for 1 min, followed by a final extension at 72 °C for 7 min. The amplified PCR products were separated by 1.5% agarose (Amersco, USA) gel electrophoresis and visualized by ethidium bromide staining. Bcl-2 and Bax levels were normal-

ized against β-actin.

Statistical analysis

The data were expressed as mean±SD. All data were analyzed using the SPSS13.0 program (SPSS Inc, Chicago, IL, USA), and statistical differences were determined by paired sample *t*-test or one way ANOVA-test (SNK post test). $P<0.05$ was considered statistically significant.

Results

AA reduces viabilities

Prior to the investigation of the toxic effect of AA on HUVECs, we sought to understand the effect of AA on cell viability by MTT assay. The cells were exposed to 5, 10, or 20 μg/mL AA for 12, 24, and 48 h, respectively. As shown in Figure 1, AA significantly inhibited cell viability compared to controls in a dose- and time-dependent manner.

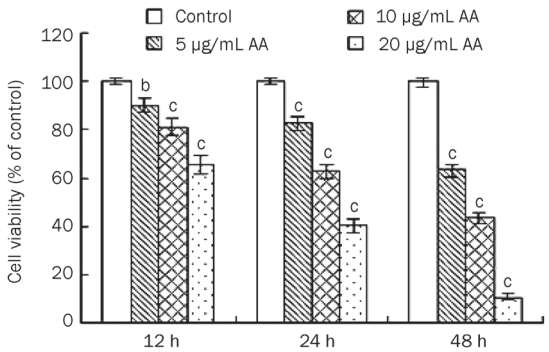

Figure 1. Effect of AA on the viability of HUVECs measured by the MTT assay. Mean±SD. $n=5$. $^bP<0.05$, $^cP<0.01$ for the AA group *vs* the control group.

AA induces apoptosis of HUVECs

To further examine morphological changes in response to AA, both control and AA-treated cells were stained with fluorescent dye Hoechst 33528 and visualized under a fluorescent microscope. Figure 2A shows the results of Hoechst 33528 staining for AA treated-cells at the concentrations of 5, 10, or 20 μg/mL for 24 h. The untreated cells stained uniformly blue. At 5 μg/mL AA, cells began to display apoptotic morphology. Fluorescence was detected in the nuclear region of HUVECs, indicating the presence of DNA fragmentation. At 10 and 20 μg/mL of AA, nuclear condensation and fragmentation became more apparent. The chromatin was condensed into lumps, exhibiting punctuated morphology typical of apoptotic cells. These observations provided evidence that AA induced apoptosis in HUVECs.

To gain further insight into the pro-apoptotic effect of AA on HUVECs quantitatively, we examined the percentage of apoptotic cells exposed to AA by flow cytometry using annexin V-FITC and PI staining. The percentage of apoptotic cells was 6.64%±0.78% in the control. After treatment with 5, 10, or 20 μg/mL AA for 24 h, the percentage of apoptotic cells

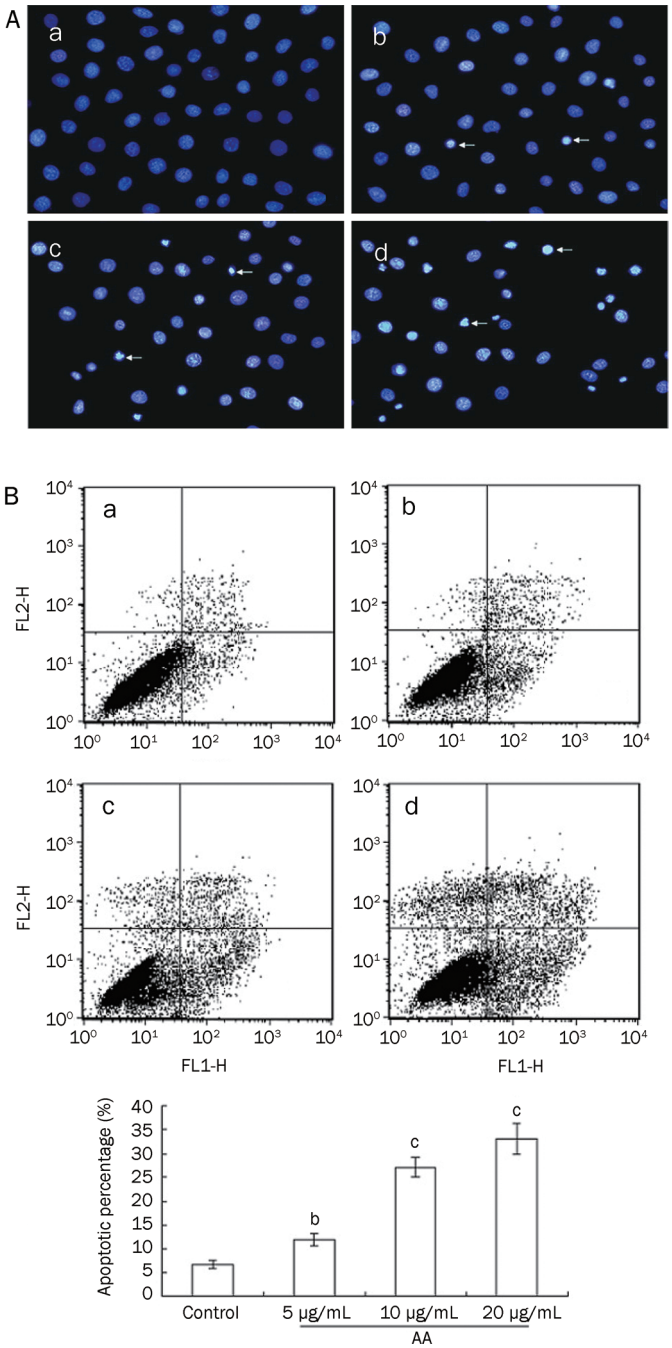

Figure 2. (A) The morphological changes of HUVECs detected by Hoechst 33258 staining. (a) Control; (b) 5 μg/mL AA; (c) 10 μg/mL AA; (d) 20 μg/mL AA. (B) The apoptotic percentage of HUVECs measured by flow cytometry. (a) Control; (b) 5 μg/mL AA; (c) 10 μg/mL AA; (d) 20 μg/mL AA. Mean±SD. $n=5$. $^bP<0.05$, $^cP<0.01$ for the AA group *vs* the control group. X-axis represents annexin V-FITC staining and y-axis represents PI staining. Left lower quadrant means annexin V-FITC and PI negative. Right lower quadrant means annexin-V FITC positive and PI negative. Right superior quadrant means annexin V-FITC and PI positive. Left superior quadrant means PI positive. Viable cells were annexin V-FITC and PI negative, cells in early-stage apoptosis were annexin-V FITC positive and PI negative, cells in late-stage apoptosis were annexin V-FITC and PI positive, dead cells were PI positive. The cells in early and late-stage apoptosis were defined as apoptotic.

increased to 11.79%±1.29%, 27.79%±2.56%, and 32.33%±3.82%, respectively. Significant difference was observed between AA treated cells and controls (P<0.05 or P<0.01) (Figure 2B).

AA suppresses the activation of Akt

To explore the possible mechanism for the pro-apoptotic effect of AA, we investigated the effect of AA on Akt activation. Western blotting studies using anti-phospho-S473 Akt antibodies analysis showed that AA (10 μg/mL) inhibited the activation of Akt in HUVECs after 15, 30, 60, or 120 min of drug exposure, with the minimum activation at approximately 30 min (Figure 3A). In addition, as indicated in Figure 3B, AA also inhibited Akt activation at 30 min in a dose-dependent manner at doses ranging from 5 to 20 μg/mL. We further tested the effect of PI3K specific inhibitors LY294002 or wortmannin on AA-induced Akt inactivation in HUVECs. The results showed that pretreatment with LY294002 or wortmannin for 30 min prior to stimulation with AA (10 μg/mL) for 30 min attenuated the inhibitory effect of AA on Akt activation, suggesting that the effect of AA on Akt inactivation was mediated through the PI3K/Akt signaling pathway (Figure 3C).

AA activates caspase-3 via the PI3K/Akt pathway

We further measured caspase-3 activity of HUVECs exposed to AA. As shown in Figure 4, a marked increase in caspase-3 activity was observed in cells incubated with 10 μg/mL AA for 24 h (1.645±0.076 *vs* 1.000±0.037 for the control, P<0.01), and the increase was attenuated when LY294002 (1.263±0.045 *vs* 10 μg/mL AA, P<0.01) or wortmannin (1.205±0.047 *vs* 10 μg/mL AA, P<0.01) was added before AA treatment, suggesting that AA induced apoptosis of HUVECs through the PI3K/Akt signaling pathway.

AA down-regulates the expression of Bcl-2

To further explore the possible mechanism of the pro-apoptotic effect of AA, we investigated the effect of AA on the expression of anti-apoptotic gene Bcl-2 in HUVECs. Exposure to 5, 10 or 20 μg/mL AA for 24 h decreased the level of Bcl-2 protein expression in HUVECs to 0.57±0.032, 0.44±0.028 or 0.35±0.031, respectively, which was significantly lower than that of controls (0.65±0.026) (P<0.05 or P<0.01) (Figure 5A).

We further detected the effect of AA on the expression of Bcl-2 mRNA. Treatment with various concentrations of AA (5, 10, 20 μg/mL) for 24 h significantly reduced the expressions of Bcl-2 mRNA (0.58±0.037, 0.42±0.03 and 0.36±0.024, respectively) compared with the controls (0.66±0.022) (P<0.05 or P<0.01) (Figure 5B).

AA up-regulates the expression of Bax

The Bax/Bcl-2 family are important apoptotic regulating factors in the intrinsic apoptotic pathway and the ratio of Bax/Bcl-2 is critical to cell survival. We next determined the expression of Bax protein by Western blotting. Following a 24-h treatment with 5, 10, or 20 μg/mL AA, we detected increased levels of the Bax protein (0.38±0.022, 0.56±0.032, and 0.45±0.028, respectively) compared with the control

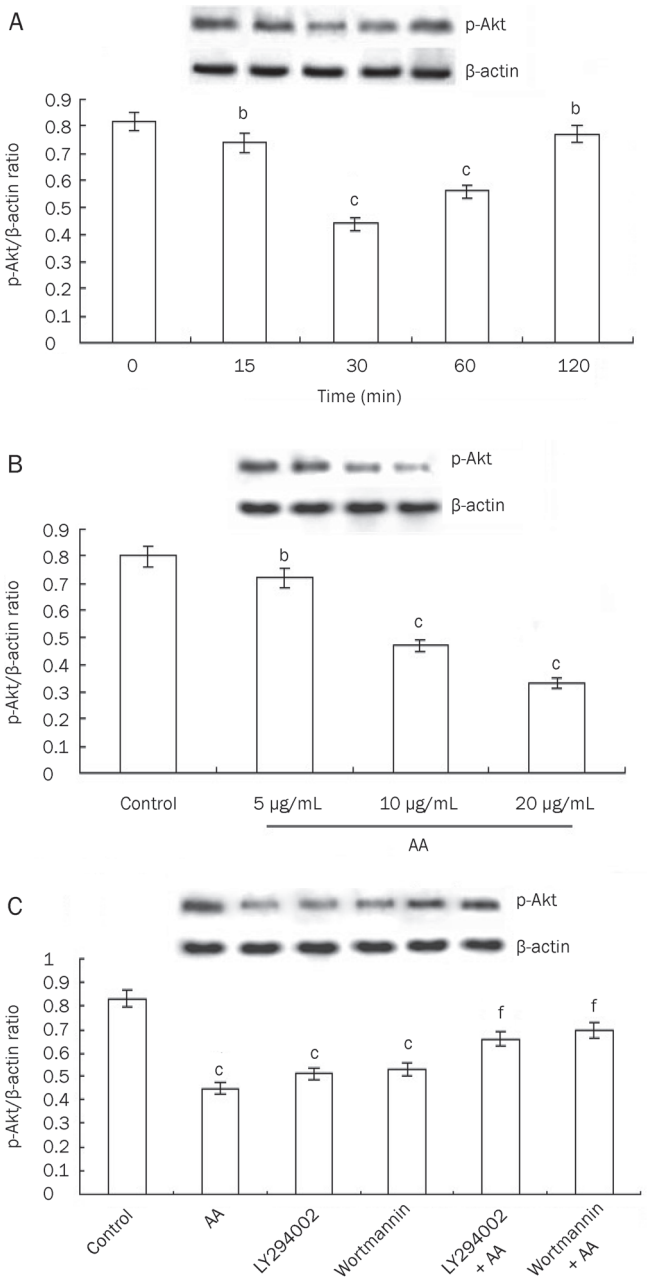

Figure 3. Phosphorylated Akt in HUVECs detected by Western blotting. (A) 10 μg/mL AA for 0, 15, 30, 60, or 120 min; (B) 5, 10 and 20 μg/mL AA for 30 min; (C) effects of LY294002 and wortmannin on phospho-Akt expression induced by AA in HUVECs. Mean±SD. n=5. ^bP<0.05, ^cP<0.01 for the AA group *vs* the control group; ^fP<0.01 for the LY294002+AA group and wortmannin+AA group *vs* the AA group.

(0.32±0.027). There was a significant difference in Bax expression levels between AA-induced cells and the control (P<0.05 or P<0.01, Figure 6A).

This study also detected the effect of AA on the expression of Bax mRNA. The results showed that the expression of Bax mRNA stimulated by AA (5, 10, or 20 μg/mL) for 24 h was significantly increased (0.41±0.031, 0.55±0.038 and 0.48±0.023, respectively) compared with that of the control (0.35±0.024)

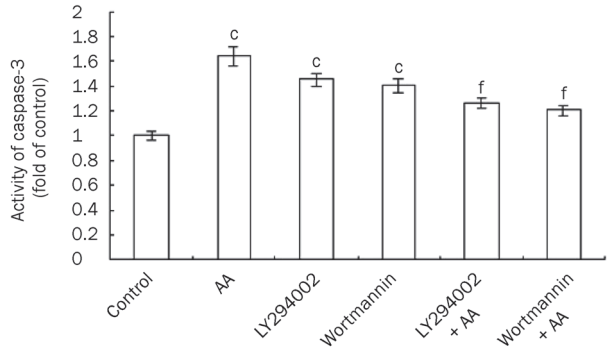

Figure 4. Caspase-3 activity of HUVECs determined by the colorimetric method. Mean±SD. n=5. ^{c}P<0.01 for the AA group *vs* control group; ^{f}P<0.01 for the LY294002+AA group and the wortmannin+AA group *vs* the AA group.

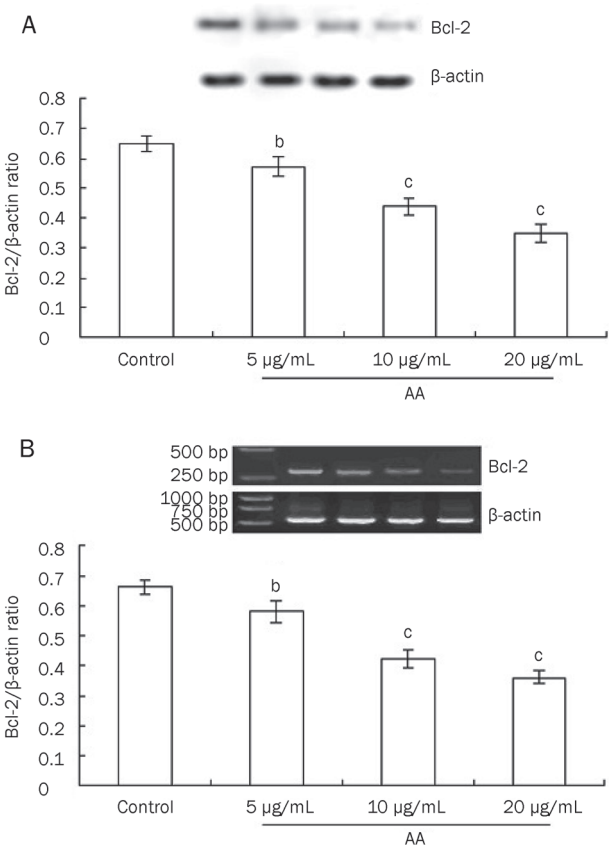

Figure 5. (A) The expression of Bcl-2 protein detected by Western blotting. (B) The expression of Bcl-2 mRNA detected with RT-PCR. Mean±SD. n=5. ^{b}P<0.05, ^{c}P<0.01 for the AA group *vs* the control group.

(P<0.05 or P<0.01, Figure 6B).

Discussion

Many Chinese medicinal herbs contain AA, which has been extensively used to treat digestive and urogenital system diseases. AA reacts with cellular proteins and DNA, resulting in multiple forms of toxicity[21]. AAN is a progressive tubulointerstitial renal disease caused by AA intake. Progressive loss of peritubular capillaries was demonstrated in AAN model, which was associated with decreased expression of VEGF[22]. Recently, VEGF has emerged as a crucial element in vascular homeostasis. VEGF is an angiogenic factor and an endothelial cell survival factor[6]. Withdrawal of VEGF by targeted inactivation of the VEGF gene results in massive endothelial cell apoptosis[9, 10]. Vascular endothelial cells form the inner lining of all blood vessels and play an important role in regulating vascular function. Since the vascular endothelium is involved in various physiological processes, endothelial cell apoptosis (and dysfunction) may constitute an initial step in a variety of pathological situations such as atherosclerosis and hypertension. The data document the inhibitory effect of AA on vessel development indirectly. The direct effects of AA on vascular endothelial cells are unclear. Our study showed that AA could induce endothelial cell apoptosis and increase activation of caspase-3. Moreover, we determined the signaling pathway involved in the pro-apoptotic effect of AA: we found that exposure of cells to AA or the PI3K inhibitor (wortmannin or LY294002) alone could likewise cause inactivation of Akt, and pretreatment with PI3K inhibitor (LY294002 or wortmannin) to block primarily the PI3K/Akt pathway before AA treatment could attenuate the effect of AA on the activation of Akt and

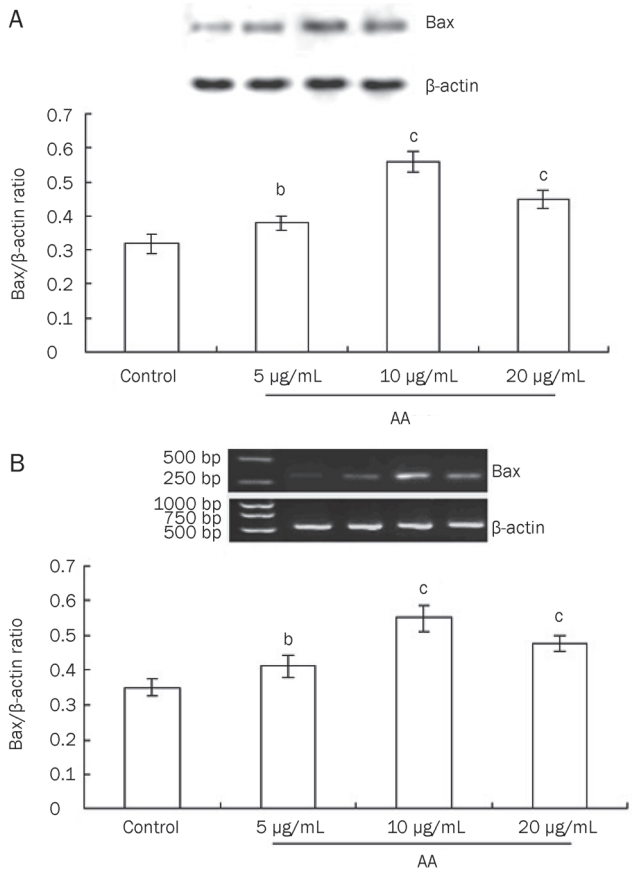

Figure 6. (A) The expressions of Bax protein detected by Western blotting. (B) The expression of Bax mRNA by RT-PCR. Mean±SD. n=5. ^{b}P<0.05, ^{c}P<0.01 for the AA group *vs* the control group.

caspase-3 activity, suggesting that AA-induced endothelial cell apoptosis may be, at least partly, through inhibiting the PI3K/Akt signaling pathway. Akt, also known as protein kinase B (PKB), was recognized as a major downstream target of PI3K[23]. The full activation of Akt requires phosphorylation at both Thr 308 and Ser 473. VEGF inhibits endothelial cell apoptosis through activating the PI3K/Akt signal pathway[6, 11, 12]. In endothelial cells, Akt activation has been reported to promote cell survival[15]. LY294002 and wortmannin are two broad-specific inhibitors of P13K. They can completely inhibit PI3K activity, thereby blocking the activation of Akt. Our study directly observed Akt (Ser 473) phosphorylation after treatment with AA. The results of our study indicated that AA has a pro-apoptotic effect on endothelial cells, and, at least partly, via blocking PI3K/Akt pathway.

Moreover, there was evidence that VEGF prevents the apoptosis of endothelial cells via up-regulating the expression of anti-apoptotic gene *Bcl-2*[20]. The Bcl-2 family play a crucial role in the control of apoptosis. The Bcl-2 family of proteins contain both inhibitors (Bcl-2, Bcl-x_L) and inducers (Bcl-x_S, Bax, Bid, Bad, Bak) of apoptosis. The balance between anti-apoptotic and pro-apoptotic Bcl-2 family members is critical to determining if a cell undergoes apoptosis. In the present study, we observed that AA could reduce Bcl-2 expression and improve Bax expression. The level of Bax protein expression was significantly decreased in cells incubated with 20 μg/mL AA; the explanation could be the massive necrosis.

Our study demonstrates that AA can cause the apoptosis of endothelial cells. This apoptosis may be related to the inhibition of PI3K/Akt signaling pathway and modulating the ratio of Bcl-2 and Bax.

Acknowledgements

We wish to thank the Tumor Research Institute of China Medical University for its valuable help.

Author contribution

Jiang-min FENG and Hong SHI designed the research; and Hong SHI performed the research, analyzed the data and wrote the manuscript.

References

1 Depierreux M, Van Damme B, Vanden Houte K, Vanherweghem JL. Pathologic aspects of a newly described nephropathy related to the prolonged use of Chinese herbs. Am J Kidney Dis 1994; 24: 172–80.
2 Yang L, Li XM, Wang SX, Wang HY. Peritubular capillary injury in Chinese herb guan-mu-tong-induced acute tubular necrosis. Zhonghua Nei Ke Za Zhi 2005; 44: 525–9.
3 Yang L, Li X, Wang H. Possible mechanisms explaining the tendency towards interstitial fibrosis in aristolochic acid-induced acute tubular necrosis. Nephrol Dial Transplant 2007; 22: 445–56.
4 Sun D, Feng JM, Dai C, Sun L, Jin T, Wang ZQ, *et al*. Influence of hypoxia caused by impairment of peritubular capillary on the progression of chronic aristolochic acid nephropathy. Zhonghua Yi Xue Za Zhi 2006; 86: 1464–9.
5 Ferrara N, Houck K, Jakeman L, Leung DW. Molecular and biological properties of the vascular endothelial growth factor family of proteins. Endocr Rev 1992; 13: 18–32.
6 Gerber HP, McMurtrey A, Kowalski J, Yan M, Keyt BA, Dixit V, *et al*. Vascular endothelial growth factor regulates endothelial cell survival through the phosphatidylinositol 3′-kinase/Akt signal transduction pathway. Requirement for Flk-1/KDR activation. J Biol Chem 1998; 273: 30336–43.
7 Fujio Y, Walsh K. Akt mediates cytoprotection of endothelial cells by vascular endothelial growth factor in an anchorage-dependent manner. J Biol Chem 1999; 274: 16349–54.
8 Araki S, Simada Y, Kaji K, Hayashi H. Role of protein kinase C in the inhibition by fibroblast growth factor of apoptosis in serum-depleted endothelial cells. Biochem Biophys Res Commun 1990; 172: 1081–5.
9 Carmeliet P, Ferreira V, Breier G, Pollefeyt S, Kieckens L, Gertsenstein M, *et al*. Abnormal blood vessel development and lethality in embryos lacking a single VEGF allele. Nature 1996; 380: 435–9.
10 Ferrara N, Carver-Moore K, Chen H, Dowd M, Lu L, O'Shea KS, *et al*. Heterozygous embryonic lethality induced by targeted inactivation of the VEGF gene. Nature 1996; 380: 439–42.
11 Kim I, Kim HG, So JN, Kim JH, Kwak HJ, Koh GY. Angiopoietin-1 regulates endothelial cell survival through the phosphatidylinositol 3′-Kinase/Akt signal transduction pathway. Circ Res 2000; 86: 24–9.
12 Dimmeler S, Zeiher AM. Akt takes center stage in angiogenesis signaling. Circ Res 2000; 86: 4–5.
13 Khwaja A. Akt is more than just a Bad kinase. Nature 1999; 401: 33–4.
14 Dimmeler S, Fleming I, Fisslthaler B, Hermann C, Busse R, Zeiher AM. Activation of nitric oxide synthase in endothelial cells by Akt-dependent phosphorylation. Nature 1999; 399: 601–5.
15 Fulton D, Gratton JP, McCabe TJ, Fontana J, Fujio Y, Walsh K, *et al*. Regulation of endothelium-derived nitric oxide production by the protein kinase Akt. Nature 1999; 399: 597–601.
16 Dimmeler S, Haendeler J, Nehls M, Zeiher AM. Suppression of apoptosis by nitric oxide via inhibition of interleukin-1beta-converting enzyme (ICE)-like and cysteine protease protein (CPP)-32-like proteases. J Exp Med 1997; 185: 601–8.
17 Papapetropoulos A, Fulton D, Mahboubi K, Kalb RG, O'Connor DS, Li F, *et al*. Angiopoietin-1 inhibits endothelial cell apoptosis via the Akt/survivin pathway. J Biol Chem 2000; 275: 9102–5.
18 O'Connor DS, Schechner JS, Adida C, Mesri M, Rothermel AL, Li F, *et al*. Control of apoptosis during angiogenesis by survivin expression in endothelial cells. Am J Pathol 2000; 156: 393–8.
19 Tran J, Rak J, Sheehan C, Saibil SD, LaCasse E, Korneluk RG, *et al*. Marked induction of the IAP family antiapoptotic proteins survivin and XIAP by VEGF in vascular endothelial cells. Biochem Biophys Res Commun 1999; 264: 781–8.
20 Gerber HP, Dixit V, Ferrara N. Vascular endothelial growth factor induces expression of the antiapoptotic proteins Bcl-2 and A1 in vascular endothelial cells. J Biol Chem 1998; 273: 13313–6.
21 Chen T, Guo L, Zhang L, Shi L, Fang H, Sun Y, *et al*. Gene expression profiles distinguish the carcinogenic effects of aristolochic acid in target (kidney) and non-target (liver) tissues in rats. BMC Bioinformatics 2006; 7: S20.
22 Sun D, Feng J, Dai C, Sun L, Jin T, Ma J, *et al*. Role of peritubular capillary loss and hypoxia in progressive tubulointerstitial fibrosis in a rat model of aristolochic acid nephropathy. Am J Nephrol 2006; 26: 363–71.
23 Burgering BM, Coffer PJ. Protein kinase B (c-Akt) in phosphatidylinositol-3-OH kinase signal transduction. Nature 1995; 376: 599–602.

Acta Pharmacologica Sinica (2011) 32: 1031–1037
 1671-4083/11 $32.00
www.nature.com/aps

Original Article

Combination of raloxifene, aspirin and estrogen as novel paradigm of hormone replacement therapy in rabbit model of menopause

Fa-lin YANG[1, #], Ke-qing HU[2, #], Xin WANG[3, #], Zi-mo LIU[4], Qin HU[4], Ji-fu LI[4], Hong HE[4, *]

[1]Clinical Laboratory, Qilu Hospital, Shandong University, Ji-nan 250012, China; [2]Department of Cardiology, Ji-nan Central Hospital Affiliated to Shandong University, Ji-nan 250012, China; [3]Department of Internal Medicine, the Second Affiliated Hospital, Shandong University, Ji-nan 250012, China; [4]Key Laboratory of Cardiovascular Remodeling and Function Research, Chinese Ministry of Education and Chinese Ministry Of Health, and Department of Cardiology, Qilu Hospital, Shandong University, Ji-nan 250012, China

Aim: To assess a novel hormone replacement therapy (HRT) paradigm using raloxifene, aspirin combined with estrogen in rabbit model of menopause.
Methods: Female New Zealand white rabbits were ovariectomized or sham-operated. The ovariectomized rabbits were divided into 7 groups: estradiol valerate (E_2), raloxifene, aspirin, E_2 /raloxifene, E_2/aspirin, E_2 /raloxifene/aspirin and vehicle. Two weeks after the operation, the rabbits were administered the above drugs for 12 weeks. Then, the mammary glands were examined histologically, uterus was weighted, and blood sample was collected for analyzing the levels of estrogen, serum lipids and monocyte chemoattractant protein (MCP)-1, and platelet aggregation. The aortic tissue was examined morphometrically.
Results: Compared with E_2 0.1 mg·kg^{-1}·d^{-1} treatment alone, the pairing of raloxifene 10 mg·kg^{-1}·d^{-1} with E_2 significantly decreased the extent of mammary gland branches and ducts (5.53%±1.23% *vs* 15.4%±2.17%, P<0.01), as well as the uterine weight (2.16±0.35 g *vs* 4.91±0.75 g, P<0.01). However, E_2/raloxifene or E_2 alone treatment significantly stimulated platelet aggregation relative to vehicle group. Addition of aspirin 5 mg·kg^{-1}·d^{-1} reduced platelet aggregation to almost the same level as the vehicle group. E_2 treatment exerted a positive effect on serum lipids and MCP-1, and a regression in aortic intimal plaque size compared to the vehicle. Raloxifene reinforced the positive effects of E_2.
Conclusion: The combination of raloxifene, aspirin and E_2 exhibits positive lipid, MCP-1 and atherosclerotic responses with minimal stimulation of breast and uterine tissues as well as platelet aggregation in a rabbit model of the menopause.

Keywords: estrogen; raloxifene; aspirin; atherosclerosis; hormone replacement therapy

Acta Pharmacologica Sinica (2011) 32: 1031–1037; doi: 10.1038/aps.2011.87; published online 18 Jul 2011

Introduction

The beneficial effects of estrogen are well described and include reductions in low density lipoprotein cholesterol (LDL-C) and inflammatory cytokines, such as monocyte chemoattractant protein-1 (MCP-1), an increase in high density lipoprotein cholesterol (HDL-C), and enhanced vascular function, amongst others[1–3]. In animal models, estrogen has been reported to reduce atherosclerosis[4] and a clinical study also demonstrated a lower calcified plaque burden in the coronary arteries of postmenopausal women aged 50 to 59 years old assigned to estrogen therapy than in those assigned to placebo[5]. However, estrogen therapy has also been reported to be linked with an increased risk of tissue-specific side effects, including uterine endometrial hyperplasia, which may result in uterine cancer, and proliferative effects on mammary tissue, which may result in an increased risk of breast cancer[6, 7]. The ideal hormone replacement therapy (HRT) should reproduce the beneficial effects of estrogen without producing these adverse responses. This concept has led to the development of HRT with combined estrogen and progestin, with progestin serving to reverse the endometrial hyperplasia induced by estrogen. However, findings from randomized placebo-controlled trials in postmenopausal women do not support any cardiovascular benefits of estrogen plus progestin, and demonstrate an increase in the risk of breast cancer[8, 9]. Although

These three authors contribute to the paper equally.
* To whom correspondence should be addressed.
E-mail hehong@medmail.com.cn
Received 2011-01-01 Accepted 2011-05-19

the role of progestin remains poorly defined, preclinical and clinical studies have suggested that the co-administration of progestin may oppose the cardioprotective effects of estrogen[10–12]. Furthermore, progestin has no anti-estrogenic effect on mammary tissue and, as a result, women on combined estrogen-progestin treatment had an increase in the relative risk for breast cancer[8, 9].

Continued efforts to provide efficacious HRT with improved safety and tolerability for postmenopausal women have generated interest in the development of selective estrogen receptor (ER) modulators (SERMs). Estrogen typically exhibits an ER agonist effect in all tissues, whereas SERMs demonstrate mixed functional activity (ER agonist/antagonist) depending on the target tissue[13]. To date, no SERM alone has been able to achieve an ideal balance of ER agonist and antagonist activity for an optimal postmenopausal therapy. However, it may be possible to achieve optimal results based on the blended tissue-selective activities of a SERM and estrogen in a novel approach.

The SERM chosen in this study to test our hypothesis was raloxifene, as it has been confirmed to have estrogen agonist effects on lipids and estrogen antagonist effects on the breast and uterus[14, 15]. It is also the only SERM being specifically studied for its effects on coronary heart disease events in a prospective randomized controlled trial, which demonstrated that the incidence of coronary events was significantly lower in postmenopausal women <60 years of age assigned to raloxifene compared with those assigned to the placebo[16]. Although raloxifene has been reported to be associated with an increased incidence of vasomotor symptoms[17, 18], a previous study confirmed that combined use of 17β-estradiol with raloxifene was able to decrease the frequency of vasomotor symptoms in comparison with raloxifene treatment alone[19]. Based on these observations, the pairing of raloxifene with estrogen may represent an attractive therapeutic option.

However, estrogen has been reported to increase the risk of venous thrombosis and arterial thrombotic events, such as stroke[20–22]. Aspirin, one of the most widely used blood-thinning agents in the world, is used long-term in low doses to prevent heart attacks, strokes and blood clot formation in people at high risk for these events. In animal tests, low-dose aspirin has been shown to have a preventive effect on thrombus formulation[23] and in a clinical trial, it has been shown to prevent deep venous thrombosis and pulmonary embolism in patients postoperatively[24].

Therefore, based on the available evidence, it may be postulated that combined use of raloxifene and aspirin with estrogen might serve as a new treatment paradigm for HRT. To determine whether this regimen would result in a physiological profile that was distinct from that of estrogen alone, we evaluated breast, uterine, platelet aggregation, lipid, MCP-1 and atherosclerotic lesion responses in a rabbit model of the menopause.

Materials and methods

Eighty healthy and sexually mature (age, 3 months; weight, 2.25±0.20 kg) female New Zealand White rabbits (Agricultural Sciences Institute Products; Ji-nan, China) were used in the present study. The rabbits were housed individually in standard rabbit cages with a room temperature of 20±2 ^{o}C and 12-h light cycle. After 2 weeks of acclimation, bilateral ovariectomies were performed in 70 rabbits under general anesthesia (sodium pentobarbital 30 mg/kg, intravenously). All rabbits subsequently received a 1.5% cholesterol diet for 12 weeks. The rabbits were randomized into seven groups of 10 rabbits: (A) a placebo-control group receiving vehicle control (saline: 2% Tween 80, 0.5% methylcellulose; OVX+Veh group); (B) estradiol valerate (E_2, Delpharm Lille SAS, Lyslez-Lannoy, France) 0.1 mg·kg^{-1}·d^{-1} (OVX+E_2 group); (C) raloxifene hydrochloride (Lilly SA, Madrid, Spain) 10 mg·kg^{-1}·d^{-1} (OVX+Ral group); (D) aspirin (Huanghai Company, Shandong, China) 5 mg·kg^{-1}·d^{-1} (OVX+ASA group); (E) raloxifene paired with E_2 (OVX+E_2+Ral group); (F) aspirin paired with E_2 (OVX+E_2+ASA group); and (G) raloxifene and aspirin in combination with E_2 (OVX+E_2+Ral+ASA group). Compounds were administered orally in a saline vehicle to the rabbits. The dose of E_2 (0.1 mg·kg^{-1}·d^{-1}) selected was the dose commonly used for research, which has been shown not to cause serious disorders in the major organs of cholesterol-fed rabbits[25]. The dose of raloxifene (10 mg·kg^{-1}·d^{-1}) was chosen based on previous pharmacokinetic data that showed this dosage generates a plasma raloxifene concentration comparable with that observed in clinical settings and which reduces aortic accumulation of cholesterol in rabbits[26]. Furthermore, it has been reported that, at a dose of 10 mg·kg^{-1}·d^{-1}, raloxifene is able to counteract the effects of 0.1 mg·kg^{-1}·d^{-1} of E_2 and maintain the uterine weight at levels that are indistinguishable from those of vehicle-treated controls in animal tests[27]. Aspirin was used at an antithrombotic dosage (5 mg·kg^{-1}·d^{-1}). One group of 10 rabbits was sham-operated, and also received a 1.5% cholesterol diet but no hormone treatment (sham group). The study protocol was approved by the Animal Care Committee of Shandong University, China and was performed according to the Guidelines for the Use of Experimental Animals by the Ministry of Health, China.

At the end of study, the rabbits were sacrificed after 12 h of fasting. Breast tissue specimens were fixed in 10% neutral buffered formalin, routinely processed, paraffin embedded, sectioned and stained with hematoxylin and eosin. The percentage of the extent of gland branches and ducts in the mammary gland was determined using a computer-based quantitative color image analysis system Ipp6.0 (Media Cybernetics, Bethesda, MD, USA). The acquisition of images and analysis of gland branches and ducts were performed in a blinded fashion. Uteri were excised and weighed after removal of associated fat and luminal fluids.

Platelet-rich plasma (PRP) was separated from acid citrate dextrose-anticoagulated blood. Purity of PRP was validated by Coulter counter (Qilu Hospital Hematology Laboratory, Shandong, China), yielding <0.1% of leukocyte or red blood cell contamination. The concentration of PRP was adjusted to 5×10^5/μL. Platelet aggregation to adenosine diphosphate

(ADP, 10 μmol/L) was performed in PRP by a turbidimetric method using a whole-blood aggregometer in optical mode (Model No 560-CA, Chrono-log, Havertown, PA, USA).

Serum collected from the rabbits underwent E_2 measurement using enzyme-linked immunoassay (ELISA). The ELISA kits were purchased from DRG International Inc (Mountainside, NJ, USA) and the experiments were performed following manufacturer's protocol. The laboratory personnel that performed this assay were blinded with respect to any information concerning the study groups. All samples were run in duplicate and the mean values for each sample were used in the analysis. For quality control purposes, positive controls containing known amounts of E_2 were included in each batch. This also ensured that the assay values did not dramatically shift over time. The sensitivity was 1.4 pg/mL, the intra-assay co-efficient of variation and inter-assay coefficient of variation for all assays were <5%.

The biochemical evaluation of serum lipids was carried out in the same laboratory as the other tests in this study. The laboratory adhered to the criteria of the World Health Organization Lipid Reference Laboratories. All biochemical examinations (serum total cholesterol, HDL-C and triglycerides) were carried out using a chromatographic enzymatic method in a Technicon automatic analyzer HITACHI-7180 (Hitachi High-Technologies Corporation, Tokyo, Japan). Serum for the measurement of these lipids was harvested immediately after admission onto the study. LDL-C was calculated using the Friedwald formula: LDL-C=total cholesterol–HDL-cholesterol –(1/5) triglycerides[28]. The estimation of all lipids was rigorously quality-controlled by a consultant biochemist (KL), and frequently checked with the values of another reference laboratory. Inter-assay and intra-assay variabilities of estimations were kept at less than 5%.

For the measurement of serum MCP-1, a quantitative sandwich enzyme immunoassay from R&D systems (Abingdon, UK) was used, where a monoclonal antibody specific for MCP-1 had been pre-coated onto a microplate. Briefly, assay diluent RD1A plus standard or sample was added to each well and left to incubate for 2 h at room temperature. The plates were washed four times to eliminate any unbound substances. Then, a conjugate (polyclonal antibody conjugated to horseradish peroxidase) was added to each well for detection of the cytokine. After a 2-h incubation at room temperature, the plates were washed four times and substrate solution was added to each well. A 20 min incubation at room temperature allowed color development in proportion to the amount of cytokine bound in the initial step. Finally, a stop solution was added to each well and the intensity of the coloring measured. The sensitivity was 5.0 pg/mL, the intra- and interassay variability was 4.8% and 5.8%, respectively.

The aorta was flushed with 250 mL of cold (4 °C) perfusion fixation (4% paraformaldehyde in phosphate buffered saline) at 100 mmHg, then removed from the aortic valve to the iliac bifurcation and carefully cleaned of adhering fat and connective tissue. The aorta was freed from the adventitia, opened longitudinally, pinned flat and fixed in 4% paraformaldehyde for 24 h, then rinsed with water, stained with Oil Red O solution for 4 h and rinsed with 70% alcohol. The percentage of aorta staining positively with Oil Red O was determined. Quantification was performed by capturing images of the aortas with a digital camera and analyzed using the Ipp6.0computer-based quantitative color image analysis system. A standard size of the aortic segment was used for all rabbits studied. The acquisition of images and analysis of lesions were always performed in a blinded fashion.

Data were expressed as mean±SEM. Inter-group treatment comparisons were performed with one-way ANOVA with the Dunnett test. All analyses were performed using SPSS 13.0 software (SPSS, Inc, Chicago, IL, USA). A *P*-value of 0.05 or less was considered statistically significant (two-sided).

Results

In the OVX rabbit model, an estrogenic stimulatory response was found with E_2 treatment in breast tissue. In the OVX+E_2 group, the alveoli and ducts were dilated to a variable extent, and the percentage of the extent of gland branches and ducts in the mammary glands increased significantly compared to the OVX+Veh group (15.4%±2.17% *vs* 4.88%±1.15%, $P<0.01$). No estrogenic responses were found in the OVX+Ral group, when raloxifene was co-administered with E_2 at a dose of 10 $mg\cdot kg^{-1}\cdot d^{-1}$ (OVX+E_2+Ral group), breast stimulation induced by E_2 was reduced to vehicle control levels (5.53%±1.23% *vs* 4.88%±1.15%, $P>0.05$). No effect on breast tissue was found with aspirin compared to the OVX+Veh group (Figure 1).

In the OVX rabbit model, 12-week treatment with E_2 at 0.1 $mg\cdot kg^{-1}\cdot d^{-1}$ (OVX+E_2 group) demonstrated a significant increase in uterine weight, which is a surrogate measure for an estrogenic stimulatory response ($P<0.01$ *vs* OVX+Veh group). Associated morphological changes were also observed (data not shown). Specifically, E_2 resulted in an increase in luminal epithelial hypertrophy compared with vehicle control. No significant increase in uterine weight was found in OVX+Ral group compared to the OVX+Veh group (2.12±0.4 g *vs* 2.07±0.34 g, $P>0.05$), and when raloxifene was co-administered with E_2 (OVX+E_2+Ral group), the increase in uterine weight induced by E_2 was reduced to the levels of the vehicle control group (2.16±0.35 g *vs* 2.07±0.34 g, $P>0.05$) (Figure 2).

In the OVX rabbit model, 12-week treatment with E_2 (OVX+E_2 group) demonstrated a significant increase in whole-blood platelet aggregation compared to the OVX+Veh group (83.8%±6.94% *vs* 63.1%±8.45%, $P<0.05$). Aspirin (5 $mg\cdot kg^{-1}\cdot d^{-1}$) decreased the whole-blood platelet aggregation significantly compared to the vehicle control ($P<0.01$). When aspirin was co-administered with E_2 in OVX+E_2+ASA group, the stimulation in platelet aggregation induced by E_2 was reduced to almost the same levels as in the OVX+Veh group (64.5%±7.25% *vs* 63.1%±8.45%, $P>0.05$) (Figure 3).

The serum estradiol level was much higher in the estrogen-treated groups including OVX+E_2, OVX+E_2+Ral, OVX+E_2+ASA, and OVX+E_2+Ral+ASA, than in the OVX+Veh group ($P<0.01$). Dyslipidemia was improved in the estrogen and/or raloxifene-treated animals (OVX+E_2, OVX+E_2+Ral,

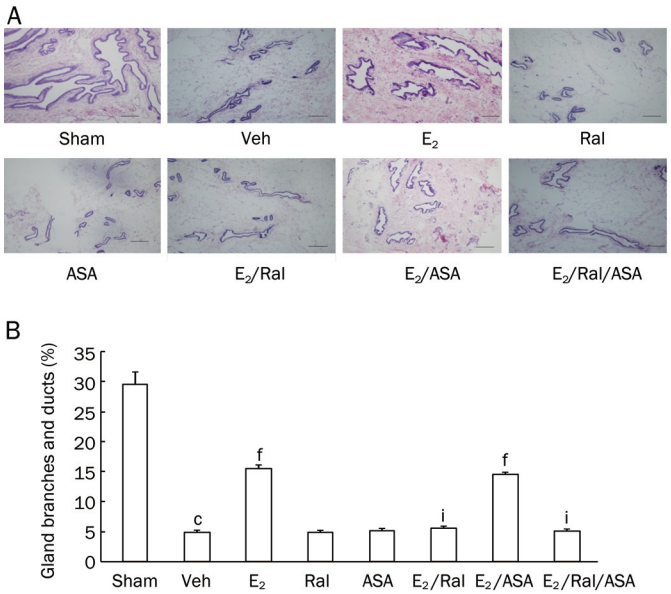

Figure 1. Breast response of E_2/raloxifene/aspirin in mature OVX rabbits. After 12 weeks of treatment, breast tissue responses to E_2 alone, raloxifene alone, aspirin alone, E_2 plus raloxifene, aspirin and E_2, aspirin paired with E_2 and combined raloxifene were analyzed (n=10 animals per treatment group). (A) In OVX rabbits, alveoli and ducts embedded in a loose fibrous stroma with varying amount of fat were variably dilated in the OVX+E_2 group, a regression of the parenchymal lobuloalveolar structures and a replacement of the loose fibrous tissue by fat and dense fibrous tissue were found in the OVX+E_2+Ral group. HE stain, Bar=200 μm. (B) The percentage of the extent of gland branches and ducts in the mammary glands. Mean±SEM. n=10. ^cP<0.01 relative to sham group; ^fP<0.01 relative to vehicle control; ^iP<0.01 relative to OVX+E_2 group. Veh, vehicle; E_2, estradiol valerate; Ral, raloxifene; ASA, aspirin.

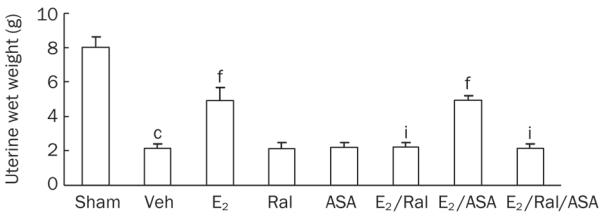

Figure 2. Uterine response of E_2/raloxifene/aspirin in mature OVX rabbits. After 12 weeks of treatment, uterine wet weights (g) in response to E_2 alone, raloxifene alone, aspirin alone, raloxifene paired with E_2, aspirin and E_2, aspirin paired with E_2 and combined raloxifene were determined. Compared with sham-operated rabbits, ovariectomy induced significant decreases in uterine wet weights. In OVX rabbits, a significant increase in uterine weight was observed in the OVX+E_2 group, no estrogenic stimulatory effect was found in the OVX+Ral group, when paired with E_2, raloxifene antagonized the E_2-induced increase in uterine wet weight to a level similar as that of vehicle control. Mean±SEM. n=10 animals per treatment group. ^cP<0.01 relative to sham group; ^fP<0.01 relative to vehicle control; ^iP<0.01 relative to OVX+E_2 group. Veh, vehicle; E_2, estradiol valerate; Ral, raloxifene; ASA, aspirin.

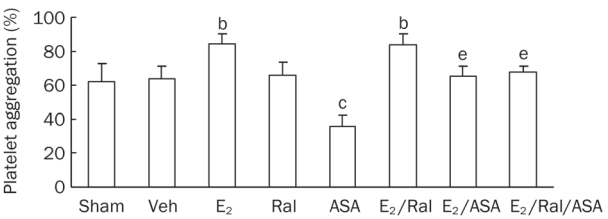

Figure 3. Platelet aggregation response of E_2/raloxifene/aspirin in mature OVX rabbits. After 12 weeks of treatment, whole-blood platelet aggregation (%) in response to E_2 (0.1 mg·kg^{-1}·d^{-1}), raloxifene (10 mg·kg^{-1}·d^{-1}), aspirin (5 mg·kg^{-1}·d^{-1}), raloxifene paired with E_2, aspirin and E_2, aspirin paired with E_2 and combined raloxifene were determined. A significant increase in platelet aggregation was observed in the OVX+E_2 and OVX+E_2+Ral groups, but not in the OVX+Ral group. Aspirin decreased the platelet aggregation significantly as compared to the vehicle control. When co-administered with E_2, the E_2-induced increase in platelet aggregation was reduced to a level with no difference to vehicle control. Mean±SEM. n=10 animals per treatment group. ^bP<0.05, ^cP<0.01 relative to vehicle control; ^eP<0.05 relative to OVX+E_2 group. Veh, vehicle; E_2, estradiol valerate; Ral, raloxifene; ASA, aspirin.

OVX+E_2+ASA, OVX+E_2+Ral+ASA, and OVX+Ral groups) compared to the vehicle-treated animals (OVX+Veh group). When raloxifene was co-administered with E_2, an approximate 15% greater reduction in total cholesterol and a 20% greater reduction in LDL-C relative to E_2 alone were observed. There were no significant differences in body weight gain before and after treatments (Table 1).

It has been reported that ovariectomy could induce an

Table 1. Changes in serum estradiol, lipids, and weight gain. Mean±SEM. n=10. ^cP<0.01 *vs* sham group. ^eP<0.05, ^fP<0.01 *vs* OVX+Veh group. ^hP<0.05 *vs* OVX+E_2 group.

	Sham	OVX+Veh	OVX+E_2	OVX+Ral	OVX+ASA	OVX+E_2+Ral	OVX+E_2+ASA	OVX+E_2+Ral +ASA
E_2 (pg/mL)	76.4±10.8	14.8±2.34^c	225.4±51.9^f	18.6±6.35	14.3±4.10	245.7±41.2^f	223.1±45.2^f	229.1±39.4^f
TC (mmol/L)	22.0±4.21	30.1±3.30^c	23.5±3.90^f	24.7±7.31^f	31.3±4.46	19.3±2.13^{fh}	22.6±3.75^f	18.2±3.58^{fh}
TG (mmol/L)	0.86±0.40	0.92±0.32	0.85±0.44	0.89±0.40	0.90±0.34	0.84±0.48	0.87±0.34	0.85±0.47
LDL-C (mmol/L)	17.1±5.30	26.4±5.03^c	16.7±6.23^f	20.1±6.61^e	25.4±7.81	13.4±3.76^{fh}	15.9±5.46^f	12.7±2.75^{fh}
HDL-C (mmol/L)	3.67±0.65	2.38±1.0^c	3.24±0.90^e	3.02±1.06^e	2.22±0.41	3.54±0.70^e	3.16±0.85^e	3.57±0.71^e
Body weight gain (kg)	0.94±0.12	0.78±0.09	0.82±0.10	0.84±0.08	0.76±0.07	0.87±0.11	0.75±0.07	0.80±0.06

TC, total cholesterol; TG, triglyceride; LDL-C, low density lipoprotein cholesterol; HDL-C, high density lipoprotein cholesterol.

increase in MCP-1 level[29], and in this study, a significant increase in MCP-1 level was observed after ovariectomy. In OVX rabbits, although reduction in MCP-1 level was not as profound as those associated with E_2 (approximately a 40% reduction *vs* control, $P<0.01$), a significant decrease in MCP-1 level was observed with raloxifene (approximately a 20% reduction *vs* control, $P<0.05$) compared with the OVX+Veh group. When raloxifene was used in combination with E_2 in the OVX+E_2+Ral group, a 20% greater reduction in MCP-1 level relative to E_2 alone was observed (Figure 4).

Histopathological analysis demonstrated that the size of atherosclerotic lesions in the aorta increased significantly after ovariectomy. In the OVX rabbit model, 12-week treatment with E_2 decreased the size of atherosclerotic lesions significantly (approximately a 40% reduction vs control, $P<0.01$). Similar results were observed with raloxifene (approximately a 20% reduction *vs* control, $P<0.05$). A slight reduction was observed with aspirin although the difference was not statistically significant compared with vehicle control ($P=0.052$). When raloxifene and aspirin were co-administered with E_2, an approximate 20% greater reduction relative to E_2 alone was seen (Figure 5).

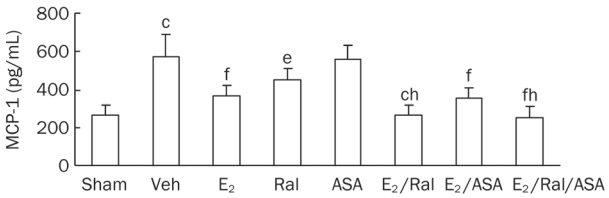

Figure 4. Effects of E_2/raloxifene/aspirin on MCP-1 level in mature OVX rabbits. After 12 weeks of treatment, serum MCP-1 levels (mmol/L) in response to E_2 alone, raloxifene alone, aspirin alone, raloxifene paired with E_2, aspirin paired with E_2 and combined raloxifene, aspirin and E_2 were determined. A significant increase in MCP-1 level was observed after ovariectomy in the OVX+Veh group compared with the sham group, and both E_2 (0.1 mg·kg^{-1}·d^{-1}) and raloxifene (10 mg·kg^{-1}·d^{-1}) decreased the MCP-1 level significantly compared to the vehicle control. When raloxifene was paired with E_2, MCP-1 level was reduced by approximately 20% relative to E_2 alone. Mean±SEM. n=10 animals per treatment group. $^{c}P<0.01$ relative to sham group; $^{e}P<0.05$, $^{f}P<0.01$ relative to vehicle control; $^{h}P<0.05$ relative to OVX+E_2 group. Veh, vehicle; E_2, estradiol valerate; Ral, raloxifene; ASA, aspirin.

Discussion

The purpose of this series of *in vivo* studies was to establish the proof-of-concept for a novel paradigm of HRT. This concept was based on the hypothesis that the combination of raloxifene and aspirin with estrogen would result in a physiological profile that was distinct from estrogen alone, and in particular, an improved pharmacological profile compared with estrogen alone.

The key physiological responses that require close monitoring in the evaluation of estrogen use are breast and uterine tissue stimulation, as estrogen functions directly through the ERs, which are abundant in those tissues. In previous

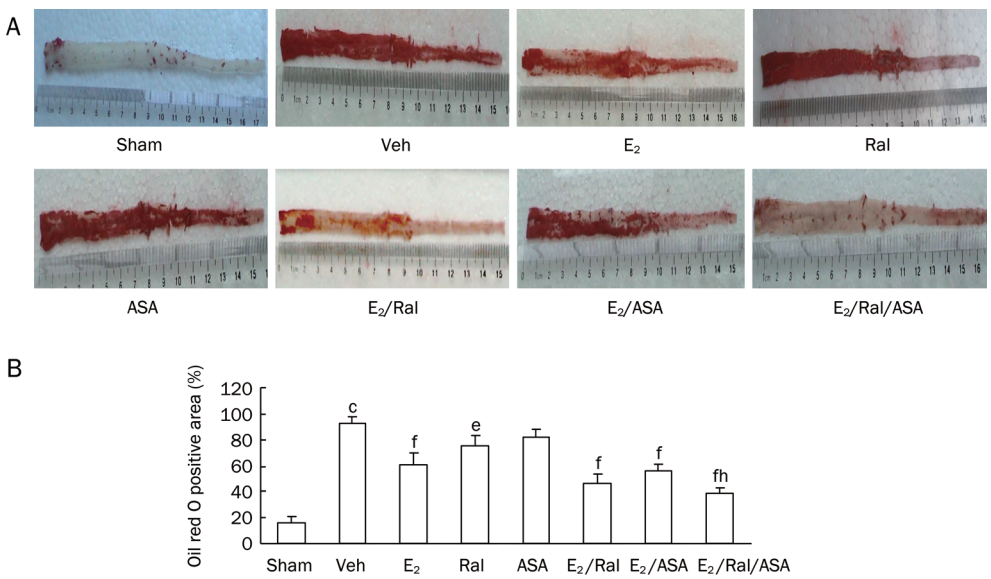

Figure 5. Effects of E_2/ raloxifene/aspirin on atherosclerotic lesion in mature OVX rabbits. After 12 weeks of treatment, atherosclerotic lesions in the aorta (%) in response to E_2, raloxifene, aspirin, raloxifene paired with E_2, aspirin paired with E_2 and combined raloxifene, aspirin and E_2 were determined by Oil Red O staining (n=10 animals per treatment group). (A) Oil Red O staining on photographs of aorta. Oil Red O positive area corresponds to lipid deposition. (B) Quantitative analysis of the percentage of Oil Red O positive area (% vessel wall staining positively±SEM). A significant increase in the size of atherosclerotic lesions (Oil Red O staining) was observed after ovariectomy compared with sham-operated animals. In OVX rabbits, although the reduction was not as profound as that associated with E_2, a significant decrease was observed in the OVX+Ral group ($P<0.05$) compared with OVX+Veh group. A mild reduction was observed with aspirin, although the difference was not significant. Further reductions relative to E_2 alone were observed with E_2/raloxifene (approximately 10% vs E_2 alone) and E_2/raloxifene/aspirin (approximately 20% *vs* E_2 alone). $^{c}P<0.01$ relative to sham group; $^{e}P<0.05$, $^{f}P<0.01$ relative to vehicle control; $^{h}P<0.05$ relative to OVX+E_2 group. Veh, vehicle; E_2, estradiol valerate; Ral, raloxifene; ASA, aspirin.

studies, ER-antagonistic activity in the breast and uterus has been found after raloxifene treatment[14, 15, 27]. In the present study, serum estradiol levels increased significantly in all the estrogen-treated animals, including animals treated with E_2 alone, E_2 plus raloxifene, and E_2 plus aspirin, as well as combined E_2, raloxifene and aspirin, compared to vehicle controls in the OVX rabbits. However, maximal breast and uterine stimulations were observed with E_2 alone and E_2 plus aspirin. In contrast, raloxifene alone did not stimulate the uterus and mammary glands, and when raloxifene was co-administered with E_2, the stimulation of the breast and uterus was reduced to vehicle control levels.

Platelets contribute to thrombosis in several ways. They provide the membrane surface for the generation of thrombin, express membrane receptors that affect platelet-platelet and platelet-vessel wall interactions. In low doses, aspirin has an antiplatelet effect by inhibiting the production of thromboxane. Platelets contain both ERα and ERβ[30, 31], but the effect of estrogen on the platelet aggregation has been controversial[32, 33]. In the current study, significant stimulation in platelet aggregation was observed with E_2 alone and E_2 plus raloxifene, but not with raloxifene alone in the OVX rabbits. As expected, aspirin reduced the platelet aggregation significantly compared with vehicle control, and addition of aspirin to E_2 decreased the platelet aggregation to the vehicle control levels.

Due to the fact that raloxifene antagonized the stimulatory effect of E_2 on the breast and uterus and aspirin reduced the stimulation of E_2 in platelet aggregation, an obvious question that arose was whether the combinatory use of raloxifene and aspirin with E_2 would unfavorably antagonize the positive effects of E_2, such as lowering levels of LDL-C and MCP-1 and inhibiting atherosclerotic lesions[1–5].

It has been well-documented that a high level of LDL-C and a low level of HDL-C are risk factors for atherosclerosis, and MCP-1, a potent chemoattractant for monocytes, has been suggested to be an especially important mediator of atherogenic signals[34, 35]. Raloxifene has been confirmed to have estrogen-agonist effects on lipid profiles[14, 15] , and an *in vitro* study has shown that raloxifene could downregulate the expression of MCP-1 in human coronary artery smooth muscle cells, although the degree of this inhibition was less than when induced by estrogen[36]. In the present study, ovariectomy induced a significant decrease in serum estradiol level and increased total cholesterol, LDL-C, and MCP-1 levels, as well as decreased HDL-C levels. However, significant reductions in total cholesterol, LDL-C, and MCP-1 levels and an increase in HDL-C level were found with E_2 treatment alone and raloxifene alone compared with the vehicle control, and further effects were observed with their co-administration, which suggested that raloxifene reinforced the positive effects of E_2. As well as its anticoagulant properties, aspirin has cardioprotective effects that include inhibiting the proliferation of vascular smooth muscle cells and improving endothelium-dependent vascular relaxation[37]. In the present study, reductions in the sizes of atherosclerotic lesions were found by Oil Red O staining assay with E_2 alone, raloxifene alone, E_2/raloxifene, E_2/aspirin, and E_2/raloxifene/aspirin compared with vehicle controls in the OVX rabbits. The maximal reduction was observed with E_2/raloxifene/aspirin, indicating an additive effect of the combination therapy.

The mechanism by which a target cell simultaneously responds to a mixture of drugs is not entirely clear. Hypothetically, the different molecules would compete for the available pool of receptors in the target cell, and simple receptor kinetics would dictate the dominant effector molecule. The final physiological response would be attributed to a blend of all of the activities of these molecules. In the current study, raloxifene was shown to abrogate the stimulatory effects of E_2 on the uterus and breast effectively, while aspirin reduced the stimulatory effect of E_2 on platelet aggregation, and both E_2 and raloxifene demonstrated positive agonistic effects on the lipid and MCP-1 profiles, and combined raloxifene, aspirin and E_2 was the most efficacious treatment in reducing atherosclerotic lesions in the aorta.

The ideal postmenopausal estrogen therapy is expected to reproduce the beneficial effects of estrogen without producing the adverse effects; however, no ideal postmenopausal estrogen therapy has been found to date. The present study demonstrated for the first time that the combination of raloxifene, aspirin and E_2 might be an attractive novel paradigm of HRT. This finding may prompt additional research with the aim of improving quality of life for peri- and postmenopausal women.

Acknowledgements

This work was supported by Grant from the Natural Science Foundation of Shandong Province, Ji-nan, Shandong, China (#Y2005C50), Grant-in-Aid for China-Japan Sasagawa Researchers, from the Ministry of Health, Beijing, China (#083). The authors are grateful to Chun-xi LIU and Zhi YANG for their excellent technical contributions.

Author contribution

Hong HE and Fa-lin YANG designed the research and wrote the paper; Ke-qing HU performed the research and analysed the data; Hong HE, Fa-lin YANG, Xin WANG, Zi-mo LIU, Qin HU, and Ji-fu LI contributed to perform the research and analyse the data.

References

1 Ross R. Atherosclerosis–an inflammatory disease. N Eng J Med 1999; 340: 115–26.
2 Blum A, Cannon Ro III. Effects of estrogens and selective oestrogen receptor modulators on serum lipoproteins and vascular function. Curr Opin Lipidol 1998; 9: 575–86.
3 Störk S, Baumann K, Clemens S, Angerer P. The effect of 17β-estradiol on MCP-1 serum levels in postmenopausal women. Cardiovasc Rev 2002; 53: 642–9.
4 Adams MR, Kaplan JR, Manuck SB, Koritnik DR, Parks JS, Wolfe MS, *et al*. Inhibition of coronary artery atherosclerosis by 17β-estradiol in ovariectomized monkeys: lack of an effect of added progesterone. Arteriosclerosis 1990; 10: 1051–7.

5 Manson JE, Allison MA, Rossouw JE, Carr JJ, Langer RD, Hsia J, *et al*. WHI and WHI-CACS Investigators. Estrogen therapy and coronary artery calcification. N Engl J Med 2007; 356: 2591–602.
6 Barrett-Connor E. Hormone replacement and cancer. Br Med Bull 1992; 48: 345–55.
7 Cauley, JA, Lucas FL, Kuller FH, Vogt MT, Browner WS, Cummings SR. Bone mineral density and risk of breast cancer in older women: the study of osteoporotic fractures. JAMA 1996; 276: 1404–8.
8 Hulley S, Grady D, Bush T, Furberg C, Herrington D, Riggs B, *et al*. Randomized trial of estrogen plus progestin for secondary prevention of coronary heart disease in postmenopausal women. Heart and Estrogen/progestin Replacement Study (HERS) research group. JAMA 1998; 280: 605–13.
9 Rossouw JE, Anderson GL, Prentice RL, LaCroix AZ, Kooperberg C, Stefanick ML, *et al*. Risks and benefits of estrogen plus progestin in healthy postmenopausal women: principal results from the women's health initiative randomized controlled trial. JAMA 2002; 288: 321–33.
10 Hanke H, Hanke J, Bruck B, Brehme U, Gugel N, Finking G, *et al*. Inhibition of the protective effect of estrogen by progesterone in experimental atherosclerosis. Atherosclerosis 1996; 121: 129–38.
11 Adams MR, Register TC, Golden DL, Wagner JD, Williams JK. Medroxyprogesterone acetate antagonizes inhibitory effects of conjugated equine estrogen on coronary artery atherosclerosis. Arterioscler Thromb Vasc Biol 1997; 17: 217–21.
12 He H, Yang F, Liu X, Zeng X, Hu Q, Zhu Q, *et al*. Sex hormone ratio changes in men and postmenopausal women with coronary artery disease. Menopause 2007; 14: 385–90.
13 Palacios S. The future of the new selective estrogen receptor modulators. Menopause Int 2007; 13: 27–34.
14 Delmas PD, Bjarnason NH, Mitlak BH, Ravoux AC, Shah AS, Huster WJ, *et al*. Effects of raloxifene on bone mineral density, serum cholesterol and uterine endometrium in postmenopausal women. N Engl J Med 1997; 337: 1641–7.
15 Cummings Sr, Eckert S, Krueger K, Grady D, Powles TJ, Cauley JA, *et al*. The effect of raloxifene on risk of breast cancer in postmenopausal women: results from the MORE randomized trial. Multiple Outcomes of Raloxifene Evaluation. JAMA 1999; 281: 2189–97.
16 Collins P, Mosca L, Geiger MJ, Grady D, Kornitzer M, Amewou-Atisso MG, *et al*. Effects of the selective estrogen receptor modulator raloxifene on coronary outcomes in the raloxifene use for heart trial: results of subgroup analyses by age and other factors. Circulation 2009; 119: 922–30.
17 Davies GC, Huster WJ, Lu Y, Plouffe L, Lakshmanan M. Adverse events reported by postmenopausal women in controlled trials with raloxifene. Obstet Gynecol 1999; 93: 558–65.
18 Cohen FJ, Lu Y. Characterization of hot flashes reported by healthy postmenopausal women receiving raloxifene or placebo during osteoporosis prevention trials. Maturitas 2000; 34: 65–73.
19 Stovall DW, Utian WH, Gass M, Qu Y, Muram D, Wong M, *et al*. The effects of combined raloxifene and oral estrogen on vasomotor symptoms and endometrial safety. Menopause 2007; 14: 510–7.
20 Grady D, Wenger NK, Herrington D, Khan S, Furberg C, Hunninghake D, *et al*. Postmenopausal hormone therapy increases risk for venous thromboembolic disease. The Heart and Estrogen/progestin Replacement Study. Ann Intern Med 2000; 132: 689–96.
21 Varas-Lorenzo C, Garcia-Rodriguez LA, Cattaruzzi C, Troncon MG, Agostinis L, Perez-Gutthann S. Hormone replacement therapy and the risk of hospitalization for venous thromboembolism: a population-based study in southern Europe. Am J Epidemiol 1998; 147: 387–90.
22 Anderson GL, Limacher M, Assaf AR, Bassford T, Beresford SA, Black H, *et al*. Effects of conjugated equine estrogen in postmenopausal women with hysterectomy: the Women's Health Initiative randomized controlled trial. JAMA 2004; 291: 1701–12.
23 Peter FW, Franken RJ, Wang WZ, Anderson GL, Schuschke DA, O'Shaughnessy MM, *et al*. Effect of low dose aspirin on thrombus formation at arterial and venous microanastomoses and on the tissue microcirculation. Plast Reconstr Surg 1997; 99: 1112–21.
24 Pulmonary Embolism Prevention (PEP) trial Collaborative Group. Prevention of pulmonary embolism and deep vein thrombosis with low dose aspirin: Pulmonary Embolism Prevention (PEP) trial. Lancet 2000; 355: 1295–302.
25 Finking G, Brehme U, Bruck B, Wehrmann M, Hanke S, Kamenz J, *et al*. Does anti-atherogenic estradiol valerate treatment cause adverse effects on liver and uterus in NZW rabbits? Vet Hum Toxicol 1998; 40: 136–40.
26 Bjarnason NH, Haarbo J, Byrjalsen I, Kauffman RF, Knadler MP, Christiansen C. Raloxifene reduces atherosclerosis: studies of optimized raloxifene doses in ovariectimized, cholesterol-fed rabbits. Clin Endocrinol 2000; 52: 225–33.
27 Al-Jamal JH, Dubin NH. The effect of raloxifene on the uterine weight response in immature mice exposed to 17beta-estradiol, 1,1,1-trichloro-2,2-*bis*(*p*-chlorophenyl)ethane, and methoxychlor. Am J Obstet Gynecol 2000; 182: 1099–102.
28 Friedewald WT, Levy RI, Fredrikson DS. Estimation of the concentration of low-density lipoprotein cholesterol in plasma without use of the preparative ultracentrifuge. Clin Chem 1972; 18: 499–502.
29 Pervin S, Singh R, Rosenfeld ME, Navab M, Chaudhuri G, Nathan L. Estradiol suppresses MCP-1 expression *in vivo*. Implications for atherosclerosis. Arterioscler Thromb Vasc Biol 1998; 18: 1838–45.
30 Jayachandran M, Miller VM. Human platelets contain estrogen receptor α, caveolin-1 and estrogen receptor associated proteins. Platelets 2003; 14: 75–81.
31 Khetawat G, Faraday N, Nealen ML, Vijayan KV, Bolton E, Noga SJ, *et al*. Human megakaryocytes and platelets contain the estrogen receptor β and androgen receptor (AR): testosterone regulates AR expression. Blood 2000; 95: 2289–96.
32 Elam MB, Limscomb GE, Chesney CM, Terragno DA, Terragno NA. Effect of synthetic estrogen on platelet aggregation and vascular release of PGI2-like material in the rabbit. Prostaglandins 1980; 20: 1039–51.
33 Nakano Y, Oshima T, Matsuura H, Kajiyama G, Kambe M. Effect of 17β-estradiol on inhibition of platelet aggregation *in vitro* is mediated by an increase in no synthesis. Arterioscler Thromb Vasc Biol 1998; 18: 961–7.
34 Tanaka E, Shimokawa H, Kamiuneten H, Eto Y, Matsumoto Y, Morishige K, *et al*. Disparity of MCP-1 mRNA and protein expressions between the carotid artery and the aorta in WHHL rabbits. Arterioscler Thromb Vasc Biol 2003; 23: 244–21.
35 Yla-Herttuala S, Lipton BA, Rosenfeld ME, Sarkioja T, Yoshimura T, Leonard E, *et al*. Expression of monocyte chemoattractant protein 1 in macrophage-rich areas of human and rabbit atherosclerotic lesions. Proc Natl Acad Sci U S A 1991; 88: 5252–6.
36 Seli E, Selam B, Mor G, Kayisli UA, Pehlivan T, Arici A. Estradiol regulate monocyte chemotactic protein-1 in human coronary artery smooth muscle cells: a mechanism for its antiatherogenic effect. Menopause 2001; 8: 296–301.
37 Awtry EH, Loscalzo J. Aspirin. Circulation 2000; 101: 1206–18.

Acta Pharmacologica Sinica (2011) 32: 1038–1044
 1671-4083/11 $32.00
www.nature.com/aps

Original Article

Tyrosine sulfation in N-terminal domain of human C5a receptor is necessary for binding of chemotaxis inhibitory protein of *Staphylococcus aureus*

Zhen-jia LIU[1, #], Yan-juan YANG[2, #], Lei JIANG[1], Ying-chun XU[3], Ai-xia WANG[4], Guan-hua DU[5], Jin-ming GAO[1, *]

[1]Department of Respiratory Diseases, [3]Department of Medical Microbiology, [4]Department of Infectious Diseases, Peking Union Medical College Hospital, Peking Union Medical College & Chinese Academy of Medical Sciences, Beijing 100730, China; [2]Department of Respiratory Diseases, Affiliated Hospital of Ningxia Medical University, Yinchuan 750004, China; [5]National Center for Drug Screening, Institute of Materia Medica, Peking Union Medical College & Chinese Academy of Medical Sciences, Beijing 100050, China

Aim: *Staphylococcus aureus* evades host defense through releasing several virulence proteins, such as chemotaxis inhibitory protein of staphylococcus aureus (CHIPS). It has been shown that extracellular N terminus of C5a receptor (C5aR) forms the binding domain for CHIPS, and tyrosine sulfation is emerging as a key factor in determining protein-protein interaction. The aim of this study was to evaluate the role of tyrosine sulfation of N-terminal of C5aR in its binding with CHIPS.
Methods: Expression plasmids encoding C5aR and its mutants were prepared using PCR and site-directed mutagenesis and were used to transfect HEK 293T cells using calcium phosphate. Recombinant CHIPS protein was purified. Western blotting was used to examine the binding efficiency of CHIPS to C5aR or its mutants.
Results: CHIPS exclusively binds to C5aR, but not to C5L2 or C3aR. A nonspecific sulfation inhibitor, sodium chlorate (50 nmol/L), diminishes the binding ability of C5aR with CHIPS. Blocking sulfation by mutation of tyrosine to phenylalanine at positions 11 and 14 of C5aR N terminus, which blocked sulfation, completely abrogates CHIPS binding. When tyrosine 14 alone was mutated to phenylalanine, the binding efficiency of recombinant CHIPS was substantially decreased.
Conclusion: The results demonstrate a structural basis of C5aR-CHIPS association, in which tyrosine sulfation of N-terminal C5aR plays an important role. Our data may have potential significance in development of novel drugs for therapeutic intervention.

Keywords: *Staphylococcus aureus;* chemotaxis inhibitory protein; tyrosine sulfation; post-translational modification; chemotactic receptor; C5aR

Acta Pharmacologica Sinica (2011) 32: 1038–1044; doi: 10.1038/aps.2011.53; published online 27 Jun 2011

Introduction

Staphylococcus aureus is a causative agent of pulmonary infections in immunocomponent normals as well as in immunocompromised individuals. In particular, the prevalence of highly virulent methicillin-resistant strains is increasingly becoming a public health challenge in hospital or community environments[1]. One possible mechanism underlying this may be that staphylococci release chemotaxis inhibitory protein of staphylococci (CHIPS) encoded by chp that contributes to the evasion of these bacteria from the immune system of the host. CHIPS has been shown to be necessary for inhibition of the early immune response by blocking the initial activation and recruitment of neutrophils and monocytes into the site of infection[2, 3].

The cellular receptor for CHIPS is C5aR with a nanomolar binding affinity[4]. C5aR is a seven-transmembrane segment belonging to the family member of rhodopsin-like G-protein coupled receptors (GPCRs)[5]. A previous study with chimeras and point mutations indicated that CHIPS exclusively bound to the N-terminal C5aR, in which acidic aspartic acid at positions 10, 15 and 18 and glycine at position 12 were specifically important for binding, whereas tyrosine at positions 11 and 14 did not involve CHIPS binding[6]. It should be pointed out that these authors used a FLAG tag fused into the N-terminus of the whole C5aR. FLAG tag is not applicable for studies regarding tyrosine sulfation because it contains a sulfatable tyrosine (DYKDDDDK) which probably provides the additional binding energy[7]. A subsequent study of the association

#These two authors contributed equally to this work.
* To whom correspondence should be addressed.
E-mail gaojm@pumch.cn
Received 2010-12-09 Accepted 2011-04-13

between CHIPS and a sulfated peptide based on N-terminus of the human C5aR using nuclear magnetic resonance (NMR) demonstrated that sulfated tyrosine at positions 11 and 14 of N-terminal C5aR significantly contributed to the tight binding[8].

Tyrosine sulfation is a post-translational modification occurring in a variety of secreted and integral membrane proteins and, in many cases, enhances the interactions between these proteins and their corresponding ligands, or invading pathogens[9, 10]. This modification tends to occur in acidic regions of proteins, usually containing multiple tyrosines[9, 11]. Several receptors for chemokines and hormones, including CCR5, CXCR3, C3XCR1, and thyroid-stimulating hormone receptor, have been shown to be sulfated on tyrosines in their amino terminal extracellular domains and some of this sulfation is critical for ligand binding[12–16]. Amino-terminal sulfation of tyrosines in the chemotactic receptor for C5a also contributes to formation of the docking site for the C5a anaphylatoxin[17]. We have previously demonstrated that sulfated tyrosine 174 in second extracellular loop of C3aR is essential for binding and signaling with native C3a[18]. Sulfotyrosine in the amino terminal sequence of CCR5 is important for binding of the natural ligands [macrophage inflammatory protein (MIP)-1α, MIP-1β, and RANTES] and certain HIV-1 gp120/CD4 complexes, and facilitates the entry of CCR5-using strains of HIV-1[13, 19]. Duffy binding protein of plasmodium vivax (*P vivax*) utilized sulfotyrosines of the Duffy antigen/receptor for chemokines for erythrocyte invasion by *P vivax*[20]. Thus, tyrosine sulfation represents a critical modification for conferring the natural function of a number of 7TMS receptors.

Here we report that C5aR, not C5L2 and C3aR, is an exclusive receptor for CHIPS binding. Furthermore, we show that two sulfotyrosines of the C5aR N-terminus are critical for CHIPS binding, and sulfated tyrosine at position 14 of N-terminal C5aR has a greater role in an association between CHIPS and C5aR. These data underscore that tyrosine sulfation plays an important role in the determining C5aR-CHIPS association and provides useful insights into how to block the binding of CHIPS to C5aR.

Materials and methods

Cells, plasmids, and constructs

HEK 293T cells were cultured in Dulbeco's modified Eagle's medium containing 10% fetal bovine serum, penicillin, and streptomycin. An expression plasmid encoding the human C5aR fused with a myc tag at its amino terminus was generated by PCR amplification of human genomic DNA, and subcloned into the pcDNA 3.1 expression vector (Invitrogen). All the C5aR variants YFY, YYF, YFF in which one or two tyrosines were mutated to phenylalanine were made by the PCR-based QuickChange method (Stratagene) and confirmed by sequencing the entire reading frame. The expression plasmids encoding the wild-type C5L2, C3aR, CXCR3, and platelet activating factor receptor (PAFR) were constructed as above described.

The plasmids encoding human tyrosyl protein sulfotransferases (TPST) 1 and 2, and small hairpin RNA (shRNA) targeting nucleotides 259-276 of TPST1 and nucleotides 73−94 of TPST2 were provided by Dr H Choe[18, 19].

Purification of recombinant CHIPS protein

Expression and purification of recombinant CHIPS was as previously described with minor modification[3, 21, 22]. Briefly, chp, with the exclusion of its signal sequence, was amplified by PCR on genomic DNA extracted from methicillin-resistant staphylococcus aureus (MRSA) ATCC 29213, cloned into pET32a (+) vector, then transformed into *Escherichia coli* BL21(DE3) plays (Invitrogen). In order to measure the expression of CHIPS, a His tag was fused into N-terminus of CHIPS. Purified inclusion bodies obtained from bacteria were induced with 1 mmol/L of isopropyl-1-thio-β-*D*-galactopyranoside (Invitrogen) overnight at 20°C and solubilized in 6 mol/L guanidine HCl. The protein was dialyzed against 10 mmol/L Tris-HCl, pH 8.0 and purified on HiTrap column (GE Healthcare Biosciences), using 10 mmol/L Tris-HCl, pH 8.0, 1 mol/L NaCl for elution. Protein concentration was determined using the BCA Protein Assay Kit (Pierce). The concentration of purified CHIPS was 96 mg/L.

Assay of chp in Clinical *S aureus* isolates in patients

Thirteen clinical MRSA and 13 MSSA strains were isolated from sputum or bloodstream in patients diagnosed with pulmonary infection. PCR was carried out on genomic DNA of using the forward primer 5′-ATGAAAAA-GAAATTAGCAACAACAG-3′ and the reverse primer 5′-TTAGTATGCATATTCATTAGTTTTTCC-3′. The size of PCR product was 450 bp.

The study protocol was reviewed and approved by the Peking Union Medical College Hospital Human Research Ethics Committee and all subjects gave informed written consent to participate in the study.

Western blotting analysis

The whole protein was prepared as previously described[23]. After removing the culture medium, cells were extensively washed three times, harvested and lysed in solubilization buffer containing a protease inhibitor cocktail (Sigma). Cell debris was removed by centrifugation at 12 000×*g* for 15 min at 4°C. The supernatants were eluted by adding an equal volume of sample loading buffer, then run on 12% SDS-PAGE gels before transferring to PVDF membranes. Memebranes were incubated in the presence of the indicated antibodies. Antibodies were as follows: anti-myc (Signal Chem), anti-His (Signal Chem). Primary antibody application was followed by incubation with horseradish peroxidase (HRP)-conjugated secondary antibodies (anti-mouse IgG) (Santa Cruz). Blots were developed using an enhanced chemiluminescence detection system (ECL) (Amersham) as per the manufacturer's instructions.

Analysis for binding of CHIPS to C5aR

Binding experiments were performed with HEK 293T cells

transfected with wild type C5aR or its variants using calcium phosphate[14, 17, 18]. One day later, cells were washed with PBS, and split into two separate aliquots, one used for binding assay and one for receptor expression analyses. CHIPS 3 μg/mL was incubated with cells expressing wild-type C5aR or C5aR variants for 30 min on ice. Western blotting was used to assay the binding efficiency and receptor expression.

Sodium chlorate treatment

Transfected cells were cultured in medium containing the various concentrations of sodium chlorate for at least 48 h at 37 ºC[14, 24].

Results

Prevalence of clinical *S aureus* isolates

The gene encoding for CHIPS, chp, lies at a bacteriophage-encoded immune cluster, seen in greater than 60% of *S aureus* isolates[3]. To examine the prevalence of chp in clinical *S aureus* isolates in our hospital, one of the major referral medical centers in China, we screened 13 methicillin-resistant strains and 13 methicillin-sensitive isolates (MSSA) from blood stream of infected individuals by PCR. Our data showed that chp was present in more than 30% of *S aureus* strains. Of note, more than 30% of MSSA was PCR-positive for chp.

Production and characteristics of recombinant CHIPS

A truncated version of CHIPS that did not contain a signal sequence at the N-terminus showed a similar C5aR blocking activity compared to the CHIPS[21]. Recombinant CHIPS was produced in *E coli* with a His tag fused into N-terminus of CHIPS to facilitate the recognition by anti-His antibody.

To demonstrate a direct interaction between CHIPS and the receptors for anaphylatoxins and chemokines, we performed transfection studies.

For this purpose, HEK cells were transfected with the expressing plasmids encoding C5aR, C5L2, C3aR, CXCR3, and PAFR. Figure 1 demonstrates the binding of CHIPS to C5aR overexpressed in HEK 293T cells. There was no binding of CHIPS to C5L2, C3aR, CXCR3, and PAFR observed even after longer exposure (Figure 1). These results indicate a direct binding of CHIPS to the C5aR.

The ATP sulfrylase inhibitor sodium chlorate decreases the binding affinity of CHIPS to C5aR but not C5aR expression

Sulfate can be added to proteins at sites of N- or O-linked glycosylation or on tyrosines via post-translational modifications[25]. C5aR has been shown to be modified by N-linked glycosylation. We treated C5aR-transfected-cells with various concentrations of sodium chlorate, a nontoxic inhibitor of ATP sulfrylase activity[14, 26], for at least 48 h in sulfate-free media. We identified a direct inhibition of the binding of CHIPS to wild-type C5aR by sodium chlorate in a concentration-dependent manner. Figure 2 shows that the binding of CHIPS to cellular C5aR was completely abolished in presence of 50 nmol/L of sodium chlorate, providing an independent evidence for the requirement of sulfation for CHIPS binding.

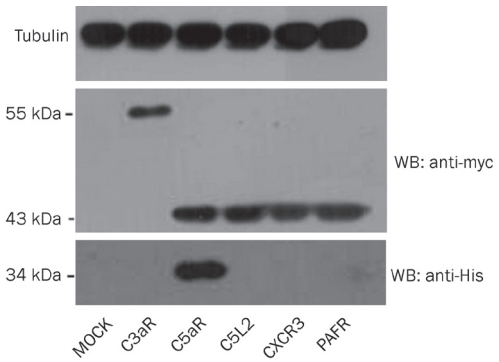

Figure 1. CHIPS exclusively binds to C5aR, but not to C5L2. HEK 293T cells were transfected with plasmids encoding the wild-type C5aR, C5L2, C3aR, CXCR3, and PAFR with N-terminal epitope tag. After 24 h they were divided into two aliquots, one was retained for analysis of receptor expression, one was used for binding experiments. N-terminally His-tagged CHIPS 3 μg/mL was incubated with transfected cells for 30 min on ice. The samples were subjected to 12% SDS-PAGE gels, transferred to PVDF membranes, detected by the indicated primary antibodies, followed by horseradish peroxidase-conjugated anti-mouse IgG. All samples were run under reducing condition. Numbers at the left indicate the positions of molecular weight markers.

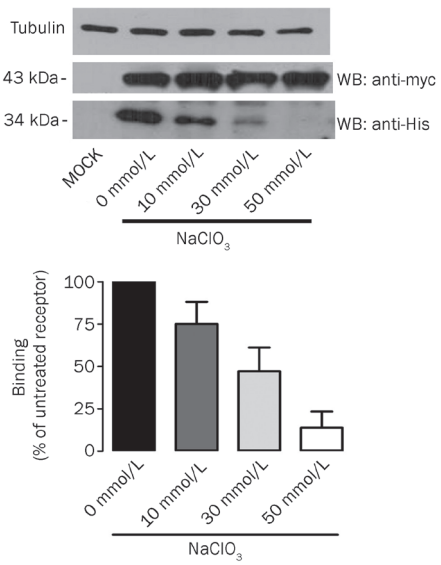

Figure 2. Effect of tyrosine sulfation of C5aR on CHIPS binding. HEK 293T cells were transfected with plasmids encoding the wild-type C5a receptor with N-terminal myc tag. After 24 h, cells were divided into two aliquots, one was retained for analysis of receptor expression, one was treated with the various concentrations of sodium chlorate for at least 48 h and then incubated with 3 μg/mL of N-terminally His-tagged CHIPS for 30 min on ice. The binding efficiency of C5aR-CHIPS was checked by Western blotting. Shown is representative of 3 independent experiments. The data represent the mean±SD of three experiments.

Sulfated tyrosines in the N-terminus of the C5aR contribute to CHIPS binding

Previous work has shown that sulfation of tyrosines on the extracellular amino terminal domain of the C5a anaphylatoxin receptor is a critically important post-translational modification for ligand recognition[17]. Given the importance of the sulfotyrosines in ligand binding, we examined whether a similar post-translational modification might be important for CHIPS as well. Tyrosines at positions 11 and 14 in N terminus were individually and doubly mutated to phenylalanine. Constructs were transfected into HEK 293T cells and tested for expression and binding.

In order to facilitate the determination of relative levels of cell surface expression by Western blotting, expression plasmids encoded for the wild-type C5aR or its mutants were fused in frame with an amino-terminal myc-tag, recognized by the antibody, 9E10. Simultaneously, cells from the same transfection were incubated with 3 μg/mL of CHIPS for 30 min on ice. Cells were extensively washed three times, lysed, and then transferred to PVDF membrane. Finally the PVDF membrane containing CHIPS-C5aRs complexes were incubated with the anti-His antibody, which is specific for the His-tag fused to the N-terminus of CHIPS. Western blot analysis of the binding of CHIPS to the wild-type C5aR or its mutants expressed in HEK 293 T cells was accomplished using the anti-His antibody.

As shown in Figure 3, when two tyrosines at positions 11 and 14 were changed to phenylalanine, the ability that C5aR YFF variant bound CHIPS was completely lost. We then investigated the specific contribution of each of the two tyrosines of the C5aR to CHIPS binding by assaying receptor variants (YFY and YYF) in which tyrosines 11 and 14 had been altered individually to phenylalanine. Figure 3 shows that cells transfected with either the YFY variant efficiently associated with CHIPS compared with cells expressing wild-type C5aR. By contrast, YYF variant bound CHIPS less efficiently than wild-type C5aR and the YFY variant, suggesting a greater role of sulfotyrosine 14 in binding CHIPS. Cell surface expression of this mutant receptor was essentially same as the wild type receptor as indicated by their fluorescence intensity of anti-His-tagged antibody staining assessed by FACS analysis (data not shown). Taken together, these data show that both tyrosine sulfate moieties of the C5aR N terminus contribute to the formation of CHIPS binding site.

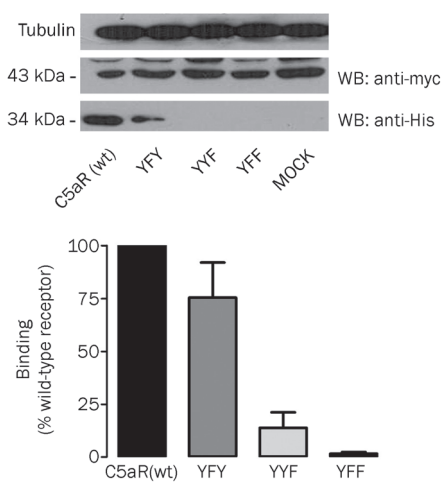

Figure 3. Tyrosine sulfation significantly contributes to the binding of CHIPS to C5aR. (A) HEK 293T cells were transfected with plamids encoding wild-type C5aR or the C5aR variants YFY, YYF or YFF. Cells were incubated with 3 μg/mL of N-terminally tagged-His CHIPS as described in Materials and Methods. Cells were extensively washed, and CHIPS bound by C5aR was determined by Western blotting using anti-His antibody. Aliquots of the same transfections were analyzed for C5aR expression levels by Western blotting using the anti-myc-tag antibody 9E10. Shown is representative of three independent experiments. The data represent the mean±SD of three experiments.

Effect of enzymatic modulation of sulfation on the binding ability of C5aR to CHIPS

One possible explanation for blockade of CHIPS binding to C5aR variant YFY is due to the absence of sulfate moiety on tyrosine 14. We cannot exclude the possibility that the expression of phenylalanine at this site changed receptor conformation due to the increase in hydrophobicity caused by the lack of the hydroxyl group[14, 26]. We assessed these possibilities by using tyrosine protein sulfotransferases 1 and 2 (TPSTs), which have been shown to increase the extent of tyrosine sulfation of GPCRs for ligand binding[14, 18, 19]. We co-transfected the plasmid encoding C5aR variant YFY with constructs for TPST1 and 2. Cells transfected with C5aR YFY alone showed the same receptor expression level compared to cells co-transfected with the plasmids encoding C5aR YFY variant and TPSTs as indicated by their fluorescence intensity of anti-His-tagged antibody staining assessed by FACS analysis (data not shown). The cells co-transfected with C5aR variant YFY and TPSTs displayed the significant increase in binding efficiency with CHIPS (Figure 4). Thus, sulfation of tyrosine 14 on the C5aR N-terminus is a critical determinant for recognition by CHIPS.

The activity of TPSTS can be modified by transfection with constructs encoding shRNAs targeting the TPSTs to decrease them. In the case of C3aR and CXCR3, tyrosine sulfation was reduced by shRNAs against TPSTs, and maximal binding was significantly decreased accordingly[14, 18]. However, blockade of the activity of TPSTs by shRNAs partially inhibited the binding of CHIPS to C5aR variant YFY (Figure 4).

Discussion

The molecular cloning of the C5a receptor places this molecule in the superfamily of G-protein coupled 7TMS receptors[27, 28]. C5a, a key component of complement system, is particularly important for recruitment of leukocytes and effective clearance of invading pathogens. C5a exerts its effect via the binding and activation of C5aR[5, 29]. More recently, we, and others have demonstrated the existence of sulfated tyrosines in amino terminal sequences of several chemoattractant receptors that play a critical role in receptor function[13, 14]. The C5a anaphylatoxin receptor has been shown to contain sulfotyrosines in

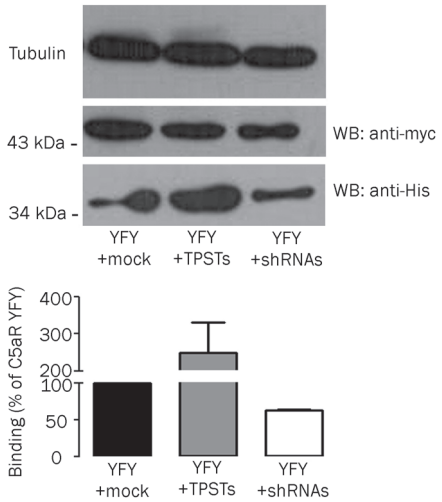

Figure 4. Effect of enzymatic modulation of tyrosine sulfation on the association between CHIPS and C5aR YFY. HEK 293T cells were co-transfected with the plasmid encoding C5aR YFY or with plasmids encoding TPSTs or with shRNAs targeting TPSTs as indicated. The binding efficiency of CHIPS to C5aR YFY was determined by Western blotting identical to Figure 2. Results are expressed as means±SD. *n*=3 independent experiments.

its amino terminus that are involved in formation of the docking site[17]. Our data showed that more than 30% of MSSA was PCR-positive for the gene encoding for CHIPS, chp. The present study shows that C5aR, but not its second receptor C5L2 and other G-protein coupled receptor, is a unique receptor for CHIPS. Furthermore, our data validate and extend the results from the previous studies on association between C5aR and CHIPS by demonstrating that inhibition of sulfation effectively interferes with the ability of CHIPS to bind cells overexpressing C5aR, and thus tyrosine sulfation appears to contribute to the proper binding of CHIPS to this receptor. Even though there are two sulfatable tyrosines in N-terminus of C5aR, sulfated tyrosine 14 is significantly involved in CHIPS binding. Our data are consistent with the previously published results showing the inability of CHIPS to bind to the second C5a receptor, C5L2, although C5L2 was also sulfated on N-terminal tyrosine residues in a very similar pattern to C5aR[30, 31]. Taken together, these data suggest the very high specificity of CHIPS binding.

A study with mutation and chimeras reported that the C5aR lacking residues 1-18 of N-terminus showed a significant decrease in binding to CHIPS compared to wild-type C5aR[6]. Nikiforovich *et al* further demonstrated that CHIPS only bound to the first binding site of C5a to C5aR 10-18 fragment containing two sulfrotyrosines[32]. Similarly, alteration of aspartic acids 10, 15, and 18 and the glycine at position 12 had a profound effect on CHIPS binding. By contrast, the NMR study demonstrated that a tyrosine-sulfated peptide at positions 11 and 14 based on C5aR N-terminus has (about 400 times) stronger affinity in binding CHIPS than the non-sulfated peptide[8]. The presence of the two sulfate moieties on C5aR that contribute to its association with CHIPS may be helpful in explaining these conflicting data. Sulfate is a charged, highly polarizable moiety that may provide significant energy to the binding[10]. This tyrosine sulfation may contribute to the association of the negatively charged receptor N-terminus of C5aR with the positively charged CHIPS. Consistently, we demonstrate the critical role of tyrosine sulfation of C5aR N-terminus in CHIPS binding. Our data raise the possibility that the C5aR N-terminal aspartic acids are perturbed by CHIPS binding probably due to interfering with acidic domain necessary for tyrosine sulfation, like C5a-C5aR interaction[17].

Tyrosines at 11 and 14 of N-terminal C5aR, which are flanked by acidic amino acids indicative of sulfation, have been demonstrated to be sulfated. Sulfated tyrosine 11 had a greater role in the C5a binding[17], whereas sulfotyrosine 14 was shown to be important for CHIPS binding in this current study. These data are in agreement with the predicted substrate requirement for TPSTs[11]. To ensure that loss of CHIPS binding commensurate with mutation of tyrosine 14 to phenylalanine reflected the loss of sulfate and not indirect structural alterations of the receptor, we attempted to first co-express the C5aR variant YFY with TPST1 and 2. We showed a greater increase in binding efficiency of CHIPS to the cells co-transfected with C5aR variant YFY and TPST than the cells transfected with the YFY variant alone, which supports the importance of the sulfate moiety for enhancement of CHIPS binding. However, when the co-transfect ions were performed using shRNA constructs targeting TPST1 and 2, binding efficiency was partially inhibited with essentially no change in receptor expression (as assessed by FACS analysis, data not shown). The observation might be reflective of the enzymatic activity of TPSTs synthesized prior to shRNA transfection[33, 34]. In addition, the partial inhibition of CHIPS to the wild-type C5aR or its mutants caused by shRNAs might suggest that optimal binding requires the participation of other component of the receptor in CHIPS binding, such as posttranslational tyrosine phosphorylation[35]. Our data are in agreement with a very recent observation using a phosphorylated analog of C5aR N-terminus that the phosphate group at tyrosine 14 was involved in stronger binding of CHIPS to C5aR[35].

Tyrosine sulfation may be important for the initial capture of C5aR-expressing cells by CHIPS and less important for other potential downstream functions. A recent study showed that a tyrosine-sulfated peptides based on the N-terminus of C5aR interacted with CHIPS and could inhibit C5a-induced calcium influx[8]. Thus, the present study might suggest that CHIPS competitively associates with the primary binding site of C5a located at the N-terminus of the C5aR, thereby preventing the C-terminal tail of C5a from contacting the activation domain of the C5aR and blocking downstream signaling. Tyrosine sulfation may represent a general mechanism utilized by the virulence proteins secreted by invading pathogens that mediate the rapid capture of circulating leukocytes.

In summary, the current study has not only defined the structural requirement for the CHIPS binding, but also demonstrated that tyrosine sulfation has a wider biological sig-

nificance. Since *S aureus* continually poses a threat to human health, a precise knowledge of the structural basis for the binding of CHIPS to C5aR as we have shown should have great significance in developing potent drugs to reduce the pathogeneticity of this infection.

Abbreviations

CHIPS, Chemotaxis inhibitory protein; C3aR, C3a receptor; C5aR, C5a receptor; CCR5, CC chemokine receptor 5; CXCR3, CXC receptor 3; PAFR, platelet activating factor receptor; 7TMS, 7 transmembrane segment; GPCR, G-protein coupled receptor. PBS, phosphate-buffered saline. WB: Western Blotting.

Acknowledgements

This work was in part supported by grants from National Natural Science Foundation of China (No 30470767), Beijing Natural Sciences Foundation (No 7072063), Education Ministry of China New Century Excellent Talent (NCET 06-0156) and Janssen Research Council China (All grants were to Jin-ming GAO).

We are grateful for Dr Hyeryun CHOE's helpful encouragement and for providing the plasmids. We thank Prof Wen-hui LI for kind help in designing the primers. We particularly thank Prof Kian Fan CHUNG for his helpful suggestions, discussion, and excellent English editing of the text.

Author contribution

Zhen-jia LIU and Yan-juan YANG performed the whole experiment; Lei JIANG helped and did some experiments; Ying-chun XU and Ai-xia WANG provided the MRSA strain and helped the experiment; Guan-hua DU supervised the experiment; Jin-ming GAO designed and supervised the experiments, and drafted the manuscript.

References

1 Pantosti A, Venditti M. What is MRSA? Eur Respir J 2009; 34: 1190–6.
2 van Wamel WJ, Rooijakkers SH, Ruyken M, van Kessel KP, van Strijp JA. The innate immune modulators staphylococcal complement inhibitor and chemotaxis inhibitory protein of *Staphylococcus aureus* are located on beta-hemolysin-converting bacteriophages. J bacteriol 2006; 188: 1310–5.
3 de Haas CJ, Veldkamp KE, Peschel A, Weerkamp F, Van Wamel WJ, Heezius EC, *et al*. Chemotaxis inhibitory protein of Staphylococcus aureus, a bacterial antiinflammatory agent. J Exp Med 2004; 199: 687–95.
4 Postma B, Poppelier MJ, van Galen JC, Prossnitz ER, van Strijp JA, de Haas CJ, *et al*. Chemotaxis inhibitory protein of Staphylococcus aureus binds specifically to the C5a and formylated peptide receptor. J Immunol 2004; 172: 6994–7001.
5 Lee H, Whitfeld PL, Mackay CR. Receptors for complement C5a. The importance of C5aR and the enigmatic role of C5L2. Immunol Cell Biol 2008; 86: 153–60.
6 Postma B, Kleibeuker W, Poppelier MJ, Boonstra M, Van Kessel KP, Van Strijp JA, *et al*. Residues 10–18 within the C5a receptor N terminus compose a binding domain for chemotaxis inhibitory protein of *Staphylococcus aureus*. J Biol Chem 2005; 280: 2020–7.
7 Choe H, Farzan M. Chapter 7. Tyrosine sulfation of HIV-1 coreceptors and other chemokine receptors. Methods Enzymol 2009; 461: 147–70.
8 Ippel JH, de Haas CJ, Bunschoten A, van Strijp JA, Kruijtzer JA, Liskamp RM, *et al*. Structure of the tyrosine-sulfated C5a receptor N terminus in complex with chemotaxis inhibitory protein of *Staphylococcus aureus*. J Biol Chem 2009; 284: 12363–72.
9 Liu J, Louie S, Hsu W, Yu KM, Nicholas HB Jr, Rosenquist GL. Tyrosine sulfation is prevalent in human chemokine receptors important in lung disease. Am J Respir Cell Mol Biol 2008; 38: 738–43.
10 Kehoe JW, Bertozzi CR. Tyrosine sulfation: a modulator of extracellular protein-protein interactions. Chem Biol 2000; 7: R57–61.
11 Monigatti F, Gasteiger E, Bairoch A, Jung E. The sulfinator: predicting tyrosine sulfation sites in protein sequences. Bioinformatics (Oxford, England) 2002; 18: 769–70.
12 Costagliola S, Panneels V, Bonomi M, Koch J, Many MC, Smits G, *et al*. Tyrosine sulfation is required for agonist recognition by glycoprotein hormone receptors. EMBO J 2002; 21: 504–13.
13 Farzan M, Mirzabekov T, Kolchinsky P, Wyatt R, Cayabyab M, Gerard NP, *et al*. Tyrosine sulfation of the amino terminus of CCR5 facilitates HIV-1 entry. Cell 1999; 96: 667–76.
14 Gao JM, Xiang RL, Jiang L, Li WH, Feng QP, Guo ZJ, *et al*. Sulfated tyrosines 27 and 29 in the N-terminus of human CXCR3 participate in binding native IP-10. Acta Pharmacol Sin 2009; 30: 193–201.
15 Fong AM, Alam SM, Imai T, Haribabu B, Patel DD. CX3CR1 tyrosine sulfation enhances fractalkine-induced cell adhesion. J Biol Chem 2002; 277: 19418–23.
16 Colvin RA, Campanella GS, Manice LA, Luster AD. CXCR3 requires tyrosine sulfation for ligand binding and a second extracellular loop arginine residue for ligand-induced chemotaxis. Mol Cell Biol 2006; 26: 5838–49.
17 Farzan M, Schnitzler CE, Vasilieva N, Leung D, Kuhn J, Gerard C, *et al*. Sulfated tyrosines contribute to the formation of the C5a docking site of the human C5a anaphylatoxin receptor. J Exp Med 2001; 193: 1059–66.
18 Gao J, Choe H, Bota D, Wright PL, Gerard C, Gerard NP. Sulfation of tyrosine 174 in the human C3a receptor is essential for binding of C3a anaphylatoxin. J Biol Chem 2003; 278: 37902–8.
19 Choe H, Li W, Wright PL, Vasilieva N, Venturi M, Huang CC, *et al*. Tyrosine sulfation of human antibodies contributes to recognition of the CCR5 binding region of HIV-1 gp120. Cell 2003; 114: 161–70.
20 Choe H, Moore MJ, Owens CM, Wright PL, Vasilieva N, Li W, *et al*. Sulphated tyrosines mediate association of chemokines and Plasmodium vivax Duffy binding protein with the Duffy antigen/receptor for chemokines (DARC). Mol Microbiol 2005; 55: 1413–22.
21 Gustafsson E, Forsberg C, Haraldsson K, Lindman S, Ljung L, Furebring C. Purification of truncated and mutated chemotaxis inhibitory protein of *Staphylococcus aureus* — an anti-inflammatory protein. Protein Expr Purif 2009; 63: 95–101.
22 Haas PJ, de Haas CJ, Poppelier MJ, van Kessel KP, van Strijp JA, Dijkstra K, *et al*. The structure of the C5a receptor-blocking domain of chemotaxis inhibitory protein of *Staphylococcus aureus* is related to a group of immune evasive molecules. J Mol Biol 2005; 353: 859–72.
23 Meissner M, Stein M, Urbich C, Reisinger K, Suske G, Staels B, *et al*. PPARalpha activators inhibit vascular endothelial growth factor receptor-2 expression by repressing Sp1-dependent DNA binding and transactivation. Circ Res 2004; 94: 324–32.
24 Baeuerle PA, Huttner WB. Chlorate — a potent inhibitor of protein sulfation in intact cells. Biochem Biophys Res Commun 1986; 141: 870–7.

25 Huttner WB. Tyrosine sulfation and the secretory pathway. Ann Rev Physiol 1988; 50: 363–76.
26 Xia L, Ramachandran V, McDaniel JM, Nguyen KN, Cummings RD, McEver RP. N-terminal residues in murine P-selectin glycoprotein ligand-1 required for binding to murine P-selectin. Blood 2003; 101: 552–9.
27 Gerard C, Gerard NP. C5A anaphylatoxin and its seven transmembrane-segment receptor. Ann Rev Immunol 1994; 12: 775–808.
28 Gerard NP, Gerard C. The chemotactic receptor for human C5a anaphylatoxin. Nature 1991; 349: 614–7.
29 Gerard C, Gerard NP. The pro-inflammatory seven-transmembrane segment receptors of the leukocyte. Curr Opin Immunol 1994; 6: 140–5.
30 Wright AJ, Higginbottom A, Philippe D, Upadhyay A, Bagby S, Read RC, *et al*. Characterisation of receptor binding by the chemotaxis inhibitory protein of *Staphylococcus aureus* and the effects of the host immune response. Mol Immunol 2007; 44: 2507–17.
31 Scola AM, Higginbottom A, Partridge LJ, Reid RC, Woodruff T, Taylor SM, *et al*. The role of the N-terminal domain of the complement fragment receptor C5L2 in ligand binding. J Biol Chem 2007; 282: 3664–71.
32 Nikiforovich GV, Baranski TJ. Structural models for the complex of chemotaxis inhibitory protein of *Staphylococcus aureus* with the C5a receptor. Biochem Biophys Res Commun 2009; 390: 481–4.
33 Baeuerle PA, Huttner WB. Tyrosine sulfation is a trans-Golgi-specific protein modification. J Cell Biol 1987; 105: 2655–64.
34 Bundgaard JR, Sen JW, Johnsen AH, Rehfeld JF. Analysis of tyrosine-O-sulfation. Methods Mol Biol 2008; 446: 47–66.
35 Bunschoten A, Feitsma LJ, Kruijtzer JA, de Haas CJ, Liskamp RM, Kemmink J. CHIPS binds to the phosphorylated N-terminus of the C5a-receptor. Bioorg Med Chem Lett 2010; 20: 3338–40.

Acta Pharmacologica Sinica (2011) 32: 1045–1054
 1671-4083/11 $32.00
www.nature.com/aps

Original Article

Interleukin-17A is involved in development of spontaneous pulmonary emphysema caused by Toll-like receptor 4 mutation

Qing-qing WANG, Hong-zhen YANG, Han-zhi LIU, Su MI, Xiao-wei ZHANG, Hui-min YAN, Yong-gang MA, Xiao-xing WANG, Zhuo-wei HU*

Molecular Immunology and Pharmacology Laboratory, State Key Laboratory of Bioactive Substances and Functions of Natural Medicines, Institute of Materia Medica, Chinese Academy of Medical Sciences & Peking Union Medical College, Beijing 100050, China

Aim: To explore the pathogenic role of Th17 cells and interleukin-17A (IL-17A)-associated signaling pathways in spontaneous pulmonary emphysema induced by a Toll-like receptor 4 mutant ($TLR4^{mut}$).

Methods: Lungs were obtained from wild-type (WT) or $TLR4^{mut}$ mice that were treated with or without recombinant mouse IL-17A (1 $\mu g \cdot kg^{-1} \cdot d^{-1}$, ip) from the age of 3 weeks to 3 months. Pulmonary emphysema was determined using histology, immunochemistry, and biochemical analysis. T cell polarization was determined with flow cytometry, the levels of cytokines were measured using ELISA, and the levels of IL-17A-associated signaling molecules were detected using Western blot.

Results: Compared to WT mice, 3 month-old $TLR4^{mut}$ mice were characterized by significantly reduced infiltration of Th17 cells into lungs (2.49%±1.13% *vs* 5.26%±1.39%), and significantly reduced expression levels of IL-17A (3.66±0.99 pg/μg *vs* 10.67±1.65 pg/μg), IL-23 (12.43±1.28 pg/μg *vs* 28.71±2.57 pg/μg) and IL-6 (51.82±5.45 pg/μg *vs* 92.73±10.91 pg/μg) in bronchoalveolar lavage fluid. In addition, p38 MAPK phosphorylation and AP-1 expression were decreased to 27%±9% and 51%±8%, respectively, of that in WT mice. Treatment of $TLR4^{mut}$ mice with IL-17A increased the infiltration of Th17 cells into lungs and expression levels of IL-17A, IL-6, and IL-23 in bronchoalveolar lavage fluid, attenuated MDA and apoptosis, and improved emphysema accompanied with increased phosphorylation of p38 MAPK and expression of AP-1.

Conclusion: Th17 cells, in particular the cytokine IL-17A, play a crucial role in the pathogenesis of $TLR4^{mut}$-induced spontaneous pulmonary emphysema. Both of them are potential targets for therapeutic strategies for pulmonary emphysema.

Keywords: emphysema; IL-17A; Th17 cells; Toll-like receptor 4

Acta Pharmacologica Sinica (2011) 32: 1045–1054; doi: 10.1038/aps.2011.67; published online 27 Jun 2011

Introduction

Chronic obstructive pulmonary disease (COPD), which is defined as airflow obstruction that is not fully reversible, was ranked fifth among causes of death globally in 2002; however, it is expected to be the third most common cause of death in 2020. The main pathological changes associated with COPD include chronic bronchitis, emphysema and small-airway disease[1]. The symptoms of emphysema partially overlap with COPD, and it is one manifestation of a group of chronic, obstructive, and frequently progressive destructive lung diseases[2]. Emphysema is characterized by destruction of the alveolar walls and permanent enlargement of the air spaces distal to the terminal bronchioles, which contribute to a reduction in the forced expiratory volume in 1 second (FEV1)[3]. Inflammation, cellular apoptosis, oxidative stress, and protease/antiprotease imbalance are involved in the pathogenesis of emphysema[4, 5]. Chemokines and other chemoattractants, such as interleukin-8 (IL-8), monocyte chemotactic protein-1 (MCP-1), and LTB4, promote the accumulation of inflammatory cells, including macrophages and neutrophils, in the lungs. Lymph follicles containing dendritic cells (DCs) and Th1 cells are present in the parenchyma, which suggests a potential role of the immune response in emphysematous destruction. Also, macrophages and neutrophils can be activated by various insults, such as cigarette smoke, and can subsequently produce reactive oxygen species (ROS) and many inflammatory cytokines, such as tumor necrosis factor (TNF)-α, IL-1β, and IL-6. In return, inflammation-activated

* To whom correspondence should be addressed.
E-mail huzhuowei@imm.ac.cn
Received 2010-12-01 Accepted 2011-04-21

macrophages and neutrophils release proteinases, including elastases and matrix metalloproteinase-9. These proteinases contribute to the degradation of extracellular matrix components and eventually to the development of emphysema. However, anti-inflammatory agents or antioxidants only reduce the symptoms, and they do not affect the decline in FEV1[6]. Thus, further investigation is needed to understand the mechanisms underlying the pathogenesis of emphysema.

There have been many studies that have indicated that Toll-like receptors (TLRs) and TLR-mediated autoimmunity play critical roles in the development and resolution of emphysema[7, 8]. TLRs, as a critical family of pattern recognition receptors, can initiate and orchestrate innate and adaptive immune responses; in addition, they function as sensors of damage-associated molecular pattern and are involved in multiple noninfectious inflammatory diseases, such as acute respiratory distress syndrome, asthma, and COPD. TLR4 and TLR2 play a prominent role in gene-environment interactions that are relevant to COPD-related phenotypes because the interaction between the microbial load and the immune system is a critical determinant of both immune function and asthma/emphysema susceptibility[9]. TLR ligands can activate DCs and subsequently determine the direction of T cell polarization[10]. TLR4 mutation results in pulmonary emphysema through upregulation of NADPH oxidase (Nox) 3 in the lungs and endothelial cells, which enhance oxidant generation and elastolytic activity[7]. Importantly, reduction/oxidation (redox) is a novel factor that has been shown to regulate T cell polarization[11]. Furthermore, the accumulation of ROS is critical for the differentiation of naïve Th cells into Th1 or Th17 cells[12]. A recent study has indicated that IL-17 promotes the growth of airway epithelial cells and that Th17 cells play an important role in inflammation and autoimmune diseases, including emphysema[13].

Therefore, we wondered whether T cell polarization, and in particular differentiation into the Th17 phenotype, was involved in the pathogenesis of TLR4^{mut}-induced spontaneous pulmonary emphysema. We found that TLR4 ^{mut}-induced spontaneous pulmonary emphysema is associated with reductions in the amount of Th17 cell infiltration into the lungs and in the production of Th17-associated cytokines. Administration of recombinant mouse IL-17A reversed TLR4^{mut}-induced pulmonary emphysema by enhancing the phosphorylation of p38 MAP kinase and the expression of AP-1, suggesting that Th17 cells and IL-17A associated signaling pathways play a crucial role in the pathogenesis of pulmonary emphysema. Furthermore, our results indicate that the IL-17A signaling pathway is a potential target for the development of therapeutics against pulmonary emphysema.

Materials and methods

Materials

In situ cell death detection kits were purchased from Roche Diagnostics Ltd (East Sussex, UK). Malondialdehyde (MDA) assay kits were purchased from the Nanjing Jiancheng Bioengineering Institute (Nanjing, China). Anti-cleaved caspase 3 was from Cell Signaling (Danvers, MA, USA). ELISA kits for IL-17A, IL-23, IL-6, and TGF-β1 were purchased from eBioscience (San Diego, CA, USA). FITC/PE-conjugated anti-CD4, FITC-conjugated anti-IFN-γ, PE-conjugated anti-IL-13, FITC-conjugated anti-CD4, PE-conjugated anti-CD25, PE-conjugated anti-IL-17A antibodies were purchased from eBioscience. Recombinant mouse IL-17A was purchased from R&D Systems (Minneapolis, MN, USA).

Animals

TLR4^{mut} (C3H/HeJ) mice and corresponding wild-type (WT) mice were obtained from Jackson Laboratories (Bar Harbor, ME, USA). Mice were maintained under specific pathogen free conditions at the Experimental Animal Center of the Institute of Materia Medica. For therapeutic treatment, TLR4^{mut} mice were randomized into 2 groups and administered recombinant mouse IL-17A (1 μg/kg body weight, ip) or an identical volume of vehicle once every day from 3 weeks of age to the end of the experiment. Mice were sacrificed by injection of excess pentobarbital sodium at 3 months of age. The study protocol was approved by the Institutional Committee for the Ethics of Animal Care and Treatment.

Bronchoalveolar lavage fluid (BALF)

Mice were anesthetized and the lungs were lavaged with 0.6 mL of ice-cold phosphate balance solution (PBS). BALF was centrifuged at 100×*g* for 15 min at 4 ^{o}C. The supernatant was decanted and stored at –80 ^{o}C for further analysis.

Measurement of lung histology and morphometry

Animals were anesthetized and the lungs were perfused with 4% neutral buffered formalin for 20 min (n=6 in each group) via the tracheal cannula at an airway pressure of 25 cm H_2O[14]. The fixed lungs were embedded in paraffin, sectioned, and stained with hematoxylin and eosin (HE) for histological analyses. The average distance between alveolar walls and the mean linear intercept (Lm) were calculated according to established methods[15]. Briefly, Lm was calculated as the total length of each line of the grid using a 100 μm×100 μm grid passing randomly through the lung and divided by the number of alveolar intercepts. For each pair of lungs, 6 histological fields were evaluated. Lung sections were processed for terminal deoxynucleotidyl transferase dUTP nick end labeling (TUNEL) assay using an *in situ* cell death detection kit.

Assay of lipid peroxides

MDA was measured using an MDA assay kit from Nanjing Jiancheng Bioengineering Institute according to the manufacturer's instructions[16].

ELISAs for cytokines in BALF

The concentrations of IL-17A, IL-23, IL-6, and TGF-β1 in BALF were detected using ELISA kits in accordance with the manufacturer's instructions.

Preparation of single-cell lung suspensions

Single-cell suspensions were prepared from the right lung, as previously described[17]. Briefly, the lung vasculature of anesthetized mice was perfused with PBS until free of blood. The lung was minced; digested with 1 mL digestion medium consisting of RPMI-1640, 1 mg/mL collagenase type 2 (Roche Diagnostics; Indianapolis, IN, USA) and 0.02 mg/mL DNase I (grade II from bovine pancreas) for 60 min at 37 °C; subjected to red blood cell lysis (eBioscience); passed through a 100 μm cell strainer; and kept on ice until labeling.

Flow cytometry

The Th1/Th2 mouse T cell subpopulations in single-cell lung suspensions were labeled with FITC-conjugated anti-CD4, PE-conjugated anti-IFN-γ, and Alexa 647-conjugated anti-IL-13 antibodies. Th1 and Th2 cells were defined as $CD4^+$ IFN-γ^+ cells and $CD4^+$ IL-13^+ cells, respectively. Similarly, regulatory T cells (Tregs) were labeled with FITC-conjugated anti-CD4 and PE-conjugated anti-CD25 antibodies and were defined as $CD4^+$ $CD25^+$ cells; Th17 cells were labeled with FITC-conjugated anti-CD4 and PE-conjugated anti-IL17 antibodies and were defined as $CD4^+$ IL-17^+ cells.

Surface molecule expression of single-cell lung suspensions was analyzed using multicolor flow cytometry, as previously described[18]. Briefly, single-cell lung suspensions were suspended in cold PBS containing 3% FBS and 0.02% NaN_3. The cells were then incubated with a mixture of rat and mouse IgG (1:1) to reduce nonspecific binding, followed by serial incubations with saturating concentrations of FITC-conjugated mAb and/or PE-conjugated mAb for 1 h at 4 °C. Isotype-matched mAbs were used in control samples. After incubation, 20,000 stained cells were analyzed using CellQuest software (BD Biosciences, Sparks, MD, USA). In addition, the levels of various cytokines, such as IFN-γ, IL-13, and IL-17, were determined by an intracellular staining method, as previously described[19]. The cells were fixed (2% paraformaldehyde), permeabilized (0.5% saponin or methanol), and stained with PE-, Alexa 647-, or PE-conjugated mAbs specific for IFN-γ, IL-13, and IL-17, respectively, or isotype-matched mAb. The fluorescence data were collected and analyzed as described above.

Western blot analysis

Cytoplasmic and nuclear proteins were extracted from mouse lungs, and Western blots were performed as previously described[20]. Briefly, protein extracts were resolved on 10% SDS-PAGE. Immunoblot analysis was performed with enhanced chemiluminescence reagents (Amersham Pharmacia Biotech, Chicago, IL, USA).

Statistical analyses

Data were expressed as means±SD. Statistical analyses were performed with SPSS 13.0 using paired-samples *t*-tests or non-parametric tests. For the therapeutic study, one-way ANOVA analysis was performed to assess data differences among various groups. Differences were considered significant at a level of $P<0.05$.

Results

TLR4 mutation enhances apoptosis and oxidative stress in the lungs

Different strains of TLR4-mutant mice (C3H/HeJ, C57BL/10ScNJ, and C57BL/6J backgrounds) all have been shown to exhibit increased lung volumes at 3 months of age, which indicates that the observed phenotypes were independent of strain[7]. In this study, C3H/HeJ $TLR4^{mut}$ mice were used to investigate the mechanisms underlying the development of $TLR4^{mut}$-induced spontaneous emphysema. The lungs of $TLR4^{mut}$ mice showed destruction of the alveolar architecture and enlargement of the air spaces at 3 months of age but not at 0.5 or 1 month of age (Figure 1A). Also, the morphometric quantitation of airspace enlargement revealed that Lm was larger in $TLR4^{mut}$ mice than in WT mice at 3 months of age (66.12±2.61 μm *vs* 55.81±3.93 μm, $P<0.05$), but there were no differences between the lungs of WT and those of $TLR4^{mut}$ mice at either 0.5 or 1 month of age (Figure 1B). In addition, compared with WT mice, TLR4 mutation increased the number of $TUNEL^+$ (blue-green) cells and the levels of MDA in the lungs at 3 months of age (5.09%±1.11% *vs* 1.92%±1.01%, $P<0.01$, and 0.74±0.11 nmol·mg^{-1} protein *vs* 0.47±0.15 nmol·mg^{-1} protein, $P<0.01$, respectively) (Figures 1C and 1E). Also, the expression of cleaved caspase 3, which contributes to cellular apoptosis, was enhanced in the lungs of $TLR4^{mut}$ mice (Figure 1D). These results indicate that TLR4 mutation causes pulmonary emphysema in mice at 3 months of age, which is consistent with the report from Zhang *et al*[7]. Therefore, three-month-old $TLR4^{mut}$ mice were used as our model of spontaneous emphysema for further studies.

Th2, Th17, and Th17-associated cytokines are attenuated in the lungs of $TLR4^{mut}$ mice

TLR activation regulates the maturity of DCs, which prime naïve T cells to determine their polarization into Th1, Th2, Treg or Th17 cells[21]. Th1 cells primarily secrete IL-1, IL-2, IL-12, IL-15, IL-18, IFN-γ, and TNF-α; Th2 cells mainly secrete IL-4, IL-5, IL-6, IL-13; Treg cells principally secrete IL-10 and TGF-β; and Th17 cells predominantly secrete IL-17, IL-6, TNF-α, and IL-22[10]. TLR4 mutation has been shown to reduce the activity of antioxidants and enhance the activity of Nox3 and the production of ROS[7], which contribute to T cell polarization by changing the redox status[11]; our results indicate that the numbers of $CD4^+$IL-17^+ Th17 cells and $CD4^+$IL-13^+ Th2 cells were decreased in the lungs of 3-month-old $TLR4^{mut}$ mice (2.49%±1.13% *vs* 5.26%±1.39%, $P<0.01$, and 6.25%±4.62% *vs* 13.1%±4.07%, $P<0.05$, respectively; Figures 2A and 2C). However, TLR4 mutation did not change the number of $CD4^+CD25^+$ Treg cells or $CD4^+$IFN-γ^+ Th1 cells (Figures 2B, 2D).

The development and differentiation of Th17 cells are regulated by many cytokines, such as IL-6, transforming growth factor (TGF)-β1, IL-23, IL-21, and IL-1. In particular, syner-

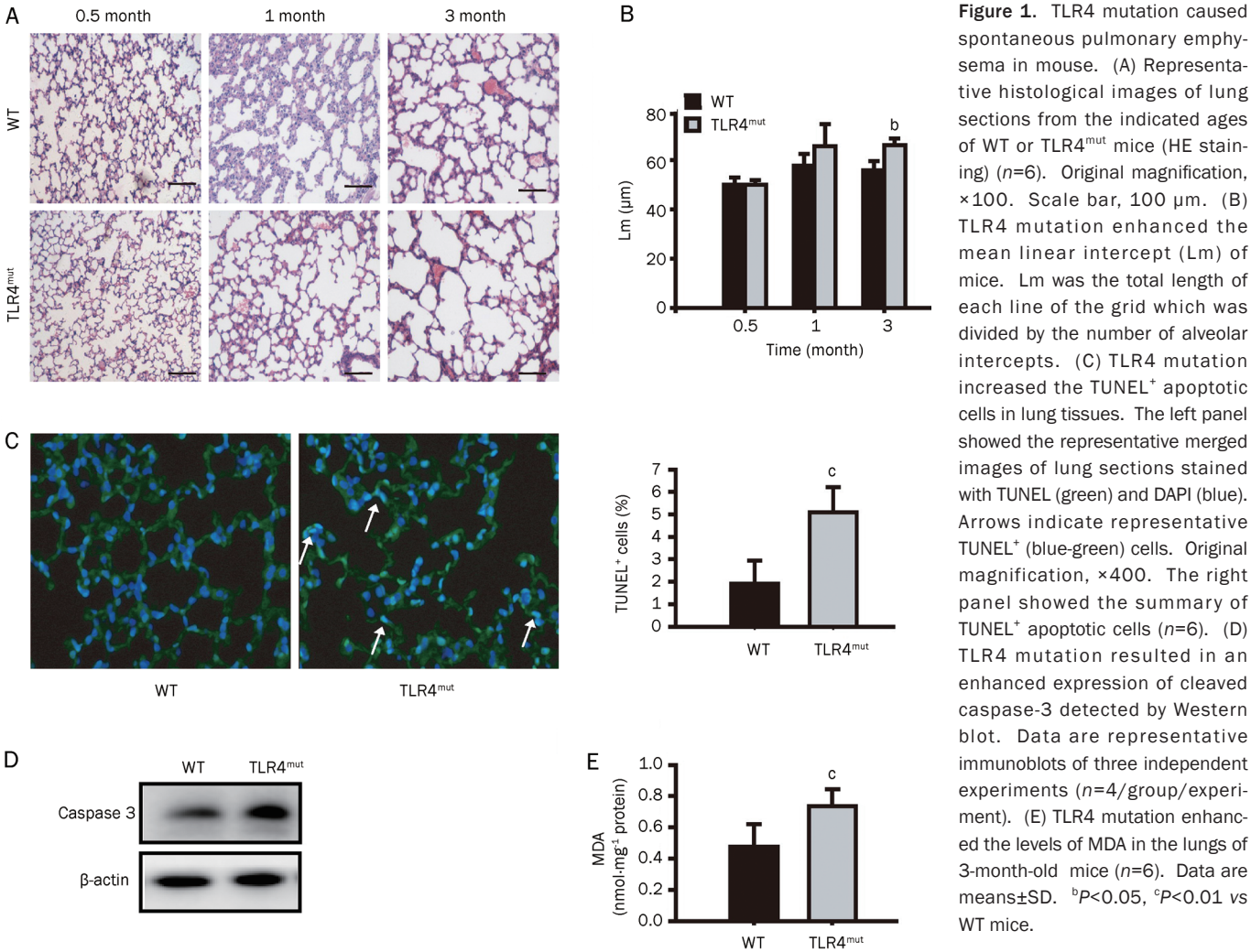

Figure 1. TLR4 mutation caused spontaneous pulmonary emphysema in mouse. (A) Representative histological images of lung sections from the indicated ages of WT or TLR4^{mut} mice (HE staining) (n=6). Original magnification, ×100. Scale bar, 100 μm. (B) TLR4 mutation enhanced the mean linear intercept (Lm) of mice. Lm was the total length of each line of the grid which was divided by the number of alveolar intercepts. (C) TLR4 mutation increased the TUNEL$^+$ apoptotic cells in lung tissues. The left panel showed the representative merged images of lung sections stained with TUNEL (green) and DAPI (blue). Arrows indicate representative TUNEL$^+$ (blue-green) cells. Original magnification, ×400. The right panel showed the summary of TUNEL$^+$ apoptotic cells (n=6). (D) TLR4 mutation resulted in an enhanced expression of cleaved caspase-3 detected by Western blot. Data are representative immunoblots of three independent experiments (n=4/group/experiment). (E) TLR4 mutation enhanced the levels of MDA in the lungs of 3-month-old mice (n=6). Data are means±SD. ^bP<0.05, ^cP<0.01 *vs* WT mice.

gistic activation of TGF-β1 and IL-6 can effectively induce the differentiation of naïve CD4$^+$ T cells into highly pathogenic Th17 cells, while IL-23 is considered to play a vital role in the generation of Th17 cells, which can mediate the immune response[22]. Compared with WT mice, TLR4^{mut} mice contained lower levels of IL-17A (Figure 2E), IL-23 (Figure 2F), and IL-6 (Figure 2H) in the BALF at 3 months of age (3.66±0.99 pg/μg *vs* 10.67±1.65 pg/μg, 12.43±1.28 pg/μg *vs* 28.71±2.57 pg/μg, and 51.82±5.45 pg/μg *vs* 92.73±10.91 pg/μg, respectively, P<0.01), while they displayed higher levels of TGF-β1 (168.18±9.09 pg/μg *vs* 102.27±6.82 pg/μg, P<0.05; Figure 2G). These results indicate that the infiltration of Th17 cells and the production of Th17-associated cytokines were attenuated in TLR4^{mut} mice at 3 months of age.

TLR4 mutation reduces phosphorylation of p38 MAPK and the expression of AP-1

TLR4^{mut} mice have been shown to be characterized by reduced antioxidant activity and enhanced Nox3 expression and ROS production[7]. Oxidative stress plays a fundamental role in the induction of inflammation through the upregulation of redox-sensitive protein kinases and transcription factors, such as MAPK, AP-1, and NF-κB, which are also the downstream signaling molecules of IL-17A[23]. Thus, we examined the changes in the levels of these signaling molecules in the lungs of 3-month-old TLR4^{mut} mice. Compared with WT mice, TLR4 mutation inhibited the phosphorylation of p38 MAPK in the lungs (0.27±0.09 fold of WT levels, P<0.01; Figure 3A) but did not affect the phosphorylation of ERK and JNK kinases in the lungs (Figures 3B and 3C). In addition, TLR4 mutation decreased the expression of AP-1 in the lungs (0.51±0.08 fold of WT levels, P<0.05; Figure 3E) but did not affect the phosphorylation of IκB and NF-κB in the lungs (Figures 3D and 3F). These results indicate that TLR4 mutation results in a reduction in p38 MAPK phosphorylation and AP-1 expression.

IL-17A administration ameliorates TLR4^{mut}-induced pulmonary emphysema

To restore the effects caused by Th17 cells, TLR4^{mut} mice were administered mouse IL-17A. As expected, IL-17A reduced the TLR4^{mut}-induced destruction of the normal alveolar architecture and enlargement of the air spaces distal to the

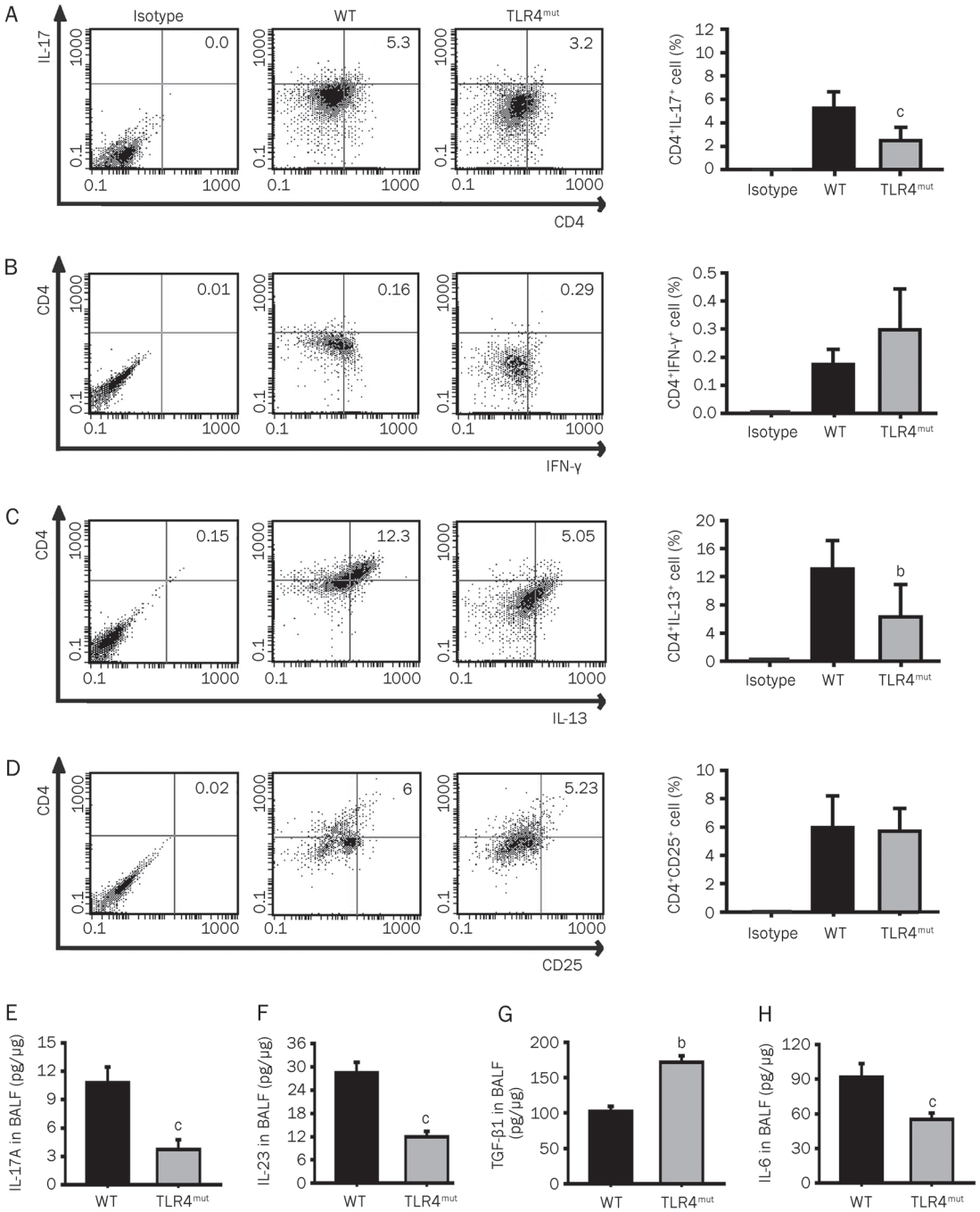

Figure 2. TLR4 mutation regulated the polarization of T cells and the production of cytokines in the lung. Lung single-cell suspensions were prepared with lung tissues from the 3-month-old WT or TLR4^{mut} mice and analyzed with flow cytometry. (A–D) TLR4 mutation reduced the counts of Th17 cells (CD4$^+$IL-17$^+$) (A) and Th2 cells (CD4$^+$IL-13$^+$) (C) but did not change the counts of Th1 cells (CD4$^+$IFN-γ$^+$) (B) and Treg cells (CD4$^+$CD25$^+$) (D). Data are means±SD (n=6). (E–H) TLR4 mutation reduced the levels of IL-17A (E), IL-23 (F), and IL-6 (H) but enhanced the levels of TGF-β1 (G) in the BALF. Data are means±SD of 3 independent experiments. ^bP<0.05, ^cP<0.01 *vs* WT mice.

terminal bronchioles, and it also decreased Lm (Figures 4A, 4C), TUNEL$^+$ apoptotic cells (Figures 4B, 4D) and the levels of MDA (Figure 4E) in the lungs. To evaluate the effectiveness of IL-17A treatment, we examined the infiltration of Th2 cells and Th17 cells into the lungs and the levels of IL-17A, IL-23, IL-6, and TGF-β1 in the BALF of TLR4^{mut} mice. IL-17A administration enhanced the production of IL-17A (Figure 5A), IL-23 (Figure 5B), and IL-6 (Figure 5C) (14.58±1.31 pg/μg *vs* 3.56±1.50 pg/μg, P<0.001; 25.30±8.22 pg/μg *vs* 16.33±5.58 pg/μg, P<0.05; and 129.6±10.87 pg/μg *vs* 57.6±3.66 pg/μg, P<0.01, respectively) but did not enhance the levels of TGF-β1 (Figure 5D). Additionally, IL-17A treatment increased

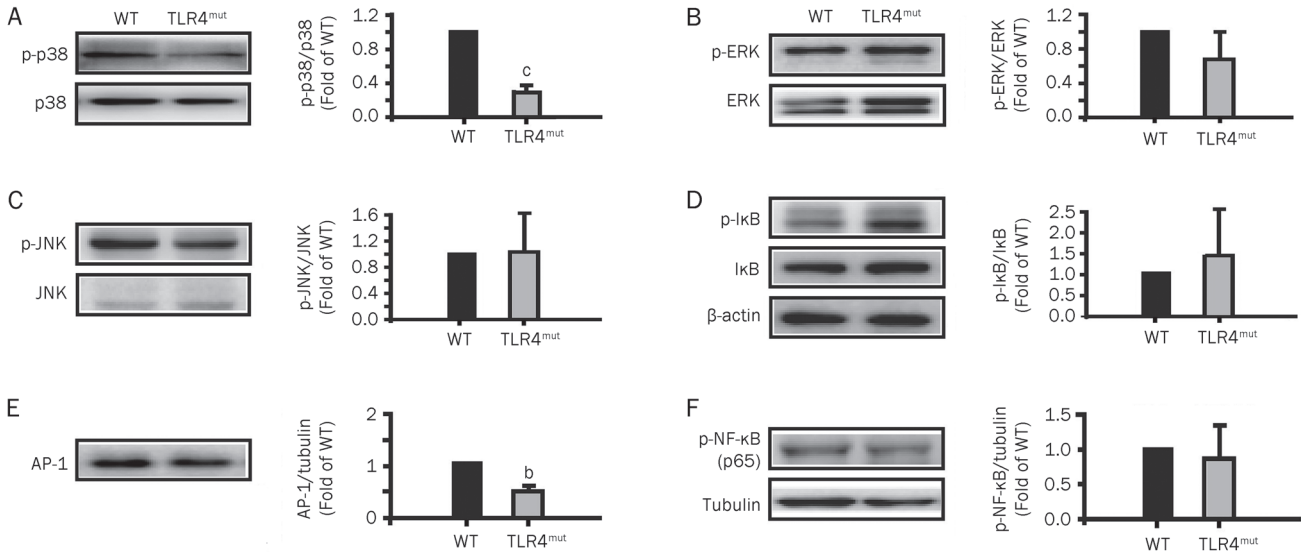

Figure 3. TLR4 mutation regulated the phosphorylation of p38 MAPK and the expression of AP-1. The lung extracts were prepared with the lung tissues obtained from the 3-month-old WT or TLR4^{mut} mice. The expression and phosphorylation of the MAPKs-NF-κB signaling molecules were detected by Western blotting with specific antibodies as indicated. Bands were quantified and presented as fold-difference compared with that of WT mice. (A) The expression and phosphorylation of p38 MAPK were reduced in the lungs from 3-month-old TLR4^{mut} mice. (B–D) The phosphorylation of ERK kinases (B), JNK kinases (C) and IκB (D) in the lungs from 3-month-old TLR4^{mut} mice had no significant change compared with WT mice. (E) TLR4 mutation reduced the expression of AP-1 in the lungs from 3-month-old mice. (F) TLR4 mutation did not change the phosphorylation of NF-κB p65 in the lungs. Data are representatives of three independent experiments with identical results. $^{b}P<0.05$, $^{c}P<0.01$ *vs* WT mice.

Th17 cell infiltration (5.77%±2.91% *vs* 2.49%±1.13%, $P<0.05$; Figure 5E), but it did not significantly enhance Th2 cell infiltration (Figure 5F). Furthermore, IL-17A treatment reversed TLR4^{mut}-reduced phosphorylation of p38 MAPK (Figure 5G) and expression of AP-1 (Figure 5H) in the lungs of 3-month-old TLR4^{mut} mice (1.06±0.08 fold higher than WT *vs* 0.27±0.09 fold of WT levels, $P<0.01$ and 2.34±0.24 fold higher than WT *vs* 0.51±0.08 fold of WT levels. $P<0.01$, respectively). These results indicate that treatment of TLR4^{mut} mice with IL-17A ameliorates pulmonary emphysema though restoration of Th17 cell infiltration and enhancement of IL-17-associated signaling.

Discussion

In this study, we observed that TLR4 mutation results in age-dependent development of spontaneous pulmonary emphysema in 3-month-old mice, which is consistent with the report by Zhang *et al*[7]. The progression of emphysema in TLR4-mutant mice is akin to the progression of emphysema that develops in humans. Therefore, spontaneous emphysema in TLR4-mutant mice is an excellent model for investigating the pathogenesis of emphysema. Emphysema is considered an autoimmune disease[8], while IL-17 has been demonstrated to play vital roles in autoimmune diseases as a major pro-inflammatory mediator that promotes the production of many chemokines, cytokines, and growth factors[24]. Thus, it is important to provide evidence to establish whether there is a relationship between Th17 cells or IL-17 cytokines and TLR4^{mut}-induced emphysema. Our studies demonstrate that infiltration of Th17 cells and expression of IL-17 are attenuated in the lungs of 3-month-old TLR4^{mut} mice with emphysema, and the p38 MAPK and AP-1 pathways are inhibited in the lung tissue of TLR4^{mut} mice with emphysema. Moreover, administration of recombinant mouse IL-17A resulted in restoration of Th17 cell infiltration and enhanced IL-17A, IL-23, and IL-6 expression, which reversed the attenuated phosphorylation of p38 MAPK and expression of AP-1, decreased the levels of MDA, inhibited cellular apoptosis, and reversed TLR4^{mut}-induced pulmonary emphysema. However, although the infiltration of Th2 cells was attenuated in the lungs of 3-month-old TLR4^{mut} mice with emphysema, administration of recombinant mouse IL-17A did not raise the levels of infiltrating Th2 cells into the lungs. Our findings indicate that Th17 cells, and in particular the cytokine IL-17A secreted from these cells, play a crucial role in lung epithelia integration during animal development, suggesting that Th17 cells and IL-17A-associated signaling pathways are potential targets for novel pulmonary emphysema therapies.

The mechanism governing the enhanced expression of IL-17A and Th17-associated cytokines after administration of IL-17A is associated with an increase in lung-infiltrating Th17 cells. TGF-β1 and IL-6 have been shown to be required for the differentiation of naïve T cells into Th17 cells in mice[22], while IL-23 has been shown to stabilize and expand the population of Th17 cells[25]. In TLR4^{mut} mice, the expression levels of IL-17, IL-6 and IL-23 in the lungs are all depressed, which results in an attenuation of the lung-infiltrating Th17 cells. A previous study indicated that IL-17 is an important inducer of IL-6

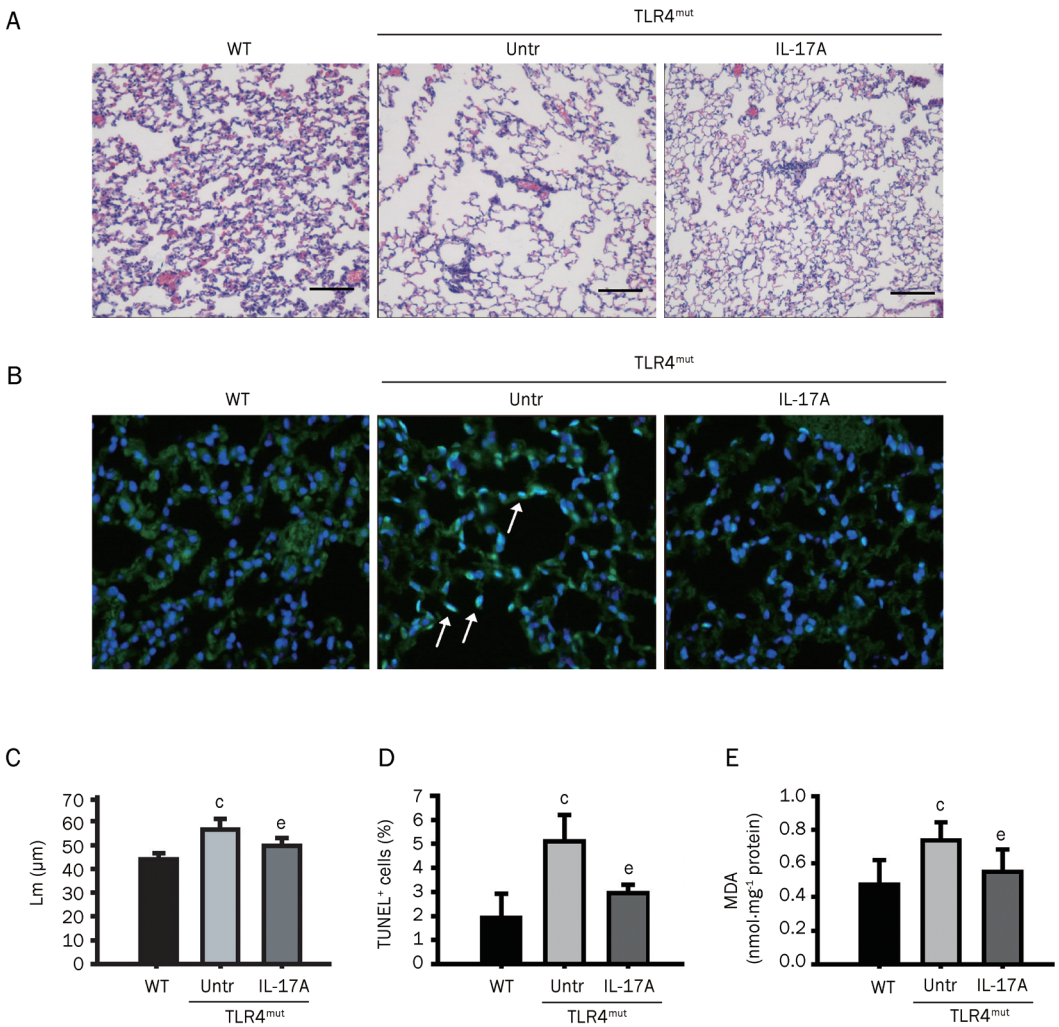

Figure 4. Treatment of TLR4^{mut} mice with IL-17A ameliorated spontaneous pulmonary emphysema. (A) IL-17A ameliorated alveolar enlargement and Lm of lung tissue in TLR4^{mut} mice. Left panel, the alveolar enlargement was detected with histological analysis lung sections by HE staining (n=6). Original magnification, ×100. Scale bar, 100 μm. (B) Treatment with IL-17A decreased the TUNEL$^+$ apoptotic cells in the lungs. The panel showed the representative merged images of lung sections stained with TUNEL (green) and DAPI staining (blue). Arrows indicate representative TUNEL$^+$ (blue-green) cells. Original magnification, ×200. (C) The summary of Lm. (D) The summary for the number of TUNEL$^+$ cells in lungs. (E) IL-17A treatment reduced the levels of MDA in the lungs from 3-month-old TLR4^{mut} mice (n=6). Data are means±SD (n=6). ^bP<0.05, ^cP<0.01 *vs* WT mice; ^eP<0.05, ^fP<0.01 *vs* TLR4^{mut} mice.

expression[26]; our recent work showed that IL-17A directly induces the expression of TGF-β1 (Mi *et al*, unpublished observations). In our current study, we found that administration of IL-17A recovers the expression of IL-6 and IL-23 in the lungs of TLR4^{mut} mice. Indeed, Mudter *et al* found that overexpression of IRF4 using retroviral infection induces IL-17 production and that IL-17 together with IL-6 induces RORγt expression, thereby controlling Th17-dependent colitis[27].

Our findings have been supported by other studies as well. Inoue *et al* have reported that IL-17A can stimulate keratinocytes to produce vascular endothelial growth factor (VEGF), granulocyte-macrophage colony-stimulating factor (GM-CSF), TNF-α, IL-8, and CXCL10 and subsequently promote the growth and repair of airway epithelial cells[13]. Additionally, up-regulation of IL-17A has been demonstrated to induce the process of tissue fibrosis, which is opposite to the process of emphysema, in chronic periodontitis sites, heart, skin and lungs[28, 29]. However, there have also been some reports that are opposed to the above-mentioned results regarding the association between IL-17A and emphysema. Others have indicated that airway infiltration of CD4$^+$CCR6$^+$ Th17 cells are associated with chronic cigarette smoke induced airspace enlargement[30, 31]. Four-month exposure to smoke, a major stimulator of emphysema, can induce significant increases in IL-17 levels in the pulmonary airway[32]. These studies indicate that the physiological concentration of IL-17A is a critical factor for lung epithelial development and for tissue repair or regeneration after tissue injury. However, excessive

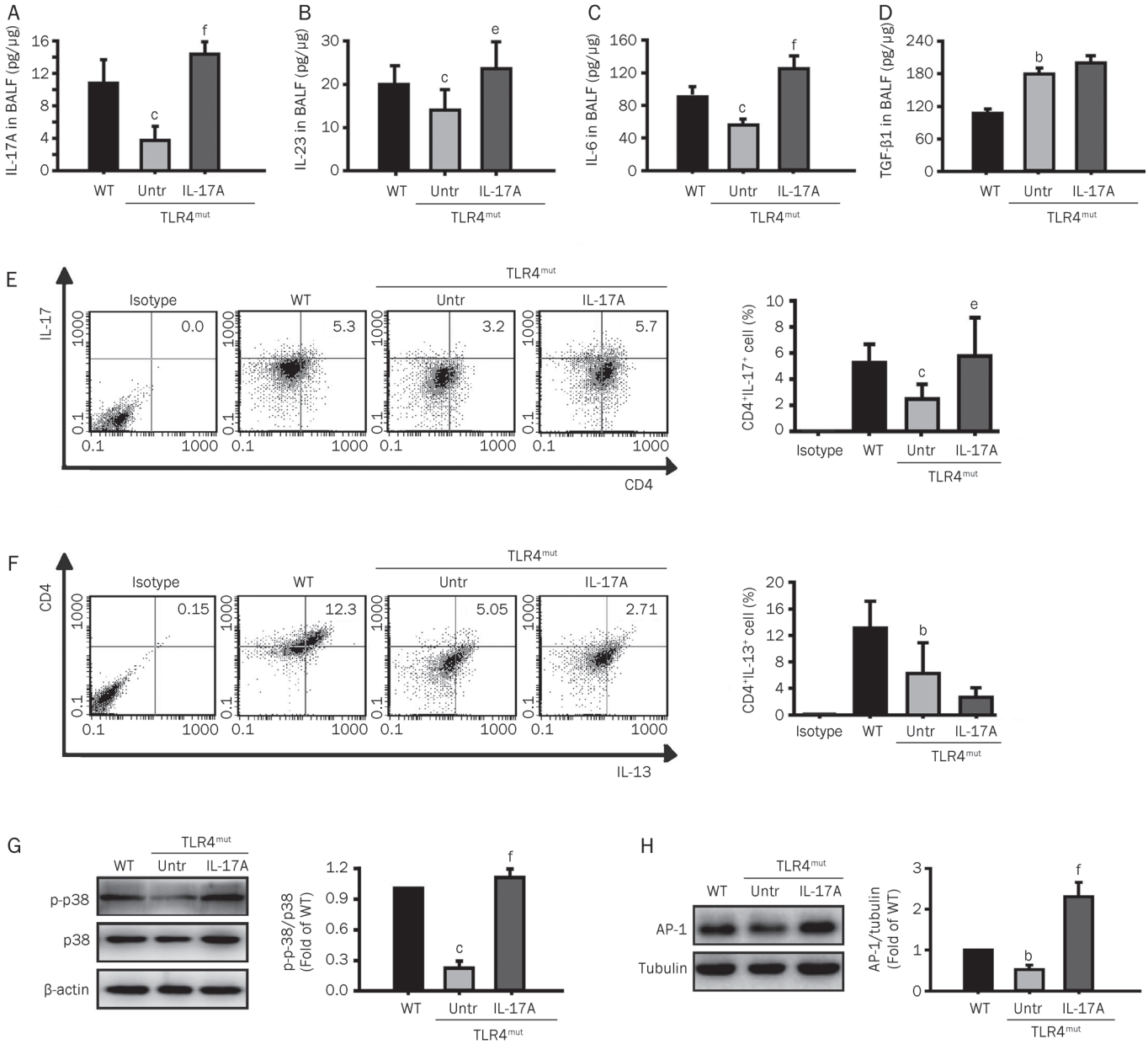

Figure 5. Administration with IL-17A reversed TLR4^{mut}-reduced IL-17A, Th17, and the phosphorylation of p38 MAPK and expression of AP-1 in the lungs. The TLR4^{mut} mice were administered with mouse IL-17A as described in the Methods section. (A–D) Treatment with IL-17A enhanced the levels of IL-17A (A), IL-23 (B), and IL-6 (C), but did not enhance the levels of TGF-β1 (D) in the BALF of TLR4^{mut} mice (n=6). (E–F) Treatment of mice with IL-17A increased the infiltration of Th17 cells into the lungs from TLR4^{mut} mice. Flow cytometry was used to analyze the levels of Th17 cells (CD4$^+$IL-17$^+$, E) and Th2 cells (CD4$^+$IL-13$^+$, F) in the lung single-cell suspensions prepared from the lung tissues of 3-month-old WT or TLR4^{mut} mice (n=6). (G–H) Administration of IL-17A reversed the TLR4^{mut}-reduced phosphorylation of p38 MAPK and expression of AP-1 in the lungs. Mouse IL-17A treatment enhanced the phosphorylation of p38 MAPK (G) and the expression of AP-1 (H) in the lungs from the 3-month-old TLR4^{mut} mice. The tissue extracts were prepared with the lung tissues obtained from the 3-month-old WT or TLR4^{mut} mice. The phosphorylation of p38 MAPK and expression of AP-1 were detected by Western blotting with indicated antibodies. Bands were quantified and presented as fold-difference of that of WT mice (n=3). Data are means±SD. ^bP<0.05, ^cP<0.01 *vs* WT mice; ^eP<0.05, ^fP<0.01 *vs* TLR4^{mut} mice.

expression levels of IL-17A (plus other inflammatory factors, such as TGF-β1) can result in tissue fibrosis and even organ dysfunction.

The attenuation of Th17 cells and IL-17A-associated factors is mainly due to a mutation in TLR4 signaling. Indeed, there are a number of studies that have indicated a regulatory role for TLR4 activation in the development of Th17 cells and the production of Th17-associated cytokines. Under physiological conditions, basal activity of TLR4 induced by damage-associated molecular pattern molecules, such as myeloid-related

protein-8 (Mrp8) and Mrp14, is required for Th17-induced protective immunity that contributes to the defense against infection and the repair of slight tissue injury[33, 34]. Under infectious conditions, pathogens induce a higher level of Th17-associated factors, such as IL-17, IL-1β, pSTAT3, and RORγt, through activation of TLR4[35]. Indeed, TLR4 activity has been shown to be required for gram-negative bacterial pneumonia-induced IL-17 production[36] and for the mycobacterium tuberculosis-induced IL-17A response[37]. TLR4-mutant mice display lower expression levels of IL-1β, TNF-α, IFN-γ, IL-17, and IL-23 in the lungs after vaccination with pertussis vaccines[38]. Interestingly, TLR2-promoted Th2/Th17 responses are caused by activation of TLR4 and TLR7/8 and subsequent abrogation of the type I IFN amplification loop[39]. However, further investigations are needed to fully understand the mechanisms concerning how TLR4 activity regulates the development of Th17 cells and the production of Th17-associated factors.

In summary, our current study indicates that Th17 cells and IL-17A-associated signaling molecules play a crucial role in TLR4^{mut}-induced spontaneous pulmonary emphysema. Importantly, treatment of TLR4-mutant mice with exogenous IL-17A enhanced the phosphorylation of p38 MAP kinase and the expression of AP-1 and subsequently decreased apoptosis levels and reversed TLR4^{mut}-induced pulmonary emphysema. Our study highlights the fact that Th17 cells and IL-17A-associated signaling molecules are potential targets for the development of therapeutic strategies against pulmonary emphysema.

Acknowledgements

This study was supported by grants from the National Major Basic Research Program of China (2006CB503808), the Creation of Major New Drugs (2009ZX09301-003-13), and the National Natural Science Foundation of China (30672468; 30901814; 81030056). Dr Zhuo-wei HU is also supported by the Cheung-Kong Scholars Programme from the Ministry of Education and the Senior Oversea Chinese Scholar Fund from the Ministry of Personnel of People's Republic of China.

Author contribution

Qing-qing WANG performed research experiments, analyzed data and wrote the manuscript; Hong-zhen YANG performed part of the research experiments and helped write the manuscript; Han-zhi LIU, Su MI, Xiao-wei ZHANG, Hui-min YAN, Yong-gang MA, and Xiao-xing WANG performed part of the research experiments together with Qing-qing WANG; and Zhuo-wei HU conceived and designed the experiments, edited and modified the manuscript.

References

1 Yoshida T, Tuder RM. Pathobiology of cigarette smoke-induced chronic obstructive pulmonary disease. Physiol Rev 2007; 87: 1047–82.
2 Taraseviciene-Stewart L, Voelkel NF. Molecular pathogenesis of emphysema. J Clin Invest 2008; 118: 394–402.
3 Barr RG, Bluemke DA, Ahmed FS, Carr JJ, Enright PL, Hoffman EA, *et al*. Percent emphysema, airflow obstruction, and impaired left ventricular filling. N Engl J Med 2010; 362: 217–27.
4 Boutten A, Goven D, Boczkowski J, Bonay M. Oxidative stress targets in pulmonary emphysema: focus on the Nrf2 pathway. Expert Opin Ther Targets 2010; 14: 329–46.
5 Horowitz JC, Martinez FJ, Thannickal VJ. Mesenchymal cell fate and phenotypes in the pathogenesis of emphysema. COPD 2009; 6: 201–10.
6 Calverley PM, Rennard SI. What have we learned from large drug treatment trials in COPD? Lancet 2007; 370: 774–85.
7 Zhang X, Shan P, Jiang G, Cohn L, Lee PJ. Toll-like receptor 4 deficiency causes pulmonary emphysema. J Clin Invest 2006; 116: 3050–9.
8 Lee SH, Goswami S, Grudo A, Song LZ, Bandi V, Goodnight-White S, *et al*. Antielastin autoimmunity in tobacco smoking-induced emphysema. Nat Med 2007; 13: 567–9.
9 Vercelli D. Gene-environment interactions in asthma and allergy: the end of the beginning? Curr Opin Allergy Clin Immunol 2010; 10: 145–8.
10 Afzali B, Lombardi G, Lechler RI, Lord GM. The role of T helper 17 (Th17) and regulatory T cells (Treg) in human organ transplantation and autoimmune disease. Clin Exp Immunol 2007; 148: 32–46.
11 Gill R, Tsung A, Billiar T. Linking oxidative stress to inflammation: Toll-like receptors. Free Radic Biol Med 2010; 48: 1121–32.
12 Won HY, Sohn JH, Min HJ, Lee K, Woo HA, Ho YS, *et al*. Glutathione peroxidase 1 deficiency attenuates allergen-induced airway inflammation by suppressing Th2 and Th17 cell development. Antioxid Redox Signal 2010; 13: 575–87.
13 Inoue D, Numasaki M, Watanabe M, Kubo H, Sasaki T, Yasuda H, *et al*. IL-17A promotes the growth of airway epithelial cells through ERK–dependent signaling pathway. Biochem Biophys Res Commun 2006; 347: 852–8.
14 Kawakami M, Matsuo Y, Yoshiura K, Nagase T, Yamashita N. Sequential and quantitative analysis of a murine model of elastase–induced emphysema. Biol Pharm Bull 2008; 31: 1434–8.
15 D'Hulst AI, Vermaelen KY, Brusselle GG, Joos GF, Pauwels RA. Time course of cigarette smoke-induced pulmonary inflammation in mice. Eur Respir J 2005; 26: 204–13 .
16 Zha RP, Xu W, Wang WY, Dong L, Wang YP. Prevention of lipopolysaccharide-induced injury by 3,5-dicaffeoylquinic acid in endothelial cells. Acta Pharmacol Sin 2007; 28: 1143–8.
17 Traidl-Hoffmann C, Mariani V, Hochrein H, Karg K, Wagner H, Ring J, *et al*. Pollen-associated phytoprostanes inhibit dendritic cell interleukin-12 production and augment T helper type 2 cell polarization. J Exp Med 2005; 201: 627–36.
18 Yang HZ, Cui B, Liu HZ, Chen ZR, Yan HM, Hua F, *et al*. Targeting TLR2 attenuates pulmonary inflammation and fibrosis by reversion of suppressive immune microenvironment. J Immunol 2009; 182: 692–702.
19 Jakob T, Walker PS, Krieg AM, Udey MC, Vogel JC. Activation of cutaneous dendritic cells by CpG-containing oligodeoxynucleotides: a role for dendritic cells in the augmentation of Th1 responses by immunostimulatory DNA. J Immunol 1998; 161: 3042–9.
20 Cai WF, Zhang XW, Yan HM, Ma YG, Wang XX, Yan J, *et al*. Intracellular or extracellular heat shock protein 70 differentially regulates cardiac remodelling in pressure overload mice. Cardiovasc Res 2010; 88: 140–9.
21 Amati L, Pepe M, Passeri ME, Mastronardi ML, Jirillo E, Covelli V. Toll-like receptor signaling mechanisms involved in dendritic cell activation: potential therapeutic control of T cell polarization. Curr Pharm Des 2006; 12: 4247–54.
22 Korn T, Bettelli E, Oukka M, Kuchroo VK. IL-17 and Th17 cells. Annu

Rev Immunol 2009; 27: 485–517.
23 Gaffen SL. Structure and signalling in the IL-17 receptor family. Nat Rev Immunol 2009; 9: 556–67.
24 Hong SC, Lee SH. Role of Th17 cell and autoimmunity in chronic obstructive pulmonary disease. Immune Netw 2010; 10: 109–14.
25 McKenzie BS, Kastelein RA, Cua DJ. Understanding the IL-23 — IL-17 immune pathway. Trends Immunol 2006; 27: 17–23.
26 Kishimoto T. Interleukin-6: from basic science to medicine — 40 years in immunology. Annu Rev Immunol 2005; 23: 1–21.
27 Mudter J, Yu J, Zufferey C, Brüstle A, Wirtz S, Weigmann B, *et al*. IRF4 regulates IL-17A promoter activity and controls RORγt-dependent Th17 colitis *in vivo*. Inflamm Bowel Dis 2011; 17: 1343–58.
28 Duarte PM, Santos VR, Dos Santos FA, de Lima Pereira SA, Rodrigues DB, Napimoga MH. Role of smoking and type 2 diabetes in the immunobalance of advanced chronic periodontitis. J Periodontol 2011; 82: 429–38.
29 Yoshizaki A, Yanaba K, Iwata Y, Komura K, Ogawa A, Akiyama Y, *et al*. Cell adhesion molecules regulate fibrotic process via Th1/Th2/Th17 cell balance in a bleomycin-induced scleroderma model. J Immunol 2010; 185: 2502–15.
30 Harrison OJ, Foley J, Bolognese BJ, Long E 3rd, Podolin PL, Walsh PT. Airway infiltration of $CD4^+$ $CCR6^+$ Th17 type cells associated with chronic cigarette smoke induced airspace enlargement. Immunol Lett 2008; 121: 13–21.
31 Lane N, Robins RA, Corne J, Fairclough L. Regulation in chronic obstructive pulmonary disease: the role of regulatory T-cells and Th17 cells. Clin Sci (Lond) 2010; 119: 75–86.
32 Melgert BN, Timens W, Kerstjens HA, Geerlings M, Luinge MA, Schouten JP, *et al*. Effects of 4 months of smoking in mice with ovalbumin-induced airway inflammation. Clin Exp Allergy 2007; 37: 1798–808.
33 Tang H, Pang S, Wang M, Xiao X, Rong Y, Wang H, *et al*. TLR4 activation is required for IL-17-induced multiple tissue inflammation and wasting in mice. J Immunol 2010; 185: 2563–9.
34 Loser K, Vogl T, Voskort M, Lueken A, Kupas V, Nacken W, *et al*. The Toll-like receptor 4 ligands Mrp8 and Mrp14 are crucial in the development of autoreactive $CD8^+$ T cells. Nat Med 2010; 16: 713–7.
35 Mu HH, Hasebe A, Van Schelt A, Cole BC. Novel interactions of a microbial superantigen with TLR2 and TLR4 differentially regulate IL-17 and Th17-associated cytokines. Cell Microbiol 2011; 13: 374–87.
36 Bhan U, Ballinger MN, Zeng X, Newstead MJ, Cornicelli MD, Standiford TJ. Cooperative interactions between TLR4 and TLR9 regulate interleukin 23 and 17 production in a murine model of gram negative bacterial pneumonia. PLoS One 2010; 5: e9896.
37 van de Veerdonk FL, Teirlinck AC, Kleinnijenhuis J, Kullberg BJ, van Crevel R, van der Meer JW, *et al*. Mycobacterium tuberculosis induces IL-17A responses through TLR4 and dectin-1 and is critically dependent on endogenous IL-1. J Leukoc Biol 2010; 88: 227–32.
38 Banus S, Stenger RM, Gremmer ER, Dormans JA, Mooi FR, Kimman TG, *et al*. The role of Toll-like receptor-4 in pertussis vaccine-induced immunity. BMC Immunol 2008; 9: 21.
39 Wenink MH, Santegoets KC, Broen JC, van Bon L, Abdollahi–Roodsaz S, Popa C, *et al*. TLR2 promotes Th2/Th17 responses via TLR4 and TLR7/8 by abrogating the type I IFN amplification loop. J Immunol 2009; 183: 6960–70.

Acta Pharmacologica Sinica (2011) 32: 1055–1062
 1671-4083/11 $32.00
www.nature.com/aps

Original Article

Cholera toxin inhibits human hepatocarcinoma cell proliferation *in vitro* via suppressing ATX/LPA axis

Qi XIA[1, #], An-mei DENG[2, #], Shan-shan WU[1], Min ZHENG[1, *]

[1]*State Key Laboratory of Infectious Disease Diagnosis and Treatment, First Affiliated Hospital, College of Medicine, Zhejiang University, Hangzhou 310003, China;* [2]*Laboratory Diagnostics, Shanghai Changzheng Hospital, Shanghai 200003, China*

Aim: To investigate the antitumor effect of cholera toxin (CT) in hepatocellular carcinoma (HCC) *in vitro* and the mechanisms underlying the effect.
Methods: Human hepatocellular carcinoma cell lines Hep3B and Huh7, which expressed moderate and high level of autotaxin (ATX), respectively, were used. Cytokine level in the cells was evaluated using ELISA assay, and cell proliferation was investigated using MTT assay. ATX expression was determined using Western blot. ATX/lyso-PLD activity in the conditioned medium was measured using FS-3, a fluorescent lysophosphatidylcholine (LPC) analogue, as substrate.
Results: Exposure to CT (7.5 and 10 ng/mL) significantly inhibited the cell growth, decreased secretion of proinflammatory cytokine TNF-α and promoted secretion of anti-inflammatory cytokines IL-4 and IL-10. CT at 10 ng/mL markedly suppressed ATX expression in Hep3B and Huh7 cells. Furthermore, ATX and lysophosphatidic acid (LPA) were found to be crucial for growth of the cancer cells. CT could inhibit TNF-α-induced expression and secretion of ATX that led to decreased activity of lysophospholipase D, thus decreasing the conversion of LPC to LPA.
Conclusion: CT inhibits hepatocellular carcinoma cell growth *in vitro* via regulating the ATX-LPA pathway.

Keywords: cholera toxin; hepatocarcinoma; autotaxin; lysophosphatidic acid; cell proliferation

Acta Pharmacologica Sinica (2011) 32: 1055–1062; doi: 10.1038/aps.2011.31; published online 18 Jul 2011

Introduction

Hepatocellular carcinoma (HCC) is the third most common cause of cancer-related death worldwide[1, 2]. The increasing incidence and poor prognosis of hepatocellular carcinoma[3] emphasize a need to develop effective chemoprevention for this disease. In recent years, many biological factors with potential prognostic significance for HCC have been associated with the invasiveness, metastasis, recurrence, and survival of HCC[4].

Autotaxin (ATX), discovered in human melanoma cells, was identified as a gene with enhanced mRNA expression in human hepatitis associated HCC[5]. ATX was initially characterized as an autocrine motility factor found in conditioned medium from A2058 melanoma cells[6]. Since then, it has been shown that ATX is an important mediator of tumorigenesis that stimulates angiogenesis, survival, growth, migration, and invasion of tumor cells[7–9]. The impact of ATX on cancer biology is mostly due to its intrinsic lysophospholipase activity, through which it hydrolyzes lysophosphatidylcholine (LPC) into lysophosphatidic acid (LPA). ATX plays an important role in inflammation related liver tumorigenesis, and aberrant ATX expression may lead to altered LPC/LPA balance and thus changes in their receptor-mediated functions, resulting in enhanced tumor progression[10].

LPA acts through the G-protein coupled EDG (endothelial differentiation gene) receptors to modulate cell motility. EDG receptor signal transduction is associated with a number of physiologic and pathophysiological effects. In the context of cancer, the pathophysiological effects of LPA include stress fiber formation, membrane ruffling, and lamellipodia formation[9], which have been linked to the malignant phenotype.

Cholera toxin (CT) is the major virulent factor of *Vibrio cholerae* and is the most recognizable enterotoxin causing diarrhea, second only to cardiovascular disease as a cause of death[11]. It is known to bind with high affinity to monosialoganglioside (GM) on the cell surface and stimulate ADP-ribosylation of the stimulating G protein of adenylate cyclase, G stimulatory, resulting in accumulation of cellular cAMP[12, 13]. CT has been

# These authors contributed equally to this work.
* To whom correspondence should be addressed.
E-mail minzheng@zju.edu.cn
Received 2010-11-15 Accepted 2011-03-18

reported to modulate cellular function, including modification of cell growth. For example, CT stimulates the growth of cultured human mammary epithelial cells[14] and epithelial cells from normal human bronchus[15] in the presence of serum or growth factors. In contrast, it has also been shown that CT influences the proliferation of hormone-dependent rat mammary cancer cells[16] and human small-cell lung cancer cells[17]. Although the mechanism behind CT-induced cellular events is not definitively known at present, it is believed that increased intracellular cAMP is a participating element. However, Viallet *et al* have reported that elevation of cellular cAMP alone could not account for CT-induced growth inhibition of human small-cell lung cancer[17]. Moreover, the effect of CT on hepatocellular carcinoma remains unclear.

In this study, we examined the direct anti-proliferative effects of CT on the human hepatocellular carcinoma cell lines, Hep3B and Huh7, and the indirect effects of CT on cell growth, through regulation of proinflammatory cytokine secretion and the ATX/LPA axis in HCC cells.

Materials and methods

Reagents

CT was purchased from Sigma Chemical Co (St Louis, MO, USA). The polyclonal antibody against ATX was generated in rabbits as previously described[18]. ATX activity assay reagents were from Echelon Biosciences, Inc (Salt lake City, UT, USA). Fatty acid-free bovine serum albumin (BSA) was from Calbiochem-Novabiochem Co (San Diego, CA, USA). LPC (1-oleoyl) was obtained from Avanti Polar Lipids, Inc (Alabaster, AL, USA). Ki16425 was from Cayman Chemical (Ann Arbor, MI, USA).

Cell lines and cell culture

The human hepatocarcinoma cell line Hep3B was purchased from ATCC (HB-8064^{TM}). The human hepatoma Huh-7 cell line was purchased from Japanese Collection of Research Bioresources (Tokyo, Japan; JCRB0403). All cells were cultured in Dulbecco's modified Eagle's medium (DMEM; Sigma-Aldrich, St Louis, Mo, USA) supplemented with 10% (*v*/*v*) fetal bovine serum (FBS) (JRH Biosciences, Lenexa, KS, USA). All cultured cells were incubated at 37 °C in a humidified atmosphere containing 5% CO_2. Cells were serum-starved overnight and then treated with CT. Total RNA was extracted or cell lysate was prepared after stimulation for the indicated time.

Proliferation assay

Cell proliferation was evaluated by 3-(4,5-dimethylthiazol-2-yl)-2,5-diphenyl tetrazolium bromide (MTT) assay. Cells were seeded at a density of 5×10^3 cells per well in 96-well plates, and the cells were treated with reagents at different concentrations for 72 h. Four hours prior to reading the plates, MTT was added under sterile conditions, and the cells were returned to the incubator. After incubation, the plates were read in an enzyme-linked immunosorbent assay (ELISA) plate reader at absorbance measurements of 570 nm. Each experiment was performed in six replicate wells and independently repeated four times.

[^{3}H]-TdR incorporation in Hep3B or Huh7 cells was performed in 96-well microtiter plates. After 48 h in culture, 1 pCi of [6-^{3}H]thymidine (Amersham, Buckinghamshire, UK) was added for 6 h. At the end of the incubation period, cells were procured on filters, and the incorporated radioactivity was counted.

siRNA transfection

The human hepatocarcinoma cell lines Hep3B or Huh7 were plated on 6-cm dishes. Sixteen hours later, siRNAs (final concentration of 3 nmol/L) were added to the cells using an RNAiMAX reagent (Invitrogen, Carlsbad, CA, USA) according to the manufacturer's instructions, and the cells were further cultured for 24 h. The ATX messenger RNA (mRNA) level was measured using real-time TaqMan technology. A cell proliferation assay was performed after 24 h of serum starvation, as described previously. The siRNAs for ATX (siATX, L-019059), LPA_1 (siLPA_1, L-003656), LPA_2 (siLPA_2, L-004602), LPA_3 (siLPA_3, L-004895), and non-silencing RNA (NS, D-001810-10) were obtained from Dharmacon (Lafayette, CO, USA).

Quantitative real time RT-PCR (qRT-PCR)

Total RNA was isolated from cells using the RNeasy kit, following the manufacturer's instructions (QIAGEN, Valencia, CA, USA). Total RNA (2 μg) was reverse-transcribed in a total reaction volume of 20 μL using the high capacity cDNA reverse transcriptase kit (Applied Biosystems, Foster City, CA, USA) as described by the manufacturer. Single stranded cDNA products were then analyzed by real-time PCR using standard commercially available TaqMan probes for ATX (Hs00196470_m1). The amount of target gene was normalized to the internal standard 18S rRNA (Hs99999901_s1) and reported as a relative value.

Cytokine concentration assay

Cytokine concentrations were determined using commercially available enzyme-linked immunosorbent assay (ELISA) kits. TNF-α, IL-4, and IL-10 secretion from Hep3B and Huh7 cells was determined by studies to measure their biological activity and by an ELISA assay. To measure the biological activity of these cytokines, Hep3B and Huh7 cells were plated at a concentration of 5×10^3 cells/well in 96-well plates, and the cells were treated with CT at different concentrations. After 12 h of incubation, TNF-α, IL-4, and IL-10 levels were determined by Quantikine high-sensitivity ELISA kits (R&D Systems; Minneapolis, MN, USA), which were used according to the manufacturer's instructions.

Preparation of conditioned media and cell lysates and immunoblot analysis

Conditioned media were prepared by incubating 80% confluent cells in dishes for 24 h in serum-free DMEM containing 0.1% fatty acid-free BSA. Media were harvested, clarified

by centrifugation, and filtered through a 0.22-μm filter. The media were concentrated by Amicon Ultra-15 Centrifugal Filter Units before being used for immunoblot analysis. At the same time, total cell lysates were prepared from cell monolayers incubated in RIPA buffer [50 mmol/L Tris-HCl, pH 7.4; 150 mmol/L NaCl; 2 mmol/L EDTA, 1 mmol/L sodium orthovanadate, 1% Nonidet P40; 1% sodium deoxycholate; 0.1% sodium dodecylsulfate (SDS), 2 mmol/L phenylmethylsulfonyl fluoride (PMSF), and protease inhibitor cocktail]. Fifteen micrograms of total cellular protein was resolved by SDS-PAGE. Blots were probed with appropriate antibodies. Anti-β-actin was used as a loading control.

ATX/lyso-PLD activity assay

The conditioned serum-free medium from Hep3B and Huh7 cells stimulated with reagents was concentrated (40-fold) using Amicon Ultra 50000 (Millipore). DMEM without cells was used as a control. ATX/lyso-PLD activity in concentrated conditioned medium was analyzed using the fluorogenic substrate FS-3 according to the manufacturer's protocol. Briefly, 10 μL concentrated medium was mixed with 5 μmol/L FS-3 and assayed in a 96-well plate. Changes in fluorescent intensity were measured with a SpectraMax Gemini EM Fluorescence Microplate Reader (Molecular Devices, Sunnyvale, CA, USA) with excitation and emission wavelengths of 485 and 525 nm, respectively.

Lipid extraction and analysis

Lipids were extracted from conditioned media and analyzed using LC-MS (API-4000, Applied Biosystems)[18, 19]. Briefly, conditioned media were incubated with 15 μmol/L LPC for 3 h at 37 °C. Samples (1.3 mL) were mixed with 3 mL of MeOH/chloroform (2:1) following the addition of 10 μL of LPA (1 μmol/L) as an internal standard and 10 μL of HCl (6 mol/L). The samples were vortexed for 1 min and incubated on ice for 10 min. Chloroform (1 mL) and PBS (1×) (0.5 mL) were added to separate the phases, and samples were vortexed for 1 min prior to centrifugation (1750×*g* for 10 min, at 10 °C). The lower phase was transferred to a new glass tube. The upper phase was re-extracted using 2 mL chloroform and combined with the lower phase. After the solvent was evaporated under nitrogen at room temperature, the dried lipids were re-extracted using 2 mL chloroform and combined with the lower phase. After evaporating the solvent under nitrogen at room temperature, the dried lipids were re-suspended in 100 μL of MeOH and 10 μL of sample, respectively, and subsequently used for mass spectrometry (MS) analyses. Typical operating parameters for MS were as follows: nebulizing gas (NEB) 15, curtain gas (CUR) 8, collision-activated dissociation (CAD) gas 35, electro-spray voltage 5000 with positive-ion MRM mode, and a heater temperature of 500 °C. Precursor mode 153 was set as the daughter ions of LPA. The dwell time in the MRM mode was 75 ms. A TARGA C18 5 μmol/L, 2.1 mm id×10 mm TR-0121-C185 (Higgins Analytical, Southborough, MA, USA) HPLC column was used for the separation of different phospholipids and for the detection of LPAs. The mobile phase A was MeOH/water/NH_4OH (90:10:0.1, *v*/*v*/*v*). The HPLC separations were performed at 12 min/sample using the following scheme: 1) 100% A for 3 min with a flow rate of 0.2 mL/min; 2) the mobile phase was changed from 100% A to 100% B for 2 min with a flow rate from 0.2 to 0.8 mL/min; 3) a constant flow rate of 0.8 mL/min for 5 min; 4) the mobile phase was changed from 100% B to 100% A for 1 min with a flow rate from 0.8 to 0.2 mL/min; and 5) a constant flow rate of 0.2 mL/min for 1 min.

Statistical analysis

All data are presented as mean±SD. Statistical significance between two groups was determined by Student's *t* test. *P* values of <0.05 were considered statistically significant.

Results

Inhibition of Hep3B and Huh7 cell proliferation by CT

To examine the effect of CT on proliferation of Hep3B and Huh7 cells, three doses of CT were tested. As shown in Figure 1, CT dose-dependently inhibited cell growth in both cell lines significantly. The inhibitory effect of CT was most pronounced in Hep3B cells (approximately 80% growth inhibition at the highest CT dose tested) but was also strong in Huh7 cells (approximately 70% growth inhibition at the highest CT dose tested).

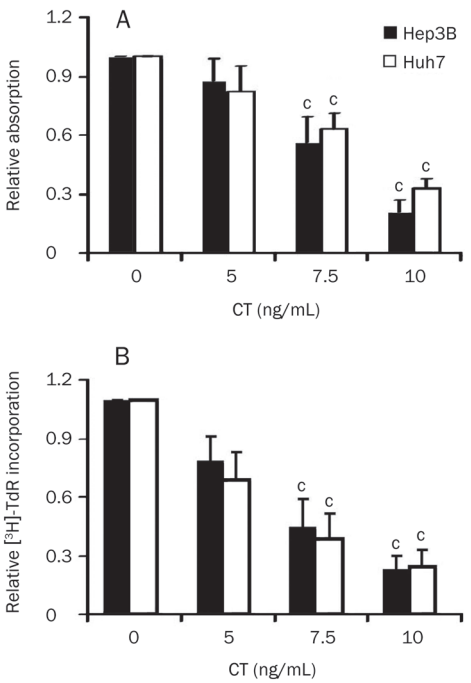

Figure 1. Effect of CT on cell proliferation of Hep3B and Huh7 cells. Hep3B or Huh7 cells were treated with the indicated doses of CT. Cells were grown for 72 h, and cell growth was measured with (A) MTT staining and (B) [^{3}H]-TdR incorporation. Data are expressed as mean±SD of four independent experiments. ^cP<0.01 compared with untreated cells (control) (paired Student's *t* test).

CT decreases production of the pro-inflammatory cytokine TNF-α and increases production of the anti-inflammatory cytokines IL-4 and IL-10 in Hep3B and Huh7 cells

To evaluate the effect of CT on the production of inflammatory cytokines, we measured TNF-α production as a pro-inflammatory marker and IL-4 and IL-10 protein production as anti-inflammatory markers by ELISA in Hep3B and Huh7 cells. The addition of CT significantly inhibited TNF-α production in both Hep3B and Huh7 cells in a dose-dependent manner, with approximately 50% inhibition compared with the control at the highest CT dose tested (Figure 2A). In contrast, CT significantly increased IL-4 protein production (approximately 2.5-fold compared with the control at the highest CT dose tested) and IL-10 protein production (approximately 3-fold compared with the control at the highest CT dose tested) in both Hep3B and Huh7 cells (Figure 2B and 2C).

CT decreased ATX expression and secretion in Hep3B and Huh7 cells

The expression of ATX is regulated by growth factors and cytokines. For example, fibroblast growth factor (FGF) and epidermal growth factor (EGF) have been shown to induce ATX expression, whereas certain cytokines, such as interleukin-4 (IL-4) and interferon-gamma (IFN-γ), decrease the expression of ATX mRNA in cultured fibroblast-like synoviocytes (SFC)[20], while TNF-α increases the expression of ATX mRNA in HCC cells[10]. Also, inflammatory cytokines are known to be associated with the inflammation related to liver diseases[21]. Here, we examined the effect of CT on the expression of ATX in human liver cell lines. As assessed by qRT-PCR assays, CT treatment decreased ATX mRNA levels more than 70% and 80%, at the highest CT dose tested, in Hep3B and Huh7 cells, respectively (Figure 3D). The inhibitory effect

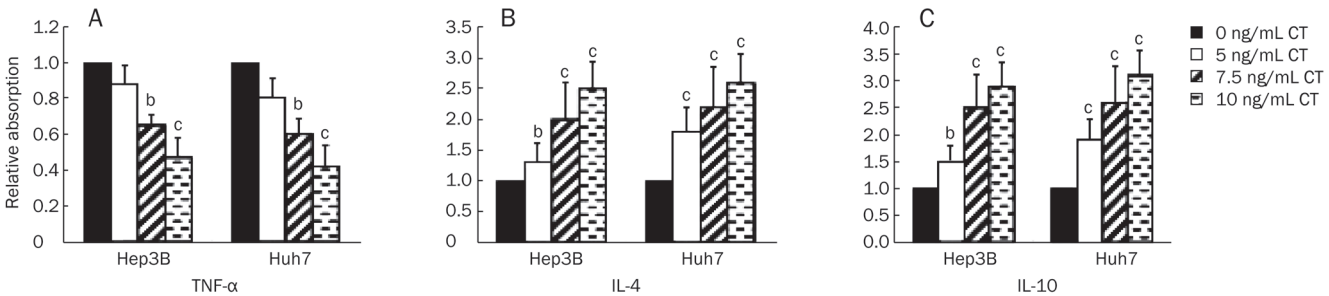

Figure 2. Effects of CT on cytokine secretion. CT reduced secretion of the pro-inflammatory cytokine TNF-α (A) and increased secretion of the anti-inflammatory cytokines IL-4 (B) and IL-10 (C). Levels of TNF-α/IL-4/IL-10 in cell culture medium were measured by ELISA kits after cells were treated with CT at doses of 0, 5, 7.5, and 10 ng/mL for 12 h. Data are expressed as mean±SD of four independent experiments. $^{b}P<0.05$, $^{c}P<0.01$ compared with untreated cells (control) (paired Student's *t* test).

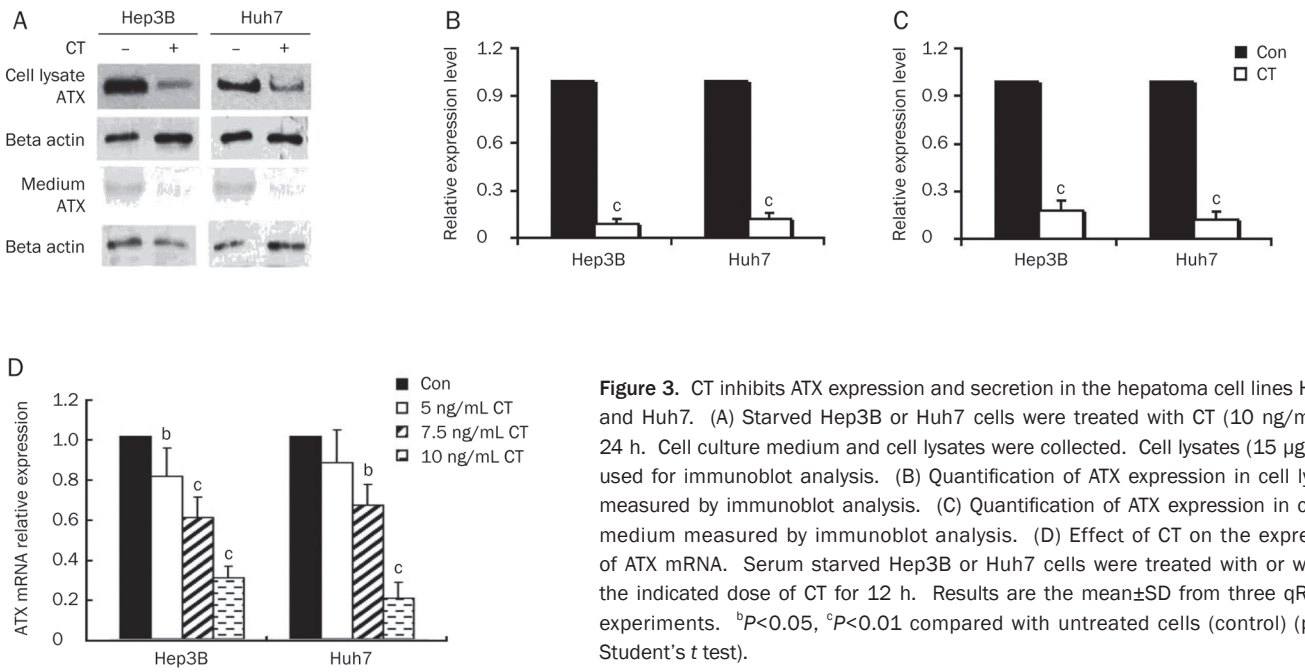

Figure 3. CT inhibits ATX expression and secretion in the hepatoma cell lines Hep3B and Huh7. (A) Starved Hep3B or Huh7 cells were treated with CT (10 ng/mL) for 24 h. Cell culture medium and cell lysates were collected. Cell lysates (15 μg) were used for immunoblot analysis. (B) Quantification of ATX expression in cell lysates measured by immunoblot analysis. (C) Quantification of ATX expression in culture medium measured by immunoblot analysis. (D) Effect of CT on the expression of ATX mRNA. Serum starved Hep3B or Huh7 cells were treated with or without the indicated dose of CT for 12 h. Results are the mean±SD from three qRT-PCR experiments. $^{b}P<0.05$, $^{c}P<0.01$ compared with untreated cells (control) (paired Student's *t* test).

of CT on cellular and secreted ATX protein expression was further demonstrated by immunoblot analyses (Figure 3A-3C).

ATX is crucial for Hep3B and Huh7 cells proliferation

To determine the relationship between the observed *in vitro* decrease in ATX levels and inhibition of cell proliferation by CT, we investigated the role of ATX in tumorigenic growth of the human hepatocellular carcinoma cell lines Hep3B and Huh7. As shown in Figure 4, CT significantly inhibited IL-4 induced cell proliferation and also decreased ATX expression in cell lysate. Moreover, knockdown of ATX in Hep3B and Huh7 cells had an anti-proliferative effect, as measured by MTT.

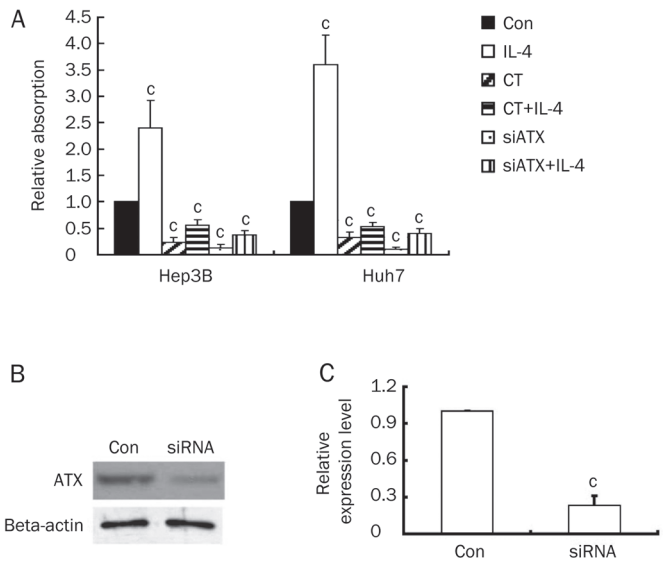

Figure 4. ATX is crucial for Hep3B and Huh7 cells proliferation. (A) Hep3B or Huh7 cells were treated with IL-4 (10 ng/mL), CT (10 ng/mL), IL-4 (10 ng/mL) plus CT (10 ng/mL), ATX siRNA, or ATX siRNA plus IL-4 (10 ng/mL). Cells were grown for 48 h, and cell survival was measured with MTT staining. (B) ATX was knocked down by treatment of siRNA against ATX. Expression of ATX was assessed by Western blot. (C) Quantification of ATX expression in Hep3B cells treated with siRNA against ATX. Data are expressed as mean±SD of four independent experiments. $^cP<0.01$ compared with untreated cells (control) (paired Student's *t* test).

Down-regulation of ATX induced by CT is associated with decreased lyso-PLD activity and conversion of LPC into LPA

Being an enzyme with lyso-PLD activity, ATX plays a critical role in LPA production[22]. To explore whether changes in ATX expression induced by CT led to a corresponding decrease in ATX/lyso-PLD activity, we collected conditioned medium at different time points from Hep3B and Huh7 cells that were treated with TNF-α, CT, both TNF-α and CT, or control (0.1% BSA/PBS). ATX/lyso-PLD activity in conditioned medium was measured using the fluorescent LPC analogue FS-3 as substrate[23]. After TNF-α stimulation, Hep3B and Huh7 cells exhibited about a 1.5-fold and 0.5-fold increase in secreted lyso-PLD activity, respectively (Figure 5A and 5B), indicating that TNF-α was able to increase lyso-PLD activity in culture medium by inducing ATX expression. Conversely, both cell lines treated with CT exhibited about a 5-fold decrease in secreted lyso-PLD activity compared with control and about a 2-fold and 3-fold decrease in secreted lyso-PLD activity induced by TNF-α, indicating that CT was able

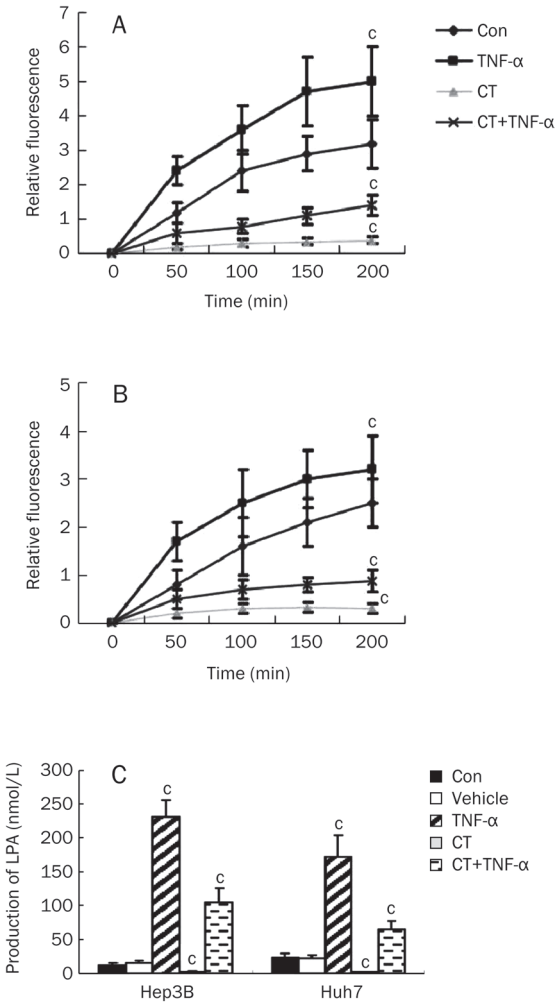

Figure 5. Down-regulation of ATX induced by CT is associated with decreased lysophospholipase D (lyso-PLD) activity, as indicated by conversion of LPC into LPA, in Hep3B and Huh7 cells. Serum starved Hep3B or Huh7 cells were treated with TNF-α (10 ng/mL), vehicle (0.1% BSA/PBS), CT (10 ng/mL) or CT (10 ng/mL) plus TNF-α (10 ng/mL) for 24 h. Hep3B (A) or Huh7 (B) cell medium from different time points were concentrated (40-fold) and assayed for ATX activity using the FS-3 compound. Results are shown as the average relative fluorescence activity±SD from three experiments. (C) Cell medium was incubated with 15 μmol/L LPC for 3 h at 37 °C. Lipids were analyzed by liquid chromatography-mass spectrometry (LC-MS). Results show the level of LPA from three experiments and are presented as mean±SD of four independent experiments. $^cP<0.01$ compared with untreated cells (control) (paired Student's *t* test).

to decrease lyso-PLD activity in culture medium by inhibiting ATX expression. We next examined LPA production by incubating the conditioned medium from Hep3B or Huh7 cells with 15 μmol/L LPC, a lyso-PLD substrate, followed by liquid chromatography/mass spectrometry (LC-MS) analysis. After supplying the cells with ATX substrate (LPC), LPA levels in the conditioned medium of Hep3B cells treated with vehicle, TNF-α or CT were detected. TNF-α treatment further elevated LPA levels by more than 10-fold, while CT treatment totally inhibited LPA levels in the medium. Also, CT significantly inhibited TNF-α mediated induction of LPA levels. A similar effect was observed in Huh7 cells, where TNF-α treatment induced an approximately 10-fold increase of LPA generation (Figure 5C). Thus, our results demonstrated that secreted ATX from Hep3B or Huh7 cells has lyso-PLD activity and that TNF-α induces ATX expression, secretion, and lyso-PLD activity, resulting in increased extracellular production of LPA from LPC. However, CT treatment had the opposite effect.

LPA is crucial for Hep3B and Huh7 cells proliferation via LPA receptor 1

Finally, we examined the role of LPA receptors in proliferation of Hep3B and Huh7 cells. For this purpose, we treated cells with Ki16425, an LPA_1 and LPA_3 antagonist, or $siLPA_1$, $siLPA_2$, or $siLPA_3$, cell viability was assessed by MTT assay. As shown in Figure 6, Ki16425 inhibited cell growth in both cell lines in the presence of LPC (1 μmol/L). Furthermore, expression levels of the LPA receptors were altered when cells were transfected with $siLPA_1$, targeting LPA_1; $siLPA_2$, targeting LPA_2; or $siLPA_3$, targeting LPA_3, in the presence of LPC (1 μmol/L). Expression of LPA receptors in Hep3B cells was shown in Figure 6A. Results from MTT assays showed that knockdown of LPA_1 in Hep3B and Huh7 cells played a role in the anti-proliferative effects of LPA (Figure 6). Therefore, LPA_1 plays a critical role in HCC cell proliferation.

Discussion

The experiments presented here demonstrate that CT is an inhibitor of cell growth in two human hepatocarcinoma cell lines, Hep3B and Huh7. A low dose of CT (7.5 ng/mL) was effective in Hep3B and Huh7, while CT inhibits the growth of small-cell lung cancers with an IC_{50} of 27–242 ng/mL[17]. The difference in sensitivity to CT between the cell types may be explained by differences in expression of cellular binding sites for CT or different levels of ATX, which plays an important role in liver tumorigenesis.

Cytokines play a major role in promoting the growth and metastatic spread of cancer cells. To evaluate the effect of CT on production of pro-inflammatory and anti-inflammatory cytokines, we measured the protein levels of tumor necrosis factor (TNF)-α, interleukin-4 (IL-4) and interleukin-10 (IL-10) in Hep3B and Huh7 cells. TNF-α secretion was suppressed by the addition of CT, but, on the contrary, secretion of the anti-inflammatory cytokines IL-4 and IL-10 was increased upon treatment with CT.

ATX is overexpressed in various cancers and promotes tumor progression by stimulating angiogenesis, tumor cell survival, growth, migration, and invasion[24–26]. TNF-α has

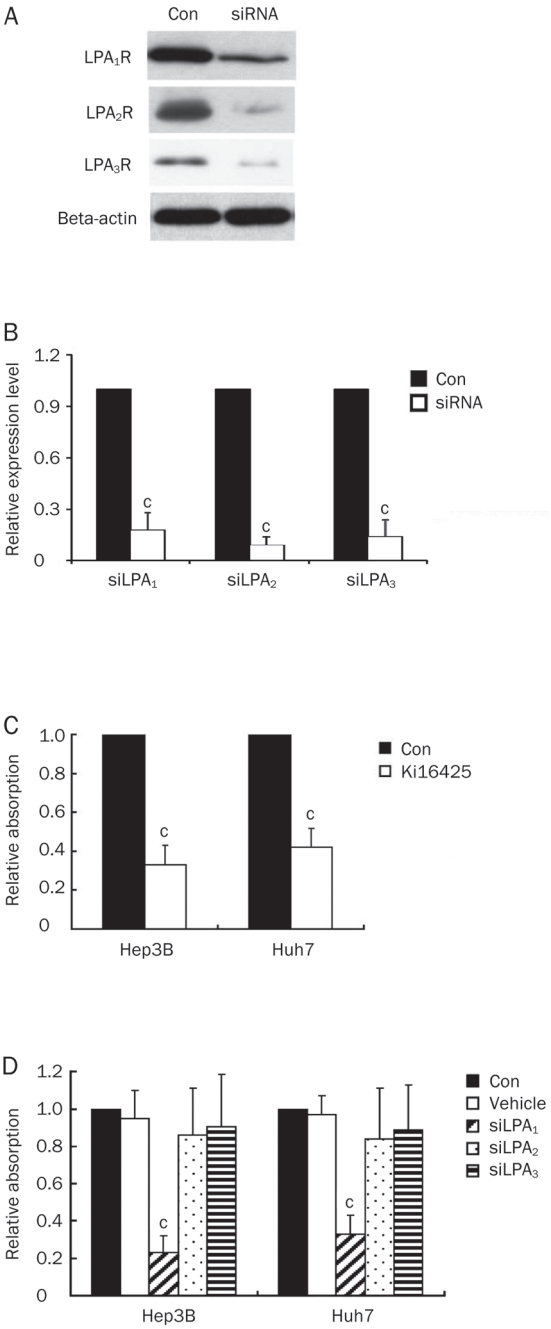

Figure 6. LPA_1 is crucial for HCC cell proliferation. (A) Knockdown of LPA using $siLPA_1$, $siLPA_2$, $siLPA_3$. Knockdown efficiency was shown by Western blot analysis. (B) Quantification of Western blot results. (C) Hep3B or Huh7 cells were treated with Ki16425 as described in "Materials and methods". Cell survival was evaluated by MTT assay. (D) Hep3B or Huh7 cells were treated with siRNA against LPA_1 receptor ($siLPA_1$), LPA_2 receptor ($siLPA_2$) or LPA_3 receptor ($siLPA_3$) as described in "Materials and methods". Non-silencing RNA (Vehicle) was transfected as vehicle. Cell survival was evaluated by MTT assay. Data are expressed as mean±SD of four independent experiments. $^cP<0.01$ compared with untreated cells (control) (paired Student's *t* test).

been reported to promote ATX secretion in both Hep3B and Huh7 cell lines, and chronic inflammation has been associated with the development of liver cancer, which is consistent with evidence that ATX expression levels are well correlated with the derivative origins of HCC cell lines related to inflammation[10]. In our study, we showed that treatment of Hep3B and Huh7 cells with CT inhibits ATX expression at both the RNA and the protein level. Furthermore, knockdown of ATX resulted in complete loss of the effect of CT on proliferation, suggesting ATX is crucial for the proliferation of liver cancer cells. Meanwhile, CT significantly inhibited TNF-α production in both Hep3B and Huh7 cells in a dose-dependent manner, suggesting CT might repress ATX expression by reduction of TNF-α production. This reduction in TNF-α secretion indicates that CT treatment leads to less chronic inflammation in HCC, suggesting that CT inhibits HCC proliferation by relieving chronic inflammation.

Moreover, as ATX is an enzyme with lyso-PLD activity, the aberrant expression of ATX has the potential to alter the delicate balance between LPA and LPC signaling. Therefore, we examined PLD activity and production of LPA from LPC in Hep3B and Huh7 cells treated with CT and TNF-α. TNF-α, a pro-inflammatory cytokine, promoted ATX secretion and LPA production in both cell lines. In contrast, CT significantly inhibited ATX secretion and LPA production. Moreover, secretion of enzymatically active ATX promoted Hep3B and Huh7 cell proliferation, which is dependent on extracellular LPC concentration and can be demonstrated to be a direct effect of increased LPA levels. Therefore, the expression of LPA is also crucial for the proliferation of HCC cells. Using an LPA_1 and LPA_3 specific antagonist[27] (Ki16425), LPA_1-specific small interfering RNA (siLPA_1), LPA_2-specific small interfering RNA (siLPA_2), and LPA_3-specific small interfering RNA (siLPA_3) in proliferation assays, we conclude that the LPA_1 receptor plays the main role in the proliferation of HCC cells. Recently, Park *et al* also determined the involvement of LPA_1 receptor activation by LPA produced by ATX activity in HCC invasion and metastasis, which suggests these could be novel biomarkers and potential therapeutic targets for HCC[28]. Despite data demonstrating the association of ATX and LPA with invasion and metastasis of HCC, whether CT inhibits HCC proliferation by interfering with LPA production is unknown. Accumulating evidence showing that the LPA/ATX axis regulates cancer cell proliferation, survival, and invasion suggests that LPA and its analogs, LPA receptors and ATX, are potential therapeutic targets for cancer treatment. Our results show that CT inhibits HCC progression by reducing LPA_1 production and ATX secretion. This suggests HCC proliferation could be inhibited by treatment with CT and that CT is a promising biological molecular for the treatment of liver cancer in patients.

Taken together, this is the first characterization of the mechanism by which CT, through regulation of ATX, influences HCC cells. CT inhibited proliferation of two human hepatocarcinoma cell lines, Hep3B and Huh7, by suppressing the ATX/LPA axis.

Acknowledgements

The work was supported by the State S&T Projects (11th Five Year) (2008ZX10002-007), the National Natural Science Foundation of China (No 30772017 and 30972730), and the Qianjiang Talent Project of Zhejiang Province (2010R10081).

Author contributions

Qi XIA performed cell culture, MTT experiments, and the ATX/lyso-PLD activity assay. An-mei DENG performed the ELISA assay and lipid extraction and analysis. Shan-shan WU performed the knock down and qRT-PCR assays. Min ZHENG conceived the study and guided the biochemical experiments.

References

1 Parkin DM, Bray F, Ferlay J, Pisani P. Global cancer statistics, 2002. CA Cancer J Clin 2005; 55: 74–108.
2 Shariff MI, Cox IJ, Gomaa AI, Khan SA, Gedroyc W, Taylor-Robinson SD. Hepatocellular carcinoma: current trends in worldwide epidemiology, risk factors, diagnosis and therapeutics. Expert Rev Gastroenterol Hepatol 2009; 3: 353–67.
3 Greten TF, Korangy F, Manns MP, Malek NP. Molecular therapy for the treatment of hepatocellular carcinoma. Br J Cancer 2009; 100: 19–23.
4 Braicu C, Burz C, Berindan-Neagoe I, Balacescu O, Graur F, Cristea V, *et al*. Hepatocellular carcinoma: tumorigenesis and prediction markers. Gastroenterol Res 2009; 2: 191–9.
5 Cooper AB, Wu J, Lu D, Maluccio MA. Is autotaxin (ENPP2) the link between hepatitis C and hepatocellular cancer? J Gastrointest Surg 2007; 11: 1628–34.
6 Stracke ML, Krutzsch HC, Unsworth EJ, Arestad A, Cioce V, Schiffmann E, *et al*. Identification, purification, and partial sequence analysis of autotaxin, a novel motility-stimulating protein. J Biol Chem 1992; 267: 2524–9.
7 Kishi Y, Okudaira S, Tanaka M, Hama K, Shida D, Kitayama J, *et al*. Autotaxin is overexpressed in glioblastoma multiforme and contributes to cell motility of glioblastoma by converting lysophosphatidylcholine to lysophosphatidic acid. J Biol Chem 2006; 281: 17492–500.
8 Black EJ, Clair T, Delrow J, Neiman P, Gillespie DA. Microarray analysis identifies Autotaxin, a tumour cell motility and angiogenic factor with lysophospholipase D activity, as a specific target of cell transformation by v-Jun. Oncogene 2004; 23: 2357–66.
9 Hama K, Aoki J, Fukaya M, Kishi Y, Sakai T, Suzuki R, *et al*. Lysophosphatidic acid and autotaxin stimulate cell motility of neoplastic and non-neoplastic cells through LPA_1. J Biol Chem 2004; 279: 17634–9.
10 Wu JM, Xu Y, Skill NJ, Sheng H, Zhao Z, Yu M, *et al*. Autotaxin expression and its connection with the TNF-alpha-NF-kappaB axis in human hepatocellular carcinoma. Mol Cancer; 2010; 9: 71.
11 Goodman L, Segreti J. Infectious diarrhea. Dis Mon 1999; 45: 268–99.
12 Holmgren J. Actions of cholera toxin and the prevention and treatment of cholera. Nature 1981; 292: 413–17.
13 Guerrant RL, Fang GD, Thielman NM, Fonteles MC. Role of platelet activating factor in the intestinal epithelial secretory and Chinese hamster ovary cell cytoskeletal responses to cholera toxin. Proc Natl Acad Sci U S A 1994; 91: 9655–8.
14 Taylor–Papadimitriou J, Purkis P, Fentiman IS. Cholera toxin and analogues of cyclic AMP stimulate the growth of cultured human mammary epithelial cells. J Cell Physiol 1980; 102: 317–21.

15 Lechner JF, Haugen A, Autrup H, McClendon IA, Trump BF, Harris CC. Clonal growth of epithelial cells from normal adult human bronchus. Cancer Res 1981; 41: 2294–304.
16 Cho-Chung YS, Clair T, Shepheard C, Berghoffer B. Arrest of hormone-dependent mammary cancer growth *in vivo* and *in vitro* by cholera toxin. Cancer Res 1983; 43: 1473–6.
17 Viallet J, Sharoni Y, Frucht H, Jensen RT, Minna JD, Sausville EA. Cholera toxin inhibits signal transduction by several mitogens and the *in vitro* growth of human small-cell lung cancer. J Clin Invest 1990; 86: 1904–12.
18 Xiao Y, Chen Y, Kennedy AW, Belinson J, Xu Y. Evaluation of plasma lysophospholipids for diagnostic significance using electrospray ionization mass spectrometry (ESI-MS) analyses. Ann N Y Acad Sci 2000; 905: 242–59.
19 Zhao Z, Xiao Y, Elson P, Tan H, Plummer SJ, Berk M, *et al.* Plasma lysophosphatidylcholine levels: potential biomarkers for colorectal cancer. J Clin Oncol 2007; 25: 2696–701.
20 Kehlen A, Lauterbach R, Santos AN, Thiele K, Kabisch U, Weber E, *et al.* IL-1 beta- and IL-4-induced down-regulation of autotaxin mRNA and PC-1 in fibroblast-like synoviocytes of patients with rheumatoid arthritis (RA). Clin Exp Immunol 2001; 123: 147–54.
21 Wullaert A, van Loo G, Heyninck K, Beyaert R. Hepatic tumor necrosis factor signaling and nuclear factor-kappaB: effects on liver homeostasis and beyond. Endocr Rev 2007; 28: 365–86.
22 Umezu-Goto M, Kishi Y, Taira A, Hama K, Dohmae N, Takio K, *et al.* Autotaxin has lysophospholipase D activity leading to tumor cell growth and motility by lysophosphatidic acid production. J Cell Biol 2002; 158: 227–33.
23 Morris AJ, Smyth SS. Measurement of autotaxin/lysophospholipase D activity. Methods Enzymol 2007; 434: 89–104.
24 Lee HY, Clair T, Mulvaney PT, Woodhouse EC, Aznavoorian S, Liotta LA, *et al.* Stimulation of tumor cell motility linked to phosphodiesterase catalytic site of autotaxin. J Biol Chem 1996; 271: 24408–12.
25 Nam SW, Clair T, Campo CK, Lee HY, Liotta LA, Stracke ML. Autotaxin (ATX), a potent tumor motogen, augments invasive and metastatic potential of ras-transformed cells. Oncogene 2000; 19: 241–7.
26 Nam SW, Clair T, Kim YS, McMarlin A, Schiffmann E, Liotta LA, *et al.* Autotaxin (NPP-2), a metastasis-enhancing motogen, is an angiogenic factor. Cancer Res 2001; 61: 6938–44.
27 Ohta H, Sato K, Murata N, Damirin A, Malchinkhuu E, Kon J, *et al.* Ki16425, a subtype-selective antagonist for EDG-family lysophosphatidic acid receptors. Mol Pharmacol 2003; 64: 994–1005.
28 Park SY, Jeong KJ, Panupinthu N, Yu S, Lee J, Han JW, *et al*. Lysophosphatidic acid augments human hepatocellular carcinoma cell invasion through LPA_1 receptor and MMP-9 expression. Oncogene 2011; 30: 1351–9.

Acta Pharmacologica Sinica (2011) 32: 1063–1070
 1671-4083/11 $32.00
www.nature.com/aps

Original Article

Investigation and management of *Toxoplasma gondii* infection in pregnancy and infancy: a prospective study

Paola DI CARLO[1], Amelia ROMANO[2], Alessandra CASUCCIO[3, *], Salvatore CILLINO[3], Maria Gabriella SCHIMMENTI[2], Giorgio MANCUSO[4], Stella LA CHIUSA[4], Vincenzo NOVARA[2], Daniela INGRASSIA[1], Valentina LI VECCHI[1], Marcello TRIZZINO[1], Lucina TITONE[1]

[1]Department of Sciences for Health Promotion, University of Palermo, Palermo, Italy; [2]Pediatric Infectious Diseases, Children's Hospital "G Di Cristina", ARNAS Civico, Palermo, Italy; [3]Department of Experimental Biomedicine and Clinical Neuroscience, University of Palermo, Palermo, Italy; [4]Clinical Pathology Department, Buccheri-La Ferla Hospital, Palermo, Italy

Aim: *Toxoplasma gondii* infection during pregnancy poses a serious risk to the fetus, therefore timely and accurate diagnosis is essential. The aim of this study was to estimate the frequency of congenital infection via evaluating mother's immunological status and the possibility to improving the diagnostic and therapeutic approaches.
Methods: Eighty five mothers with *Toxoplasma* seroconversion and their offspring were enrolled (among them, 2 spontaneous abortions were documented in the first trimester). Prenatal PCR diagnosis was carried out on 50 patients (60%), with 7 positive cases (14%). Morphological ultrasound scanning revealed anomalies in one fetus. Long-term follow-up included general physical examinations, serological status tested using Western blot, neuro-radiological, ophthalmologic and neurologic examinations, psychological and developmental tests, visual evoked potential tests and audiology tests, as well as anti-*Toxoplasma* treatment regimes.
Results: Fourteen (17%) of the infants were infected at one-year serological follow-up. Chi-square for linear trend of vertical transmission from the first to the third trimester was significant (P=0.009). Western blot analysis showed IgM and IgA in half of the infected infants. In 69 uninfected infants, anti-*Toxoplasma* IgG immunoblot analysis excluded infection within the 3 months in 18 infants (26%) and in the others within 6 months of life. The most relevant instrumental findings are described.
Conclusion: Western blot analysis may help to evaluate infection within the 6 months of life. The accuracy of ultrasound imaging to determine the brain damage in the fetus and newborns is doubtful, and should be combined with MR imaging. Multistep approaches can improve the timing of postnatal follow-up.

Keywords: *Toxoplasma gondii*; congenital infection; prenatal screening; serological response; ocular prognosis; neurological prognosis; Western blot analysis

Acta Pharmacologica Sinica (2011) 32: 1063–1070; doi: 10.1038/aps.2011.55; published online 11 Jul 2011

Introduction

Toxoplasma gondii (TG) infection during pregnancy causes severe congenital infection, and may result in *in-utero* abortion, fetal death, systemic disease or neuro-ophthalmological disorders[1–3].

Despite great progress in clinical and basic scientific research, there are many unresolved issues in congenital toxoplasmosis (CT) that need to be addressed, such as the type and timing of prenatal screening options given the variability in maternal serological response, and their cost-effectiveness[4–6].

* To whom correspondence should be addressed.
E-mail casuccio@unipa.it
Received 2011-01-24 Accepted 2011-04-13

Recent European prospective cohort studies point out that notwithstanding early maternal and post-natal standard antiparasitic treatment, the most effective approach to preventing *Toxoplasma gondii*-related injuries remains controversial. Other medical strategies, especially long-term follow-up programs, are recommended to monitor ocular and neurological prognosis[7–10].

Moreover, in the post-natal period it is crucial to be able to confirm or rule out infection as soon as possible. According to case definition criteria for CT, pediatricians should treat all infants born to mothers with a positive serological diagnosis of primary TG infection until *T gondii* IgG antibodies disappear[11].

In addition to conventional laboratory methodologies, West-

ern blot assay has been developed to differentiate between maternal specific antibodies and those synthesized by the newborn infant within the first six months of life[12, 13].

The aim of the present study was to estimate frequency of congenital infection based on the mother's immunological status in terms of infection and time of acquisition during pregnancy, and to assess the possibility of modulating the diagnostic and therapeutic approach according to the risk determined for each individual newborn. We report the results of a prospective serological and clinical follow-up program to monitor congenital *Toxoplasma gondii* infection, conducted at a Sicilian (Italy) paediatric tertiary referral centre after the introduction of Western blot analysis.

Materials and methods

Study design: 85 mothers with toxoplasmosis seroconversion and their offspring were enrolled in the study from January 2003 to December 2008.

Patients (mothers): Eighty-five HIV negative women who showed seroconversion (change from negative to positive specific IgG antibodies) to *Toxoplasma gondii* infection during pregnancy were included in the study.

Acute *Toxoplasma* infection was detected during monthly prenatal screening for toxoplasmosis at the ARNAS Hospital and Buccheri-La Ferla Hospital in Palermo, Italy.

Maternal and pediatric serological and molecular investigations were conducted at the Department of Pathology, Buccheri La Ferla Hospital, Palermo, Italy.

The study protocol was approved by the Ethics Committee of the University of Palermo (Italy) and informed consent was sought in accordance with the principles of the Declaration of Helsinki. Patients were thoroughly informed about the procedures and written informed consent was obtained from each of them.

Prenatal diagnosis: The women had a foetal ultrasound scan every two months during their pregnancy. Once informed consent was granted, amniotic fluid was drawn 4 to 5 weeks after the estimated date of seroconversion and always after 16–18 weeks of amenorrhea. PCR was performed on amniotic fluid to test for *Toxoplasma*.

Nested PCR was performed from 2003 to 2005 using the B1 gene (GenBank accession number AF179871), following the manufacturer's recommendations (SORIN BIOMEDICA-Saluggia, Vercelli, Italy)[13]. In January 2006, quantitative real time PCR using RE sequence was introduced (GenBank accession number AF146527) (BioQuant *T gondii*-529, BIORAD iCycler iQ, USA, Biodiversity-Brescia, Italy)[14].

Prenatal treatment: All the women received a standard course of spiramycin (SP) therapy (9×10^6 units/d) until their amniocentesis results were available.

If amniocentesis confirmed fetal infection, maternal infection was acquired after 23 weeks or infection was highly suspected (*eg* because of fetal abnormalities consistent with congenital toxoplasmosis detected by ultrasound examination), treatment consisted of pyrimethamine (PYR 50 mg/d) and sulphadiazine (SDX 3 g/d) until delivery.

Patients (infants): Congenital infection was defined by the persistence of specific IgG antibodies beyond 12 months of age, with or without clinical signs. From birth, long term follow-up of the infants included general physical examinations, serological status, neuro-radiological findings, ophthalmologic and neurologic examinations, psychological and developmental tests, visual evoked potential tests (VEPs) and audiology testing (using BAEPs and impedance audiometry).

All eye examinations were carried out by an experienced ophthalmologist, who recorded findings on a standardized form. Visual acuity and abnormalities relating to the anterior and posterior segments of both eyes after pupillary dilatation were considered, using direct ophthalmoscopy, Schepens binocular indirect ophthalmoscopy and/or no-contact wide-field lenses (90 diopter) for slit lamp, depending on the child's age and compliance. Under 3 years of age, visual acuity was assessed using Parinaud charts and was considered as normal when >2. Snellen charts were used for older children, and visual acuity was considered as normal when >20/25. The children were monitored for VEPs and BAEPs until 3 years of age.

Infants underwent brain ultrasound (US) examinations via the bregmatic fontanelle until six months of age (Aloke SSD-650 equipped with a 5–8 MHz sector transducer). When necessary, also a CT scan (scanning at 3-mm collimation with 5-mm interval and at 10-mm collimation) or MRI (1.6 to 4 mm slice thickness, sequence T1-W conventional spin-echo or T2-W fast spin-echo) of the head was performed.

Serological investigation: Serological analysis was carried out with well-established conventional serological methods. Congenital toxoplasmosis was diagnosed by determining the presence of *Toxoplasma*-specific IgM, IgA and IgG antibodies at birth, within the first month of life and at 3 months, and of *Toxoplasma*-specific IgG also at 6, 9, and 12 months of age [ETI TOXOK-M reverse, ETI TOXOK-G PLUS (DiaSorin, Saluggia, Italy), Toxo-IgM ISAGA, Toxo-IgG VIDAS, Toxo-IgG avidity VIDAS (BioMerieux, Marcy-l'Etoile, France)]. Consistent with NCCLS recommendations, the kits showed sensitivity and specificity of >95 and >98%–99% respectively. All patients were double-tested, with an intra-assay coefficient of variation (CV) of <2%.

Comparative immunological profile analysis of maternal serum samples, cord blood, neonatal sera and the infants' follow-up sera was performed with *Toxoplasma* IgG, IgM and IgA Western blot (WB), as well as conventional immunoenzymatic serological tests[13]. WB analysis used *Toxoplasma gondii* RH strain tachyzoite protein lysates and allowed us to identify antigens of 16, 27, 30 (p30), 35, 40, 60, 67, 70, 88, 94, and 110-kDa bands. The test was performed following the manufacturer's instructions (GenID GmbH, Strassberg, Germany), using the AID SCAN System.

Western blot was considered positive when at least two specific immunoglobulin (IgG) bands were clearly present in the infant sample but not in the mother's serum. IgM WB was performed on sera collected at birth or within 14 d after birth, and at 2 and 3 months of life, whereas IgG WB was continued

to 6 months of life.

Post-natal treatment: Different anti-*Toxoplasma* treatment regimes were initiated according to prenatal diagnosis, as follows:

Neonates born to mothers whose amniocentesis result was positive for *Toxoplasma* were treated with a combination of PYR (3 mg/kg every 3 d) and sulfadiazine (SDX) (25 mg/kg every 8 h), with 100 mg/kg of folinic acid daily for 4 weeks, followed by SP (0.375×10^6 U/kg daily) for 4 weeks. Their hematologic and renal status was monitored weekly until one year of age.

Neonates born to mothers with negative amniocentesis were given spiramycin until specific antibodies disappeared or WB analysis was negative.

Neonates born to mothers who did not have an amniocentesis were given a combination of PYR-SDX and SP as reported in paragraph 1, and hematologic and renal function was monitored weekly until serological follow-up showed that specific IgG had disappeared or IgG WB analysis was negative.

Compliance with treatment was assessed in interviews with parents; periodic blood tests (chemical evaluation) were done to identify possible side effects.

Statistical analysis

Demographic and clinical data were collected and analyzed using SPSS Software, version 14.0 (SPSS, Inc, Chicago, Ill, US). Statistical analysis of quantitative data, including descriptive statistics, was performed for all the items. The chi square test for linear trend was performed to evaluate vertical transmission of infection through the pregnancy trimesters. All *P* values were two-sided and *P* values less than 0.05 were considered to indicate statistical significance.

Results

At the final examination, the children were aged between 2 and 6 years (median age was 4.8 years), and had been followed up for at least 2 years (median 4.6 years; range 2–6 years).

Two pregnancies terminated in the first trimester, with fetal loss before amniocentesis. A total of 83 infants born to 85 mothers were included in the study and none of the mothers or the children were immunocompromised. Time of seroconversion was dated in the first trimester for 38 of the 85 pregnant women (45%), in the second trimester for 24 (28%) and in the third trimester for the remaining 23 (27%) .

Prenatal diagnosis by PCR testing on amniotic fluid was attempted for 50 of the 83 women who went on to give birth (60%), with positive results in seven cases (14%); the other women either did not consent to having the test (10, 12%) or seroconverted late in the third trimester (23, 28%). All the mothers with positive PCR results chose to continue their pregnancy, and prenatal ultrasound screening, performed every trimester on all of the patients, detected ventriculomegaly in one woman with a fetus at 31-weeks' gestation.

Fourteen of the 83 infants in the study (17%) were congenitally infected with *Toxoplasma gondii* and 69 (83%) proved to be uninfected. Chi-square test for linear trend of vertical transmission from the first to the third trimester [2/38 in the 1st trimester (OR=1.00); 5/24 in the second (OR=4.74); and 7/23 in the third trimester (OR=7.87)] was significant (*P*=0.009).

Six of the 14 infected children (43%) were asymptomatic at birth, and clinical and instrumental follow-up was negative, whereas the other 8 (57%) showed features of TG infection (Table 1). This group included all fetuses with positive prenatal PCR results; four of them showed symptoms of TG infection at birth and 6 were small for gestational age (SGA). Four children (28.6%) had cerebral lesions and ocular fundus pathologies [3 cases with foci of peripheral chorioretinitis and one with peripheral chorioretinitis in the left eye (LE) and macular chorioretinitis in the right eye (RE)]. Visual outcome was good in all cases, with normal visual acuity and VEPs within the normal range.

Seven of the TG-infected infants had received a positive prenatal diagnosis, whereas the mothers of the remaining infants either did not consent (1 pt) or seroconverted late in the third trimester (6 pts).

In accordance with guidelines for anti-parasitic treatment, all the infected newborns were treated with a combination of PYR-SDX and SP. Compliance to therapy was assessed by interviews with parents, and was good in all cases.

The serological investigation using WB showed IgM and

Table 1. Clinical and investigation findings during the pre- and post-natal era in eight symptomatic newborns with congenital *T gondii* infection.

Patient's case	Date of seroconversion week of amenorrhea	Amniotic PCR	IgM-IgA WB Positive at birth	Gestational age weeks	SGA	Retino chorioiditis	Neuroimaging features		
							Periventricular calcification	intraparen-chymatous lesions	ventriculomegaly, hydrocephaly
1	25th		+	39			Yes		
2	23rd	+	+	36	Yes		Yes		
3	26th	+	+	37			Yes		
4	20th	+		39	Yes		Yes		Yes
5	10th	+		36.5	Yes	Both eyes		Yes	Yes
6	26th	+	+	39	Yes	Both eyes		Yes	Yes
7	22nd	+	+	37	Yes	One eye	Yes		Yes
8	12th	+		35	Yes	Both eyes		Yes	Yes

IgA in 7 (50%) of the 14 infected patients, whereas IgM ISAGA combined with IgA reacted positive in 4 of them (28.6%) (Table 2). Most of these neonates had been infected after 21 weeks of gestation (Table 1). In the absence of IgM, comparative anti *Toxoplasma* IgG immunoblot analysis revealed different mother-child IgG profiles in the first trimester of life in 3 infected infants, whereas in the others the interpretation became clear within six months of life.

Table 2. Complementary detection of 83 enrolled infants' *Toxoplasma*-specific antibodies by different techniques during one year of follow-up.

Patients	Methods	Detection at following times after birth				
		0–30 d	3 month	6 month	9 month	1 year
Infected (14)	IgM-ISAGA+IgA Positive	4				
	IgM-IgA WB Positive	7				
	IgG-Western blot Positive	7	3	14		
Uninfected (69)	IgG-ELISA Positive	69	55	26	3	0
	IgG-Western blot Negative	1	17	69		

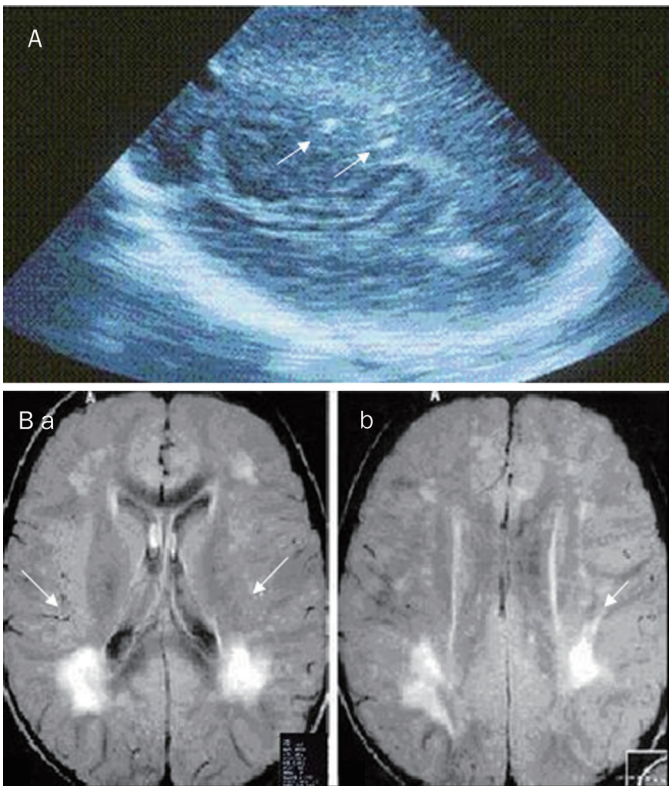

Figure 1. (A) Coronal US image using a vector scan showing brain calcification in lateral ventricle (arrows). (B) Patient 1. (a) MRI images showing focal lesions on the right side and (b) another smaller lesion in the subcortical posterior parietal area (arrows).

In infants uninfected at birth (69), comparative anti *Toxoplasma* IgG immunoblot analysis permitted us to exclude infection within the first three months of life in 18 children (26%) and in the others within six months of life, whereas the conventional immunoenzymatic serological test showed specific IgG persistence at six months of life in about one third of the infants, and in 3 cases at nine months of life.

The instrumental follow-up showed typical periventricular calcification in three cases, whereas relevant involvement of the brain was observed in five infants. In the following section we report these significant radiological findings.

In case 4, clinical neurological examination was normal and ultrasound follow-up of the brain showed intracranial calcification in the lateral ventricles and in the frontal and parietal lobes (Figure 1A). A magnetic resonance (MR) performed at 9 months of age showed intra-parenchymal brain lesions (Figure 1B). At present, the patient is in his fourth year of follow-up and his psychomotor development is normal.

In case 5, an ultrasound scan performed at 1 month of age showed a hypoechogenic area in the paraventricular white matter (Figure 2A), and at 2 months of age, MRI imaging showed encephalitic foci and cortical brain atrophy and ventricular dilation (Figure 2B). An ophthalmoscopic examination revealed peripheral bilateral inactive chorioretinitis foci with no vitreous inflammation. Tone and motor abnormalities resolved by 1 year of age, and after five years of follow-up, the

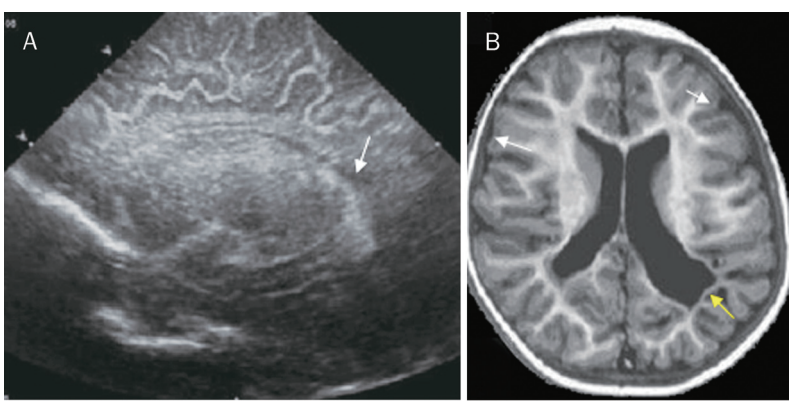

Figure 2. (A) Cranial ultrasound parasagittal views showing hypoechogenic area in the left paraventricular white matter (arrow). (B) T2 MR image showing encephalitic foci and cortical brain atrophy in the parietal area, white matter atrophy (white arrows), ventricular dilation, irregular angulated ventricles (yellow arrow).

child's psychomotor development is within normal limits.

In case 6, ventriculomegaly was detected during prenatal US follow-up. After birth, the features were confirmed by brain US and MR imaging, which showed lateral ventricular enlargement and obstructive hydrocephalus with aqueductal stenosis (Figure 3A, B). A ventriculotomy was necessary to treat the hydrocephalus, and a subsequent MR examination performed 6 months later revealed complete resolution (Figure 3C). An eye examination showed peripheral chorioretinitis without any surrounding activity. Seizures and motor abnormalities were resolved during therapy. The patient has been regularly attending our Day Hospital Service for three years and his psychomotor development is normal.

In case 7, ophthalmoscopy at birth revealed a peripheral inactive chorioretinitis scar. Ultrasound evaluation performed after delivery showed severe tetraventricular hydrocephalus and calcifications scattered around lateral ventricles (Figure 4). An MRI scan performed at 6 months of age revealed a reduction of hydrocephalus.

In case 8, pregnancy had been uneventful, although a detailed morphological ultrasound scan at 18 weeks had revealed biparietal measurement (30 mm) and head circumference (110 mm) below the 5th percentile, corresponding to 16 weeks gestation; this finding disappeared in all subsequent examinations. At birth, a visual evaluation showed microphthalmia, LE peripheral and RE macular chorioretinitis. Ultrasonography showed enlarged lateral ventricles and findings suggestive of aqueductal stenosis (Figure 5A). A comparative MRI investigation confirmed ventricular abnormalities detected by US and moreover showed brain-damage (Figure 5B). Motor abnormalities accompanied by behaviour disturbances and seizures persisted after one year of follow-up.

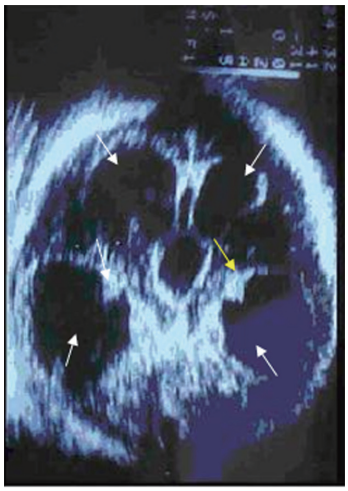

Figure 4. Axial US image using a vector transducer, showing severe tetraventricular hydrocephalus (white arrows), calcifications scattered around lateral ventricles (yellow arrow).

Discussion

The prevalence of congenital toxoplasmosis differs from one country to another. Various European works have focused on the cost-benefit ratio of wide-scale screening to prevent infec-

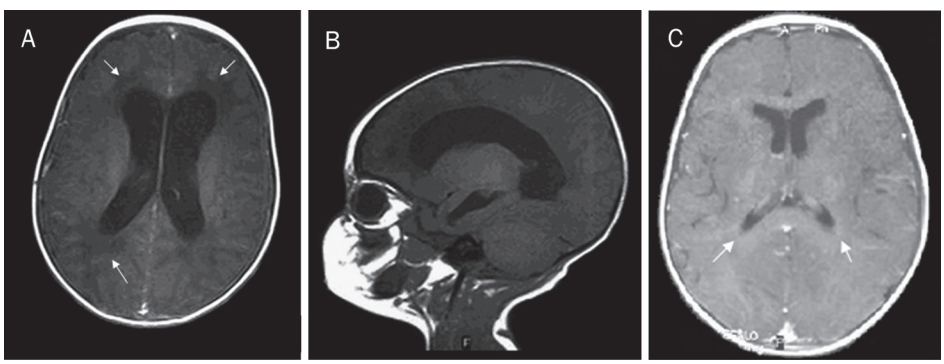

Figure 3. (A, B) Axial MR image showing evident hydrocephalic enlargement of lateral ventricles, area of hypointensity in the periventricular white matter to be attributed to ependymal transudation (arrows). (C) MR image showing a resolution of previous features (arrows).

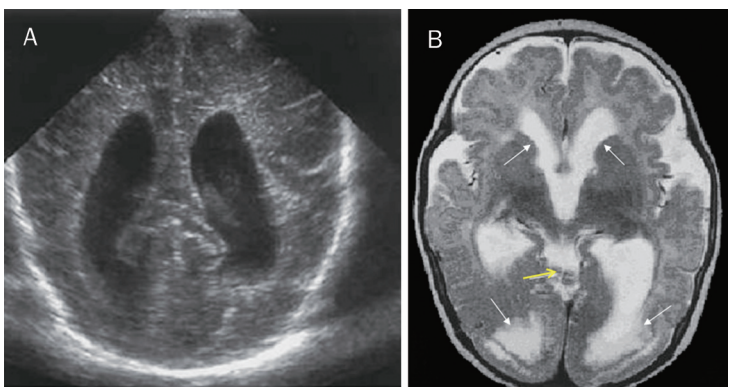

Figure 5. (A) Cranial ultrasound shows enlarged lateral ventricles. (B) Axial images show triventricular hydrocephalus, cyst-like inclusions (yellow arrow), cortical dysplasia, occipital polymicrogyria, white matter hyperintensity (transependymal transudation localized in the posterior horn of lateral ventricles) (white arrows).

tion, despite the fact that the consequences of the disease can be very disabling in childhood and adolescence and, above all, require considerations of an ethical nature regarding the pregnant woman and the well-being of the unborn child [8, 15].

Among the poorest populations living in any region like Southern Italy, parasitic diseases such as leshmaniasis and toxoplasmosis remain prevalent[16], and although our small sample size does not permit us to make any consistent conclusions about anti-parasitic treatment, the high risk for pregnant women of transmitting infection to their fetus encourages us to make a number of suggestions.

Our study collected data on a large group of children (36 cases) who were infected *in utero* by *T gondii* during the first trimester of pregnancy and whose ultrasound findings remained normal. As reported by Berrebi, our follow-up confirms that their outcome does not differ significantly from that of children infected during the second and third trimester[17].

As regards the prenatal phase, we observed a lower mother-to-child transmission rate than in other reports, and concur with a recent meta analysis by the SYROCOT group which found weak evidence that treatment initiated within 3 weeks of seroconversion could reduce the risk of transmission[18].

On the other hand, precocious maternal treatment did not prevent severe neurological and ocular disease, especially in children in whom parasitic infection was confirmed by amniotic PCR results[19]. When available, molecular investigations to detect *Toxoplasma gondii* in amniotic fluid provide useful information for patients and caregivers that can guide decision making and surveillance[14, 20]. The authors emphasize that all the infants with neuro-ophthalmological specific disease had received a positive prenatal diagnosis, whereas only in one late case of infection did monthly foetal ultrasound investigations give us any information on signs of congenital infection. However, the authors agree on the need for repeated ultrasound examinations, especially in delayed mother-to-child transmission of the disease when amniocentesis is rarely offered[21, 22].

Although ultrasound investigation via the bregmatic fontanelle is one of the techniques most frequently used by our staff in the postnatal follow-up, we prefer MRI in congenital toxoplasmosis as it offers more accurate pictures for the diagnosis and follow-up of white matter lesions in the infants, and provides excellent anatomic information on abnormalities in brain parenchyma. Fast magnetic resonance imaging (MRI) is being increasingly used to assess pregnancy management in the event of fetal central nervous system (CNS) anomalies[23].

In the neonatal phase of the study, all the infected infants were put on early treatment with PYR-SDX to one year of age and, for five of them with severe damage, until 18 months of life. Furthermore, we chose to also treat infants born to mothers who did not undergo amniocentesis with PYS-SDX.

Although the authors acknowledge that evidence is lacking on the effectiveness of early postnatal treatment in reducing the risk of subsequent specific lesions, our post-natal follow-up revealed an improvement in cerebral and ocular lesions. Moreover, some cohort studies have shown that treating an infected neonate early and effectively may lead to an improvement in ocular lesions and reduce the risk of developing ocular disease in the years after birth[24, 25]. Certainly a multidisciplinary early intervention strategy in the post-natal period can positively influence the cognitive functions of children with visual impairment.

In this case, it is vital that the clinician informs the parents accordingly and motivates their adherence to a long-term follow-up.

Western blot analysis has improved the timing of toxoplasmosis diagnosis in post natal follow-up to about six months of life. In some cases the situation is clear before then, but our own experience suggests that it is advisable not to anticipate diagnosis as the presence of maternal antibodies strongly inhibits the neonate's immunological response[26, 27].

It is generally accepted that maternal antibodies can block the offspring's immune response, making it particularly difficult to identify neonatal immunoglobulin soon after birth[1, 2, 20]. Moreover, immunological markers can vary depending on the trimester of infection, and also maternal and neonatal therapeutic treatment received during pregnancy can block or retard the neonate's immune response[26, 27]. Therefore, even if comparison of maternal and neonatal IgG by immunoblot does not show neonatal immune response to any *Toxoplasma gondii* antigens in the first trimester of life, this does not unequivocally exclude congenital infection.

In fact, recent studies which have evaluated B-cell subsets and their functional development have shown that memory B-cells are very low at birth and increase significantly at 6 months of life[28].

WB analysis is useful in managing children whose mother did not have amniocentesis, and in knowing with greater certainty when to stop therapy in children whose mother had a negative amniocentesis result. In about one third of cases, this reduces the costs associated with treatment and follow-up. It is true that in most cases the clinical picture is already clear by nine months of age, even with conventional methods, and that WB can anticipate the time of diagnosis by about two to three months.

A previous overview of investigation strategies has provided vital information to determine what is the most suitable multi-step laboratory investigation strategy for appropriate and timely clinical management of the infection[29, 30].

WB analysis should be incorporated in these TG infection investigation programs and performed in reference centers for the diagnosis of *Toxoplasmosis* in pregnancy and children. In particular, the authors suggest that WB analysis is useful both in pregnancy, as part of a panel of tests to determine if the mother has an acute *Toxoplasma gondii* infection, in which case she then has to undergo specific treatment and amniocentesis, and also after birth, when WB results may help pediatricians to clarify any pitfalls that may be encountered during the interpretative process of investigations, especially in the first few months of life.

Toxoplasma gondii is a parasite within the protozoan phylum *Apicomplexa* that contains pathogens of considerable medical

and veterinary importance, such as *Plasmodium, Toxoplasma, Cryptosporidium, Eimeria, Neospora* and *Theileria* species[31]. The apicomplexan parasites *Cryptosporidium spp* and *Neospora spp* are epidemiologically relevant for humans; in particular, it is well-known that *C parvum* is responsible for clinical manifestations in immunodeficient patients. *N caninum* does not infect humans, although there is some evidence that it might occur as antibodies to *N caninum* have also been detected in human samples[32, 33]. Because there are some similarities in molecular composition between both of these parasites and *Toxoplasma gondii*, the use of whole tachyzoites or tachyzoite-derived antigens in standard serological investigations may result in false positives due to a cross-reaction[34]. Although variations in the protein expression profiles of tachyzoites and bradyzoites of *N caninum* may be identified by Western blotting[35], a cross-reactivity cannot be excluded, and combined molecular diagnostic assays must be applied to confirm *Toxoplasma gondii* etiology[36, 37]. Thus, it is important to identify a readily-available serological test that is highly sensitive and specific in detecting the infection as early as possible.

In conclusion, clinical recognition and effective management of congenital toxoplasmosis is challenging and the strategy to reduce damages needs a multistep approach in the pre- rather than post-natal era to reduce the high costs of multidisciplinary follow-up.

Author contribution

Paola DI CARLO, Amelia ROMANO and Lucina TITONE designed and organized the study; Paola DI CARLO, Salvatore CILLINO and Giorgio MANCUSO performed clinical and serological follow-up; Alessandra CASUCCIO analyzed the data and vouch for the analysis results; Maria Gabriella SCHIMMENTI, Stella LA CHIUSA, Valentina LI VECCHI, Daniela INGRASSIA, Vincenzo NOVARA, and Marcello TRIZZINO contributed to collecting data and to enrolling patients at the participating centres. All the authors contributed to writing the paper.

References

1 Montoya JG, Liesenfeld O. Toxoplasmosis. Lancet 2004; 363: 1965–76.
2 Remington JS, McLeod R, Thulliez P, Desmonts G. Toxoplasmosis. In: Infectious Diseases of the Fetus and Newborn Infant, 6th edn. Editors: Remington JS, Klein JO, Wilson CB, Baker CJ. Philadelphia, PA: Elsevier-Saunders; 2006. p948–1091.
3 Embleton. The Northern Region's Perinatal Mortality Survey. Fetal and neonatal death from maternally acquired infection. Paediatr Perinat Epidemiol 2001; 15: 54–60.
4 Sterkers Y, Varlet-Marie E, Marty P, Bastien P, on behalf of the ANOFEL Toxoplasma-PCR Quality Control Group. Diversity and evolution of methods and practices for the molecular diagnosis of congenital toxoplasmosis in France: a four years survey. Clin Microbiol Infect Clin Microbiol Infect 2010; 16: 1594-602
5 Maudry A, Chene G, Chatelain R, Patural H, Bellete B, Tisseur B, *et al*. Bicentric evaluation of six anti-toxoplasma immunoglobulin G (IgG) automated immunoassays and comparison to the Toxo II IgG Western blot. Clin Vaccine Immunol 2009; 16: 1322–6.
6 Lago EG, Neto EC, Melamed J, Rucks AP, Presotto C, Coelho JC, *et al*. Congenital toxoplasmosis: late pregnancy infections detected by neonatal screening and maternal serological testing at delivery. Paediatr Perinat Epidemiol 2007; 21: 525–31.
7 Bénard A, Petersen E, Salamon R, Chêne G, Gilbert R, Salmi LR, *et al*. Survey of European programmes for the epidemiological surveillance of congenital toxoplasmosis. Euro Surveill 2008; 13. pii: 18834.
8 Röser D, Nielsen HV, Petersen E, Saugmann-Jensen P, Nørgaard-Pedersen PB. Congenital toxoplasmosis–a report on the Danish neonatal screening programme 1999–2007. J Inherit Metab Dis 2010; 33: S241–247.
9 Berrébi A, Assouline C, Bessières MH, Lathière M, Cassaing S, Minville V, *et al*. Long-term outcome of children with congenital toxoplasmosis. Am J Obstet Gynecol 2010; 203: 552.e1–6.
10 Wallon M, Kodjikian L, Binquet C, Garweg J, Fleury J, Quantin C, *et al*. Long-term ocular prognosis in 327 children with congenital toxoplasmosis. Pediatrics 2004; 113: 1567–72.
11 Lebech M, Joynson DH, Seitz HM, Thulliez P, Gilbert RE, Dutton GN, *et al*. Classification system and case definitions of *Toxoplasma gondii* infection in immunocompetent pregnant women and their congenitally infected offspring. European Research Network on Congenital Toxoplasmosis. Eur J Clin Microbiol Infect Dis 1996; 15: 799–805.
12 Tridapalli E, Capretti M, Farneti G, Marangoni A, Cevenini R, Faldella G. Congenital toxoplasmosis: the importance of the Western blot method to avoid unnecessary therapy in potentially infected newborns. Acta Paediatr 2008; 97: 1298–300.
13 Di Carlo P, Casuccio A, La Chiusa S, Mazzola A, Pampinella D, Romano A, *et al*. Diagnosis of congenital toxoplasmosis: pre- and post-natal evaluation in Sicilian (Italy) epidemiological area. Preliminary data. Parassitologia 2007; 49: 39–41.
14 Cassaing S, Bessières MH, Berry A, Berrebi A, Fabre R, Magnaval JF. Comparison between two amplification sets for molecular diagnosis of toxoplasmosis by real-time PCR. J Clin Microbiol 2006; 44: 720–4.
15 Cortina-Borja M, Tan HK, Wallon M, Paul M, Prusa A, Buffolano W, *et al*. Prenatal treatment for serious neurological sequelae of congenital toxoplasmosis: an observational prospective cohort study. PLoS Med 2010; 7. pii: e1000351.
16 Vesco G, Buffolano W, La Chiusa S, Mancuso G, Caracappa S, Chianca A, *et al. Toxoplasma gondii* infections in sheep in Sicily, southern Italy. Vet Parasitol 2007; 146: 3–8.
17 Berrebi A, Bardou M, Bessieres MH, Nowakowska D, Castagno R, Rolland M, *et al*. Outcome for children infected with congenital toxoplasmosis in the first trimester and with normal ultrasound findings: a study of 36 cases. Eur J Obstet Gynecol Reprod Biol 2007; 135: 53–7.
18 SYROCOT (Systematic Review on Congenital Toxoplasmosis) study group, Thiebaut R, Leproust S, Chene G, Gilbert R. Effectiveness of prenatal treatment for congenital toxoplasmosis: a meta-analysis of individual patients' data. Lancet 2007; 369: 115–22.
19 Garcia-Méric P, Franck J, Dumon H, Piarroux R. Management of congenital toxoplasmosis in France: current data. Presse Med 2010; 39: 530–8.
20 Montoya JG, Remington JS. Management of *Toxoplasma gondii* infection during pregnancy. Clin Infect Dis 2008; 47: 554–66.
21 Gay-Andrieu F, Marty P, Pialat J, Sournies G, Drier de Laforte T, Peyron F. Fetal toxoplasmosis and negative amniocentesis: necessity of an ultrasound follow-up. Prenat Diagn 2003; 23: 558–60.
22 Villena I, Bory JP, Chemla C, Hornoy P, Pinon JM. Congenital toxoplasmosis: necessity of clinical and ultrasound follow-up despite negative amniocentesis. Prenat Diagn 2003; 23: 1098–9.
23 Herman-Sucharska I, Bekiesińska-Figatowska M, Urbanik A. Fetal

central nervous system malformations on MR images. Brain Dev 2009; 31: 185–99.
24 Freeman K, Tan HK, Prusa A, Petersen E, Buffolano W, Malm G, *et al*. European Multicentre Study on Congenital Toxoplasmosis. Predictors of retinochoroiditis in children with congenital toxoplasmosis: European, prospective cohort study. Pediatrics 2008; 121: e1215–22.
25 Roizen N, Kasza K, Karrison T, Mets M, Noble AG, Boyer K, *et al*. Impact of visual impairment on measures of cognitive function for children with congenital toxoplasmosis: implications for compensatory intervention strategies. Pediatrics 2006; 118: e379–90.
26 Bessières M H, Berrebi A, Rolland M, Bloom MC, Roques C, Cassaing S, *et al*. Neonatal screening for congenital toxoplasmosis in a cohort of 165 women infected during pregnancy and influence of in utero treatment on the results of neonatal tests. Eur J Obstet Gynecol Reprod Biol 2001; 94: 37–45.
27 Meroni V, Genco F, Tinelli C, Lanzarini P, Bollani L, Stronati M, *et al*. Spiramycin treatment of *Toxoplasma gondii* infection in pregnant women impairs the production and the avidity maturation of *T gondii*-specific immunoglobulin G antibodies. Clin Vaccine Immunol 2009; 16: 1517–20.
28 Avanzini MA, Maccario R, Belloni C, Carrera G, Bertaina A, Cagliuso M, *et al*. B lymphocyte subsets and their functional activity in the early months of life. Int J Immunopathol Pharmacol 2010; 23: 247–54.
29 Pinon JM, Dumon H, Chemla C, Franck J, Petersen E, Lebech M, *et al*. Strategy for diagnosis of congenital toxoplasmosis: evaluation of methods comparing mothers and newborns and standard methods for postnatal detection of immunoglobulin G, M, and A antibodies. J Clin Microbiol 2001; 39: 2267–71.
30 Sensini A. *Toxoplasma gondii* infection in pregnancy: opportunities and pitfalls of serological diagnosis. Clin Microbiol Infect 2006; 12: 504–12.
31 Kim K, Weiss LM. *Toxoplasma gondii*: the model apicomplexan. Int J Parasitol 2004; 34: 423–32.
32 Barratt JL, Harkness J, Marriott D, Ellis JT, Stark D. Importance of nonenteric protozoan infections in immunocompromised people. Clin Microbiol Rev 2010; 23: 795–836.
33 Ibrahim HM, Huang P, Salem TA, Talaat RM, Nasr MI, Xuan X, *et al*. Short report: prevalence of *Neospora caninum* and *Toxoplasma gondii* antibodies in northern Egypt. Am J Trop Med Hyg 2009; 80: 263–7.
34 Chahan B, Gaturaga I, Huang X, Liao M, Fukumoto S, Hirata H, *et al*. Serodiagnosis of *Neospra caninum* infection in cattle by enzyme-linked immunosorbent assay with recombinant truncated NcSAG1. Vet Parasitol 2003; 118: 177–85.
35 Kang SW, Lee EH, Jean YH, Choe SE, Van Quyen D, Lee MS. The differential protein expression profiles and immunogenicity of tachyzoites and bradyzoites of *in vitro* cultured *Neospora caninum*. Parasitol Res 2008; 103: 905–13.
36 Wang CR, Zhai YQ, Zhao XC, Tan QJ, Chen J, Chen AH, *et al*. Preliminary application of PCR-based assay for the detection of *Neospora caninum* in bovine aborted fetus. Zhongguo Ji Sheng Chong Xue Yu Ji Sheng Chong Bing Za Zhi 2009; 27: 140–3.
37 Edelhofer R, Loeschenberger K, Peschke R, Sager H, Nowotny N, Kolodziejek J, *et al*. First PCR-confirmed report of a *Neospora caninum*-associated bovine abortion in Austria. Vet Rec 2003; 152: 471–3.

Acta Pharmacologica Sinica (2011) 32: 1071–1077
 1671-4083/11 $32.00
www.nature.com/aps

Original Article

Polymorphisms of *VEGFA* gene and susceptibility to hemorrhage risk of brain arteriovenous malformations in a Chinese population

Zhi-ping GONG[1], Ni-dan QIAO[2], Yu-xiang GU[2], Jian-ping SONG[2], Pei-liang LI[2], Hui-jia QIU[2], Wei-wei FAN[3], Ying MAO[2], Hong-yan CHEN[3, *], Yao ZHAO[2, *]

[1]*Operation Room, First Affiliated Hospital, College of Medicine, Zhejiang University, Hangzhou 310003, China;* [2]*Department of Neurosurgery, HuaShan Hospital, Shanghai Medical College, Fudan University, Shanghai 200040, China;* [3]*State Key Laboratory of Genetic Engineering and MOE Key Laboratory of Contemporary Anthropology, School of Life Sciences, Fudan University, Shanghai 200433, China*

Aim: To evaluate the influence of the vascular endothelial growth factor A (VEGFA) polymorphisms on risk of presentation with intracerebral hemorrhage (ICH).
Methods: Nine selected VEGFA single-nucleotide polymorphisms (SNPs) were genotyped in 311 patients with brain arteriovenous malformations (BAVM) in a Chinese population. Associations between individual SNPs/haplotypes and the hemorrhage risk of BAVMs were evaluated using logistic regression analysis.
Results: In the single-locus analysis, rs1547651 was associated with increased risk of ICH (adjusted OR=2.11, 95% CI=1.01–4.42 compared with the AA genotype). In particular, an increased risk for ICH was associated with this variant in female patients (adjusted OR=3.21, and 95% CI=0.99–10.36). Haplotype-based analyses revealed that haplotype 'GC' in block 1 and haplotype 'ACC' in block 2 were associated with a 30%–38% reduction in the risk of ICH in patients with BAVMs compared to the most common haplotype (P_{sim}=0.033 and P_{sim}=0.005, respectively). The protective effect of haplotype 'ACC' in block 2 was more evident in male patients and subjects with BAVMs of a size ≥3 cm (adjusted OR=0.57, 95% CI=0.34–0.97 and adjusted OR=0.57, 95% CI=0.31–0.86, respectively).
Conclusion: The results suggest that VEGFA gene variants may contribute to ICH risk of BAVM.

Keywords: brain arteriovenous malformations; cerebral hemorrhage; vascular endothelial growth factor A (VEGFA); single-nucleotide polymorphism (SNPs)

Acta Pharmacologica Sinica (2011) 32: 1071–1077; doi: 10.1038/aps.2011.76; published online 27 Jun 2011

Introduction

Brain arteriovenous malformations (BAVMs) are a common cause of intracerebral hemorrhage (ICH), especially in young adults[1]. An accurate estimate of ICH risk in patients harboring BAVMs is needed to help guide clinical management. Although features of BAVM associated with ICH have been identified, additional robust and reproducible indices are still needed. Genetic variation may influence the pathogenesis and the clinical course of BAVMs. The identification of genetic polymorphisms associated with clinical manifestations would facilitate risk stratification as well as illuminate the underlying biology[2].

Vascular endothelial growth factor A (VEGFA) plays an important role in the migration, proliferation and survival of endothelial cells[3, 4]. It has been hypothesized to be involved in the pathogenesis of cancer metastasis, retinopathy, age-related macular degeneration, rheumatoid arthritis and psoriasis[5–7]. Molecular characterization of BAVM tissue has provided evidence for the involvement of angiogenesis, and Hashimoto *et al*[8] have shown that a prominent feature of the BAVM tissue is relative overexpression of VEGFA at both the mRNA and protein levels. Furthermore, VEGFA may contribute to the hemorrhagic tendency of BAVMs, as extrapolated from animal models[9].

The *VEGFA* gene is located on chromosome 6p21.3 and comprises a 14 kb coding region with eight exons. Over thirty single nucleotide polymorphisms (SNPs) have been described

* To whom correspondence should be addressed.
E-mail chenhy@fudan.edu.cn (Hong-yan CHEN);
zhaoyaohs@hotmail.com (Yao ZHAO)
Received 2011-03-30 Accepted 2011-05-11

in the region of the *VEGFA*. To date, several case-control studies have confirmed the association of *VEGFA* SNPs with a risk of developing several types of tumors[10–13] and other diseases[14, 15]; however, to our knowledge, there is little data on the role of *VEGFA* SNPs in relation to ICH risk in patients with BAVMs, in spite of the importance of *VEGFA* gene in the hemorrhagic tendency of BAVMs. Because of the dearth of knowledge in this area, we evaluated both potential functional SNPs and tag SNPs spanning the *VEGFA* for effects on the risk of presentation with ICH.

Materials and methods

BAVM sample population

Using the same recruitment method as described previously[16], we recruited 311 patients diagnosed with incident BAVM (as demonstrated by pathology or angiography), all of whom were genetically unrelated ethnic Han Chinese. These patients were recruited between January 2004 and December 2007 at Huashan Hospital, Fudan University (Shanghai, China). Patients with a family history or diagnosis of hereditary hemorrhagic telangiectasia (HHT) were excluded. Patients with signs of new intracranial hemorrhage on computed tomography (CT) or magnetic resonance imaging (MRI) were defined as ICH. Patients (symptomatic or not), who had non-hemorrhagic intracranial lesions initially detected by CT scan or MRI and were proven to harbor BAVMs by angiography were coded as unruptured cases. The BAVM size and venous drainage pattern were determined by angiography and were classified using standard guidelines[17]. Each participant provided informed consent, and the studies were approved by the Human Subjects Review Committee of Huashan Hospital, Fudan University.

Polymorphism selection and genotyping

We selected tagging SNPs (tSNPs) in the VEGFA gene (6p21.3, NT_007592.14) with genotype data of Han Chinese from the International HapMap Project (HAPMAP), Public Release#20/ Phase II on April 7th, 2007 (http://www.hapmap.org). tSNPs were selected to cover the whole VEGFA gene. tSNPs with a minor allele frequency (MAF) greater than 0.05 (based on pair-wise LD analysis) were selected to capture unmeasured SNPs with a minimum r^2>0.8. In addition, four potentially functional SNPs (rs1547651, rs2010963, rs1413711, and rs3025039) in *VEGFA* that were identified in previous reports were also included in this study. As a result, nine SNPs of the *VEGFA* were investigated.

We used white blood cell fractions from whole blood samples for the extraction of genomic DNA using the Qiagen Blood Kit (Qiagen, Chatsworth, CA, USA). Genotyping was performed with the MassARRAY iPLEX platform (Sequenom, San Diego, CA, USA) using an allele-specific MALDI-TOF mass spectrometry assay[18]. Primers for amplification and extension reactions were designed using the MassARRAY Assay Design Version 3.1 software (Sequenom), and SNP genotypes were obtained according to the iPLEX protocol provided by the manufacturer. We examined the quality of the genotyping with a detailed QC procedure that ensured a >95% successful call rate with duplicate calling of genotypes, internal positive control samples and Hardy-Weinberg Equilibrium (HWE) testing. The consistency rate observed in these duplicated samples was 100%.

Statistical analyses

Genotype frequencies in ICH and unruptured cases were compared using a χ^2-test. Estimate odds ratios (ORs) and 95% confidence intervals (CIs) were calculated by unconditional logistic regression with adjustments for age and gender. Akaike's information criterion (AIC) was employed to determine the best fitting model for each SNP[19]. The issue of multiple tests was controlled with 10 000 time permutation tests. Pairwise linkage disequilibrium (LD) among the markers was examined using Lewontin's standardized coefficient *D*′ and LD coefficient r^2 [20]. Haplotype blocks were defined by Haploview V4.1, as detailed by Gabriel *et al*[21]. PHASE 2.0 was used to infer the haplotype frequencies based on the observed genotypes[22]. All the statistical analyses were performed using SPSS17.0 software with two-sided tests and a significance level set at 0.05, unless otherwise indicated.

Results

Characteristics of study participants

Demographic and clinical characteristics of the patients with BAVMs are shown in Table 1. Of the 311 patients genotyped, 58.2% presented with hemorrhage, and 41.8% presented with unruptured BAVMs. The ages (mean±SD) of the patients were 33±14 years in unruptured cases and 30±15 years in ICH cases, with males accounting for 61.5% of unruptured cases and 55.8% of ICH cases. ICH presentation was not significantly associated with gender (χ^2, P=0.312) or age at diagnosis (*t* test, P=0.063), but it was associated with deep venous drainage (χ^2, P<0.001) and small BAVM size (χ^2, P<0.001).

Table 1. Demographics and BAVM characteristics.

	Unruptured	%	ICH	%	Total	*P*
Demographics						
Total BAVM cases	130	41.8%	181	58.2%	311	
Age at diagnosis						
Mean age±SD, year	33±14		30±15		31±15	0.063
n	130		181		311	
Gender						
Female	50	38.5%	80	44.2%	130	0.312
Male	80	61.5%	101	55.8%	181	
BAVM characteristics						
BAVM size	19	18.6%	83	81.4%	102	7.2×10^{-9}
	111	53.1%	98	46.9%	209	
Venous drainage						
Exclusively deep	25	19.2%	108	59.7%	133	8.78×10^{-24}
Any superficial	105	80.8%	73	40.3%	178	

Analysis of single SNPs association with ICH risk in patients with BAVMs

In the single locus analysis, the genotype frequency of the rs1547651 and rs3025030 SNPs was significantly different between unruptured cases and ICH cases (χ^2, uncorrected P=0.049 and P=0.047, respectively); the association of rs1547651 still remained after the logistic regression analysis was adjusted for age and gender (adjusted OR=2.11; 95% CI=1.01 to 4.42 compared with the AA genotype). The remaining 7 SNPs did not reach the statistically significant level (Table 2).

Table 2. Frequency of the distribution of VEGFA SNP genotypes and their association with risk of hemorrhagic presentation.

Genetic model	Location in gene region	Genotype	BAVM presentation			Logistic regression	
			Unruptured No (%)	ICH No (%)	*P* value χ^2 test	Adjusted OR (95% CI)[a]	*P* value
Genotype:							
rs1547651	Promoter				**0.049**		
–		A/A	115 (91.3%)	149 (83.2%)		1.00 (reference)	
		A/T	11 (8.7%)	30 (16.8%)		2.11 (1.01–4.42)	**0.047**
rs2010963	5' UTR				0.260		
		CC	40 (32.0%)	52 (30.1%)		1.00 (reference)	
Codominant		CG	66 (52.8%)	82 (47.4%)		0.95 (0.56–1.61)	0.845
		GG	19 (15.2%)	39 (22.5%)		1.54 (0.77–3.07)	0.221
Dominant		CG/CC	106 (84.8%)	134 (77.5%)		0.63 (0.34–1.16)	0.535
rs1413711	Intron_1				0.282		
		GG	78 (61.4%)	98 (54.4%)		1.00 (reference)	
Codominant		GA	43 (33.9%)	73 (40.6%)		1.35 (0.83–2.2)	0.221
		AA	6 (4.7%)	9 (5.0%)		1.22 (0.41–3.63)	0.715
Dominant		GA/AA	49 (38.6%)	82 (45.6%)		0.75 (0.47–1.19)	0.22
rs833069	Intron_2				0.117		
		AA	36 (29.8%)	44 (25.6%)		1.00 (reference)	
Codominant		AG	67 (55.4%)	88 (51.2%)		1.05 (0.61–1.82)	0.856
		GG	18 (14.8%)	40 (23.2%)		1.78 (0.87–3.63)	0.116
Recessive		AA/AG	103 (85.1%)	132 (76.7%)		1.00 (reference)	
		G/G	18 (14.9%)	40 (23.3%)		0.58 (0.31–1.08)	0.081
rs3024994	Intron_2				0.203		
		CC	116 (91.3%)	153 (86.9%)		1.00 (reference)	
Codominant		CT	11 (8.7%)	22 (12.5%)		1.51 (0.70–3.26)	0.298
		TT	0 (0%)	1 (0.6%)		1.25E9 (0.0–)	1
Log-additive		–	–	–		0.62 (0.30–1.30)	0.2
rs3025010	Intron_5				0.999		
		TT	67 (52.8%)	97 (53.9%)		1.00 (reference)	
Codominant		TC	54 (42.5%)	72 (40.02%)		0.92 (0.57–1.47)	0.715
		CC	6 (4.7%)	11 (6.1%)		1.31 (0.46–3.74)	0.616
Recessive		TT/TC	121 (95.3%)	169 (93.9%)		1.00 (reference)	
		CC	6 (4.7%)	11 (6.1%)		0.74 (0.26–2.06)	0.55
rs3025030	Intron_7				**0.047**		
		GG	81 (64.3%)	131 (74.0%)		1.00 (reference)	
Codominant		GC	39 (30.9%)	42 (23.7%)		0.70 (0.41–1.18)	0.181
		CC	6 (4.8%)	4 (2.3%)		0.42 (0.11–1.55)	0.194
Log-additive		–	–	–		1.47 (0.96–2.26)	0.077
rs3025035	Intron_7				0.211		
		CC	95 (75.4%)	122 (70.1)		1.00 (reference)	
Codominant		TC	30 (23.8)	47 (27.0%)		1.19 (0.70–2.03)	0.523
		TT	1 (0.8%)	5 (2.9%)		3.84 (0.44–33.96)	0.226
Recessive		CC/CT	125 (99.2%)	169 (97.1%)		1 (reference)	
		TT	1 (0.8%)	5 (2.9%)		0.27 (0.03–2.40)	0.19
rs3025039	Exon_8				0.188		
		CC	83 (67.4%)	129 (73.7%)		1.00 (reference)	
Codominant		CT	35 (28.5%)	42 (24.0%)		0.81 (0.48–1.39)	0.449
		TT	5 (4.1%)	4 (2.3%)		0.53 (0.14–2.06)	0.36
Log-additive		–	–	–		1.28 (0.82–1.99)	0.27

Analysis of haplotype association with ICH risk in patients with BAVMs

The reconstructed LD plot of the nine SNPs in the 333 controls was described in our previous report[16]. Three blocks were defined by the nine SNPs in *VEGFA*. Block 1 covered the region of *VEGFA* from the 5′ UTR to the first intron with a length of 2 kb (SNPs 2–3). Block 2 extended 4 kb (SNPs 4–6) and encompassed the middle part of the gene from intron 2 to intron 5. Block 3 contained the terminal section of the gene, ranging mainly from intron 7 to the 3′ UTR (SNPs 7–9, size=1 kb). The overall distribution of haplotypes in block 2 was significantly different between unruptured cases and ICH cases (Table 3). Haplotype-specific analysis revealed the haplotype 'GC' in block 1 (P_{sim}=0.033) and the haplotype 'ACC' in block 2 (P_{sim}=0.005) correlated with a significant protective effect against ICH risk in patients with BAVMs (adjusted OR=0.70; 95% CI=0.49–1.02 and adjusted OR=0.62, 95% CI=0.4–0.93, respectively) compared to the most common haplotype.

Association analysis with stratification

We further evaluated whether the rs1547651 variant and haplotype 'ACC' in block 2 were associated with ICH risk in patients with BAVMs, as stratified by age, sex, BAVM size and venous drainage status. As shown in Table 4, compared with the common wild-type homozygous genotype, the increased risk associated with genotype AT of rs1547651 was more pronounced in female subjects (adjusted OR=3.21, 95% CI=0.99–10.36). Moreover, the protective effect of haplotype 'ACC' in block 2 was more evident in males and subjects with BAVMs of a size ≥3 cm (adjusted OR=0.57, 95% CI=0.34–0.97 and adjusted OR=0.57, 95% CI=0.31–0.86, respectively).

Discussion

VEGFA has the ability to increase vascular permeability and cause vasodilatation, and it has been shown to be associated with various hemorrhagic disorders. Overexpression of VEGFA was reported recently in patients with brain tumor-associated ICH[23]. In this study, we reported the association between multiple common *VEGFA* polymorphisms and the hemorrhagic risk of BAVMs in a Han Chinese population. We found that one SNP out of nine selected SNPs showed a significant association with ICH risk. Moreover, haplotype analyses revealed that the haplotype 'GC' in block 1 (P_{sim}=0.033), and the haplotype 'ACC' in block 2 (P_{sim}=0.005) showed a decreased ICH risk in patients with BAVMs compared with those of the common haplotype. Our findings suggested that VEGFA gene variants might contribute to an increased ICH risk in patients with BAVMs.

Genetic variants within the conventional regulatory region, such as the 5′ UTR and the 3′ UTR, were analyzed as a priority in several previous studies. rs1547651, which is located in the promoter region, was reported to be significantly associated with bladder cancer; moreover, the TT genotype was linked to a three-fold increased risk for bladder cancer[24]. In our study, the heterozygous genotype was significantly associated with increased ICH risk (adjusted OR=2.11, 95% CI =1.01–4.42) compared with the AA genotype. Moreover, our stratified analyses revealed that the AT genotype had a three-fold increased risk of ICH compared with the AA genotype in females (adjusted OR=3.21, 95% CI=0.99–10.36). Despite the fact that the single SNP association of rs1547651 was not significant after using the stringent Bonferroni correction, the association might still be noteworthy. Using the TFSEARCH

Table 3. Frequency of the distribution of haplotypes in the *VEGFA* gene and their association with risk of hemorrhagic presentation.

Block	Haplotype[a]	Total	ICH	(%)	Unruptured	(%)	*P* value	P_{sim} value[b]	Adjusted OR (95% CI)[c]	*P* value[c]
Block 1	CC	277	168	46.4	109	41.9	0.277	0.283	1.00 (reference)	
	GC	199	103	28.5	96	36.9	**0.030**	**0.033**	0.70 (0.49–1.02)	0.063
	GA	146	91	25.1	55	21.2	0.288	0.324	1.09 (0.72–1.65)	0.692
	Global-stat=4.79			*df*=2		*P*=0.091		P_{sim}[b]=0.089		
Block 2	GCT	285	174	48.1	111	42.7	0.115	0.114	1.00 (reference)	
	ACT	160	94	26	66	25.4	0.993	0.985	0.92 (0.62–1.37)	0.672
	ACC	141	69	19.1	72	27.7	**0.007**	**0.005**	0.62 (0.41–0.93)	**0.020**
	Others[d]	36	25	6.9	11	4.2	0.243	0.231	1.43 (0.68–3.07)	0.341
	Global-stat=9.32			*df*=4		*P*=0.054		P_{sim}[b]=0.043		
Block 3	GCC	428	252	69.8	176	67.7	0.662	0.665	1.00 (reference)	
	CCT	100	51	14.1	49	18.8	0.105	0.117	0.75 (0.48–1.17)	0.202
	GTC	89	57	15.7	32	12.3	0.165	0.169	1.23 (0.76–1.99)	0.393
	Others[d]	5	2	0.6	3	1.2	0.328	0.288	0.48 (0.08–2.95)	0.428
	Global-stat=5.01			*df*=4		*P*=0.286		P_{sim}[b]=0.296		

[a] Polymorphic bases were in 5′–3′ order, as listed in Table 2. Loci chosen for block 1: SNPs 2–3, Loci chosen for block 2: SNPs 4–6, Loci chosen for block 3: SNPs 7–9.

[b] Generated by permutation test with 10 000 times simulation.

[c] Adjusted for age and gender.

[d] Haplotypes with a frequency of less than 0.1 were pooled into one mixed group.

Table 4. Stratified analyses of the associations between the *VEGFA* rs1547651 genotypes and haplotypes in block 2 with risk of hemorrhagic presentation by selected variables.

Variables	rs1547651				Block2			
	Unruptured/ICH		OR (95% CI)[a]		Unruptured/ICH		OR (95% CI)[a]	
	AA No (%)	AT No (%)	AA	AT	GCT No (%)	ACC No (%)	GCT	ACC
Age at diagnosis								
>30	63 (87.5)/ 68 (81.9)	7 (9.7)/ 15 (18.1)	1.00 (reference)	1.96 (0.74–5.15)	61 (42.4)/ 77 (46.4)	42 (29.2)/ 32 (19.3)	1.00 (reference)	0.59 (0.33–1.05)
<=30	52 (89.7)/ 81 (82.7)	4 (6.9)/ 15 (15.3)	1.00 (reference)	2.42 (0.76–7.73)	50 (43.1)/ 97 (49.5)	30 (25.9)/ 37 (18.7)	1.00 (reference)	0.66 (0.37–1.20)
Gender								
Female	44 (88.0)/ 63 (78.8)	4 (8.0)/ 17 (21.3)	1.00 (reference)	**3.21 (0.99–10.36)**	43 (43.0)/ 75 (46.0)	27 (27.0)/ 30 (18.8)	1.00 (reference)	0.68 (0.35–1.29)
Male	71 (88.8)/ 86 (85.1)	7 (8.8)/ 13 (12.9)	1.00 (reference)	1.53 (0.58–4.04)	68 (42.5)/ 99 (49.0)	45 (28.1)/ 39 (19.3)	1.00 (reference)	**0.57 (0.34–0.97)**
BAVM size								
<3 cm	17 (89.5)/ 66 (79.5)	2 (10.5)/ 15 (18.1)	1.00 (reference)	2.11 (0.43–10.35)	16 (42.1)/ 79 (47.6)	9 (23.7)/ 36 (21.7)	1.00 (reference)	0.90 (0.36–2.28)
≥3 cm	98 (88.3)/ 83 (84.7)	9 (8.1)/ 15 (15.3)	1.00 (reference)	1.95 (0.80–4.72)	95 (42.8)/ 95 (48.5)	63 (28.4)/ 33 (16.8)	1.00 (reference)	**0.52 (0.31–0.86)**
Venous drainage								
Exclusively deep	23 (92.0)/ 86 (79.6)	2 (8.0)/ 20 (18.5)	1.00 (reference)	2.88 (0.62–13.4.2)	22 (44.0)/ 104 (48.1)	13 (26.0)/ 40 (18.5)	1.00 (reference)	0.63 (0.29–1.40)
Any superficial	92 (87.6)/ 63 (86.3)	9 (8.6)/ 10 (13.7)	1.00 (reference)	1.52 (0.58–4.01)	89 (42.4)/ 70 (47.9)	59 (28.1)/ 29 (19.9)	1.00 (reference)	0.62 (0.36–1.06)

[a] Adjusted for age and gender.

program (http://mbs.cbrc.jp/research/db/TFSEARCH.html), we found that two possible transcriptional factors, GATA-1 and GATA-3, could bind to the A allele of rs1547651. We hypothesized that this polymorphism variation may affect the expression of *VEGFA* by changing the binding affinity of factors to the mRNA.

Increasing evidence indicates the importance of intronic *VEGFA* polymorphisms as markers of disease susceptibility[24–26]. One Canadian study suggested that rs3025030 was associated with a higher risk of retinopathy. In our study, the genotype distribution of rs3025030 was significantly different between cases and controls (P=0.047). Furthermore, no association was found via logistic regression analyses after adjustment for age and sex. Although the variants of rs3025030 were predicted to cause changes in the binding sites of transcription factors, which may result in the dysfunction of VEGFA expression using FASTSNP[27], the effects of this variant needed to be validated in further studies.

Because we were confident that haplotype-based analysis is more powerful than single-marker analysis[28, 29], we performed this type of analysis to elucidate which haplotype was associated with an increased or a diminished risk of ICH. Although a few studies have been conducted regarding the involvement of *VEGFA* haplotypes in certain diseases[30-32], the haplotypes analyzed in those studies are not comparable with ours because they genotyped different SNPs. In our study, we found that the 'GC' haplotype in block 1 and the 'ACC' haplotype in block 2 were significantly associated with ICH risk (adjusted OR=0.70, 95% CI=0.49–1.02, P_{sim}=0.033 and adjusted OR=0.62, 95% CI=0.41–0.93, P_{sim}=0.005, respectively); moreover, we observed a protective effect of the haplotype 'ACC' derived from rs833069, rs3024994, and rs3025010 in females and those with BAVMs of a size ≥3 cm. We did not, however, see an independent association with the individual SNP present in the haplotype associated with ICH risk. Our hypothesis is that a combined haplotype, rather than a single SNP, is important for ICH.

Despite the fact that our study has several strengths, including a haplotype-based design and a homogeneous population of the same ethnicity, some inherent limitations must be noted. Some selection bias due to hospital-based controls cannot be ruled out. To limit the potential selection bias, we recruited patients by matching the controls to the individuals with BAVMs on the categories of age, sex and residential area. Only nine out of the exhaustive list of SNPs in *VEGFA* were genotyped in this study, and therefore, it is possible that we did not fully capture or represent the genetic variability of the gene; however, SNPs with high priority were selected for this

study based on a careful review of previous functional analyses and association studies of *VEGFA* variation.

In conclusion, the results from our case-control study in a Chinese population suggest that the genetic variants of the VEGFA gene may modulate ICH risk in patients with BAVMs. In particular, we found two haplotypes with a significantly protective effect with respect to ICH risk in patients with BAVMs. Large-scale studies with ethnically diverse populations and functional evaluation of these studies are warranted to confirm our findings.

Acknowledgements

This study was supported by the National Natural Science Foundation of China (No 30500524, 30973103, 81070936, 30800622, and 81001114), and the Scientific Research Foundation for the Returned Overseas Chinese Scholars.

Author contribution

Dr Hong-yan CHEN and Dr Yao ZHAO designed the research and revised the paper; Zhi-ping GONG conducted the experiments and wrote the paper; Ni-dan QIAO, Yu-xiang GU, Jian-ping SONG, Pei-liang LI, and Hui-jia QIU performed the experiments; Wei-wei FAN analyzed the data; and Ying MAO designed the research.

References

1 Arteriovenous Malformation Study Group. Arteriovenous malformations of the brain in adults. N Engl J Med 1999; 340: 1812–8.
2 Pawlikowska L, Tran MN, Achrol AS, McCulloch CE, Ha C, Lind DL, *et al*. UCSF BAVM Study Project: Polymorphisms in genes involved in inflammatory and angiogenic pathways and the risk of hemorrhagic presentation of brain arteriovenous malformations. Stroke 2004; 35: 2294–300.
3 Connolly DT, Heuvelman DM, Nelson R, Olander JV, Eppley BL, Delfino JJ, *et al*. Tumor vascular permeability factor stimulates endothelial cell growth and angiogenesis. J Clin Invest 1989; 84: 1470–8.
4 Ferrara N, Davis-Smyth T. The biology of vascular endothelial growth factor. Endocr Rev 1997; 18: 4–25.
5 Ferrara N. Role of vascular endothelial growth factor in regulation of physiological angiogenesis. Am J Physiol Cell Physiol 2001; 280: C1358–66.
6 Bates DO, Harper SJ. Regulation of vascular permeability by vascular endothelial growth factors. Vascul Pharmacol 2002; 39: 225–37.
7 Ferrara N. Vascular endothelial growth factor as a target for anticancer therapy. Oncologist 2004; 9: 2–10.
8 Hashimoto T, Lawton MT, Wen G, Yang GY, Chaly T Jr, Stewart CL, *et al*. Gene microarray analysis of human brain arteriovenous malformations. Neurosurgery 2004; 54: 410–23.
9 Lee CZ, Xue Z, Zhu Y, Yang GY, Young WL. Matrix metalloproteinase-9 inhibition attenuates vascular endothelial growth factor-induced intracranial hemorrhage. Stroke 2007; 38: 2563–8.
10 Sfar S, Hassen E, Saad H, Mosbah F, Chouchane L. Association of VEGF genetic polymorphisms with prostate carcinoma risk and clinical outcome. Cytokine 2006; 35: 21–8.
11 Howell WM, Bateman AC, Turner SJ, Collins A, Theaker JM. Influence of vascular endothelial growth factor single nucleotide polymorphisms on tumour development in cutaneous malignant melanoma. Genes Immun 2002; 3: 229–32.
12 Kataoka N, Cai Q, Wen W, Shu XO, Jin F, Gao YT, *et al*. Population-based case-control study of VEGF gene polymorphisms and breast cancer risk among Chinese women. Cancer Epidemiol Biomarkers Prev 2006; 15: 1148–52.
13 Lee SJ, Lee SY, Jeon HS, Park SH, Jang JS, Lee GY, *et al*. Vascular endothelial growth factor gene polymorphisms and risk of primary lung cancer. Cancer Epidemiol Biomarkers Prev 2005; 14: 571–5.
14 Awata T, Inoue K, Kurihara S, Ohkubo T, Watanabe M, Inukai K, *et al*. A common polymorphism in the 5′-untranslated region of the VEGF gene is associated with diabetic retinopathy in type 2 diabetes. Diabetes 2002; 51: 1635–9.
15 Vannay A, Dunai G, Bányász I, Szabó M, Vámos R, Treszl A, *et al*. Association of genetic polymorphisms of vascular endothelial growth factor and risk for proliferative retinopathy of prematurity. Paediatr Res 2005; 57: 396–8.
16 Chen HY, Gu YX, Wu WT, Chen D, Li PL, Fan WW, *et al*. Vascular endothelial growth factor A gene polymorphisms and susceptibility to sporadic brain arteriovenous malformations in a Chinese population. J Clin Neurosci 2011; 18: 549–53.
17 Joint Writing Group of the Technology Assessment Committee American Society of Interventional and Therapeutic Neuroradiology; Joint Section on Cerebrovascular Neurosurgery a Section of the American Association of Neurological Surgeons and Congress of Neurological Surgeons; Section of Stroke and the Section of Interventional Neurology of the American Academy of Neurology, Atkinson RP, Awad IA, Batjer HH, Dowd CF, Furlan A, Giannotta SL, *et al*. Reporting terminology for brain arteriovenous malformation clinical and radiographic features for use in clinical trials. Stroke 2001; 32: 1430–42.
18 Jurinke C, van den Boom D, Cantor CR, Koster H. Automated genotyping using the DNA MassArray technology. Methods Mol Biol 2002; 187: 179–92.
19 Akaike H. A new look at the statistical model identification. IEEE Trans Automat Contr 1974; 19: 716–23.
20 Lewontin RC. On measures of gametic disequilibrium. Genetics 1988; 120: 849–52.
21 Gabriel SB, Schaffner SF, Nguyen H, Moore JM, Roy J, Blumenstiel B, *et al*. The structure of haplotype blocks in the human genome. Science 2002; 296: 2225–9.
22 Stephens M, Donnelly P. A comparison of Bayesian methods for haplotype reconstruction from population genotype data. Am J Hum Genet 2003; 73: 1162–9.
23 Jung S, Moon KS, Jung TY, Kim IY, Lee YH, Rhu HH, *et al*. Possible pathophysiological role of vascular endothelial growth factor (VEGF) and matrix metalloproteinases (MMPs) in metastatic brain tumor-associated intracerebral hemorrhage. J Neurooncol 2006; 76: 257–63.
24 García-Closas M, Malats N, Real FX, Yeager M, Welch R, Silverman D, *et al*. Large-scale evaluation of candidate genes identifies associations between VEGF polymorphisms and bladder cancer risk. PLoS Genet 2007; 3: e29.
25 Churchill AJ, Carter JG, Lovell HC, Ramsden C, Turner SJ, Yeung A, *et al*. VEGF polymorphisms are associated with neovascular age-related macular degeneration. Hum Mol Genet 2006; 15: 2955–61.
26 Al-Kateb H, Mirea L, Xie X, Sun L, Liu M, Chen H, *et al*. Multiple variants in vascular endothelial growth factor (VEGFA) are risk factors for time to severe retinopathy in type 1 diabetes: the DCCT/EDIC genetics study. Diabetes 2007; 56: 2161–8.
27 Yuan HY, Chiou JJ, Tseng WH, Liu CH, Liu CK, Lin YJ, *et al*. FASTSNP: an always up-to-date and extendable service for SNP function analysis and prioritization. Nucleic Acids Res 2006; 34: W635–41.

28 Clark AG. The role of haplotypes in candidate gene studies. Genet Epidemiol 2004; 27: 321–33.
29 Han SW, Kim GW, Seo JS, Kim SJ, Sa KH, Park JY, *et al*. VEGF gene polymorphisms and susceptibility to rheumatoid arthritis. Rheumatology (Oxford) 2004; 43: 1173–7.
30 Churchill AJ, Carter JG, Lovell HC, Ramsden C, Turner SJ, Yeung A, *et al*. VEGF polymorphisms are associated with neovascular age-related macular degeneration. Hum Mol Genet 2006; 15: 2955–61.
31 Churchill AJ, Carter JG, Ramsden C, Turner SJ, Yeung A, Brenchley PE, *et al*. VEGF polymorphisms are associated with severity of diabetic retinopathy. Invest Ophthalmol Vis Sci 2008; 49: 3611–6.
32 Tsai SJ, Hong CJ, Liou YJ, Chen TJ, Chen ML, Hou SJ, *et al*. Haplotype analysis of single nucleotide polymorphisms in the vascular endothelial growth factor (VEGFA) gene and antidepressant treatment response in major depressive disorder. Psychiatry Res 2009; 169: 113–7.

Acta Pharmacologica Sinica (2011) 32: 1078–1084
 1671-4083/11 $32.00
www.nature.com/aps

Original Article

Association of the antihypertensive response of iptakalim with KCNJ11 (Kir6.2 gene) polymorphisms in Chinese Han hypertensive patients

Rui-feng DUAN[1, #], Wen-yu CUI[1, #], Hai WANG[1, 2, *]

[1]Cardiovascular Drug Research Center, Institute of Health and Environmental Medicine, Academy of Military Medical Sciences, Beijing 100850, China; [2]Thadweik Academy of Medicine, Beijing 100039, China

Aim: To study the relationship between the antihypertensive response of iptakalim and KCNJ11 polymorphisms in Chinese Han hypertensive patients.
Methods: One hundred sixty two Chinese Han hypertensive patients were administered iptakalim (5 or 10 mg/d, po) for 8 weeks. Before the treatment and 24 h after completing the treatment blood pressure (BP) was measured. Genotyping was performed using direct sequencing.
Results: Four common A190A, E23K, I337V and 3'UTR +62 G/A polymorphisms were found in KCNJ11. The E23K, I337V and 3'UTR +62 G/A polymorphisms were in complete linkage disequilibrium, and I337V was used as a representative. There were no significant differences in age, body mass index, sex, baseline systolic BP (SBP) and diastolic BP (DBP) among the 3 genotypes for the four polymorphisms. Significant association was found between SBP response and the polymorphisms (adjusted regression coefficient: 3.5 [1.2] mmHg; *P*=0.003 for the A190A polymorphism; adjusted regression coefficient: 3.1 [1.2] mmHg; *P*=0.012 for the I337V polymorphism). The patients with TT genotype for A190A polymorphism had higher clinical efficacy than those with CC genotype.
Conclusion: The results suggest the KCNJ11 polymorphisms are associated with the SBP-lowering response of short-term iptakalim therapy in Chinese Han hypertensive patients.

Keywords: KCNJ11; Kir6.2; genotype; hypertension; ATP-sensitive potassium channel opener; iptakalim; polymorphisms; systolic blood pressure; diastolic blood pressure

Acta Pharmacologica Sinica (2011) 32: 1078–1084; doi: 10.1038/aps.2011.85; published online 18 Jul 2011

Introduction

Essential hypertension is the leading cause of cardiovascular morbidity and mortality worldwide, affecting about 20% of the adult population and only 23%–41% of hypertensive patients receiving antihypertensive drugs achieve adequate blood pressure control[1, 2]. Many drugs are effective in treating hypertension, although individuals can respond differently to the same drug. Interindividual variation in the efficacy of medications may be influenced by genetic variations[2–4]. Hypertension pharmacogenetics seeks to find genetic predictors of response to drugs that lower blood pressure. More and more studies have investigated associations between genetic polymorphisms and response to antihypertensive drugs[5–7].

Iptakalim is a novel K_{ATP} opener with antihypertensive properties targeting small arteries of hypertensive status in different models of hypertension in rats and dogs. It can produce long-lasting hypotensive effects without tolerance. At the same time it exertes a protective effect against hypertensive damage to target organs[8–15]. Iptakalim is an effective and well tolerated antihypertensive drug. Individual variations for its antihypertensive effects have been observed[16]. Genetic variations that alter the structure, configuration, activity, or quantity of the drug target receptors or target-related regulation factors may contribute to individual variations in drug response[17]. Among the 3 different subtypes of K_{ATP} channels heterologously expressed in human embryonic kidney cells and *Xenopus* oocytes, iptakalim exhibits significant selectivity for SUR2B/Kir6.1 channels, mild effects on SUR2A/Kir6.2 channels, and fails to open SUR1/Kir6.2 channels. The KCNJ11 gene, which encodes the Kir6.2 subunit of the K_{ATP} channel, is among the candidate target genes for antihyperten-

# These authors contributed equally to this work.
* To whom correspondence should be addressed.
E-mail wh9588@yahoo.com.cn
Received 2011-02-27 Accepted 2011-05-18

sive drug iptakalim[8].

In this study, we aimed to investigate the polymorphisms of KCNJ11 in 162 Chinese patients with essential hypertension and their possible association with the antihypertensive response of iptakalim.

Materials and methods

Subjects

The material studied comes from all subjects who finished the trials in 5 centers of the phase-three clinical trials of iptakalim which is a randomized and double-blind trial performed in 14 centers in 11 cities in China. We studied 162 non-related Chinese Han patients with essential hypertension (81 men, 81 women; mean age±SD: 55±9 years; range: 26–74 years). Patients met World Health Organization-International Society of Hypertension criteria for hypertension (systolic BP [SBP]≥140 mmHg or diastolic BP [DBP]≥90 mmHg). Trained investigators assessed patents' BP on at least three different occasions. All patients underwent a complete physical examination. Secondary causes of hypertension and heart, liver, and kidney diseases were excluded by history and by physical and laboratory examinations. The diabetic patients (the fasting plasma glucose concentration>11 mmol/L) were excluded in this study. After a 2-weeks single-blind placebo run-in period, all patients were treated orally with iptakalim (Thadweik Academy of Medicine, Beijing, China) at a single daily fixed dosage of 5 mg (one tablet per day) for 4 consecutive weeks. After that, patients whose BP was less than 140/90 mmHg continued the same dose regimen for another 4 weeks. In patients whose BP was not adequately controlled (BP≥140/90 mmHg), the dose was doubled for the following 4 weeks. Patients were required to take their iptakalim around 9 am and carefully record the time they took the tablet. Blood pressure was measured before taking medicine on the first day and 24 h after 8 weeks of treatment. Three consecutive measurements were taken on the right arm of quietly seated participants with 1 min interval between replicates. If the difference between the measurements was more than 4 mmHg, the patient was asked to rest for 5 min, and then repeated the measurements. In all of our analysis, the average of three consecutive blood pressure readings was used. Written informed consent was obtained from all patients enrolled in the study in accordance with principles of the Declaration of Helsinki. The protocol of the study was approved by the institutional Ethics Committee.

Genotyping analysis

Genomic DNA was isolated from peripheral leukocytes. KCNJ11 gene was amplified by PCR and sequenced. The multiple sequence alignment program ClustalW2 (http://www.ebi.ac.uk/Tools/msa/clustalw2/) and Chromas program were used for genotyping. The primers of KCNJ11 were designed using Primer3 (http://frodo.wi.mit.edu/primer3/). For specific amplification of DNA samples, two rounds of PCR amplification were carried out for KCNJ11. The primers and the amplification conditions for the first PCR were as follows: forward F1, 5′-ACTGGGATTACAGGCGTGAG-3′ and reverse R1, 5′-CCTGACCACAGGCACTTCTT-3′, initial denaturation at 95 °C for 5 min followed by 35 cycles of denaturation at 95 °C for 30 s, annealing at 58 °C for 30 s, and extension at 72 °C for 2 min, and final extension at 72 °C for 5 min. The PCR product is a 1824-bp fragment which was diluted (1:50) with water and used as templates to the second PCR. Amplification conditions for the second PCR were the same as that given above but the primers used were different (forward F2, 5′-GACTCTGCAGTGAGGCCCTA-3′ and reverse R2, 5′-CCTGCTGAGGCCAGAAATAG-3′). The product of the second PCR was a 1421-bp fragment which was sequenced (ABI 3730XL sequencer, PE Applied Biosystem, USA). cDNA and protein sequences were numbered according to NCBI ORF finder (http://www.ncbi.nlm.nih.gov/gorf/orfig.cgi; GenBank NM_000525.3) with nucleotide numbering beginning with the first Met.

Statistical analysis

Values are expressed as the mean±SD. The means for continuous variables in the 2 groups were compared using *t*-test and the differences among three groups were analyzed by one-way analysis of variance (ANOVA). The prevalence of categorical variables was compared using χ^2-test. The blood pressure (BP) response was defined as the blood pressure before treatment minus the blood pressure at the end of 8 weeks of treatment. Multiple linear regression and logistic regression analyses were used to assess the influence of KCNJ11 polymorphisms on baseline BP and antihypertensive efficacy, with adjustment for potential confounding factors, including baseline BP, age, sex, and BMI. The SPSS 13.0 statistical package (SPSS, Chicago, IL, USA) was used for analysis. All tests were two-tailed and $P<0.05$ was considered statistically significant. Linkage disequilibrium and haplotypes analysis were done with a SHEsis software[18, 19].

Results

Clinical characteristics

For the 162 patients in this study, there were no significant differences in age, sex, BMI, smoking status, alcohol consumption, baseline BP, heart rate and biochemical parameters among the three genotypes of the four polymorphisms before iptakalim treatment. Significant decreases in SBP and DBP occurred after treatment in all genotype groups ($P<0.01$). The posttreatment DBP was not different among the three groups, while the posttreatment SBP was both lower in patients with TT genotype of the A190A polymorphism and AA genotype of the I337V polymorphism (Table 1).

Allele and genotype frequencies

Five polymorphisms were identified in 162 Chinese hypertensive patients. Four known polymorphisms were E23K, A190A, I337V and 3′UTR +62 G/A (Figure 1). Complete information on genotypes and phenotypes was available for 162 patients. For A190A polymorphism, the frequencies of the C and T alleles were 55.6% and 44.4%, respectively, and the frequencies

Table 1. Clinical characteristics and biochemical parameters by KCNJ11 gene polymorphisms.

Variable	KCNJ11 A190A genotype				KCNJ11 I337V genotype			
	CC (*n*=58)	CT (*n*=64)	TT (*n*=40)	*P*#	GG (*n*=35)	GA (*n*=70)	AA (*n*=57)	*P*#
Dose (no increase/increase)	24/34	39/25	24/16	0.063	17/18	35/35	35/22	0.352
Sex (male/female)	30/28	34/30	17/23	0.544	18/17	35/35	28/29	0.977
Age (years)	55.6 (8.5)	55.3 (9.0)	55.5 (9.7)	0.981	54.7 (8.6)	55.1 (8.2)	56.4 (10.0)	0.631
Smoking status (never/current)	43/15	46/18	33/7	0.463	27/8	48/22	47/10	0.191
Alcohol consumption (never/current)	43/15	49/15	32/8	0.800	24/11	55/15	45/12	0.458
BMI (kg/m^2)	25.2 (2.4)	25.3 (2.7)	25.5 (2.9)	0.845	25.1 (2.4)	25.0 (2.7)	25.8 (2.7)	0.197
Sodium (mmol/L)	141.5 (3.2)	141.9 (3.0)	141.4 (2.6)	0.558	141.1 (3.1)	141.9 (2.9)	141.7 (3.1)	0.459
Potassium (mmol/L)	4.1 (0.3)	4.1 (0.4)	4.2 (0.4)	0.058	4.1 (0.3)	4.1 (0.4)	4.2 (0.4)	0.235
Chloride (mmol/L)	104.0 (3.1)	103.4 (2.9)	103.6 (3.0)	0.568	103.8 (3.0)	103.7 (3.1)	103.5 (2.8)	0.833
Glucose (mmol/L)	5.7 (1.4)	5.5 (1.3)	5.3 (1.3)	0.338	5.7 (1.5)	5.6 (1.5)	5.4 (1.1)	0.512
Uric acid (μmol/L)	307.4 (79.3)	314.8 (96.8)	324.2 (75.9)	0.638	308.8 (74.7)	313.4 (98.3)	319.3 (75.7)	0.841
Total cholesterol (mmol/L)	5.3 (1.1)	5.1 (0.9)	5.2 (0.8)	0.446	5.3 (1.3)	5.2 (0.9)	5.1 (0.8)	0.441
Triglyceride (mmol/L)	2.3 (1.8)	2.0 (1.3)	1.8 (1.0)	0.271	2.2 (1.8)	2.2 (1.6)	1.8 (1.0)	0.264
HDL cholesterol (mmol/L)	1.3 (0.3)	1.4 (0.4)	1.4 (0.5)	0.365	1.4 (0.3)	1.3 (0.4)	1.4 (0.4)	0.548
GPT (U/L)	25.9 (13.3)	24.7 (13.9)	25.6 (13.0)	0.875	28.1 (15.1)	24.1 (12.8)	25.2 (12.9)	0.353
Pretreatment SBP (mmHg)	153.6 (14.0)	152.6 (12.1)	151.4 (11.6)	0.710	151.1 (12.1)	153.8 (13.3)	152.2 (12.2)	0.564
Posttreatment SBP (mmHg)	145.0 (14.3)^c	141.3 (12.0)^c	137.3 (11.4)^c	0.015	142.8 (13.9)^c	144.1 (13.3)^c	137.8 (11.4)^c	0.019
Pretreatment DBP (mmHg)	100.4 (4.3)	99.7 (3.8)	99.8 (4.1)	0.622	99.7 (3.9)	100.2 (4.3)	99.8 (3.8)	0.791
Posttreatment DBP (mmHg)	90.4 (10.9)^c	88.2 (7.1)^c	87.5 (8.0)^c	0.208	89.0 (10.2)^c	90.0 (8.9)^c	87.3 (8.0)^c	0.247
Pretreatment HR (beats/min)	72.0 (10.2)	70.1 (9.3)	71.0 (11.1)	0.582	72.0 (9.4)	70.1 (9.3)	71.4 (11.3)	0.628
Posttreatment HR (beats/min)	70.1 (8.5)	70.1 (8.4)	71.0 (9.6)	0.523	70.7 (7.8)	69.8 (8.5)	67.5 (9.4)	0.186
Change in HR at 8 weeks (beats/min)	1.9 (8.4)	0.9 (10.2)	3.0 (9.4)	0.544	1.3 (8.4)	0.3 (9.2)	3.8 (9.8)	0.103

Data are presented as the mean (SD). #ANOVA and Pearson's χ^2 tests were applied to continuous and categorical variables, respectively. The E23K, I337V and 3′UTR +62 G/A polymorphisms are in complete linkage disequilibrium (LD). c*P*<0.01 between pretreatment and posttreatment BP. Change in HR at 8 weeks is pretreatment HR minus posttreatment HR.

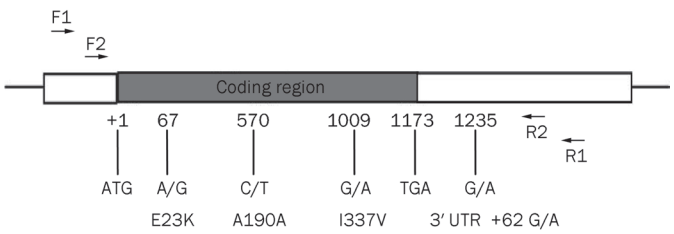

Figure 1. The most common polymorphisms in KCNJ11 were E23K, A190A, I337V, 3′ UTR +62 G/A.

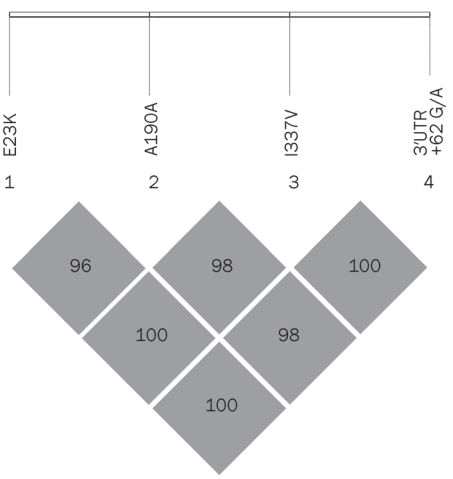

Figure 2. Linkage disequilibrium plot of computed pairwise LD statistics for four polymorphisms.

of the CC, CT, and TT genotypes were 58/162 (35.8%), 64/162 (39.5%), and 40/162 (24.7%), respectively. E23K, I337V, and 3′UTR +62 G/A were found to be in complete LD (D′=1, Figure 2). We will use I337V polymorphism as a representative polymorphism for the next analysis. The frequencies of the G and A alleles were 43.2% and 56.8%, respectively, and the frequencies of the GG, GA, and AA genotypes were 35/162 (21.6%), 70/162 (43.2%), and 57/162 (35.2%), respectively. Patients with TT genotype of the A190A polymorphism are all AA genotype of the I337V polymorphism. The study population showed no deviation in genotype frequencies from those predicted by the Hardy-Weinberg equilibrium. In addition, we identified two synonymous mutations (C480T, N160N; C579T, H193H) and one missense mutation (C1105T, R369C) in three patients, and they are all heterozygous. Blood pressure of the patient with the novel R369C missense mutation which is yet unknown functional consequences can be well controlled by iptakalim. The fifth polymorphism found in this population is I284I, and the frequencies of genotypes were 157 CC, 3 CA, 1 AA, and 1 CT. Haplotype frequencies were calcu-

lated with the SHEsis program. There are 16 possible haplotypes of these four loci (E23K, A190A, L267L, and I337V), but only three haplotypes were observed due to complete linkage disequilibrium among E23K, L267L, and I337V. They are H1 (A-C-G-G, 43%), H2 (G-C-A-A, 13%), and H3 (G-T-A-A, 44%). Two kinds of Kir6.2 pore-forming proteins may be seen in this population: one is 23K/337V, and the other is 23E/337I. The patients with H1H1 genotype (A-C-G-G/A-C-G-G, *n*=35) may have 23K/337V pore-forming proteins. Those with H1H2 or H1H3 genotypes (A-C-G-G/G-C-A-A or A-C-G-G/G-T-A-A, *n*=70) may have 23K/337V and 23E/337I pore-forming proteins. Those with H2H2, H2H3 or H3H3 genotypes (G-C-A-A/G-C-A-A, G-C-A-A/G-T-A-A, or G-T-A-A/G-T-A-A, *n*=57) may have 23E/337I pore-forming proteins. Due to complete LD among E23K, I337V, and 3'UTR +62 G/A, these genotypes can be represented by the GG (H1H1, *n*=35), GA (H1H2 or H1H3, *n*=70) and AA (H2H2, H2H3, or H3H3, *n*=57) genotypes of the I337V polymorphism, respectively. Therefore I337V can be used as a representative polymorphism for the next analysis.

Association of antihypertensive response with the four polymorphisms

The reduction in SBP and DBP was both largest in the TT (AA) group and smallest in the CC (GG) group. Reductions in SBP were statistically significant between the TT (AA) group and CC (GG) group for the A190A and I337V polymorphisms (-14.8 [10.3] and -9.0 [14.7] mmHg, respectively for the A190A polymorphism, *P*=0.042; -14.4 [10.7] and -8.3 [12.8] mmHg, respectively for the I337V polymorphism, *P*=0.037). The relationship between antihypertensive response and the A190A and I337V polymorphisms was further examined by multiple linear regression analysis, with adjustment for age, sex, BMI and baseline BP (Table 2). Significant association was found between SBP response and the A190A and I337V polymorphisms (SBP response-crude β±SE: 2.8 [1.4], *P*=0.042; adjusted β±SE: 3.5 [1.2], *P*=0.003 for the A190A polymorphism; crude β±SE: 3.2 [1.4], *P*=0.026; adjusted β±SE: 3.1 [1.2], *P*=0.012 for the I337V polymorphism).

These findings were confirmed in the logistic regression analysis, in which the continuous BP values were transformed to dichotomous variables based on clinical antihypertensive efficacy (Table 3). Antihypertensive efficacy was based on achievement of the normal clinical standard, defined as a SBP<140 mmHg (SBP analysis), a DBP<90 mmHg (DBP analysis), and a SBP<140 mmHg and a DBP<90 mmHg (SBP and DBP analysis); failure to achieve this standard constituted lack of antihypertensive efficacy. After adjustment for age, sex, BMI and baseline BP, the proportion of patients achieving antihypertensive efficacy was significantly larger in those with the TT genotype than those with the CC genotype for the A190A polymorphism (SBP analysis – 60.0% *vs* 34.5%; adjusted odds ratio [OR]: 3.33; 95% CI: 1.30–8.55; *P*=0.012; DBP analysis – 67.5% *vs* 44.8%; adjusted odds ratio [OR]: 2.47; 95% CI: 0.97–6.3; *P*=0.057; SBP and DBP analysis – 50.0% *vs* 25.9%; adjusted odds ratio [OR]: 3.65; 95% CI: 1.36–9.83; *P*=0.010). Though the proportion of patients achieving antihypertensive efficacy in those with the AA genotype was all highest for the I337V polymorphism, it was only significantly larger compared with those with the GG genotype in DBP analysis (DBP analysis – 68.4% *vs* 48.6%; adjusted odds ratio [OR]: 2.66; 95% CI: 0.96–6.0; *P*=0.049).

Discussion

Kir6.2 is one of the pore-forming subunits of the K_{ATP} channels which provide a unique link between cellular energetics and electrical excitability[20]. The KCNJ11 gene encoding human K_{ATP} subunit Kir6.2 is located on chromosome 11p15.1 with only one 1173-bp exon. This work investigated the polymorphisms of KCNJ11 gene in 162 Chinese hypertensive population treated by iptakalim. Our data revealed that five polymorphisms were found in this population. Four known polymorphisms were E23K, A190A, I337V, and 3'UTR +62 G/A. E23K/I337V/3'UTR +62 G/A were found to be in complete LD in this population. The fifth polymorphism found in this population is I284I, and the frequencies of genotypes were 157

Table 2. Multiple linear regression analysis of the association between blood pressure (BP) response and the KCNJ11 A190A and I337V polymorphisms.

	Fall in BP mean (SD), mmHg			Difference in BP response			
				Alone		Adjust	
	CC (GG)	CT (GA)	TT (AA)	β (SE)	*P*	β (SE)	*P*
KCNJ11 A190A							
Systolic	8.6 (14.5)	11.2 (14.4)	14.3 (10.4)	2.8 (1.4)	0.042	3.5 (1.2)	0.003
Diastolic	10.0 (9.5)	11.6 (7.1)	12.3 (6.9)	1.2 (0.8)	0.144	1.2 (0.8)	0.114
KCNJ11 I337V							
Systolic	8.3 (12.8)	9.8 (15.7)	14.4 (10.7)	3.2 (1.4)	0.026	3.1 (1.2)	0.012
Diastolic	10.7 (8.8)	10.3 (8.2)	12.5 (7.2)	1.0 (0.8)	0.221	1.0 (0.8)	0.210

Each polymorphism was first considered by itself (*ie*, alone) as a predictor of BP response, then after adjustment for the concomitant variables(*ie*, after covariates) which included pretreatment (baseline) BP, gender, age, and body mass index. β (SE) is the regression coefficient (standard error). Genotype in the bracket is for the I337V polymorphism.

Table 3. Logistic regression analysis of the association between antihypertensive efficacy and KCNJ11 A190A and I337V polymorphisms.

		KCNJ11 A190A polymorphism					
	Clinical efficacy[a]	Crude			Adjusted[b]		
	No (%)	OR	95% CI	*P*	OR	95% CI	*P*
SBP							
CC (GG)	20 (34.5)	1.00	–	–	1.00	–	–
CT (GA)	27 (42.2)	1.386	0.665–2.889	0.383	1.403	0.609–3.232	0.426
TT(AA)	24 (60.0)	2.850	1.239–6.553	0.014	3.332	1.298–8.551	0.012
DBP							
CC (GG)	26 (44.8)	1.00	–	–	1.00	–	–
CT (GA)	40 (62.5)	2.051	0.995–4.230	0.052	2.218	0.987–4.986	0.054
TT (AA)	27 (67.5)	2.556	1.103–5.920	0.029	2.474	0.972–6.297	0.057
SBP and DBP							
CC (GG)	15 (25.9)	1.00	–	–	1.00	–	–
CT (GA)	25 (39.1)	1.838	0.848–3.981	0.123	2.058	0.849–4.987	0.110
TT (AA)	20 (50.0)	2.867	1.220–6.735	0.016	3.651	1.356–9.830	0.010
		KCNJ11 I337V polymorphism					
	Clinical efficacy[a]	Crude			Adjusted[b]		
	No (%)	OR	95% CI	*P*	OR	95% CI	*P*
SBP							
CC (GG)	15 (42.9)	1.00	–	–	1.00	–	–
CT (GA)	25 (35.7)	0.741	0.323–1.697	0.478	0.806	0.316–2.055	0.651
TT(AA)	31 (54.4)	1.590	0.681–3.714	0.284	2.186	0.826–5.785	0.115
DBP							
CC (GG)	17 (48.6)	1.00	–	–	1.00	–	–
CT (GA)	37 (52.9)	1.187	0.527–2.674	0.679	1.376	0.497–2.735	0.494
TT (AA)	39 (68.4)	2.294	0.964–5.457	0.061	2.658	0.957–5.983	0.049
SBP and DBP							
CC (GG)	11 (31.4)	1.00	–	–	1.00	–	–
CT (GA)	23 (32.9)	1.068	0.447–2.550	0.883	1.220	0.453–3.289	0.694
TT (AA)	26 (45.6)	1.830	0.756–4.428	0.180	2.715	0.971–7.594	0.057

BP, blood pressure; SBP, systolic BP; DBP, diastolic BP. Genotype in the bracket is for the I337V polymorphism. [a]Clinical efficacy was defined as a SBP<140 mmHg (SBP analysis), a DBP<90 mmHg (DBP analysis), and a SBP<140 mmHg and DBP<0 mmHg (SBP and DBP analysis). [b]The generalized estimating equation model was adjusted for age, sex, body mass index, and baseline BP.

CC, 3 CA, 1 AA, and 1 CT. In addition, we identified two synonymous mutations (C480T, N160N; C579T, H193H) and one nonsynonymous mutation (C1105T, R369C) in three patients, respectively. The other polymorphisms reported in Germans were not found in this population[21]. This might somewhat reflect the racial difference.

The association of the four common polymorphisms of KCNJ11 gene and the BP response to iptakalim were further investigated. The four polymorphisms were significantly associated with SBP response to iptakalim (adjusted regression coefficient: 3.5 [1.2] mmHg; *P*=0.003 for the A190A polymorphism; adjusted regression coefficient: 3.1 [1.2] mmHg; *P*=0.012 for the I337V polymorphism). Patients with the TT (for the A190A polymorphism) and AA genotype (for the I337V polymorphism) exhibited greater systolic BP reduction and higher clinical efficacy than those with the CC (for the A190A polymorphism) and GG genotype (for the I337V polymorphism), respectively. Therefore the four polymorphisms may be used as genetic markers to predict SBP response and antihypertensive efficacy to iptakalim. To our knowledge, this study appears to be the first study to investigate the polymorphisms of KCNJ11 gene and the association of these polymorphisms with BP and BP response to antihypertensive drugs in Chinese Han hypertensive patients.

E23K and I337V are missense mutations which have functional consequences, however, A190A is synonymous mutation which has not very likely important functional consequences. The reason for A190A as a better marker for predicting SBP response of iptakalim may be explained by its linkage disequilibrium with other putative effective polymor-

phisms/mutations or the transcription level of the different genotypes. Only three haplotypes were observed due to complete LD among E23K, I337V, and 3′UTR +62 G/A. They are H1 (A-C-G-G, 43%), H2 (G-C-A-A, 13%), and H3 (G-T-A-A, 44%). Therefore there are two kinds of Kir6.2 pore-forming proteins in this population, one is 23K/337V, and the other is 23E/337I. The SBP response to iptakalim in the patients with the 23E/337I homozygotes (GG genotype for E23K polymorphism; AA genotype for I337V polymorphism) is greater than those with the 23K/337V homozygotes (AA genotype for E23K polymorphism; GG genotype for I337V polymorphism). The difference of Kir6.2 subunit may affect the function of K_{ATP} channels. Kir6.2 (23K/337V) polymorphic K_{ATP} channel has been reported that it decreases ATP sensitivity of K_{ATP} channels at physiological ATP concentrations and it has increased acyl CoA sensitivity which resides primarily in the Kir6.2 subunit[22]. The E23K polymorphism in KCNJ11 gene appeared to be related to high susceptibility to coronary heart disease[23]. This polymorphism is also associated with left ventricular size in hypertensive individuals[24]. The results of Kir6.2-knockout mice experiment indicate that the Kir6.2 subunit mediates the depression of cardiac excitability and contractility induced by KCOs and it plays no discernible role in the arterial tree[25]. KCNJ11 E23K polymorphisms may also affect therapeutic efficacy of repaglinide[26, 27]. Iptakalim exhibits mild effects on SUR2A/Kir6.2 channels[8]. It is possible that the different composition of Kir6.2 pore-forming proteins might in part account for the different SBP response to iptakalim in Chinese Han hypertensive patients.

The limitation of this study is the lack of normal control group. This study shows that the four KCNJ11 polymorphisms were not related to baseline BP in the hypertensive patients. KCNJ11 polymorphisms were reported to be associated with blood pressure variation and hypertension in the Japanese and Korean population[28–30]. Further large scale association studies compared with control subjects are needed to clarify whether these polymorphisms are associated with the pathogenesis of hypertension in Chinese Han population.

In conclusion, we found five polymorphisms in KCNJ11 and demonstrated that polymorphisms of KCNJ11 are associated with the antihypertensive response of iptakalim in Chinese Han hypertensive patients. Patients with the TT genotype (for the A190A polymorphism) exhibited a more pronounced SBP reduction and higher clinical efficacy in response to iptakalim compared to patients with the CC genotype. It may be used as marker for predicting SBP response to iptakalim. This implies the advantage of genotyping for selecting the optimal antihypertensive treatment for individual patient.

Acknowledgements

We thank the patients for their participation. This study was supported by the grants from National Key Technologies R&D program of China (No 2008ZXJ09004-018).

Author contribution

Hai WANG designed research; Rui-feng DUAN performed research; Wen-yu CUI recruited patients; and Rui-feng DUAN analyzed data and wrote the paper.

References

1 Zhang S, Mao G, Zhang Y, Tang G, Wen Y, Hong X, *et al*. Association between human atrial natriuretic peptide Val7Met polymorphism and baseline blood pressure, plasma trough irbesartan concentrations, and the antihypertensive efficacy of irbesartan in rural Chinese patients with essential hypertension. Clin Ther 2005; 27: 1774–84.

2 Taverne K, de Groot M, de Boer A, Klungel O. Genetic polymorphisms related to the renin-angiotensin-aldosterone system and response to antihypertensive drugs. Expert Opin Drug Metab Toxicol 2010; 6: 439–60.

3 Trotta R, Donati MB, Iacoviello L. Trends in pharmacogenomics of drugs acting on hypertension. Pharmacol Res 2004; 49: 351–6.

4 Arnett DK, Claas SA. Pharmacogenetics of antihypertensive treatment: detailing disciplinary dissonance. Pharmacogenomics 2009; 10: 1295–307.

5 Sherva R, Ford CE, Eckfeldt JH, Davis BR, Boerwinkle E, Arnett DK. Pharmacogenetic effect of the stromelysin (MMP3) polymorphism on stroke risk in relation to antihypertensive treatment: the genetics of hypertension associated treatment study. Stroke 2011; 42: 330–5.

6 Niu Y, Gong Y, Langaee TY, Davis HM, Elewa H, Beitelshees AL, *et al*. Genetic variation in the beta2 subunit of the voltage-gated calcium channel and pharmacogenetic association with adverse cardiovascular outcomes in the international verapamil SR-trandolapril study genetic substudy (INVEST-GENES). Circ Cardiovasc Genet 2010; 3: 548–55.

7 Johnson JA, Boerwinkle E, Zineh I, Chapman AB, Bailey K, Cooper-DeHoff RM, *et al*. Pharmacogenomics of antihypertensive drugs: rationale and design of the Pharmacogenomic Evaluation of Antihypertensive Responses (PEAR) study. Am Heart J 2009; 157: 442–9.

8 Pan Z, Huang J, Cui W, Long C, Zhang Y, Wang H. Targeting hypertension with a new adenosine triphosphate-sensitive potassium channel opener iptakalim. J Cardiovasc Pharmacol 2010; 56: 215–28.

9 Wang H, Zhang YL, Chen YP. Targeting small arteries of hypertensive status with novel ATP-sensitive potassium channel openers. Curr Vasc Pharmacol 2005; 3: 119–24.

10 Gao S, Long CL, Wang RH, Wang H. K_{ATP} activation prevents progression of cardiac hypertrophy to failure induced by pressure overload via protecting endothelial function. Cardiovasc Res 2009; 83: 444–56.

11 Wang H, Tang Y, Wang L, Long CL, Zhang YL. ATP-sensitive potassium channel openers and 2,3-dimethyl-2-butylamine derivatives. Curr Med Chem 2007; 14: 133–55.

12 Wang H, Long CL, Zhang YL. A new ATP-sensitive potassium channel opener reduces blood pressure and reverses cardiovascular remodeling in experimental hypertension. J Pharmacol Exp Ther 2005; 312: 1326–33.

13 Chen YP, Qiu CR, Wang H. Cardiovascular pharmacological characterization of novel 2,3-dimethyl-2-butylamine derivatives in rats. Life Sci 2004; 75: 2131–42.

14 Chen YP, Cui WY, Wang H. Selective actions of iptakalim on the subtypes of K_{ATP} channels. Chin Pharmacol Bull 2006; 22: 278–84.

15 Long CL, Qin XC, Pan ZY, Chen K, Zhang YF, Cui WY, *et al*. Activation of ATP-sensitive potassium channels protects vascular endothelial cells from hypertension and renal injury induced by hyperuricemia. J Hypertens 2008; 26: 2326–38.

16 Duan RF, Cui WY, Gao HY, Wang XP, Hu SK, Liu W, *et al*. Correlation between ACE gene I/D polymorphism and clinical efficacy of iptakalim in Chinese Han hypertensive population. Chin J Clin Pharmacol Ther

2010; 15: 961–6.
17 Evans WE, Relling MV. Pharmacogenomics: translating functional genomics into rational therapeutics. Science 1999; 286: 487–91.
18 Shi YY, He L. SHEsis, a powerful software platform for analyses of linkage disequilibrium, haplotype construction, and genetic association at polymorphism loci. Cell Res 2005; 15: 97–8.
19 Li Z, Zhang Z, He Z, Tang W, Li T, Zeng Z, *et al*. A partition-ligation-combination-subdivision EM algorithm for haplotype inference with multiallelic markers: update of the SHEsis (http://analysis.bio-x.cn). Cell Res 2009; 19: 519–23.
20 Nichols CG. K_{ATP} channels as molecular sensors of cellular metabolism. Nature 2006; 440: 470–6.
21 Jeron A, Hengstenberg C, Holmer S, Wollnik B, Riegger GA, Schunkert H, *et al*. KCNJ11 polymorphisms and sudden cardiac death in patients with acute myocardial infarction. J Mol Cell Cardiol 2004; 36: 287–293.
22 Riedel MJ, Boora P, Steckley D, de Vries G, Light PE. Kir6.2 polymorphisms sensitize beta-cell ATP-sensitive potassium channels to activation by acyl CoAs: a possible cellular mechanism for increased susceptibility to type 2 diabetes? Diabetes 2003; 52: 2630–5.
23 Xiong C, Zheng F, Wan J, Zhou X, Yin Z, Sun X. The E23K polymorphism in Kir6.2 gene and coronary heart disease. Clin Chim Acta 2006; 367: 93–7.
24 Reyes S, Terzic A, Mahoney DW, Redfield MM, Rodeheffer RJ, Olson TM. K_{ATP} channel polymorphism is associated with left ventricular size in hypertensive individuals: a large-scale community-based study. Hum Genet 2008; 123: 665–7.
25 Suzuki M, Li RA, Miki T, Uemura H, Sakamoto N, Ohmoto-Sekine Y, *et al*. Functional roles of cardiac and vascular ATP-sensitive potassium channels clarified by Kir6.2-knockout mice. Circ Res 2001; 88: 570–7.
26 He YY, Zhang R, Shao XY, Hu C, Wang CR, Lu JX, *et al*. Association of KCNJ11 and ABCC8 genetic polymorphisms with response to repaglinide in Chinese diabetic patients. Acta Pharmacol Sin 2008; 29: 983–9.
27 Yu M, Xu XJ, Yin JY, Wu J, Chen X, Gong ZC, *et al*. KCNJ11 Lys23Glu and TCF7L2 rs290487(C/T) polymorphisms affect therapeutic efficacy of repaglinide in Chinese patients with type 2 diabetes. Clin Pharmacol Ther 2010; 87: 330–5.
28 Koo BK, Cho YM, Park BL, Cheong HS, Shin HD, Jang HC, *et al*. Polymorphisms of KCNJ11 (Kir6.2 gene) are associated with Type 2 diabetes and hypertension in the Korean population. Diabet Med 2007; 24: 178–86.
29 Kokubo Y, Tomoike H, Tanaka C, Banno M, Okuda T, Inamoto N, *et al*. Association of sixty-one non-synonymous polymorphisms in forty-one hypertension candidate genes with blood pressure variation and hypertension. Hypertens Res 2006; 29: 611–9.
30 Sakamoto Y, Inoue H, Keshavarz P, Miyawaki K, Yamaguchi Y, Moritani M, *et al*. SNPs in the KCNJ11-ABCC8 gene locus are associated with type 2 diabetes and blood pressure levels in the Japanese population. J Hum Gene 2007; 52: 781–93.